ČESKÉ VYSOKÉ UČENÍ TECHNICKÉ V PRAZE
FAKULTA STROJNÍ
ÚSTAV MATERIÁLOVÉHO INŽENÝRSTVÍ

HABILITAČNÍ PRÁCE

Funkční povlaky pro tribologické aplikace
Functional coatings for tribological applications

Ladislav Cvrček

PRAHA 2018

Anotace

Práce prezentuje souhrn poznatků, které mají za cíl objasnit závislosti mezi strukturou povlaků a jejich tribologickými vlastnostmi. Zaměřuje se především na tribologické systémy pracující v extrémních podmínkách za vysokých teplot nebo v korozním prostředí. Představeny jsou povlaky se schopností samovolné adaptace na pracovní prostředí. Úvodní část je zaměřena na optimalizaci depozičních parametrů a jejich přenosu z laboratorního do průmyslového měřítka. Následuje část věnovaná vlivu rostoucí teploty na strukturní změny a tribologické chování povlaku. Popsán je také vliv korozního prostředí a vliv dopujících prvků v povlaku. Na závěr jsou uvedeny aplikace využívající optimalizované povlaky.

Annotation

The thesis presents a summary of knowledge aimed at clarifying the dependence of tribological properties of coatings on their structure. It focuses primarily on tribological systems operating in extreme conditions of high temperatures or corrosive environments. Coatings with the ability to spontaneously adapt to the working environment are described. The introductory part is focused on the optimization of deposition parameters and their transfer from laboratory to industrial scale. The next part deals with the influence of increasing temperature on structural changes and the tribological behaviour of the coating. The influence of the corrosive environment and the dopant elements on the coating properties is also described. Finally, applications using optimized coatings are presented.

Klíčová slova

Otěruvzdorné povlaky; magnetronové naprašování; vysokoteplotní tribologie; korozní odolnost; lékařské implantáty; simulátor pohybu; adheze proteinů; obrábění

Keywords

Wear resistant coatings; Magnetron sputtering; High temperature tribology; Corrosion resistance; Medical implants; Motion simulator; Protein adhesion; Machining

Obsah

1 Úvod

Tření a otěr jsou děje, které doprovázejí většinu pohybujících se systémů. Může to být pohyb vzduchu nebo vody nesoucí abrazivní částice nebo kontakt dvou navzájem pohybujících se povrchů. Děje probíhající v dynamickém kontaktu mezi dvěma povrchy je možné popsat na makroskopické úrovni, například koeficientem tření nebo rychlostí opotřebení. To většinou platí pro ideální případy za nízkých teplot a na vzduchu. V případě vysokých teplot nebo korozního prostředí se začínají uplatňovat tribochemické děje. Pro pochopení a vysvětlení takového tribologického chování je nutné znát mechanismy probíhající na atomární úrovni mezi pohybujícími se povrchy. Na základě těchto znalostí je potom možné navrhnout vhodný tribologický systém.

Jedním z hlavních parametrů ovlivňující chování tribologického systému je chemické složení povrchu. To určuje, zda bude třecí mechanismus založen pouze na přímém kontaktu dvou povrchů nebo může být kontakt zprostředkován třecí mezivrstvou vytvořenou mezi pohybujícími se povrchy. Vznik takové mezivrstvy je ovlivněn působením tlaku, rychlostí pohybu, teploty nebo vlivem prostředí. Pokud je nově vzniklá třecí mezivrstva mechanicky odolná a snižuje tření, systém se může dlouhodobě chovat stabilně. Podobně může ke změně třecího mechanismu dojít i za pomocí aditiv obsažených v kapalném prostředí, která se chemicky vážou na povrch a mění jeho třecí vlastnosti. Mluvíme tedy o systému schopném adaptovat se na působení vnějšího prostředí.

Prvním krokem při návrhu tribologického systému je volba vhodného základního materiálu třecí dvojice. K dispozici je ale většinou pouze omezený výběr standardně používaných materiálů. Pokud je potřeba cíleně přizpůsobit chemické složení povrchu, je mnohem efektivnější použití moderních povrchových úprav. Mezi takové patří například aplikace tribologických povlaků, které umožňují změnit jak chemické, tak i mechanické vlastnosti povrchu v místě kontaktu.

Kromě chemického složení a působení okolního prostředí je nutné brát v úvahu i další parametry. Například elastickou deformaci tribologického systému nebo povrchovou drsnost, které ovlivňují geometrii kontaktu určující styčnou plochu a tím i síly působící v místě tření. Proto je potřeba k návrhu povlakového systému přistupovat komplexně a zahrnout celé spektrum vstupních parametrů na mikro i makro úrovni.

Výzkum v této oblasti byl a stále je zaměřen na hledání univerzálního tribologického povlaku, který by mohl fungovat například ve většině běžně používaných olejů nebo mohl obrábět jakékoliv hliníkové nebo titanové slitiny. Pokrok v tomto směru umožnilo počítačové

modelování, kde jsou získané poznatky stále více využívány k modelování dějů probíhajících v místě kontaktu a následně ověřovány na experimentálních modelech [1], [2], [3], [4], [5], [6].

Předmětem této práce je souhrn dílčích poznatků o růstu a struktuře povlaků, které byly využity při návrhu vhodného povlakového systému pro tribologické systémy pracující v extrémních podmínkách za vysokých teplot nebo v korozním prostředí. V úvodní části se práce věnuje optimalizaci depozičních parametrů a jejich přenosu z laboratorního do průmyslového měřítka. Následuje část věnovaná vlivu rostoucí teploty na strukturní změny a tribologické chování povlaku. Testován je i vliv korozního prostředí a vliv dopujících prvků v povlaku. Na závěr jsou uvedeny aplikace využívající optimalizované povlaky.

Hlavním záměrem práce bylo nalezení klíčových parametrů, které zásadním způsobem mohou ovlivnit vlastnosti tribologických povlaků vytvářených v průmyslovém měřítku. Proto byly pro výše uvedené experimenty provedeny pouze v průmyslových zařízeních. Tím bylo možné zohlednit i působení vnějších parametrů, které se u povlaků připravovaných v laboratorním měřítku neuplatňují, jako je například vliv rotace na růst povlaku nebo generování nečistot ze stěn zařízení a rotujících držáků.

2 Depozice povlaků

2.1 Depoziční procesy

Tribologické povlaky lze vytvářet metodami zahrnující jak chemické, tak i fyzikální procesy [7]. Pokud se zaměříme na depoziční procesy založené na generování výbojů v plynech, patří mezi nejvíce rozšířené magnetronové naprašování a katodové obloukové napařování, které patří do kategorie PVD (physical vapour deposition) metod. V obou případech lze vytvořit povlaky se srovnatelnými mechanickými a chemickými vlastnostmi. Magnetronové naprašování (obrázek 2.1) využívá ke generování plazmatu doutnavého výboje a umožňuje rozprašovat i nevodivé materiály (konfigurace s pulzním nebo RF zdrojem). Naopak pro katodové obloukové napařování (obrázek 2.2) založené na obloukovém výboji to není možné. V následujícím textu budou popsány výhody a nevýhody těchto metod pro tribologické aplikace.

Magnetronové naprašování

Metoda magnetronového naprašování (obrázek 2.1) je výhodnější pro tribologické aplikace, u kterých je nežádoucí změna výsledné drsnosti povrchu. Povlak je vytvářen tokem neutrálů a iontů z rozprašovaného terče, který tvoří katodu. Anodou je celá depoziční komora z vodivého materiálu, která je uzemněna. Stupeň ionizace může dosáhnout až 10 % v závislosti na použitém napájecím zdroji (DC, pulzní DC nebo pro nevodivé materiály RF), který udržuje napětí na katodě typicky mezi 500 až 1000 V. Za ideálních depozičních podmínek lze docílit kompaktní struktury povlaku, který dokonale kopíruje povrch základního materiálu. To platí pro tloušťky povlaku nepřesahující jednotky mikrometrů. V takovém případě nemá převážně sloupcovitý růst povlaku vliv na výslednou povrchovou drsnost. Její změna se začíná projevovat až pro větší tloušťky povlaku. Důvodem je formováním a orientace nově vznikajících povrchových zrn. Výrazný vliv na iniciaci mechanismu růstu povlaku má i mikrostruktura základního materiálu.

Snaha ovlivnit tento růstový mechanismus vede k vývoji nových výkonných zdrojů pro efektivní odprašování a zvýšenou ionizaci nanášeného materiálu. Mezi takové perspektivní zdroje patří pulzní zdroj HIPIMS (high power impulse magnetron sputtering). Velmi vysoký výkon je aplikován po dobu desítek mikrosekund v krátkém pulzu nepřevyšující 10 % pracovního cyklu. Tím dojde ke vzniku mnohem větší koncentrace jednonásobně i vícenásobně ionizovaných kovových iontů a výsledný stupeň ionizace plazmatu může dosáhnout hodnoty mezi 30 % až 70 %. Protože podstatná část výkonu je aplikována ve velmi krátkém pulzu, bude celkový průměrný výkon srovnatelný s klasickým magnetronovým naprašováním využívající DC nebo pulzní DC zdroje. Srovnatelný je i průměrný tepelný tok na povlakovaný povrch a je

tedy možné povlakovat materiály se stejnou teplotní citlivostí jako u klasického magnetronového naprašování. Jednoznačným přínosem použití HIPIMS zdrojů je vysoký stupeň ionizace umožňující urychlovat a směrovat tok většiny stavebních částic a tím i výrazně ovlivnit výslednou strukturu povlaku [8]. Metodou je možné docílit hustý kompaktní povlaku s minimem defektů a bez sloupcovité struktury.

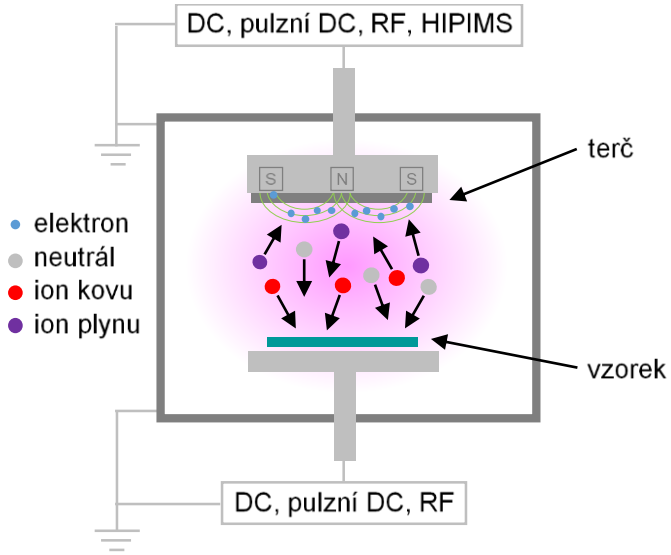

Obrázek 2.1 Magnetronové naprašování

Katodové obloukové napařování

U katodového obloukového napařování (obrázek 2.2) je materiál kovového terče odpařován pomocí nízkonapěťového obloukového výboje v místě pohybující se katodové skvrny (cathode spot) [8]. Pro udržení obloukového výboje ve vakuu se používají DC nebo pulzní DC zdroje s pracovními parametry typicky kolem 50 V a proudem mezi 50 a 100 A. Materiál se v tomto místě nataví a vytvoří tok částic obsahující jednak neutrály a ionty, ale také makročástice odpařovaného materiálu (droplets), které zvyšují výslednou drsnost povrchu a přispívají k nehomogenní struktuře povlaku. Stupeň ionizace může dosáhnout hodnoty až 90 %. Velký podíl kladně nabitých iontů umožňuje řídit růst struktury povlaku pomocí záporného předpětí a přispívá k zajištění velmi dobré adheze rostoucího povlaku k základnímu materiálu.

Z tribologických aplikací je metoda vhodná například pro řezné nebo lisovací nástroje, u kterých se povrchová drsnost tvořená měkkými makročásticemi odpařeného kovu po záběhové fázi sníží vlivem otěru. V porovnání s magnetronovým naprašováním, není metoda

příliš vhodná pro těsnící části pracující za vysokých tlaků, například vstřikovací systémy motorů, kde makročástice mohou mít vliv na dokonalé dosednutí těsnících ploch.

Pomocí filtrovaného obloukového napařování se podařilo vyřešit separaci makročástic v rostoucím povlaku. Silné magnetické pole vychýlí pouze tok iontů směřujících k povlakovanému materiálu. Makročástice díky své vyšší hmotnosti nejsou magnetickým polem vychýleny a usazují se mimo rostoucí povlak. Nevýhodou je snížení depoziční rychlosti, typicky o 75 %. Z ekonomického hlediska je tato technologie vhodná například pro aplikace v elektrotechnice.

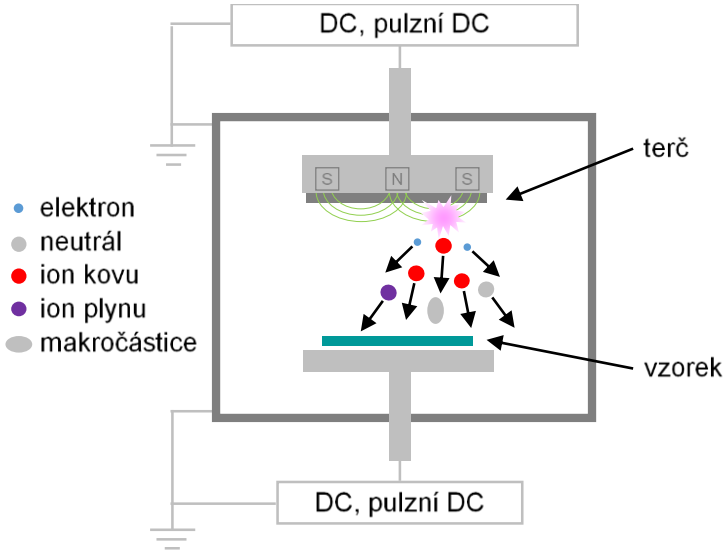

Obrázek 2.2 Katodové obloukové napařování

3 Návrh struktury povlaků

Použití povlaků pro tribologické aplikace je závislé na několika klíčových parametrech, jako je například teplota nebo chemické složení okolního prostředí, ve kterých bude tribologický systém pracovat. Těmto podmínkám je nutné přizpůsobit mechanické a chemické vlastnosti povlaku, aby odolával nebo se adaptoval v dostatečně širokém rozpětí pracovních podmínek.

Existují tři základní směry pro optimální návrh takového povlaku [9], [10]. První směr využívá pevné lubrikanty nanesené na povrch, například Ag, MoS_2 nebo WS_2, které výrazně snižují tření a fungují, dokud nedojde k jejich úplnému otěru. Druhý směr využívá povlaky na bázi uhlíku (DLC), které mohou být dopovány prvky F, Si, W. Dochází k tvorbě tenké grafitické, v případě W oxidické a pro Si polymerní vrstvy s velmi nízkým koeficientem tření. Třetí směr je založen na samovolné tvorbě tribologické oxidické vrstvy na povrchu povlaků. Tomu musí odpovídat vhodné chemické složení, kde z tribologického hlediska je ideální vznik oxidů prvků Cr, Mo, Ti, V a W. Oproti prvním dvou směrům je princip oxidace ideální pro vysokoteplotní aplikace, kde například DLC nebo MoS_2 povlaky degradují.

Abychom mohli navrhnout vhodnou funkční strukturu povlaku pro vysoké teploty, bude nejprve nutné analyzovat změnu mechanických a chemických vlastností povlaku s rostoucí teplotou. Pro tento účel, byly navrženy experimenty na modelovém případu vybraných povlaků [11] a v následujících experimentech byly testovány tribologické vlastnosti povlaků a vliv prostředí [12], [13], vliv dopujících prvků v povlaku na třecí a otěrové vlastnosti [14], [15], [16], [17], [18] a také korozní odolnost povlaků [19], [20].

3.1 Vliv depozičních parametrů

U metod magnetronového naprašování a katodového obloukového napařování lze pomocí depozičních parametrů řídit výsledné mechanické a chemické vlastnosti povlaků, mezi které patří například tloušťka, adheze, nanotvrdost nebo stechiometrie. Depoziční parametry lze měnit na úrovni vstupních veličin (teplota, tlak, tok plynů, příkon na katodách, urychlovací předpětí na stolku, proud vnější UBM cívky), ale také konfigurací depozičního systému (uspořádání magnetického systému katod, stínění katod, geometrické uspořádání systému). To jsou parametry, které nám zároveň pomáhají nastavit a udržovat vnitřní parametry plazmatu, zejména iontový tok nebo teplotu elektronů. Bez jejich znalosti by nebylo možné zajistit opakovatelnost a přenositelnost depozičního procesu nebo řídit reaktivní procesy.

Monitorovat vnitřní parametry je možné pomocí diagnostických metod plazmatu. Mezi nejpoužívanější metody patří sondová diagnostika a optická emisní spektroskopie. Pro prvotní

diagnostiku lze použít jednoduchou a účinnou metodu, která je založena na měření prostorového rozložení iontového toku v depozičním systému pomocí ploché sondy. Tato metoda byla použita pro pochopení závislosti vnitřních parametrů plazmatu na růst a strukturu povlaku. Byl proto navržen experiment v laboratorním systému (obrázek 3.1) s konfigurací pro DC magnetronové naprašování [21]. Naprašován byl povlak TiN z titanového terče ve směsi plynů argonu a dusíku.

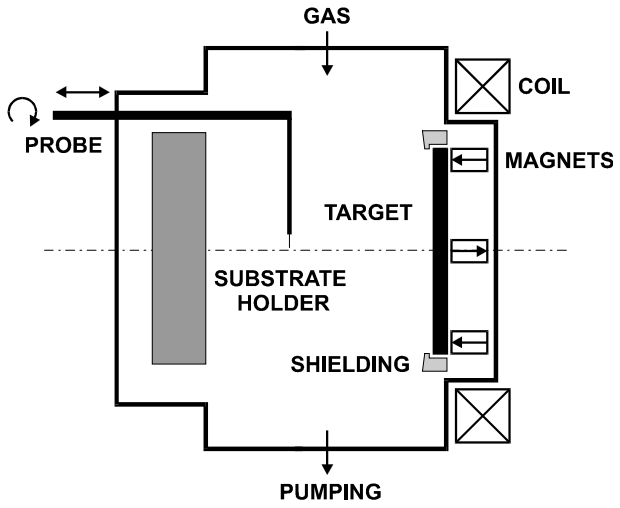

Obrázek 3.1 Schéma laboratorního systému pro DC magnetronové naprašování s plochou sondou pro měření prostorového iontového toku [21]

Pro monitorování prostorového rozložení iontového toku byla použita dělená plochá sonda (obrázek 3.2). Skutečná sběrná plocha pro ionty je na okrajích sondy deformována a neodpovídá skutečné ploše sondy, která je ve skutečnosti menší. V případě rozdělení plochy sondy na vnitřní (d 5 mm) a vnější (d 10 mm) část můžeme proud (I = U / R) snímat nezávisle pouze na vnitřní sondě. Sběrná plocha vnitřní sondy je shodná se skutečnou plochou sondy. V experimentálním uspořádání měla sonda izolovanou zadní stěnou a byla umístěna kolmo ke katodě v prostoru mezi terčem a stolkem. Elektroda sondy byla napájena záporným napětím -100 V (stav saturace) a z měřeného proudu byl přepočítána hustota iontového proudu na plochu vnitřní elektrody.

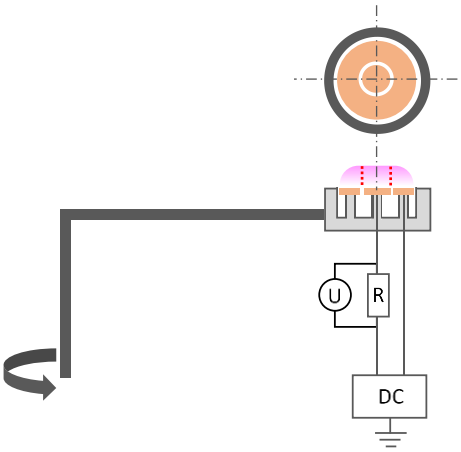

Obrázek 3.2 Dělená plochá sonda

Z prostorového rozložení hustoty iontového proudu v axiálním i radiálním směru byl potom určen iontový tok (rovnice 1) a z depoziční rychlosti měřené v odpovídajících místech v radiálním směru na rostoucím povlaku byl vypočítán tok kovových atomů (rovnice 2):

$$\varphi_i = \frac{I_i}{e \,.\, A_{ef}} \tag{1}$$

$$\varphi_{Ti} = \frac{\rho_{TiN}.N_A.R_d}{M_{TiN}} \tag{2}$$

kde v rovnici pro výpočet iontového toku je I_i proud na sondu o sběrné ploše A_{ef} a e je náboj elektronu. V rovnici pro výpočet toku kovových atomů je ρ_{TiN} je hustota TiN, N_A Avogadrova konstanta, R_d depoziční rychlost a M_{TiN} relativní atomová hmotnost TiN [22].

Závislost poměru iontového toku a toku kovových atomů udává poměr počtu iontů k počtu kovových atomů (ion to metal ratio). V prostoru určeném poloměrem terče a vzdáleností od terče je zobrazena na obrázku 3.3. Je zde patrný vliv magnetického pole, které je řízené pomocí externí UBM cívky. S rostoucím proudem UBM cívky (obrázek 3.3b) dochází k větší koncentraci magnetického pole směrem od katody a tím i ke kontaktu povlaku s plazmou. To může být výhodné zejména pro změnu mechanismu růstu povlaku, protože vyšší poměr nabitých částic umožňuje jejich urychlení záporným předpětím. Naopak pro povlakování plastů je vyšší tok iontů na rostoucí povlak nežádoucí z důvodu lokálního přehřátí povrchu [23].

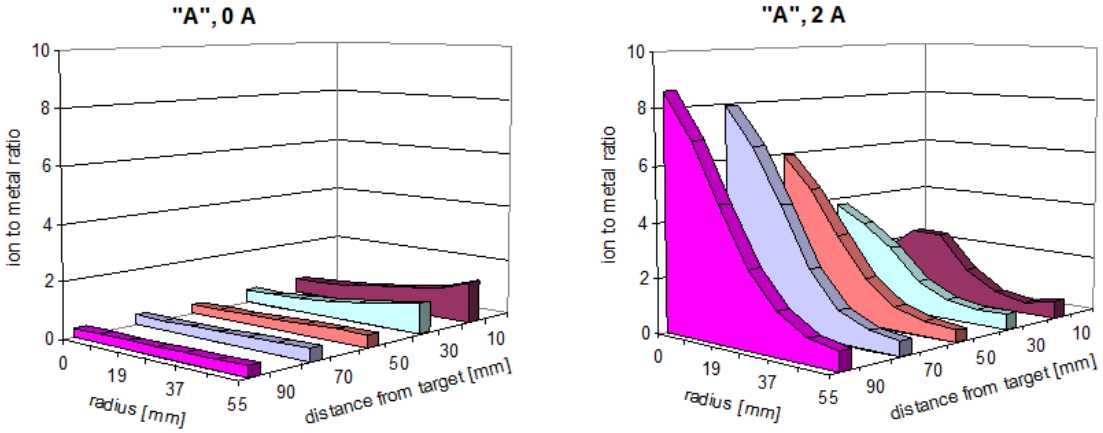

(a) (b)

Obrázek 3.3 Prostorové rozložení iontového toku: a) s anodovým stíněním katody a proudem na vnější UBM cívce 0 A a b) s anodovým stíněním katody a proudem na vnější cívce 2 A

Ověření výše uvedených měření bylo prokázáno na experimentu depozice povlaku TiN s různým iontovým tokem a záporným předpětím na rostoucím povlaku. Hodnocena byla výsledná tvrdost a stechiometrie. Na obrázku 3.4 jsou znázorněny oblasti, které definují povlak TiN jako stechiometrický (žlutě), přechodový (červeně) a podstechiometrický (modře). Z této závislosti lze potom stanovit rozpětí pro depoziční parametry nutné pro zachování stechiometrie pro TiN povlak [24], [25].

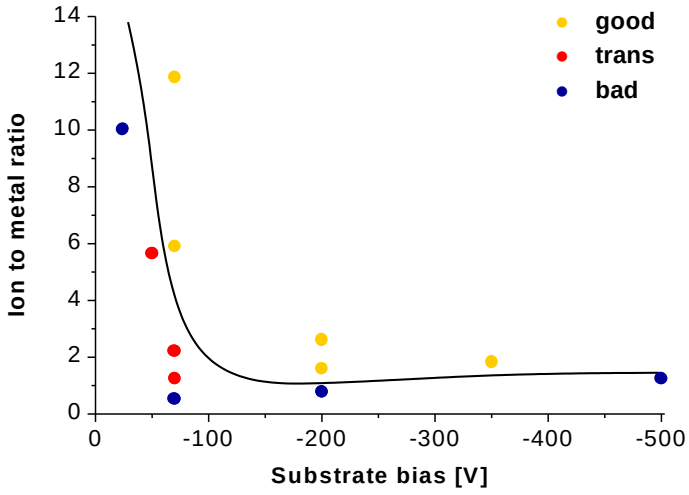

Obrázek 3.4 Depozice povlaku TiN v závislosti na změně záporného urychlovacího předpětí a poměru iontů ke kovovým atomům. Znázorněna je oblast stechiometrického (žlutě), přechodového (červeně) a podstechiometrického (modře) povlaku TiN.

3.2 Struktura a vliv teploty

Růst teploty má výrazný vliv na změnu tribologických vlastností povlaků. Dochází především k oxidaci povrchu a fázovým změnám struktury povlaku. Vlivem oxidace může dojít ke snížení tření nebo otěru nebo naopak k nežádoucí degradaci mechanických vlastností. Pro pochopení dějů probíhajících v závislosti na teplotě byla vybrána skupina povlaků na bázi chromu, kde se předpokládá s rostoucí teplotou vznik povrchové oxidické vrstvy s velmi dobrými tribologickými vlastnostmi.

Povlaky Cr-N a Cr-C-N

Pro vysokoteplotní tribologické aplikace se velmi často používají povlaky na bázi nitridů chromu, které za běžných podmínek vykazují vysokou tvrdost, korozní odolnost, nízké opotřebení, ale naopak poměrně vysoký koeficient tření proti oceli.

Povlaky Cr-N lze vytvořit s různou stechiometrií. Nejčastěji se používají dva základní typy povlaků, C_2N dosahující vyšší tvrdost až 29 GPa a povlak CrN s tvrdostí 18 GPa. Povlaky jsou deponovány metodou reaktivního magnetronového naprašování nebo katodovým obloukovým napařováním z Cr terčů. Poměr N_2 a pracovního plynu Ar určuje, zda se bude vytvářet fáze CrN nebo Cr_2N [26].

Nízké opotřebení a zároveň vysoká odolnost proti oxidaci až do teploty kolem 700 °C jsou zajištěny tvorbou oxidické ochranné vrstvy Cr_2O_3 [27]. U povlaků Cr-N dochází s rostoucí teplotou k difúzi dusíku do vrstvy a na povrchu zůstává Cr, který reaguje s atmosférickým kyslíkem. Pokud budeme nitridy chromu dopovat uhlíkem, bude s rostoucí teplotou probíhat oxidická reakce na povrchu a dojde k nahrazení atomů N a C v jejich mřížkových polohách atomy O (viz obrázek 3.5).

Různé mechanismy oxidace mají vliv na průběh tribologických vlastností s rostoucí teplotou. Pro pochopení dějů vedoucích ke změně povrchové a vnitřní struktury byl navržen následující experiment [11]. Povlaky na bázi Cr-N, Cr-C-N a Cr-C byly deponovány metodou katodového obloukového napařování za použití reaktivních plynů N_2 a C_2H_2. Byly připraveny tři typy povlaků s odlišným chemickým složením, které byly označeny $Cr_{60}N_{40}$, $Cr_{41}N_{27}C_{32}$ a $Cr_{67}C_{33}$. U povlaků byla analyzována strukturní stabilita pomocí in situ HTXRD (high temperature X-ray difraction) v ochranné atmosféře při zahřívání na teploty do 1000 °C.

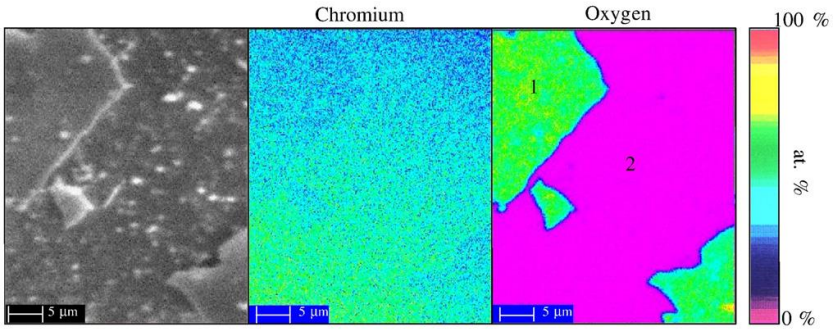

layer	O (at.%)	N (at.%)	C (at.%)	Cr (at.%)
1	44.9	0.76	12.4	41.9
2	0.8	6.1	36.0	57.1

Obrázek 3.5 Morfologie povrchu vzorku Cr41N27C32 ze skenovacího elektronového mikroskopu a příslušná mapa elementárního chemického složení získaná metodou EPMA pro chrom a kyslík po tepelném zatížení: vrstva 1 - vnější vrstva Cr3O2; vrstva 2 - vnitřní neoxidovaný

Po depozici povlak $Cr_{60}N_{40}$ vykazoval strukturu s nízkým stupněm uspořádání a průměrnou velikostí zrn menší než 10 nm. Tvořen byl převážně hexagonální fázi β-Cr_2N, která byla stabilní do 900 °C před rekrystalizací a růstem zrn. Po rekrystalizaci byla průměrná velikost zrn 34 nm.

Povlak $Cr_{41}N_{27}C_{32}$ s průměrnou velikostí zrn 4 nm je tvořen metastabilní fází δ-Cr(N,C), která je stabilní do teploty 600 °C. K fázové přeměně na orthorhombickou fázi karbonitridu chromu $Cr_3(C_xN_{1-x})_2$ dochází při teplotě do 800 °C a následně se s rostoucí teplotou mění na fázi karbidu chromu Cr_3C_2. Nebyly detekovány fáze nitridu chromu, přestože z poměru N a C lze takové fázové uspořádání očekávat.

U povlaku $Cr_{67}C_{33}$ začíná fázový přechod při 700 °C. Po žíhání na 1000 °C povlak rekrystalizoval na směs karbidických fází, převážně Cr_3C_2 a $Cr_{23}C_6$.

Obloukově napařené povlaky Cr-N-C mají méně kompaktní morfologii než binární povlaky Cr-N a Cr-C. Oxidační proces probíhal u povlaku Cr-N-C mnohem intenzivněji než v případě binárních povlaků, jak vyplývá ze srovnávací analýzy intenzity píků oxidu [11].

3.3 Tribologické vlastnosti a vliv prostředí

Vliv teploty

Mechanismus tření je za pokojové teploty zprostředkován přímým kontaktem mezi dvěma pohybujícími se povrchy. To platí, pokud se povrchy chovají inertně a nereagují s okolním prostředím nebo mezi sebou. Vlivem působícího tlaku v místě kontaktu dochází k výraznému lokálnímu nárůstu teploty a tvorbě velmi tenké oxidické vrstvy, která je ale vzájemným

pohybem opětovně narušována. Vzniklé otěrové produkty mohu fungovat jako pevný lubrikant nebo naopak mohou způsobit nestability třecího mechanismu.

Pokud děj probíhá za teploty vyšší než 200 °C, tvoří se oxidická vrstva rychleji a dosahuje několikanásobně větší tloušťku. Přímý kontakt dvou povrchů se přemění na kontakt zprostředkovaný nově vzniklou oxidickou mezivrstvou, která je díky své tloušťce a kompaktnosti schopná odolávat danému zatížení. Při návrhu povlaku pro vysoké teploty je snaha tento mechanismus adaptace využít s cílem zachovat nebo dokonce zlepšit tření s rostoucí teplotou [10], [28], [29], [3].

Uvedený třecí mechanismus založený na tvorbě povrchových oxidů je například dominantní pro povlaky Cr-N, kde se primárně vytváří oxid Cr_2O_3. V teplotním rozmezí pohybujícím se od pokojové teploty až k teplotám přesahujících 700 °C, vykazují povlaky velmi dobrou otěruvzdornost, ale poměrně vysoký koeficient tření. Pro zlepšení třecích vlastností byl proto navržen povlakový systém s uhlíkem Cr-C-N [12]. Předpokladem bylo, že se s rostoucí teplotou uhlík transformuje na grafitickou formu a bude se chovat jako samomazná složka.

Testovány byly dva systémy Cr-C-N s rozdílným množstvím uhlíku (8 % a 19 %). Chemické složení povlaků uvedené v atomárních procentech bylo určováno metodou EPMA ($Cr_{68}N_{24}C_8$ a $Cr_{67}N_{14}C_{19}$) a metodou RBS ($Cr_{65}N_{27}C_8$ a $Cr_{58}N_{21}C_{19}$). Z výsledků vysokoteplotních tribologických testů pin-on-disk do teploty 500 °C bylo potvrzeno, že s rostoucí teplotou dochází ke snížení opotřebení a u povlaku s dvojnásobným množstvím uhlíku je opotřebení a koeficient tření nižší. Jako třecí protikus byla použita kulička z materiálu Al_2O_3 a Si_3N_4.

Pro jednoznačné potvrzení vlivu uhlíku byl navržen vysokoteplotní tribologický test pin-on-disk povlaků Cr-C-N s uhlíkem v rozmezí od 0 do 31 at.% [14]. Povlaky byly deponované pomocí katodového obloukového napařování a jako třecí protikus byla použita kulička z materiálu Al_2O_3 a Si_3N_4. Na obrázku 3.6 je vidět, že povlak CrCN-00 s obsahem uhlíku 0 at. % byl tvořen β-fází Cr_2N a fází α-Cr a u povlaků CrCN-12, CrCN-24 a CrCN-48 s obsahem uhlíku od 12 do 31 at. % byla detekována fáze δ-Cr(C,N). Povlaky s vyšším obsahem uhlíkem se chovaly velmi podobně. Pouze při kritické teplotě 400 °C došlo k nárůstu rychlosti opotřebení, ale s rostoucí teplotou až do 700 °C se rychlost otěru výrazně zmenšila. Naopak povlaky Cr-N a Cr-C-N s nízkým obsahem uhlíku se chovaly velmi nestabilně a při teplotě 500 °C vykazovaly výrazný nárůst rychlosti opotřebení.

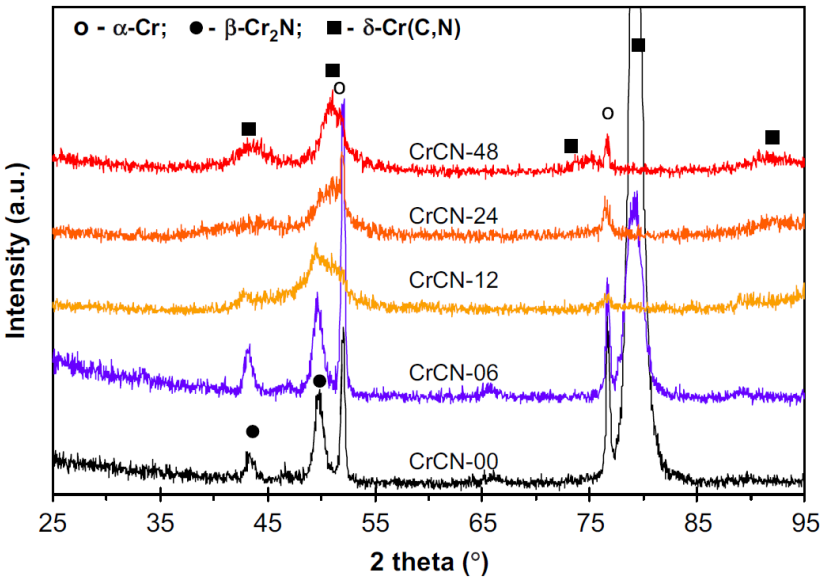

Obrázek 3.6 XRD difraktogram povlaků Cr-C-N s různým obsahem uhlíku [14]

Vliv korozního prostředí

Korozní prostředí v tribologických aplikacích může být tvořeno agresívními plyny nebo kapalinami. Jedná se například o spaliny nebo mořskou vodu. V náročných aplikacích se navíc může vliv prostředí zesílit působením vysoké teploty. Příkladem jsou třecí mechanismy ve spalovací části automobilového nebo leteckého motoru.

Nemusí se jednat pouze o neživé systémy. Z pohledu tribologie je velmi zajímavým systémem samotné lidské tělo, přesněji kloubní spojení. Pokud je původní kloub nahrazen povlakovaným kovovým implantátem, musí odolávat prostředí, které je tvořeno kloubní (synoviální) tekutinou sloužící jako lubrikant. Chemické složení této tekutiny obsahuje kromě dalších složek, ionty Na^+, K^+ a Cl^-a působí na povlak jako elektrolyt. Za standardních podmínek se chemické složení příliš nemění, ale v případě zánětlivých nebo septických kloubních chorob může dojít ke změně viskozity nebo pH a vliv prostředí se výrazně zesílí.

Použité povlaky jsou téměř vždy korozně ušlechtilejší, než je základní materiál. Měly by tedy sloužit jako velmi dobrá korozní ochrana. Díky rozdílné korozní ušlechtilosti může ale dojít ke vzniku elektrochemického článku a urychlení koroze. Kritická jsou místa případných defektů nebo zarostlých nečistot v povlaku nebo samotná struktura povlaku ovlivněná sloupcovitým mechanismem růstu (typický pro PVD metody), který snižuje bariérovou funkci povlaku. To jsou nevýhody dané principem použité povlakovací technologie.

Z korozního a zároveň tribologického hlediska jsou velmi často využívány povlaky DLC. Jejich chemické složení může být čistě uhlíkové ta-C (H pod 1 at. %) nebo mohou obsahovat určité množství vodíku a-C:H (H do 50 at. %). Tribologické vlastnosti výrazně

závisejí na okolním prostředí a můžou být ovlivněny například teplotou nebo vlhkostí. Povlaky DLC mohou být modifikovány pro určité prostředí legováním prvky jako jsou například B, F, N, Si, Cr, Nb, Ti nebo W [30]. Tyto dopující prvky slouží ke změně chemicky inertního DLC povlaku na chemicky aktivní. V závislosti na prostředí aktivují tvorbu tribologické mezivrstvy nebo aktivují adhezi aditiv k povrchu.

Pro testování vhodného povlaku pro kloubní spojení byl vybrán povlakový systém Ti-C:H s adhezní mezivrstvou Ti a gradientním přechodem z Ti na Ti-C:H [13], [15]. Použita byla metoda reaktivního magnetronového naprašování z Ti terčů ve směsi plynů C_2H_2 a Ar. Změnou toku C_2H_2 byla připravena sada vzorků s chemickým složením měnícím se od Ti přes TiC až po nanokompozitní strukturu TiC/a-C: H. Tribologické testy (obrázek 3.7) byly provedeny metodou pin-on-disk na vzduchu, ve fyziologickém roztoku (PS) a v roztoku s fetálním hovězím sérem (FBS).

Nejlepší tření a otěr povlaku bylo dosaženo pro nejvyšší toky C_2H_2, kterému odpovídá chemické složení povlaku tvořené z 9-12 at. % Ti a 88-91 at. % C. Naopak nejhorší tření a otěr povlaku bylo dosaženo pro nejnižší toky C_2H_2 s převládajícím obsahem Ti v povlaku, kde zároveň docházelo k vysokému otěru protikusu, zejména při testování ve fyziologickém roztoku.

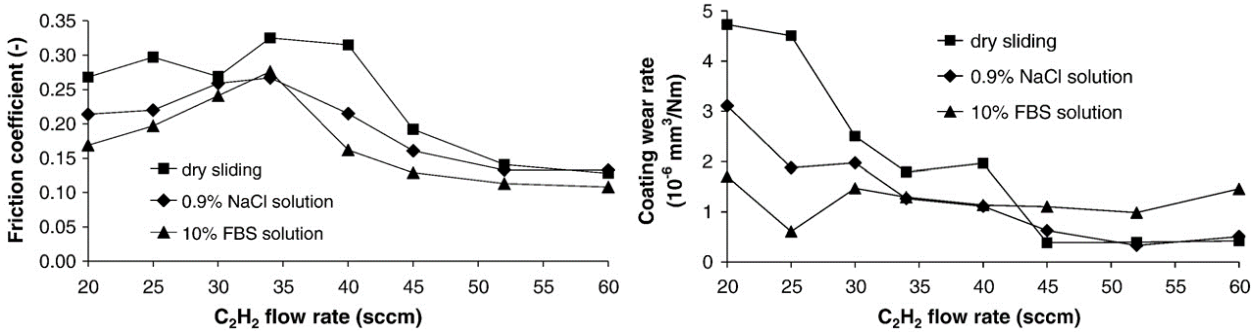

(a) (b)

Obrázek 3.7 Tření (a) a otěr (b) povlaku Ti-C:H na vzduchu, v roztoku 0,9 % NaCl a v 10ti % roztoku fetálního hovězího séra [13]

Mechanismus tření za přítomnosti biologických roztoků je silně ovlivněn tribokorozí. V roztocích PS nebo FBS se vytváří tribologická mezivrstva odlišná od mezivrstvy vytvářené na vzduchu. Pro testy koroze byly vybrány povlaky s výrazně odlišným chemickým složením, povlak deponovaný při toku 30 sccm C_2H_2 (FR30), který je tvořený převážně TiC a povlak deponovaný při toku 52 sccm C_2H_2 (FR52) s převládající strukturou Ti-C:H. Potenciál otevřeného obvodu (OCP) pro povlak FR30 byl -0,37 V a pro povlak FR52 byl -0,43 V. Povlak

FR30 je tedy elektrochemicky ušlechtilejší materiál. Jeho OCP se v průběhu korozního testu snížil na úroveň odpovídající základnímu materiálu (-0,55 V), zatímco OCP povlaku FR52 dosáhla stabilní hladiny -0,52 V poté, co od poloviny testu (300 minut) zůstal konstantní. Pokles OCP může být spojen s postupným růstem existujících pórů. Stabilní OCP pro FR52 indikuje zastavení nebo snížení množství pórů, což je podpořeno mírným zvýšením kapacity na obrázku 3.8. Na druhé straně kapacita pro povlak FR30 roste a OCP klesá, což naznačuje galvanickou stimulaci koroze v pórech. Výsledkem je generování korozních produktů (oxidy kovů nebo hydroxidy kovů), které mohou působit jako abrazivní materiál. Povlak FR52 se strukturou Ti-C:H funguje částečně jako difúzní bariéra a zároveň vykazuje velmi nízké tření a otěr v biologických kapalinách.

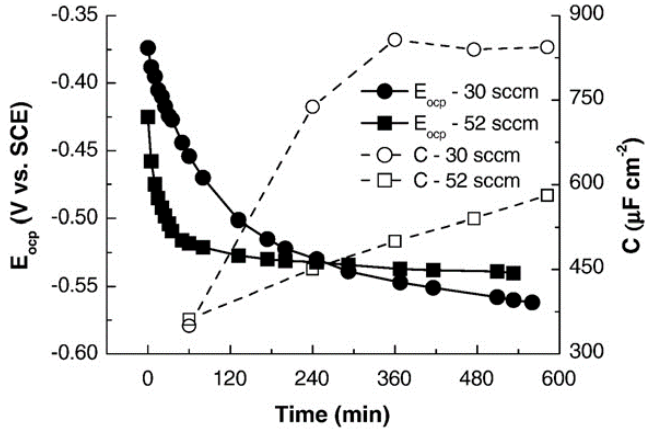

Obrázek 3.8 Časová závislost korozního potenciálu a elektrodové kapacity během elektrochemických testů povlaků Ti-C:H [13]

3.4 Role dopujících prvků

Modifikace chemického složení povlaků pomocí dopujících prvků má za cíl zlepšit jejich tribologické vlastnosti ve specifickém pracovním prostředí, jako je například agresivní atmosféra, která může být umocněna s rostoucí teplotu. Nebo pokud se tření odehrává v oleji, je výhodné chemické složení povrchu optimalizovat pro chemické navázání aditiv z oleje, které slouží jako třecí mezivrstva. Na tomto podobném principu fungují také pohyblivá spojení implantátů v prostředí lidského těla, kde je žádoucí na povrch pohyblivých spojení implantátů navázat určité makromolekuly, které vytváří přirozený lubrikant [31]. Navíc musí být zajištěno, že nedojde ke změně chemického složení povrchu během celé životnosti povlakovaného iplantátu.

Na opačném principu fungují povlaky pro vysokoteplotní aplikace, kde chemické složení povlaku může urychlit oxidaci nebo vytvoření samomazného povrchu, tzv. povlaky

schopné samovolné adaptace („self-adaptive coatings“) [32], [33]. Většinou tak dochází ke zlepšení tribologických vlastností s rostoucí teplotou a chemické složení povrchu povlaku se změní okamžitě nebo již po několika teplotních cyklech.

Vliv uhlíku ve struktuře povlaků CrCN

Povlaky na bázi nitridů se s úspěchem používají pro aplikace vyžadující vysokou teplotní a oxidační odolnost, jako jsou například řezné a lisovací nástroje nebo povlaky pro pístní kroužky. Vysoká tvrdost a otěruvzdornost spolu s korozní odolností umožňují jejich použití ve většině tribologických aplikacích.

Jednou z velkých výhod povlaku CrN je, že se za rostoucí teploty vytváří povrchová vrstva Cr_2O_3, která pozitivně ovlivňuje tření. Na rozdíl od pokojové teploty, při které je koeficient tření poměrně vysoký. Tento vliv na tribologické vlastnosti byl testován i pro ternární povlaky Cr-X-N, u kterých byl analyzován vliv dopujících prvků X jako je Al [34], [35], Ti [36] nebo Si [37] na změnu třecích a otěrových vlastností s rostoucí teplotou, ale například vliv C byl zatím relativně málo publikován.

Pro pochopení vlivu C v povlakovém systému Cr-C-N byl navržen experiment [14], ve kterém byly hodnoceny tribologické vlastnosti s rostoucí teplotou do 700 °C s různým obsahem C. Povlaky byly současně porovnávány s tribologickými vlastnostmi povlaku CrN. Především bylo hodnoceno, zda je možné pomocí určitého množství C zlepšit třecí vlastnosti při zachování vyhovujících mechanických vlastností povlaku.

Povlaky byly vytvořeny metodou katodového obloukového napařování s obsahem C od 0 at. % (CrN) až do 31 at. % (CrCN). Tření a otěr s rostoucí teplotou se testovaly pomocí vysokoteplotního tribometru pin-on-disk. Jako třecí protikusy sloužily kuličky z Al_2O_3 a Si_3N_4 o průměru 6 mm. Výsledné tribologické vlastnosti testovaných povlaků byly velmi podobné u povlaků s obsahem uhlíku mezi 12-31 at. %. Při teplotě 400 °C docházelo shodně pro všechny povlaky k nárůstu opotřebení povlaků. Další zvýšení teploty vedlo ke zlepšení odolnosti proti opotřebení, což bylo způsobeno změnou mechanismu opotřebení, které bylo ovlivněno vzniklou třecí mezivrstvou. Povlaky CrN a povlaky CrCN s obsahem pod 12 at. % C vykazovaly horší tribologické vlastnosti a v průběhu testování tření se chovaly nestabilně.

Povlaky a-C:H a vliv dopujících prvků

Chemická aktivita DLC povlaků je dána jejich chemickým složením, které může být na bázi uhlíku ta-C nebo s obsahem určitého množství vodíku a-C:H. Obecně platí, že se jejich povrch

chová inertně vůči okolnímu prostředí. Nelze tedy využít mechanismu navázání aditiv obsažených v olejích nebo proteinů u lékařských implantátů pro zlepšení jejich tribologických vlastností.

Konkrétním příkladem může být implantát kyčelního kloubu, u kterého je kovová hlavice povlakovaná DLC vrstvou a jako protikus slouží jamka z UHMWPE. V pohybu se kloubní tekutina dostává mezi třecí plochy a působí jako přirozený lubrikant. Pokud je implantát v klidové poloze, třecí plochy na sebe těsně dosedají. Kritická je fáze, kdy k pohybu dochází z klidové polohy. Třecí dvojice se začíná pohybovat a zůstává v přímém kontaktu. Dochází ke zvýšenému namáhání a opotřebení povrchu až do doby, než se lubrikant dostane mezi třecí plochy a přeruší přímý kontakt [38].

Lubrikační povrchová vrstva se vytváří z kloubní (synoviální) tekutiny, která je tvořena převážně z makromolekul (proteoglykany, nekolagenní proteiny, lipidy, kyselina hyaluronová) [31]. Za normálních podmínek se váže na kolagenovou síť kloubního spojení a podílí se na jeho mazání. Pro navázání makromolekul na povrch je nutné změnit chemické složení povrchu DLC povlaku a současně i jeho bioaktivitu. Jednou z možností je dopování povlaku kovovými prvky, jako je například Ta, Ti, Nb a Zr.

Aby bylo možné ověřit, zda se schopnost vázat makromolekuly na povrch zvýší, je potřeba zvolit vhodnou metodu umožňující hodnotit počet, ale i kvalitu vazby. V našem případě byly navrženy experimenty, které porovnávaly amorfní uhlovodíkové povlaky a-C.H s povlaky Ti-C:H dopovanými titanem v různém množství [16], [18]. Adsorpce vybraného proteinu, kterým byl lidský fibrinogen (HPF), byla hodnocena senzorem založeném na difrakčním optickém elementu (DOE) a metodou optické elipsometrie. Porovnávána byla změna optické drsnosti a permitivity na povrchu povlaků v elektrolytu s a bez přidání HPF.

Proteiny HPF nejlépe adsorbovaly na referenčních vzorcích z leštěného a chemicky leptaného titanu, stejně tak jako na povrchu Ti-C:H s chemickým složením v poměru $Ti_{0.38}$-$C_{0.62}$ a $Ti_{0.09}$-$C_{0.91}$. Z pohledu tribologických vlastností [13], [15] vykazuje povlak dopovaný Ti v množství 9 at. % menší koeficient tření a otěr, než povlak s obsahem 38 at. %, který byl tvořen převážně z karbidů TiC. Dále bylo potvrzeno, že k adsorpci proteinů nedochází u nedopovaného povlaku a-C:H.

Kromě hodnocení množství adsorbovaných proteinů je možné hodnotit také sílu jejich adheze k povrchu. K tomu sloužil experiment založený na hodnocení smykového napětí, při kterém dojde k uvolnění proteinů, pomocí reometru [17]. Mezi rotující kotouč a vzorek umístěný na stacionárním kotouči udržovaný na konstantní teplotě 37 °C je aplikována simulovaná tělní tekutina (SBF). Kotouče mají mezi sebou mezeru 500 µm a po roztočení se

vytváří smykové napětí působící na adherované proteiny. Následně se vyhodnotí pomocí analýzy obrazu, zda se proteiny pro dané smykové napětí uvolnily.

Testovány byly povlaky Ti-C:H s povrchovým chemickým složením Ti 4,2, C 77,6 a O 18,2 at. % ve vazebních stavech Ti–C a C–C, které byly analyzovány metodou XPS. Porovnávány byly s referenčním materiálem Ti6Al4V ELI, který byl z pohledu adheze proteinů srovnatelný s povlakem Ti-C:H.

3.5 Korozní odolnost

Pracovní prostředí tribologických systémů má zásadní vliv na stabilitu povlakového systému. Například v kapalném prostředí s oxidační schopností a přítomností depasivujících chloridových iontů (fyziologický roztok, mořská voda atd.), které funguje jako elektrolyt, může docházet v místě defektů nebo pórů v povlaku k přímému kontaktu elektrolytu se základním materiálem. V místě poruchy se vytvoří galvanický článek, kde katodu tvoří elektrochemicky ušlechtilejší povlak a anodu dno z elektrochemicky méně ušlechtilého základního materiálu. Malá plocha katody vůči anodě způsobí vysokou proudovou hustotu na anodě a výsledkem je vysoká korozní rychlost vedoucí k podkorodování povlaku a lokálnímu porušení adheze povlaku k základnímu materiálu. Tento mechanismus je znázorněn na obrázku 3.9b a platí pro většinu používaných tribologických povlaků na bázi nitridů a karbidů. Na opačném principu znázorněném na obrázku 3.9a fungují elektrochemicky méně ušlechtilé povlaky, například na bázi hliníku, které ale z hlediska mechanických vlastností nejsou příliš vhodné pro tribologické aplikace [39].

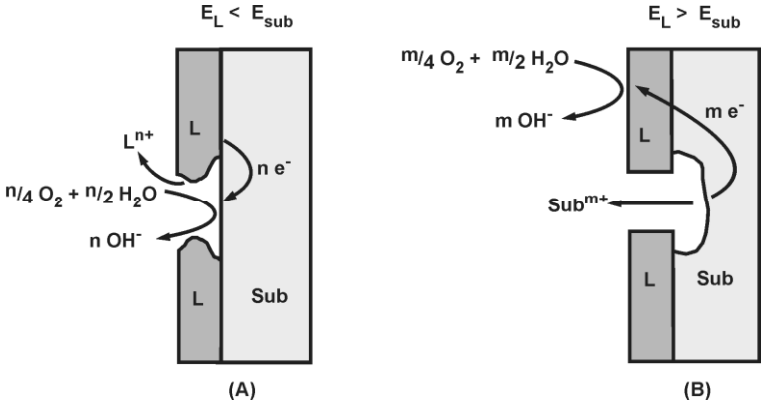

Obrázek 3.9 Schéma korozního procesu s kyslíkovou depolarizací, probíhajícího v systému vodivý porézní povlak (L) - kovový substrát (Sub) o různé elektrochemické ušlechtilosti; (a) substrát ušlechtilejší než povlak - v pórech probíhá preferenčně katodický děj, (b) povlak ušlechtilejší než substrát - anodický děj probíhá preferenčně v pórech [39]

Zlepšení korozní odolnosti povlakového systému závisí především na funkci povlaku jako difúzní bariéry, která má za úkol odstínit vliv základního materiálu, zejména v případě volby korozně méně odolného základního materiál. Naopak pro korozně odolné materiály, které se používají pro výrobu lékařských implantátů, může bariérový efekt povlaku snížit uvolňování toxických kovových iontů ze základního materiálu do prostředí lidského těla.

Aby povlak mohl fungovat jako účinná bariéra je z technologického hlediska nutné zajistit následující podmínky:

a) Dokonalá čistota depozičního zařízení, aby nedocházelo k zarůstání nečistot a prachových částí do povlaku. V průmyslovém měřítku je to poměrně obtížně dosažitelné, protože depoziční komora obsahuje rotační držáky, které jsou zdrojem nečistot.
b) Volba vhodného chemického složení adhezní a funkční vrstvy vzhledem k elektrochemickému působení okolního prostředí. Zohledněna musí být i rozdílná elektrochemická ušlechtilost povlaku a základního materiálu.
c) Optimalizace mechanismu růstu povlaku pomocí depozičních parametrů. Struktura povlaků nanášených metodami PVD se ve většině případů vyznačuje sloupcovitým růstem s výslednou vertikální porézností vůči povrchu. Změna mechanismu růstu povlaku může být ovlivněna například u metody magnetronového naprašování použitím pulzního zdroje s vysokoenergetickými pulzy HIPIMS [40]. Stupeň ionizace lze tak zvýšit až na 90 %. Potom budou většinu stavebních částic tvořit kladné ionty, které lze urychlit k substrátu záporným předpětím. Možnost řídit energii a směr dopadajících iontů zajistí vytvoření kompaktního povlaku s minimem růstových defektů.

Výše uvedené podmínky je nutné splnit současně, aby byl bariérový efekt maximální. Pro pochopení, jaký podíl mají na bariérové funkci a zároveň korozní odolnosti jednotlivé podmínky, byl nejprve zkoumán vliv chemického složení, a to adhezní mezivrstvy a následně funkčního povlaku.

Korozní odolnost adhezní mezivrstvy

Pro ověření bariérové funkce povlakového systému byl vybrán povlakový systém, který je primárně určen pro pohyblivá spojení lékařských implantátů nebo pro dentální implantáty. Byl navržen experiment, který měl za úkol zhodnotit korozní odolnost adhezní mezivrstvy u DLC povlaků nanesených na titan a titanovou slitinu Ti6Al4V ELI [20]. Povlaky DLC byly

vytvořeny metodou PACVD s pracovním plynem acetylenem. Výsledné chemické složení povlaků odpovídalo amorfnímu uhlovodíku a-C:H a použity byly dvě varianty adhezní mezivrstvy. Porovnávány tak byly dva povlakové systémy, první Ti/Ti-C:H/a-C:H s adhezní mezivrstvou Ti a s postupným gradientním přechodem na Ti-C:H a druhý Cr/Cr-C:H/a-C:H, kde Ti byl nahrazen Cr.

Korozní odolnost byla testována metodou EIS (electrochemical impedance spectroscopy) a množství uvolněných kovových iontů se hodnotilo metodou ICP-MS (inductively coupled plasma mass spektrometry). Vliv korozního prostředí simuloval fyziologický solný roztok. Ověřen byl také vliv přidaných fluoridových iontů, které simulují prostředí dentálních implantátů.

Oba povlakové systémy na titanu i slitině Ti6Al4V ELI se chovaly srovnatelně v prostředí bez fluoridových iontů. Přídavek fluoridů prokázal existenci defektů zasahující až k základnímu materiálu a nejlepší korozní chování bylo prokázáno u povlaků s chromovou mezivrstvou. U titanové mezivrstvy byla korozní odolnost povlaků nanesených na Ti6Al4V ELI vyšší než u povlaků nanesených na titanu.

Provedené testy uvolňování kovových iontů do fyziologického roztoku potvrdily, že během 24 hodin nedošlo k uvolnění chromu v množství, které by bylo možné detekovat metodou ICP-MS. Provedené biologické testy ukázaly použitelnost mezivrstvy chromu pro implantáty s povlakem DLC [20].

Korozní odolnost funkčního povlaku

Korozní odolnost povlakového systém závisí kromě vhodné volby adhezní mezivrstvy a základního materiálu také na chemickém složení a struktuře samotného funkčního povlaku. Pro ověření tohoto předpokladu byl navržen experiment, kde byla hodnocena korozní odolnost DLC povlaků dopovaných Ti a porovnávána s povlakem DLC bez dopování [19]. Povlaky jsou určeny pro pohyblivá kloubní spojení a byly vytvořeny metodou reaktivního magnetronového naprašování z titanových terčů ve směsi plynů acetylenu a argonu. Ve všech případech adhezní mezivrstvu tvořil Ti s gradientním přechodem na Ti-C:H. Povlak DLC bez legování byl nanesen metodou PACVD z acetylenu jak amorfní uhlovodík a-C:H.

Korozní testy byly provedeny na povlakovém systému Ti/Ti-C:H ve třech úrovních legování, kde množství Ti 3,4; 10,2 a 23,6 uvedené v atomových % bylo určeno metodou XPS. Jako reference pro porovnání sloužil povlakový systém Ti/Ti-C:H/a-C:H. Jako základní materiál byla u všech variant použita vždy titanová β-slitina TiNbTa. Metoda EIS ve fyziologickém solném roztoku potvrdila, že korozní chování vzorků s legovanou vrstvou se

výrazně lišilo od čistých DLC povlaků. Elektrochemické reakce prostředí na povrchu grafitu byly překryty interakcí titanu s elektrolytem. Pro tribologické chování může mít legování titanem příznivý vliv, protože vedlo k mírnému zvýšení povrchové kolonizace buněk a tím i k zvýšení bioaktivity povrchu vedoucí ke zvýšení adheze proteinů fungujících jako lubrikant.

4 Aplikace povlaků

Tribologické vlastnosti povlaků lze ověřit pomocí testů simulující podmínky reálného prostředí, například na tribometru za vysokých teplot, popřípadě v korozně agresivním prostředí. Přesto takové testy nemohou zahrnout působení vedlejších vlivů, které mají zásadní vliv na životnost povlaku (tuhost celého tribologického systému, vibrace, rychlost a směr pohybu nebo synergie těchto vlivů). Povlaky je proto nutné testovat buď přímo v provozních podmínkách nebo použít testovací zařízení schopné tyto podmínky simulovat. V následujícím textu budou popsány vrtací testy a testy na simulátoru pohybu pro vybrané povlaky.

4.1 Povlaky pro obrábění

Vliv uhlíku v povlaku CrCN na obrábění hliníkových slitin

Obrábění hliníkových slitin používaných pro automobilový nebo letecký průmysl vyžaduje přesné a kvalitní obrobení povrchu. Výsledný povrch by měl být bez vneseného povrchového pnutí nebo defektů, které by mohly iniciovat vznik trhlin [41]. Toho lze dosáhnout obráběním s relativně nízkou řeznou rychlostí a za použití řezných kapalin. Snaha snížit náklady a ekologickou zátěž vede k jejich odstranění, a proto je stále více preferované vysokorychlostní suché obrábění [42]. Pro jeho úspěšnou aplikaci je nutné optimalizovat tribologické vlastnosti povrchu nástroje, aby se obráběný materiál nenalepoval na řezných hranách nebo povrchu nástroje. Musí být splněny dvě základní podmínky a) vhodně zvolená geometrie nástroje umožňující plynulý odvod třísky snižující lokální přehřátí nástroje [43] a b) volba vhodného chemického složení povrchu nástroje zamezující nalepování obráběného materiálu [44].

Používají se například PCD (polycrystaline diamond) nástroje [45], ale jejich nevýhodou je vyšší cena, omezená volba geometrie nástroje a přítomnost Co v základním materiálu jako pojiva, které zvyšuje riziko nalepování hliníku na povrchu nástroje. Pro univerzální použití mohou být vhodnější standardní nástroje opatřené povlakem s optimalizovaným chemickým složením [46], [47], [48]. Obecně u povrchů obsahující Cr, Ti, Co může dojít při suchém nebo MQL (minimum quantity lubrication) obrábění hliníkových slitin k jejich nalepování nebo navařování. Výsledkem je lokální přehřátí nástroje, vedoucí k jeho destrukci nebo zlomení. V současné době se pro výše jmenované aplikace používají převážně nepovlakované nástroje, většinou nástroje s nitridovanou řeznou hranou. Použití těchto nástrojů je často limitované parametry obrábění, jako je nízká rychlost obrábění a nutnost použití MQL chlazení, aby nedocházelo k degradaci nitridované hrany vlivem vysoké teploty. Naopak u povlakovaných nástrojů lze cílenou optimalizací chemického složení a mechanických

vlastností povrchu nástroje docílit ideální tribologické podmínky pro obrábění hliníkových slitin.

Z rozsáhlého výzkumu zaměřeného na suché obrábění hliníkových slitin se nejvíce osvědčily povlaky ZrN a CrCN. Naopak problematické mohou být povlaky obsahující pouze Cr a Al, které mohou za zvýšených teplot vlivem difúze a schopnosti vytvářet smíšené rozhraní, zvyšovat tření vedoucí až k samotnému svaření.

Cílem navrženého experimentu bylo objasnit vliv uhlíku u povlaku CrCN v přímém kontaktu s obráběnou hliníkovou slitinou za mezních podmínek, například bez chlazení nebo při maximálních doporučených otáčkách. Povlaky CrN a CrCN byly naneseny na iontově nitridované vrtáky z HSS-Co pomocí reaktivního magnetronového naprašování. Hodnocena byla jejich tvrdost H a redukovaný modul elasticity E_r, které byly testovány pomocí nanoindentoru. Naměřené hodnoty jsou uvedeny v tabulce 4.1. Vyšší poměr H/E_r pro povlak CrCN udává vyšší elastickou odolnost proti poškození povlaku a vyšší poměr H^2/E_r^3 zase vyšší odolnost proti plastické deformaci [4]. Mechanické vlastnosti povlaku CrCN odpovídají vlastnostem definovaným pro flexibilní tvrdé povlaky [49].

Tabulka 4.1 Nanotvrdost H a redukovaný modul elasticity E_r pro povlaky CrN, CrCN a nepovlakovaný základní materiál HSS-Co (zatížení 50 mN)

	Nanotvrdost [GPa]	**E_r [**GPa]	**H/E_r**	**H^2/E_r^3**
bez povlaku*	13.03 ± 1.66	245.81 ± 16.24	0,05	0,32
CrN	20.25 ± 0.46	248.99 ± 6.03	0,08	0,49
CrCN	15.03 ± 0.50	118.11 ± 3.51	0,13	0,76

* *iontově nitridováno*

Pro vrtací zkoušku byla jako vhodný referenční materiál zvolena hliníková slitina AlSi9Cu3, která je při aplikaci řezných kapalin dobře obrobitelná. Vrtací zkouška byla provedena na stojanové vrtačce s volitelným posuvem. Abychom mohli vyhodnotit chování v mezních podmínkách, vrtání probíhalo za sucha při maximálních otáčkách 1440 ot./min. doporučené výrobcem vrtáků a s konstantní rychlostí posuvu 0.11 mm/ot. pro každý test. Vrtací hloubka 16 mm odpovídala 2D vrtáku. Hodnocen byl stav povrchu vrtáku a vnitřku děr po vyvrtání 80ti děr.

Při vrtacím testu byl snímán točivý moment, který pro povlak CrN dosahoval více jak dvojnásobných hodnot (8,2 Nm) oproti hodnotám povlaku CrCN (3,6 Nm) a nepovlakovanému vrtáku (3,9 Nm). To odpovídalo také výsledkům z vysokoteplotních tribologických testů

provedených pomocí tribometru pin-on-disk. Jako třecí protikus byl vyroben pin s poloměrem 3 mm ze shodného materiálu AlSi9Cu3, který byl použit pro vrtací testy a povlak byl nanesen na ploché vzorky d 40 x 5 mm z HSS. Testy probíhaly při normálovém zatížení 5 N a lineární rychlosti 0,1 $m.s^{-1}$. Přestože byl koeficient tření velmi podobný pro oba povlaky (obrázek 4.1a), byla rychlost opotřebení výrazně nižší pro povlak CrCN (obrázek 4.1b). Opotřebení v případě povlaku CrN je tak výrazně ovlivněno vznikem tuhého lubrikantu tvořeného směsí abrazivních částic, převážně na bázi oxidů hliníku.

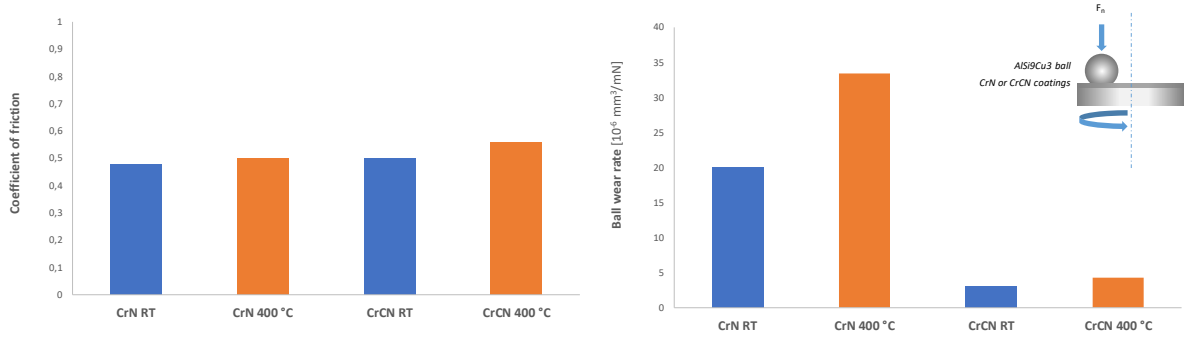

(a) (b)

Obrázek 4.1 Vysokoteplotní tribologické testy povlaků CrN a CrCN na tribometru pin-on-disk: a) koeficient tření a b) rychlost opotřebení

Výrazně odlišný mechanismus obrobeného povrchu uvnitř děr na obrázku 4.2 dole odpovídá předchozím tribologickým testům. Pro povlak CrN je povrch obráběn mechanismem založeném na abrazivním působení formujících se oxidických částí za vysokých teplot během vrtání. Pro povlak CrCN a vrták bez povlaku převládá adhezní mechanismus opotřebení a výsledkem je formování větších šupin vzniklých tažením obráběné slitiny.

Vliv uhlíku jako blokující složky pro potlačení nalepování obráběné hliníkové slitiny je viditelný na obrázku 4.2 nahoře. Pro povlak CrCN bylo na povrchu vrtáku detekováno nejméně nalepeného materiálu. Uplatňuje se zde potlačení difúze mezi povlakem obsahující určité množství uhlíku a obráběnou slitinou obsahující hliník a křemík. Chemické složení povlaku je tedy možné optimalizovat pro obrábění materiálu s předem určeným chemickým složením.

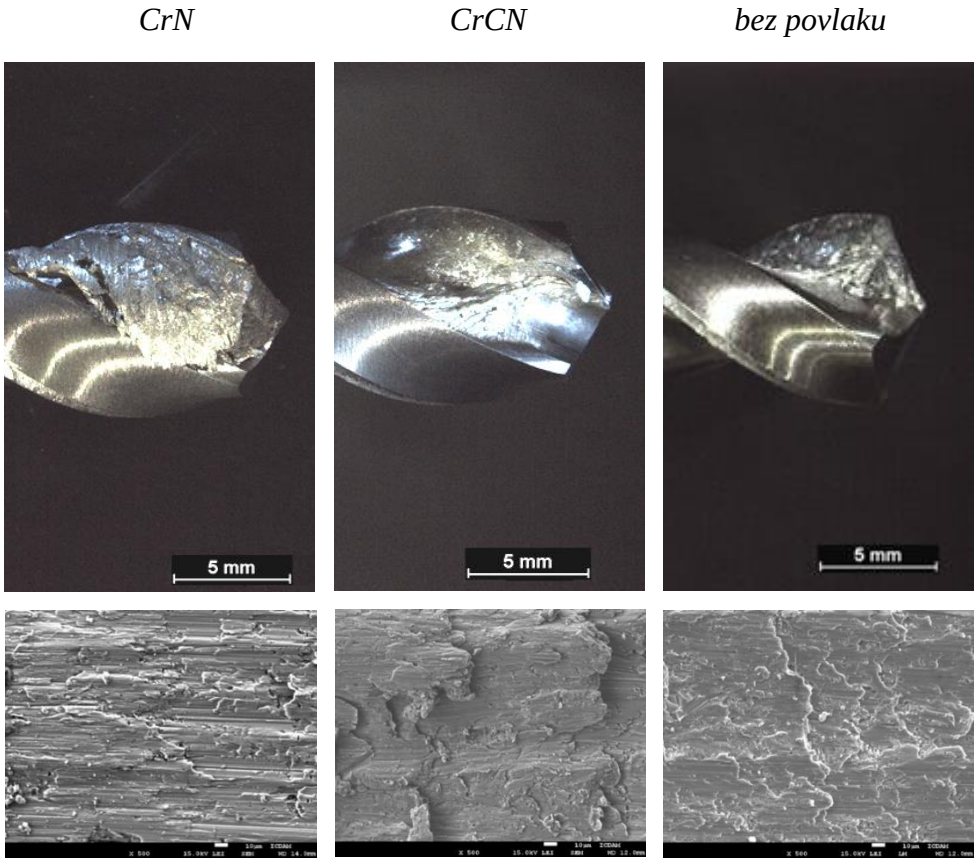

Obrázek 4.2 Porovnání schopnosti potlačení nalepování obráběné hliníkové slitiny na vrtácích s povlaky CrN, CrCN a bez povlaku po vrtacím testu (nahoře) a porovnání obrobeného povrchu uvnitř děr (dole).

Bylo potvrzeno, že mechanické vlastnosti povlaku CrCN mohou být optimalizovány velmi blízce k vlastnostem flexibilních tvrdých nanokompozitních povlaků, kde je definován poměr H/E_r vyšší než 0,1. Dále bylo potvrzeno, že uhlík v povlaku CrCN snižuje adhezi obráběné Al-Si slitiny k povrchu vrtáku a rychlost opotřebení slitiny Al-Si jednoznačně ovlivňuje uhlík, ale vliv na koeficient tření je pouze minimální.

4.2 Povlaky pro lékařské implantáty

Pohyblivé kloubní spojení v lidském těle představuje důmyslný tribologický systém, který je ovlivněn mnoha časově proměnnými parametry. Kromě teploty, která se může pohybovat pro tribologii v přijatelném rozmezí kolem 37 °C, je mnohem podstatnější působení chemického složení okolního prostředí. To je z větší části tvořeno synoviální tekutinou s pH běžně se pohybujícím v rozmezí mezi 7,4-7,6 které se ale v případě zánětlivé reakce může měnit [50], [51]. Při působení tohoto korozně agresívního prostředí v kombinaci s tribolgickou zátěží se

začínají projevovat tribochemické děje. Souhrnně se těmito jevy zabývá biotribologie, která byla vyčleněna z oblasti tribologie speciálně pro zkoumání pohyblivých systémů v biologickém prostředí.

Při návrhu kloubního implantátu je nutné zvolit chemicky stabilní a korozně odolné materiály. Osvědčené třecí dvojice kloubních implantátů, které představují například CoCrMo – UHMWPE nebo Al_2O_3 – UHMWPE, jsou sice spolehlivé, ale prodloužit jejich životnost je stále předmětem výzkumu. Ne vždy může základní materiál splnit náročné tribologické podmínky. V takovém případě se nabízí aplikace povlaků na povrch třecích dílů.

Volba vhodného povlaku musí zajistit chemicky stabilní povrch a splnit požadavky na dlouhodobou adhezi povlaku k základnímu materiálu. Kromě toho může povlak fungovat i jako difúzní bariéra proti uvolňování toxických iontů (například Co, Cr, Mo, Ni, V nebo Al) ze základního materiálů (CoCrMo, Ti6Al4V ELI nebo korozivzdorné oceli). Nejnovější studie prokázaly, že pro dlouhodobou životnost kloubních spojení implantátů je podstatná také schopnost vázat proteiny na povrch třecích ploch. Tím dojde k výraznému snížení tření vlivem zajištění lubrikace povrchu v mezních stavech nastávajících při pohybu z klidové polohy [52], [53].

V následujícím textu budou popsány experimenty navržené pro ověření funkčnosti a životnosti optimalizovaných povlakových systémů nanesených na reálných implantátech. Životní cyklus implantátu byl testován na simulátoru pohybu. Hodnocen byl také vliv ostatních parametrů, jako je korozní odolnost nebo vliv geometrie implantátu.

Test povlaku DLC na simulátoru pohybu

Povlaky DLC pro ortopedické implantáty firmy ProSpon byly testovány na simulátoru pohybu KKK ELO 2007 (obrázek 4.1) podle normy ISO 14 243 [54]. Testy probíhaly ve fyziologickém roztoku (PS) obsahujícím 9 g/L chloridu sodného při teplotě 37,0 ± 0,2 °C. Simulátor byl doplněn o možnost online monitorování korozního potenciálu a pH [55]. Především změna korozního potenciálu může okamžitě signalizovat porušení povlaku během testu. Po přerušení testu lze potom snadněji nalézt a analyzovat poškozené místo. To je velká výhoda oproti standardnímu postupu, kde se kontrola provádí až po uběhnutí předepsaného počtu cyklů.

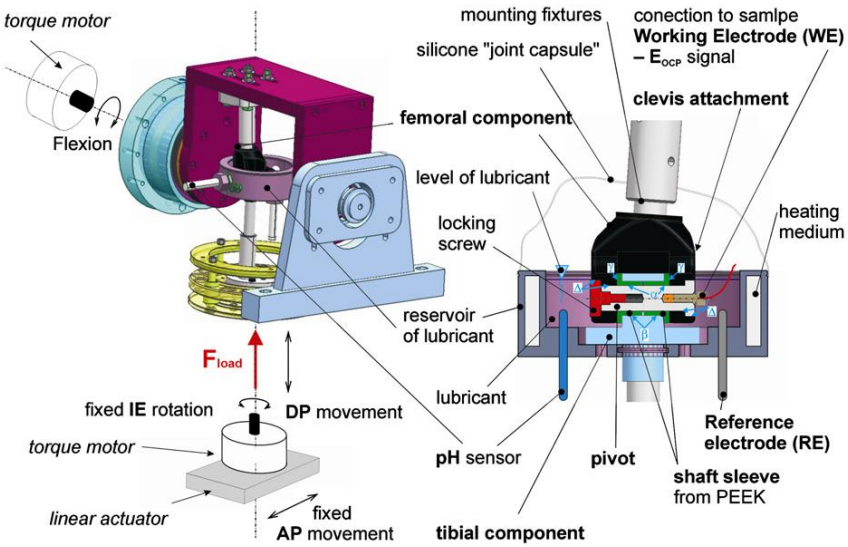

Obrázek 4.3 Schéma simulátoru pohybu rozšířeného o monitorování korozního potenciálu [55]

Ověřována byla funkce onkologického implantátu zamčeného kolene. Implantát (obrázek 4.2) byl vyroben ze slitiny Ti6Al4V ELI a opatřen povlakovým systémem Ti/Ti-C:H/a-C:H optimalizovaným pro lékařské aplikace. Jeden z důvodů povlakování bylo ošetřit povrch titanové slitiny proti otěru pohybujících se vazů a měkkých tkání. Tento otěr dlouhodobě způsobuje uvolňování kovových prvků z povrchu implantátu a jejich usazovaní v okolní tkáni, vzniká tzv. metalóza. Druhým důvodem rozhodujícím pro dlouhodobou funkci implantátu bylo snížení tření a otěru v čepu z Ti6Al4V ELI a lůžka z PEEK (viz obrázek 4.2).

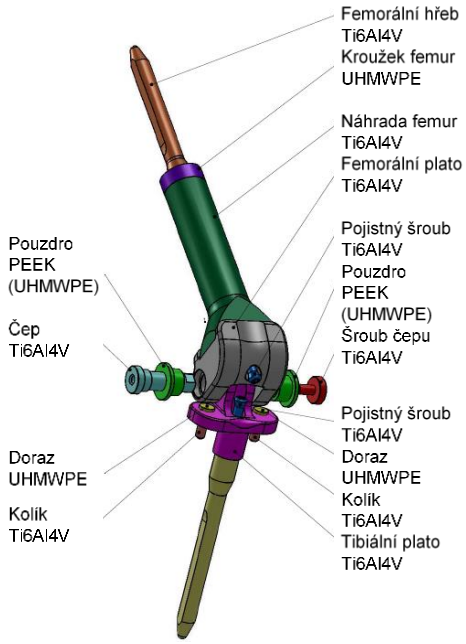

Obrázek 4.4 Onkologický implantát kolenního kloubu [ProSpon]

Povlaky byly nanášeny metodou PACVD z acetylenu při teplotě 200 °C. Celková tloušťka povlakového systému Ti/Ti-C:H/a-C:H na zvolených místech implantátu se pohybovala kolem 4,9 µm, z toho na funkční povlak a-C:H připadalo 1,9 µm. Nejprve byl testován implantát bez povlaku, kde došlo k totálnímu selhání již při 3,00 x 10^5 cyklech, protože třecí kombinace titanových slitin a materiálu PEEK není pro tribologické aplikace vhodná. Pokud byl stejný implantát povlakován, výrazně se zvýšila jeho životnost. Přesto byl po 1,98 x 10^6 cyklech test přerušen, protože na průběhu korozního potenciálu byla zaznamenána výrazná změna, která odhalila lokální poškození povlaku na povrchu čepu. Vliv na poškození měla příliš vysoká drsnost povrchu, která způsobila selhání adheze povlaku v nejvíce namáhaných místech. Při výrobě čepu se tento poznatek zohlednil a nově byla předepsána nižší hodnota přípustné drsnosti povrchu čepu před povlakováním.

Po doporučené úpravě implantátu byl test na simulátoru zopakován. Navržený systém splnil požadavky dané normou, které nařizují minimální životnost implantátu alespoň 5 x 10^6 cyklů. Test tedy prokázal jednoznačné zvýšení životnosti povlakovaných implantátů a rozšíření o monitorování korozního potenciálu umožnilo odhalit problematická místa povlakovaných částí krátce po jejich vzniku.

Vliv na životnost povlakovaných implantátů mohou ovlivnit i další parametry. Volba vhodné geometrie a elasticita základního materiálu mají rozhodující vliv na namáhání povlaku a následné selhání jeho adheze. Tento problém byl řešen pro totální endoprotézu kořenového kloubu palce ruky firmy Beznoska. Nový implantát byl navržen jako třecí dvojice kov-kov oproti původní variantě kov-UHMWPE a to především s cílem zvětšit průměr hlavičky z 5 mm na 7 mm a tím zvýšit stabilitu kloubu.

Pro ověření možnosti použít titanovou slitinu Ti6Al4V ELI pro výrobu implantátu palce, byly provedeny testy na tribometru pin-on-disk ve fyziologickém roztoku. Testováno bylo tření povlakované kuličky o různém průměru (6, 10 a 28 mm) proti disku se stejným povlakovým systémem Ti/Ti-C:H/a-C:H. Použit byl stejný povlakový systém jako v předešlém experimentu s uzamčeným onkologickým kolenem. Pro průměry 6 a 10 mm docházelo ke zvýšenému opotřebení, průměr 28 mm vyhověl testům. V případě malých průměrů působí na povlak poměrně vysoký bodový tlak, ale v případě reálného implantátu s geometrií dotyku hlavička-jamka, bude tlak pro povlak mnohem nižší.

Na základě těchto poznatků byl navržen model implantátu palce pro testování na simulátoru pohybu (obrázek 4.3). Vyroben byl z titanové slitiny Ti6Al4V ELI, ale během testování na simulátoru pohybu (počet cyklů 5,00 x 10^5, zatížení 150 N, frekvence 3 Hz, úhel ± 8°) došlo k totální destrukci povlaku. Z následné analýzy vyplynulo, že je potřeba zvolit jiný

materiál, který bude mít při daném dynamickém zatížení větší tvarovou stálost. Pro další testy byl model implantátu palce vyroben ze slitiny CoCrMo, která je vhodnější vzhledem ke své vyšší mechanické pevnosti, vyššímu modulu pružnosti a snadné leštitelnosti.

Obrázek 4.5 Model implantátu totální endoprotézy kořenového kloubu palce ruky pro testování na simulátoru pohybu [Beznoska]

Po sérii provedených testů vyplynuly následující poznatky pro zlepšení funkce a životnosti implantátu. Zásadním parametrem je vliv výrobních rozdílů kulové plochy jamky a hlavice. Rozdíl průměrů hlavice a jamky by neměl překročit rozmezí 0,12±0,02 mm. V případě menšího rozdílu se lubrikant nedostane mezi třecí plochy a v případě většího rozdílu se již výrazně projeví působení bodového tlaku v místě dotyku hlavičky s jamkou. Při výrobě je také nutné povrch hlavičky a jamky leštit před povlakováním na drsnost alespoň R_a 0,05 µm.

5 Závěr

Práce prezentuje souhrn poznatků, které mají za cíl objasnit závislosti mezi strukturou povlaků a jejich tribologickými vlastnostmi. Vychází z aktuálních požadavků na zvýšení výkonu, snížení spotřeby nebo prodloužení životnosti tribologických systémů pracujících za vysokých teplot nebo v korozním prostředí. Experimenty byly provedeny v průmyslových depozičních systémech zohledňující vlivy, které v laboratorních depozičních zařízeních nelze simulovat. Například vliv víceosé rotace na růstový mechanismus povlaku nebo vliv nečistot a defektů v povlaku pocházející převážně z pohyblivých částí průmyslového zařízení.

Samotná struktura povlaků není ovlivněna pouze v průběhu depozice, ale také po depozici, například po zahřátí ve vysokoteplotních aplikacích. Toho lze s úspěchem využít k samovolné tvorbě oxidické třecí mezivrstvy, která má funkci tzv. pevného lubrikantu. Jedná se o povlaky se schopností samovolné adaptace na pracovní prostředí. S úspěchem byl tento mechanismus využit v experimentech zaměřených na povlaky CrN a CrCN.

Dalším příkladem povlaků se schopností samovolné adaptace na pracovní prostředí jsou amorfní uhlovodíkové povlaky a-C:H obsahující legující kovové prvky. Samotné povlaky a-C:H mají velmi dobré tribologické vlastnosti, které jsou silně závislé na vnějších parametrech, především na vzdušné vlhkosti. Pro ostatní typy prostředí, například fyziologický roztok nebo olej s aditivy se chovají převážně inertně. Dopováním těchto povlaků titanem bylo úspěšně přizpůsobeno bioaktivní chování povrchu s možností vázat proteiny na povrchu jako přirozeného lubrikantu.

V aplikacích pro řezné nástroje je rozhodujícím parametrem vhodné chemické složení povlaku, které vytváří bariéru pro difúzní děje probíhající mezi povlakem a obráběným materiálem a zároveň snižuje nalepování obráběného materiálu na povrch nástroje. Současně musí být vzhledem k základnímu materiálu nástroje zvolena odpovídající tvrdost a elasticita povlaku. Není cílem dosažení co nejvyšší tvrdosti, ale mnohem důležitější může být kombinace tvrdosti a elasticity povlaku daná jejich podílem H/E. Nižší tvrdost oproti standardním tvrdým povlakům a současně mnohem nižší modul pružnosti umožňuje docílení lepší elastické odolnosti proti poškození povlaku. Při obrábění slitiny Al-Si byla funkce povlakového systému CrCN ověřena během vysokorychlostních vrtacích testů za sucha.

Pro mnohé aplikace je povlak nezbytnou součástí, bez kterého by nebylo možné dosažení požadovaného tření a otěru Další zlepšení mechanických vlastností a funkce povlaku jako korozní bariéry je omezeno mechanismem sloupcovitého růstu povlaku. Současný směr vývoje je zaměřen na využití zdrojů s pulzy o vysokém výkonu pro magnetronové naprašování,

které umožňují vytvářet kompaktní hustou strukturu povlaku a zároveň slouží pro zlepšení adheze povlaku k základnímu materiálu.

Získané poznatky potvrzují, že povlak a základní materiál by měly být navrženy současně s ohledem na danou aplikaci. Pouhé vylepšení povrchu již stávajícího základního materiálu nemůže poskytnout maximální využití tribologických vlastností povlaků.

Literatura

[1] HOLMBERG, Kenneth, Allan MATTHEWS a Helena RONKAINEN. Coatings tribology—contact mechanisms and surface design. *Tribology International*. 1998, **31**(1-3), 107-120. ISSN 0301679X.

[2] HOLMBERG, Kenneth, Anssi LAUKKANEN, Helena RONKAINEN, Kim WALLIN, Simo VARJUS a Jari KOSKINEN. Tribological contact analysis of a rigid ball sliding on a hard coated surface. *Surface and Coatings Technology* [online]. 2006, **200**(12-13), 3793-3809 [cit. 2018-07-08]. DOI: 10.1016/j.surfcoat.2005.03.040. ISSN 02578972. Dostupné z: http://linkinghub.elsevier.com/retrieve/pii/S0257897205004755

[3] DONNET, C a A ERDEMIR. Historical developments and new trends in tribological and solid lubricant coatings. *Surface and Coatings Technology* [online]. 2004, **180-181**, 76-84 [cit. 2018-06-28]. DOI: 10.1016/j.surfcoat.2003.10.022. ISSN 02578972. Dostupné z: http://linkinghub.elsevier.com/retrieve/pii/S025789720301154X

[4] MATTHEWS, A, S FRANKLIN a K HOLMBERG. Tribological coatings: contact mechanisms and selection. *Journal of Physics D: Applied Physics* [online]. 2007, **40**(18), 5463-5475 [cit. 2018-07-08]. DOI: 10.1088/0022-3727/40/18/S07. ISSN 0022-3727. Dostupné z: http://stacks.iop.org/0022-3727/40/i=18/a=S07?key=crossref.8c8ff780076e33881f7eb5900b1d1245

[5] HABCHI, Wassim. Coated EHL Contacts. *Finite Element Modelling of Elastohydrodynamic Lubrication Problems* [online]. 2018. Chichester, UK: John Wiley & Sons, 2018, s. 383-404 [cit. 2018-07-08]. DOI: 10.1002/9781119225133.ch11. ISBN 9781119225133. Dostupné z: http://doi.wiley.com/10.1002/9781119225133.ch11

[6] VAKIS, A.I., V.A. YASTREBOV, J. SCHEIBERT et al. Modeling and simulation in tribology across scales: An overview. *Tribology International* [online]. 2018, **125**, 169-199 [cit. 2018-07-08]. DOI: 10.1016/j.triboint.2018.02.005. ISSN 0301679X. Dostupné z: https://linkinghub.elsevier.com/retrieve/pii/S0301679X18300756

[7] HOLMBERG, K. a A. MATTHEWS. *Coatings tribology: properties, mechanisms, techniques and applications in surface engineering*. 2nd ed. Boston: Elsevier Science, 2009. Tribology and interface engineering series, 56. ISBN 9780444527509.

[8] ANDERS, André. A review comparing cathodic arcs and high power impulse magnetron sputtering (HiPIMS). *Surface and Coatings Technology* [online]. 2014, **257**, 308-325 [cit.

2018-09-02]. DOI: 10.1016/j.surfcoat.2014.08.043. ISSN 02578972. Dostupné z: https://linkinghub.elsevier.com/retrieve/pii/S0257897214007531

[9] MAYRHOFER, Paul, Christian MITTERER, Lars HULTMAN a Helmut CLEMENS. Microstructural design of hard coatings. *Progress in Materials Science* [online]. 2006, **51**(8), 1032-1114 [cit. 2018-06-30]. DOI: 10.1016/j.pmatsci.2006.02.002. ISSN 00796425. Dostupné z: http://linkinghub.elsevier.com/retrieve/pii/S0079642506000119

[10] DONNET, C. a A. ERDEMIR. Solid Lubricant Coatings: Recent Developments and Future Trends. *Tribology Letters* [online]. 2004, **17**(3), 389-397 [cit. 2018-06-28]. DOI: 10.1023/B:TRIL.0000044487.32514.1d. ISSN 1023-8883. Dostupné z: http://link.springer.com/10.1023/B:TRIL.0000044487.32514.1d

[11] NEVES, A.M., V. SEVERO, L. CVRČEK, T. POLCAR, C. LOURO a A. CAVALEIRO. In situ structural evolution of arc-deposited Cr-based coatings. *Surface and Coatings Technology* [online]. 2008, **202**(22-23), 5550-5555 [cit. 2017-01-03]. DOI: 10.1016/j.surfcoat.2008.06.102. ISSN 02578972. Dostupné z: http://linkinghub.elsevier.com/retrieve/pii/S025789720800501X

[12] POLCAR, T., L. CVRČEK, P. ŠIROKÝ a R. NOVÁK. Tribological characteristics of CrCN coatings at elevated temperature. *Vacuum* [online]. 2005, **80**(1-3), 113-116 [cit. 2017-01-03]. DOI: 10.1016/j.vacuum.2005.07.033. ISSN 0042207x. Dostupné z: http://linkinghub.elsevier.com/retrieve/pii/S0042207X05002654

[13] VITU, Tomas, Tomas POLCAR, Ladislav CVRCEK, Rudolf NOVAK, Jan MACAK, Jiri VYSKOCIL a Albano CAVALEIRO. Structure and tribology of biocompatible Ti–C: H coatings. *Surface and Coatings Technology* [online]. 2008, **202**(22-23), 5790-5793 [cit. 2017-01-03]. DOI: 10.1016/j.surfcoat.2008.06.040. ISSN 02578972. Dostupné z: http://linkinghub.elsevier.com/retrieve/pii/S0257897208005562

[14] POLCAR, T., T. VITU, L. CVRCEK, J. VYSKOCIL a A. CAVALEIRO. Effects of carbon content on the high temperature friction and wear of chromium carbonitride coatings. *Tribology International* [online]. 2010, **43**(7), 1228-1233 [cit. 2017-01-03]. DOI: 10.1016/j.triboint.2009.12.010. ISSN 0301679x. Dostupné z: http://linkinghub.elsevier.com/retrieve/pii/S0301679X09003478

[15] POLCAR, Tomas, Tomas VITU, Ladislav CVRCEK, Rudolf NOVAK, Jiri VYSKOCIL a Albano CAVALEIRO. Tribological behaviour of nanostructured Ti-C: H coatings for biomedical applications. *Solid State Sciences* [online]. 2009, **11**(10), 1757-1761 [cit.

2017-01-03]. DOI: 10.1016/j.solidstatesciences.2008.10.006. ISSN 12932558. Dostupné z: http://linkinghub.elsevier.com/retrieve/pii/S1293255808003154

[16] SILVENNOINEN, Raimo, Stanislav HASOŇ, Vladimír VETTERL et al. Diffractive-optics-based sensor as a tool for detection of biocompatibility of titanium and titanium-doped hydrocarbon samples. *Applied Optics* [online]. 2010, **49**(29), 5583- [cit. 2017-01-03]. DOI: 10.1364/AO.49.005583. ISSN 00036935. Dostupné z: https://www.osapublishing.org/abstract.cfm?URI=ao-49-29-5583

[17] FENG, F., Y. ZHOU, H. YUN, A. ROCHA, T. POLCAR, L. CVRCEK, H. LIANG a A. BANDYPADHYAY. Potential Application of a Ti-C: H Coating in Implants. *Journal of the American Ceramic Society* [online]. 2012, **95**(9), 2741-2745 [cit. 2017-01-03]. DOI: 10.1111/j.1551-2916.2011.05000.x. ISSN 00027820. Dostupné z: http://doi.wiley.com/10.1111/j.1551-2916.2011.05000.x

[18] SILVENNOINEN, Raimo, Vladimir VETTERL, Stanislav HASON et al. Sensing of human plasma fibrinogen on polished, chemically etched and carbon treated titanium surfaces by diffractive optical element based sensor. *Optics Express* [online]. 2008, **16**(14), 10130- [cit. 2017-01-03]. DOI: 10.1364/OE.16.010130. ISSN 10944087. Dostupné z: https://www.osapublishing.org/oe/abstract.cfm?uri=oe-16-14-10130

[19] JOSKA, L., J. FOJT, L. CVRČEK, V. BŘEZINA a J. MÁLEK. Corrosion behavior of DLC coating alloyed by titanium. In: *21st International Conference on Metallurgy and Materials, METAL 2012*. Brno: TANGER Ltd., 2012, s. 1342-1348. ISBN 978-808729431-4.

[20] JOSKA, L., J. FOJT, O. MESTEK, L. CVRCEK a V. BREZINA. The effect of a DLC coating adhesion layer on the corrosion behavior of titanium and the Ti6Al4V alloy for dental implants. *Surface and Coatings Technology* [online]. 2012, **206**(23), 4899-4906 [cit. 2017-01-03]. DOI: 10.1016/j.surfcoat.2012.05.089. ISSN 02578972. Dostupné z: http://linkinghub.elsevier.com/retrieve/pii/S025789721200504X

[21] CVRČEK, Ladislav, Jiří VYSKOČIL a Jan VALTER. ION BOMBARDMENT IN MAGNETRON SPUTTERING OF HARD COATINGS: PLASMA CONTROL AND FILM PROPERTIES. In: *Seventh Sheffield ABS Days*. Sheffield, England: Sheffield Hallam University, 2001.

[22] DUQUENNE, C., P. TESSIER, M. BESLAND, B. ANGLERAUD, P. JOUAN, R. AUBRY, S. DELAGE a M. DJOUADI. Impact of magnetron configuration on plasma

and film properties of sputtered aluminum nitride thin films. *Journal of Applied Physics* [online]. 2008, **104**(6) [cit. 2018-09-21]. DOI: 10.1063/1.2978226. ISSN 0021-8979. Dostupné z: http://aip.scitation.org/doi/10.1063/1.2978226

[23] PETROV, I., P. BARNA, L. HULTMAN a J. GREENE. Microstructural evolution during film growth. *Journal of Vacuum Science & Technology A: Vacuum, Surfaces, and Films* [online]. 2003, **21**(5), 117-128 [cit. 2018-09-21]. DOI: 10.1116/1.1601610. ISSN 0734-2101. Dostupné z: http://avs.scitation.org/doi/10.1116/1.1601610

[24] ABADIAS, G, W LEROY, S MAHIEU a D DEPLA. Influence of particle and energy flux on stress and texture development in magnetron sputtered TiN films. *Journal of Physics D: Applied Physics* [online]. 2013, **46**(5) [cit. 2018-09-21]. DOI: 10.1088/0022-3727/46/5/055301. ISSN 0022-3727. Dostupné z: http://stacks.iop.org/0022-3727/46/i=5/a=055301?key=crossref.8757935bcda63aaed66ad3ee9ccadfbb

[25] MAHIEU, S a D DEPLA. Reactive sputter deposition of TiN layers: modelling the growth by characterization of particle fluxes towards the substrate. *Journal of Physics D: Applied Physics* [online]. 2009, **42**(5) [cit. 2018-09-21]. DOI: 10.1088/0022-3727/42/5/053002. ISSN 0022-3727. Dostupné z: http://stacks.iop.org/0022-3727/42/i=5/a=053002?key=crossref.a5b7a4af93460c709483c6bf9ad4f186

[26] MAYRHOFER, P.H., G. TISCHLER a C. MITTERER. Microstructure and mechanical/thermal properties of Cr–N coatings deposited by reactive unbalanced magnetron sputtering. *Surface and Coatings Technology* [online]. 2001, **142-144**, 78-84 [cit. 2018-06-26]. DOI: 10.1016/S0257-8972(01)01090-8. ISSN 02578972. Dostupné z: http://linkinghub.elsevier.com/retrieve/pii/S0257897201010908

[27] MAYRHOFER, P.H, H WILLMANN a C MITTERER. Oxidation kinetics of sputtered Cr–N hard coatings. *Surface and Coatings Technology* [online]. 2001, **146-147**, 222-228 [cit. 2017-08-15]. DOI: 10.1016/S0257-8972(01)01471-2. ISSN 02578972. Dostupné z: http://linkinghub.elsevier.com/retrieve/pii/S0257897201014712

[28] AIZAWA, T., A. MITSUO, S. YAMAMOTO, T. SUMITOMO a S. MURAISHI. Self-lubrication mechanism via the in situ formed lubricious oxide tribofilm. *Wear* [online]. 2005, **259**(1-6), 708-718 [cit. 2018-06-28]. DOI: 10.1016/j.wear.2005.02.025. ISSN 00431648. Dostupné z: http://linkinghub.elsevier.com/retrieve/pii/S004316480500150X

[29] AOUADI, S.M., B. LUSTER, P. KOHLI, C. MURATORE a A.A. VOEVODIN. Progress in the development of adaptive nitride-based coatings for high temperature tribological

applications. *Surface and Coatings Technology* [online]. 2009, **204**(6-7), 962-968 [cit. 2018-06-28]. DOI: 10.1016/j.surfcoat.2009.04.010. ISSN 02578972. Dostupné z: http://linkinghub.elsevier.com/retrieve/pii/S025789720900348X

[30] SUSKI, Cassio a C. DE OLIVIERA. Coating and Aplications. DAVIM, J. Paulo, ed., J. DAVIM. *Tribology in manufacturing technology*. 1. New York: Springer, 2012, s. 175-194. Materials forming, machining and tribology. ISBN 9783642316821.

[31] JAHN, Sabrina a Jacob KLEIN. Lubrication of articular cartilage. *Physics Today* [online]. 2018, **71**(4), 48-54 [cit. 2018-08-22]. DOI: 10.1063/PT.3.3898. ISSN 0031-9228. Dostupné z: http://physicstoday.scitation.org/doi/10.1063/PT.3.3898

[32] HULTMAN, Lars a Christian MITTERER. Thermal Stability of Advanced Nanostructured Wear-Resistant Coatings. CAVALEIRO, Albano, ed. a Jeff Th. M. DE HOSSON, ed., Albano CAVALEIRO, Jeff DE HOSSON. *Nanostructured Coatings* [online]. New York, NY: Springer New York, 2006, s. 464-510 [cit. 2018-07-22]. Nanostructure Science and Technology. DOI: 10.1007/978-0-387-48756-4_11. ISBN 978-0-387-25642-9. Dostupné z: http://link.springer.com/10.1007/978-0-387-48756-4_11

[33] FOX-RABINOVICH, German a George TOTTEN. *Self-organization during friction: advanced surface-engineered materials and systems design*. Boca Raton, FL: CRC/Taylor & Francis, 2007. Materials engineering (Taylor & Francis), 31. ISBN 9781574447194.

[34] VETTER, J., E. LUGSCHEIDER a S.S. GUERREIRO. (Cr: Al)N coatings deposited by the cathodic vacuum are evaporation. *Surface and Coatings Technology* [online]. 1998, **98**(1-3), 1233-1239 [cit. 2018-08-22]. DOI: 10.1016/S0257-8972(97)00238-7. ISSN 02578972. Dostupné z: http://linkinghub.elsevier.com/retrieve/pii/S0257897297002387

[35] UCHIDA, M., N. NIHIRA, A. MITSUO, K. TOYODA, K. KUBOTA a T. AIZAWA. Friction and wear properties of CrAlN and CrVN films deposited by cathodic arc ion plating method. *Surface and Coatings Technology* [online]. 2004, **177-178**, 627-630 [cit. 2018-08-22]. DOI: 10.1016/S0257-8972(03)00937-X. ISSN 02578972. Dostupné z: http://linkinghub.elsevier.com/retrieve/pii/S025789720300937X

[36] PANJAN, P., B. NAVINŠEK, A. CVELBAR, A. ZALAR a J. VLCEK. High-temperature oxidation of TiN/CrN multilayers reactively sputtered at low temperatures. *Surface and Coatings Technology* [online]. 1998, **98**(1-3), 1497-1502 [cit. 2018-08-22]. DOI:

10.1016/S0257-8972(97)00395-2. ISSN 02578972. Dostupné z: http://linkinghub.elsevier.com/retrieve/pii/S0257897297003952

[37] LEE, H.Y., W.S. JUNG, J.G. HAN, S.M. SEO, J.H. KIM a Y.H. BAE. The synthesis of CrSiN film deposited using magnetron sputtering system. *Surface and Coatings Technology* [online]. 2005, **200**(1-4), 1026-1030 [cit. 2018-08-22]. DOI: 10.1016/j.surfcoat.2005.02.006. ISSN 02578972. Dostupné z: http://linkinghub.elsevier.com/retrieve/pii/S0257897205001908

[38] PAWLAK, Zenon, Kehinde YUSUF, Raghuvir PAI a Wieslaw URBANIAK. Repulsive surfaces and lamellar lubrication of synovial joints. *Archives of Biochemistry and Biophysics* [online]. 2017, **623-624**, 42-48 [cit. 2018-08-22]. DOI: 10.1016/j.abb.2017.05.009. ISSN 00039861. Dostupné z: http://linkinghub.elsevier.com/retrieve/pii/S0003986117301844

[39] MACÁK, Jan, Martina PAZDEROVÁ, Ivo JIŘÍČEK, Pavel MALÝ, Karel OLYŠAR, Ladislav CVRČEK a Jan VOŠTA. KOROZNÍ VLASTNOSTI FYZIKÁLNĚ NANÁŠENÝCH TENKÝCH VRSTEV. *Chemické listy*. 2007, **101**(9), 713-721.

[40] BISWAS, Barnali, Yashodhan PURANDARE, Imran KHAN a Papken HOVSEPIAN. Effect of substrate bias voltage on defect generation and their influence on corrosion and tribological properties of HIPIMS deposited CrN/NbN coatings. *Surface and Coatings Technology* [online]. 2018, **344**, 383-393 [cit. 2018-08-22]. DOI: 10.1016/j.surfcoat.2018.03.009. ISSN 02578972. Dostupné z: http://linkinghub.elsevier.com/retrieve/pii/S0257897218302561

[41] BASSOLI, Elena, Luca IULIANO a Alessandro SALMI. Deep Drilling of Aluminium Die-Cast Parts: Surface Roughness, Dimensional Tolerance, and Tool–Chip Interaction. *Materials and Manufacturing Processes* [online]. 2010, **25**(6), 442-449 [cit. 2017-03-30]. DOI: 10.1080/10426910903124795. ISSN 10426914. Dostupné z: http://www.tandfonline.com/doi/abs/10.1080/10426910903124795

[42] RIVERO, A., G. ARAMENDI, S. HERRANZ a L.N. LÓPEZ DE LACALLE. An experimental investigation of the effect of coatings and cutting parameters on the dry drilling performance of aluminium alloys. *The International Journal of Advanced Manufacturing Technology* [online]. 2006, **28**(1-2), 1-11 [cit. 2018-09-25]. DOI: 10.1007/s00170-004-2349-3. ISSN 0268-3768. Dostupné z: http://link.springer.com/10.1007/s00170-004-2349-3

[43] NOUARI, M., G. LIST, F. GIROT a D. COUPARD. Experimental analysis and optimisation of tool wear in dry machining of aluminium alloys. *Wear* [online]. 2003, **255**(7-12), 1359-1368 [cit. 2017-03-30]. DOI: 10.1016/S0043-1648(03)00105-4. ISSN 00431648. Dostupné z: http://linkinghub.elsevier.com/retrieve/pii/S0043164803001054

[44] ATLATI, S., A. MOUFKI, M. NOUARI a B. HADDAG. Interaction between the local tribological conditions at the tool–chip interface and the thermomechanical process in the primary shear zone when dry machining the aluminum alloy AA2024–T351. *Tribology International* [online]. 2017, **105**, 326-333 [cit. 2017-03-30]. DOI: 10.1016/j.triboint.2016.10.006. ISSN 0301679x. Dostupné z: http://linkinghub.elsevier.com/retrieve/pii/S0301679X16303693

[45] HU, J., Y.K. CHOU a R.G. THOMPSON. Nanocrystalline diamond coating tools for machining high-strength Al alloys. *International Journal of Refractory Metals and Hard Materials* [online]. 2008, **26**(3), 135-144 [cit. 2017-04-07]. DOI: 10.1016/j.ijrmhm.2007.05.012. ISSN 02634368. Dostupné z: http://linkinghub.elsevier.com/retrieve/pii/S0263436807000558

[46] FOX-RABINOVICH, G., J.M. DASCH, T. WAGG, K. YAMAMOTO, S. VELDHUIS, G.K. DOSBAEVA a M. TAUHIDUZZAMAN. Cutting performance of different coatings during minimum quantity lubrication drilling of aluminum silicon B319 cast alloy. *Surface and Coatings Technology* [online]. 2011, **205**(16), 4107-4116 [cit. 2017-03-30]. DOI: 10.1016/j.surfcoat.2011.03.006. ISSN 02578972. Dostupné z: http://linkinghub.elsevier.com/retrieve/pii/S0257897211001848

[47] RIVERO, A., G. ARAMENDI, S. HERRANZ a L.N. LÓPEZ DE LACALLE. An experimental investigation of the effect of coatings and cutting parameters on the dry drilling performance of aluminium alloys. *The International Journal of Advanced Manufacturing Technology* [online]. 2006, **28**(1-2), 1-11 [cit. 2017-03-30]. DOI: 10.1007/s00170-004-2349-3. ISSN 02683768. Dostupné z: http://link.springer.com/10.1007/s00170-004-2349-3

[48] ROY, P., S.K. SARANGI, A. GHOSH a A.K. CHATTOPADHYAY. Machinability study of pure aluminium and Al–12% Si alloys against uncoated and coated carbide inserts. *International Journal of Refractory Metals and Hard Materials* [online]. 2009, **27**(3), 535-544 [cit. 2017-03-30]. DOI: 10.1016/j.ijrmhm.2008.04.008. ISSN 02634368. Dostupné z: http://linkinghub.elsevier.com/retrieve/pii/S0263436808000413

[49] MUSIL, J. Flexible hard nanocomposite coatings. *RSC Advances* [online]. 2015, **5**(74), 60482-60495 [cit. 2018-09-25]. DOI: 10.1039/C5RA09586G. ISSN 2046-2069. Dostupné z: http://xlink.rsc.org/?DOI=C5RA09586G

[50] LIU, Yangping a Jeremy GILBERT. The effect of simulated inflammatory conditions and Fenton chemistry on the electrochemistry of CoCrMo alloy. *Journal of Biomedical Materials Research Part B: Applied Biomaterials* [online]. 2018, **106**(1), 209-220 [cit. 2018-08-22]. DOI: 10.1002/jbm.b.33830. ISSN 15524973. Dostupné z: http://doi.wiley.com/10.1002/jbm.b.33830

[51] MILOŠEV, Ingrid, Vesna LEVAŠIČ, Janja VIDMAR, Simon KOVAČ a Rihard TREBŠE. PH and metal concentration of synovial fluid of osteoarthritic joints and joints with metal replacements. *Journal of Biomedical Materials Research Part B: Applied Biomaterials* [online]. 2017, **105**(8), 2507-2515 [cit. 2018-08-22]. DOI: 10.1002/jbm.b.33793. ISSN 15524973. Dostupné z: http://doi.wiley.com/10.1002/jbm.b.33793

[52] PARKES, Maria, Connor MYANT, Philippa CANN a Janet WONG. Synovial Fluid Lubrication: The Effect of Protein Interactions on Adsorbed and Lubricating Films. *Biotribology* [online]. 2015, **1-2**, 51-60 [cit. 2018-08-22]. DOI: 10.1016/j.biotri.2015.05.001. ISSN 23525738. Dostupné z: http://linkinghub.elsevier.com/retrieve/pii/S2352573815000086

[53] MYANT, C., R. UNDERWOOD, J. FAN a P.M. CANN. Lubrication of metal-on-metal hip joints: The effect of protein content and load on film formation and wear. *Journal of the Mechanical Behavior of Biomedical Materials* [online]. 2012, **6**, 30-40 [cit. 2018-08-22]. DOI: 10.1016/j.jmbbm.2011.09.008. ISSN 17516161. Dostupné z: http://linkinghub.elsevier.com/retrieve/pii/S1751616111002426

[54] *ISO 14243 (1-3): Implants for surgery -- Wear of total knee-joint prostheses*. 2009.

[55] FRANTA, Lukas, Jaroslav FOJT, Ludek JOSKA, Jakub KRONEK, Ladislav CVRCEK, Jiri VYSKOCIL a Zdenek CEJKA. Hinge-type knee prosthesis wear tests with a mechanical load and corrosion properties monitoring. *Tribology International* [online]. 2013, **63**, 61-65 [cit. 2017-01-03]. DOI: 10.1016/j.triboint.2012.02.014. ISSN 0301679x. Dostupné z: http://linkinghub.elsevier.com/retrieve/pii/S0301679X12000680

Zkratky

DC	direct current
DLC	diamond-like carbon
DOE	diffractive optical element
EIS	electrochemical impedance spectroscopy
EPMA	electron probe microanalyzesis
FBS	fetal bovine serum
HIPIMS	high power impulse magnetron sputtering
HPF	human plasma fibrinogen
HTXRD	high temperature X-ray difraction
ICP-MS	inductively coupled plasma mass spektrometry
MQL	minimum quantity lubrication
OCP	open circuit potential
PEEK	polyetheretherketone
PS	physiological solution
PVD	physical vapour deposition
RBS	Rutherford backscattering spektrometry
SBF	simulated body fluid
SEM	scanning electron microscopy
UHMWPE	ultra high molecular weight polyethylene
XPS	X-ray photoelectron spectroscopy

Příloha A: Seznam použitých prací

CVRČEK, Ladislav, Jiří VYSKOČIL a Jan VALTER. ION BOMBARDMENT IN MAGNETRON SPUTTERING OF HARD COATINGS: PLASMA CONTROL AND FILM PROPERTIES. In: Seventh Sheffield ABS Days. Sheffield, England: Sheffield Hallam University, 2001.

POLCAR, T., L. CVRČEK, P. ŠIROKÝ a R. NOVÁK. Tribological characteristics of CrCN coatings at elevated temperature. Vacuum. 2005, 80(1-3), 113-116. DOI: 10.1016/j.vacuum.2005.07.033. ISSN 0042207x. **A1**

NEVES, A.M., V. SEVERO, L. CVRČEK, T. POLCAR, C. LOURO a A. CAVALEIRO. In situ structural evolution of arc-deposited Cr-based coatings. Surface and Coatings Technology. 2008, 202(22-23), 5550-5555. DOI: 10.1016/j.surfcoat.2008.06.102. ISSN 02578972. **A5**

SILVENNOINEN, Raimo, Vladimir VETTERL, Stanislav HASON, Heikki TUONONEN, Martti SILVENNOINEN, Kari MYLLER, Ladislav CVRČEK, Jiří VANĚK and Patrik PRACHÁR. Sensing of human plasma fibrinogen on polished, chemically etched and carbon treated titanium surfaces by diffractive optical element based sensor. Optics Express. 2008, 16(14), 10130-10140. DOI: 10.1364/OE.16.010130. ISSN 10944087. **A11**

VITU, Tomas, Tomas POLCAR, Ladislav CVRCEK, Rudolf NOVAK, Jan MACAK, Jiri VYSKOCIL a Albano CAVALEIRO. Structure and tribology of biocompatible Ti–C: H coatings. Surface and Coatings Technology. 2008, 202(22-23), 5790-5793. DOI: 10.1016/j.surfcoat.2008.06.040. ISSN 02578972. **A22**

POLCAR, Tomas, Tomas VITU, Ladislav CVRCEK, Rudolf NOVAK, Jiri VYSKOCIL a Albano CAVALEIRO. Tribological behaviour of nanostructured Ti-C: H coatings for biomedical applications. Solid State Sciences. 2009, 11(10), 1757-1761. DOI: 10.1016/j.solidstatesciences.2008.10.006. ISSN 12932558. **A26**

SILVENNOINEN, Raimo, Stanislav HASOŇ, Vladimír VETTERL, Niko PENTTINEN, Martti SILVENNOINEN, Kari MYLLER, Pavlína ČERNOCHOVÁ, Sonia BARTÁKOVÁ, Patrik PRACHÁR and Ladislav CVRČEK. Diffractive-optics-based sensor as a tool for detection of biocompatibility of titanium and titanium-doped hydrocarbon samples. Applied Optics. 2010, 49(29), 5583-5591. DOI: 10.1364/AO.49.005583. ISSN 00036935. **A31**

POLCAR, T., T. VITU, L. CVRCEK, J. VYSKOCIL a A. CAVALEIRO. Effects of carbon content on the high temperature friction and wear of chromium carbonitride coatings. Tribology International. 2010, 43(7), 1228-1233. DOI: 10.1016/j.triboint.2009.12.010. ISSN 0301679x. **A40**

JOSKA, L., J. FOJT, L. CVRČEK, V. BŘEZINA a J. MÁLEK. Corrosion behavior of DLC coating alloyed by titanium. In: 21st International Conference on Metallurgy and Materials, METAL 2012. Brno: TANGER, 2012, s. 1342-1348. ISBN 978-808729431-4. **A46**

FENG, F., Y. ZHOU, H. YUN, A. ROCHA, T. POLCAR, L. CVRCEK, H. LIANG a A. BANDYPADHYAY. Potential Application of a Ti-C: H Coating in Implants. **A52**

Journal of the American Ceramic Society. 2012, 95(9), 2741-2745. DOI: 10.1111/j.1551-2916.2011.05000.x. ISSN 00027820.

JOSKA, L., J. FOJT, O. MESTEK, L. CVRCEK a V. BREZINA. The effect of a DLC coating adhesion layer on the corrosion behavior of titanium and the Ti6Al4V alloy for dental implants. Surface and Coatings Technology. 2012, 206(23), 4899-4906. DOI: 10.1016/j.surfcoat.2012.05.089. ISSN 02578972. **A57**

FRANTA, Lukas, Jaroslav FOJT, Ludek JOSKA, Jakub KRONEK, Ladislav CVRCEK, Jiri VYSKOCIL a Zdenek CEJKA. Hinge-type knee prosthesis wear tests with a mechanical load and corrosion properties monitoring. Tribology International. 2013, 63, 61-65. DOI: 10.1016/j.triboint.2012.02.014. ISSN 0301679x. **A65**

Available online at www.sciencedirect.com
SCIENCE DIRECT®
Vacuum 80 (2005) 113–116
VACUUM
SURFACE ENGINEERING, SURFACE INSTRUMENTATION & VACUUM TECHNOLOGY
www.elsevier.com/locate/vacuum

Tribological characteristics of CrCN coatings at elevated temperature

T. Polcar[a,*], L. Cvrček[b], P. Široký[b], R. Novák[c]

[a]*Department of Applied Mathematics, Faculty of Transportation Sciences, CTU in Prague, Na Florenci 25, Prague 1, Czech Republic*
[b]*HVM Plasma Ltd., Na Hutmance 2, 158 00 Prague 5, Czech Republic*
[c]*Department of Physics, Faculty of Mechanical Engineering, CTU in Prague, Technická 4, Prague 6, Czech Republic*

Abstract

Dry sliding wear experiments at specific temperatures ranging from 20 to 500 °C were conducted on CrCN coatings deposited onto steel substrates. The coatings were worn against 100Cr6 bearing steel balls, Si_3N_4 and Al_2O_3 balls, using a pin-on-disc sliding configuration at a contact load of 5 N. Friction coefficient and coating wear rates were measured, and wear tracks were analysed using SEM equipped with EDX. Coatings exhibited good wear performance and unexpected behaviour at elevated temperatures.

Keywords: CrCN coatings; Tribological properties; Elevated temperature

1. Introduction

Materials and coatings are often exposed to high temperatures, due to either frictional heating or high ambient temperatures. High temperature strongly influences wear mechanisms because of softening of the coating and substrate, changes in internal stress and, particularly, oxidation of the surface.

Chromium nitride is an excellent protective coating because of its hardness and corrosive resistance. However, the tribological behaviour of CrN coatings is found to vary according to the substrate material, coating thickness, type of wear and operating conditions. Although chromium nitride is brittle, a considerable reduction of yield stress resulting from a large increase of surface temperature enhances the plasticity of the coating. Thus, plastic deformation, brittle fracture and tribochemical process are reported to be the main mechanisms involved in chromium nitride wear [1–3].

CrCN is a relatively less studied coating promising improved tribological behaviour compared to CrN. Up to now the main attention has

*Corresponding author. Tel./fax: +420 2224352439.
E-mail address: Tomas.Polcar@fs.cvut.cz (T. Polcar).

0042-207X/$ - see front matter © 2005 Elsevier Ltd. All rights reserved.
doi:10.1016/j.vacuum.2005.07.033

been to use this coating as a protective coating in hip prostheses. Wear tests have shown that CrCN is superior to CrN in some respects [4]. Nevertheless, the friction and wear characteristics of CrCN coatings are not well known, particularly at elevated temperatures. In order to remedy this lack of data, the present study reports on the friction and wear characteristics of CrCN coatings.

2. Experiment

HSS substrates mechanically polished to roughness $R_a = 30$ nm were used in this study. The coatings were tested on a pin-on-disc high-temperature tribometer at temperatures ranging from room temperature to 500 °C. The riders were spheres of either 100Cr6 steel or Si_3N_4 or Al_2O_3 with a diameter of 6 mm. All measurements were done with a linear speed of 0.05 m/s and a load of 5 N; the number of cycles was 500 and the relative humidity of the air was in the range 30–40%.

Morphologies of wear tracks were examined using a scanning electron microscope (SEM) and an energy-dispersive X-ray spectrometer (EDX). Phase composition of coatings was checked by X-ray diffractometry. Wear rates of the tested balls and coatings were evaluated according to the method used by Holmberg et al. [5] and the profiles of wear tracks were measured by a mechanical profilometer. In order to get an insight into the morphology of CrCN coatings, X-ray diffraction (XRD) data were studied. We used a rotating anode Rigaku R4-300E and a spectrometer HZG3 (monochromatic Cu Kα, Bragg-Brentano geometry).

3. Results and discussion

3.1. Coatings characterization

Substrates were arranged in the sputtering system in a way necessary to obtain a homogeneous set of samples with identical coating thickness and chemical composition. The coatings were deposited in a HTC-625-Multilab coating machine, fabricated by Hauzer Techno Coating Europe BV., Venlo, the Netherlands. We used reactive arc deposition from Cr targets in an Ar and N_2 atmosphere with an addition of C_2H_2 reactive gas. DC substrate bias voltage was –70 V, working pressure during deposition of the order was 0.1 Pa and substrate temperature was 220 °C. Different chemical compositions of coatings were obtained by varying the C_2H_2 flow rate; for better adhesion a Cr interlayer was used. Chemical compositions of coatings were obtained by EPMA and, for comparison, by RBS, together with other parameters and are presented in Table 1. The CrCN-1 samples are nitrogen-rich, while the CrCN-2 samples have a ratio C:N = 1:1.

The observed XRD lines are too weak for a complete phase analysis. We expected to be able to identify at least Cr, CrN and Cr_2N and some Cr carbide phase, but in practice only Cr_2N (35-803) was clearly recognized and maybe $Cr_{23}C_6$ (35-783) or Cr_7C_3 (36-1482) can be present (Fig. 1). Of course there is an indication of pure Cr (6-694) but it is not clear if this signal is from the coating or from the interlayer. X-ray experiments also confirmed expected relaxation of residual tensile stress after temperature treatment during wear test at elevated temperatures.

All coatings exhibited very good adhesion with minimum critical force $L_c \geqslant 50$ N and class II in a

Table 1
Coating properties

Sample	Thickness (μm)	Adhesion (HRc category)	Microhardness HV0.01	Composition (at%)—EMPA	Composition (at%)—RBS
CrCN-1	3.2	Class II	1750	$Cr_{68}N_{24}C_8$	$Cr_{65}N_{27}C_8$
CrCN-2	3.9	Class II	1800	$Cr_{67}N_{14}C_{19}$	$Cr_{58}N_{21}C_{19}$

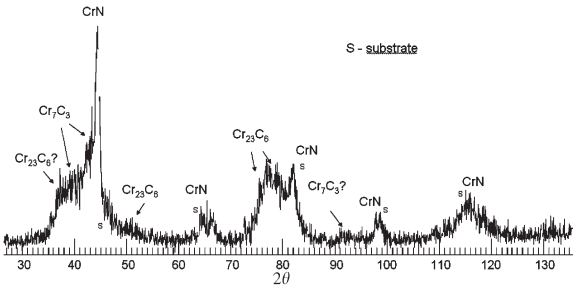

Fig. 1. X-ray spectra of CrCN-1 sample and possible phase composition.

Rc indentation test. All coatings data are collected in Table 1.

3.2. Friction and wear of coatings sliding against the 100Cr6 ball

Running-in is characterized by an increase of the friction coefficient during the first 200 cycles for all measured temperatures. The friction tests with 100Cr6 balls show that the average friction coefficient, stable after the running-up interval, is almost independent of temperature up to 300 °C, reaching values 0.6–0.67, and decreases to values 0.56 and 0.48 at 400 and 500 °C, respectively. Wear of CrCN coating sliding against the 100Cr6 ball was not measurable. On the contrary, transfer of ball material to the coating surface was very strong and the coating surface was fully covered by a layer of oxidized iron derived from the ball. As a result, the ball wear rate was very high. Wear debris was analysed and it was found that it contained only ball material, particularly iron oxides. The tribological behaviour described above is identical for both CrCN coatings.

3.3. Friction and wear against the Si_3N_4 and Al_2O_3 and balls

The friction curves of CrCN-1 sample sliding against Si_3N_4 ball at room temperature (20 °C) and 400 °C are presented in Fig. 2. In previous studies, chromium oxides have been shown to act as a lubricant in sliding wear situations [3,6]. However, despite the strong presence of chromium oxides at elevated temperature, the average friction

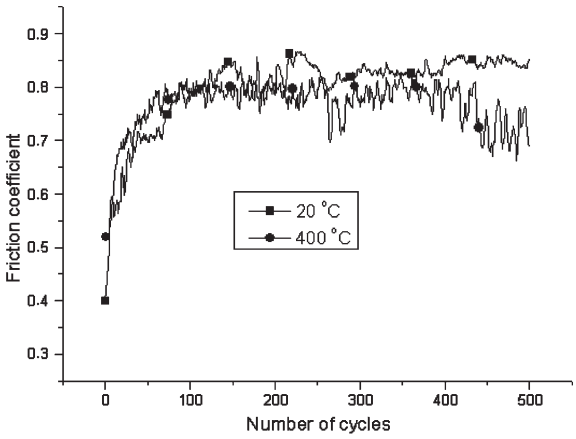

Fig. 2. Friction curves of CrCN-1 sample sliding against Si_3N_4 ball at 20 and 400 °C.

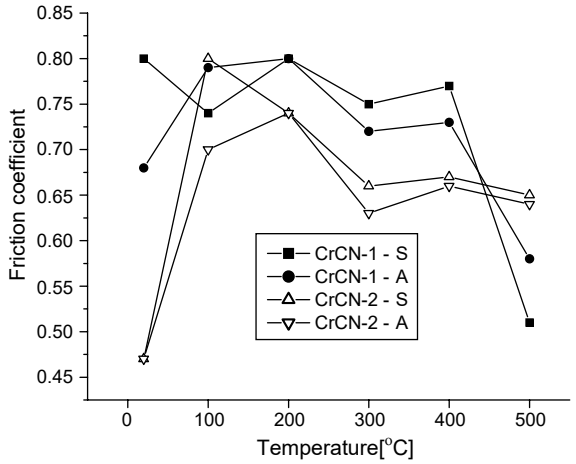

Fig. 3. Variation of the friction coefficient with temperature, Si_3N_4 balls (S) and Al_2O_3 balls (A).

coefficient was independent of temperature and it decreased only at 500 °C to 0.51. Coating wear rate slightly decreased with temperature. The CrCN-2 sample exhibits a very different friction and wear behaviour. The friction coefficient reaches the maximum at 100 °C and then decreases to a stable value of 0.65. The wear rate is very low at room temperature, then sharply rises up at a temperature of 200 °C and decreases again to a relatively low level in the temperature range 300–500 °C. The variation of friction coefficient with temperature for CrCN samples is shown in Figs. 3 and 4; Fig. 4

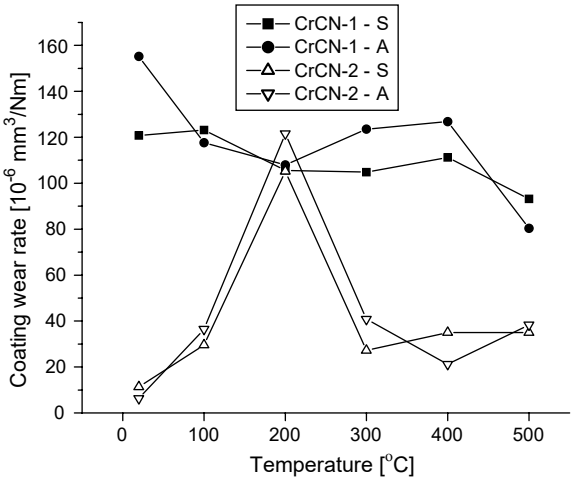

Fig. 4. Dependence of coating wear rate on temperature, Si_3N_4 balls (S) and Al_2O_3 balls (A).

represents coating wear as a function of temperature. Comparison of X-ray spectra taken at room temperature and that of the sample heated up to 400 °C (and measured at room temperature) showed an increase in grain size and decrease of internal stress. Moreover, spectra of heated sample are simplified: only the Cr_2N phase is recognizable. A possible explanation of the anomalous wear behaviour of CrCN-2 samples is the change of structure in the temperature between 200 and 300 °C, which can improve wear resistance at higher temperatures. The wear resistance of CrCN coatings at elevated temperatures is surprising, because almost all coatings widely used in industrial applications have shown a rapid increase of wear with temperature [2].

4. Conclusion

This work has studied the tribological properties of CrCN coatings. Samples of different coatings were prepared by reactive arc deposition and the chemical composition was tuned by changing the amount of C_2H_2 reactive gas. Prepared coatings were characterized by SEM and XRD. All samples exhibited good mechanical properties (i.e. microhardness and adhesion).

Pin-on-disc experiments have shown that the friction coefficient of CrCN coatings sliding against Si_3N_4 and Al_2O_3 balls is relatively high and stable at temperatures up to 500 °C. The coatings were not damaged by the sliding against 100Cr6 steel balls. Wear resistance, which does not increase with temperature, is the most interesting feature.

Some tribological properties of our coatings are difficult to understand and therefore a more detailed study is planned. Mainly we are going to prepare further CrCN coatings with different carbon content with the aim of showing the influence of carbon on tribological performance and main wear mechanisms of coatings.

Acknowledgements

The authors thank Dr. V. Peřina from the Institute of Nuclear Physics of the Czech Academy of Sciences, Řež near Prague, for providing RBS data, and Dr. Marian Čerňanský from the Institute of Physics, the Czech Academy of Sciences, Prague, for X-ray data. This work has been supported by research project MPO FD-K3/104 and research project MSM 21220008.

References

[1] Lin JF, Liu MH, Wu JD. Wear 1996;198:7–14.
[2] Su YL, Yao SH, Leu ZL, Wei CS, Wu CT. Wear 1997;213:165–74.
[3] Scheerer H, Hoche H, Broszeit E, Berger C. Surf Coat Technol 2001;142–144:1017–22.
[4] Fisher J, Hu XQ, Steward TD, et al. J Mater Sci: Mater Med 2004;15:225–35.
[5] Holmberg K, Matthews A. Coating tribology. Amsterdam: Elsevier; 1994.
[6] Sue J, Chang TP. Surf Coat Technol 1995;76–77:61–9.

Surface & Coatings Technology 202 (2008) 5550–5555

Contents lists available at ScienceDirect

Surface & Coatings Technology

journal homepage: www.elsevier.com/locate/surfcoat

In situ structural evolution of arc-deposited Cr-based coatings

A.M. Neves [a], V. Severo [a], L. Cvrček [b], T. Polcar [c], C. Louro [a], A. Cavaleiro [a,*]

[a] SEG-CEMUC, Mechanical Engineering Department, University of Coimbra, 3030-788 Coimbra, Portugal
[b] HVM Plasma Ltd., Na Hutmance 2, 158 00 Prague 5, Czech Republic
[c] Department of Control Engineering, Faculty of Electrical Engineering, Czech Technical University in Prague, Technická 2, Prague 6, Czech Republic* Corresponding author.

ARTICLE INFO

Available online 15 June 2008

Keywords:
Arc evaporation
Chromium nitride
Carbonitride coatings
Thermal stability
HTXRD

ABSTRACT

Cr-based coatings were prepared by cathode arc-evaporation technology using N_2 and C_2H_2 as reactive gases. Three compositions were investigated, $Cr_{60}N_{40}$, $Cr_{41}N_{27}C_{32}$ and $Cr_{67}C_{33}$.
The present investigation is centred on the structural stability via coatings tempering up to 1000 °C, by *in situ* X-ray diffraction in protective atmosphere. As-deposited coatings present low order structure with a medium feature size less then 10 nm. The hexagonal β-Cr_2N phase, characteristic of binary $Cr_{60}N_{40}$ coating, was stable up to 900 °C, before recrystallization and grain growth takes place. For $Cr_{41}N_{27}C_{32}$ film the phase transition varies from the metastable δ-Cr(N,C) to orthorhombic chromium carbonitride $Cr_3(C_xN_{1-x})_2$ phase up to 800 °C and then to chromium carbide phase. No chromium nitride phases were detected in spite of the similar N and C contents after the deposition. The Cr–C coating recrystallizes into a mixture of carbide phases, mainly Cr_3C_2 and $Cr_{23}C_6$ after 1000 °C annealing treatment.

1. Introduction

Chromium nitride coatings, which exhibit high hardness and excellent wear, corrosion and oxidation resistance, have been extensively used as protective coating on various tools and dies [1,2]. The oxidation resistance could be considered as the dominant factor for the successful application at elevated temperature conditions. The high oxidation limit of CrN coatings, typically about 700 °C [3], was attributed to the formation of a protective Cr_2O_3 layer.

Ternary Cr–X–N coatings were prepared with the goal to improve the oxidation resistance and the tribological properties at elevated temperature. Compared to other alloying elements, such as Al [4,5], Ti [6], Si [7], V [5] or B [8], Cr–C–N has been relatively less studied. Cekada et al. [9] analyzed Cr–C–N coatings deposited by evaporation. The films were subjected to oxidation tests showing the formation of a thin chromium oxide layer on the top followed by a nitrogen-rich layer demonstrating that nitrogen diffused towards the surface [9]. The microstructure and the thermal stability of arc-deposited Cr–C–N system were complexly analyzed by Almer et al. [10]. The comparison of the tribological properties between CrN and Cr–C–N coatings [11] showed the advantage of the latter; however, the difference in the friction coefficient and the wear rate is only minimal. In our previous study [12], Cr–C–N coatings were tribologically tested *in situ* up to 500 °C showing that the wear rate was almost independent on the temperature and lower than that of CrN coatings deposited and tested under similar conditions. Thus, in the present paper the thermally induced phase transitions of Cr–N, Cr–C–N and Cr–C coatings have been undertaken to infer the necessary knowledge to support the conclusion drawn in our previous studies [12,13].

2. Experimental procedures

Three series of Cr-based coatings were deposited onto high-temperature resistant Fecralloy substrates (72.8% Fe, 22% Cr, 5% Al, 0.1% Y, 0.1% Zr—Goodfellow) by cathodic arc evaporation from two rectangular cathodes using the aforementioned apparatus system [13]. The arc parameters were kept constant for all depositions: the current 80 A, the substrate bias −70 V and the substrate temperature 350 °C. The chromium was evaporated from a Cr target (99.8% purity) in N_2 (99.999% purity) and C_2H_2 (99.6% purity) atmospheres. For binary Cr–N and Cr–C coatings a partial pressure reactive gas of 0.17 Pa was set up at a constant value of 100 sccm, while for Cr–N–C films the flow of acetylene was fixed at 48 sccm. The corresponding increase of the total pressure from 0.17 to 0.20 Pa was measured by a capacitance manometer Leybold CERAVAC Transmitters CTR/91.

High temperature X-ray diffraction (HTXRD) measurements were done using a Philips X' Pert diffractometer with cobalt radiation (K_α = 0.178897 nm) in Bragg–Brentano geometry. The samples (12 × 10 mm) were fixed on a Pt plate and heated from RT up to 1000 °C in steps of 100 °C. The heating rate was 40 °C/min between each temperature step followed by maintenance of ~20 min for XRD acquisition in 35–60° range. The samples were cooled down to RT and new XRD patterns were acquired in the range 20–110°. The analyses were performed in a vacuum chamber HT16, coupled to the diffractometer and specially designed for *in situ* analysis. The experiments were performed under continuous gas (Ar-5%H_2) flux at low pressure (1–10 Pa) after evacuating the chamber down to a value lower than 10^{-3} Pa. The measured profile scans were deconvoluted by Origin program,

* Corresponding author.
E-mail address: albano.cavaleiro@dem.uc.pt (A. Cavaleiro).

0257-8972/$ – see front matter © 2008 Elsevier B.V. All rights reserved.
doi:10.1016/j.surfcoat.2008.06.102

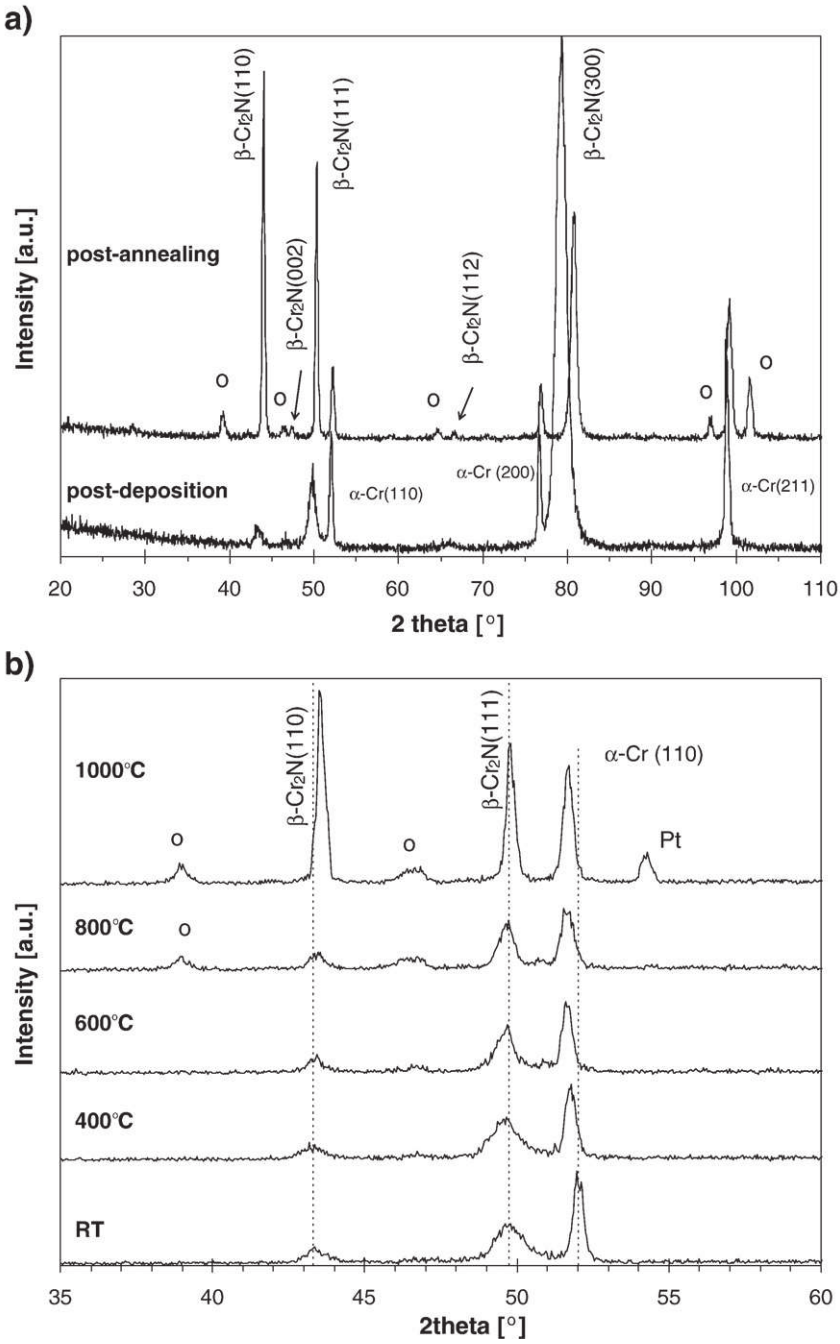

Fig. 1. XRD patterns of $Cr_{60}N_{40}$ sample: a) as-deposited and post annealing structure, b) structural evolution with annealing temperature; ○=Cr_2O_3, Pt=platinum plate.

assuming to be Voigt functions to yield the peak position, integrated intensity and integrated width (IntW). These parameters allow calculating the interplanar distance (d_{hkl}), preferential orientation and grain size (ϕ), using the Scherrer formula, respectively.

A Cameca SX-50 Electron Probe Microanalysis (EPMA) apparatus was used to determine the chemical composition of the coatings.

3. Results and discussion

Figs. 1 to 3 present the *in situ* XRD structural evolution up to 1000 °C of the three Cr-based coatings. The XRD patterns before and post annealing, acquired at RT in [20–110°] 2θ range, are also shown. The compositions investigated are summarized in Table 1. To facilitate reading, the coatings were denominated according to their chemical composition measured by EPMA, e.g. $Cr_{60}N_{40}$ is coating with 60 and 40 at.% of chromium and nitrogen, respectively.

The structure of the post-deposited binary Cr–N coating is dominated by the hexagonal β-Cr_2N [ICDD 35-0803] with a mean crystallite size of 12 nm and a preferred (300) orientation. Besides nitride phase, also bcc α-Cr phase is detected in all coatings. This phase can be attributed to small Cr-rich droplets. This phenomenon is a characteristic of Cr-based coatings deposited by arc evaporation [10]. XRD analysis, Fig. 1a), reveals that the β-Cr_2N phase is thermally stable up to 1000 °C. The only remarks are: (i) the narrowing of the peaks and (ii) the shift towards the equilibrium position with increasing temperature in comparison to the post-deposition state. These two effects could be understood more clearly by analyzing simultaneously Fig. 1b) and Fig. 4. This last one shows the *in situ* structural parameters, calculated after peak fitting of corresponding

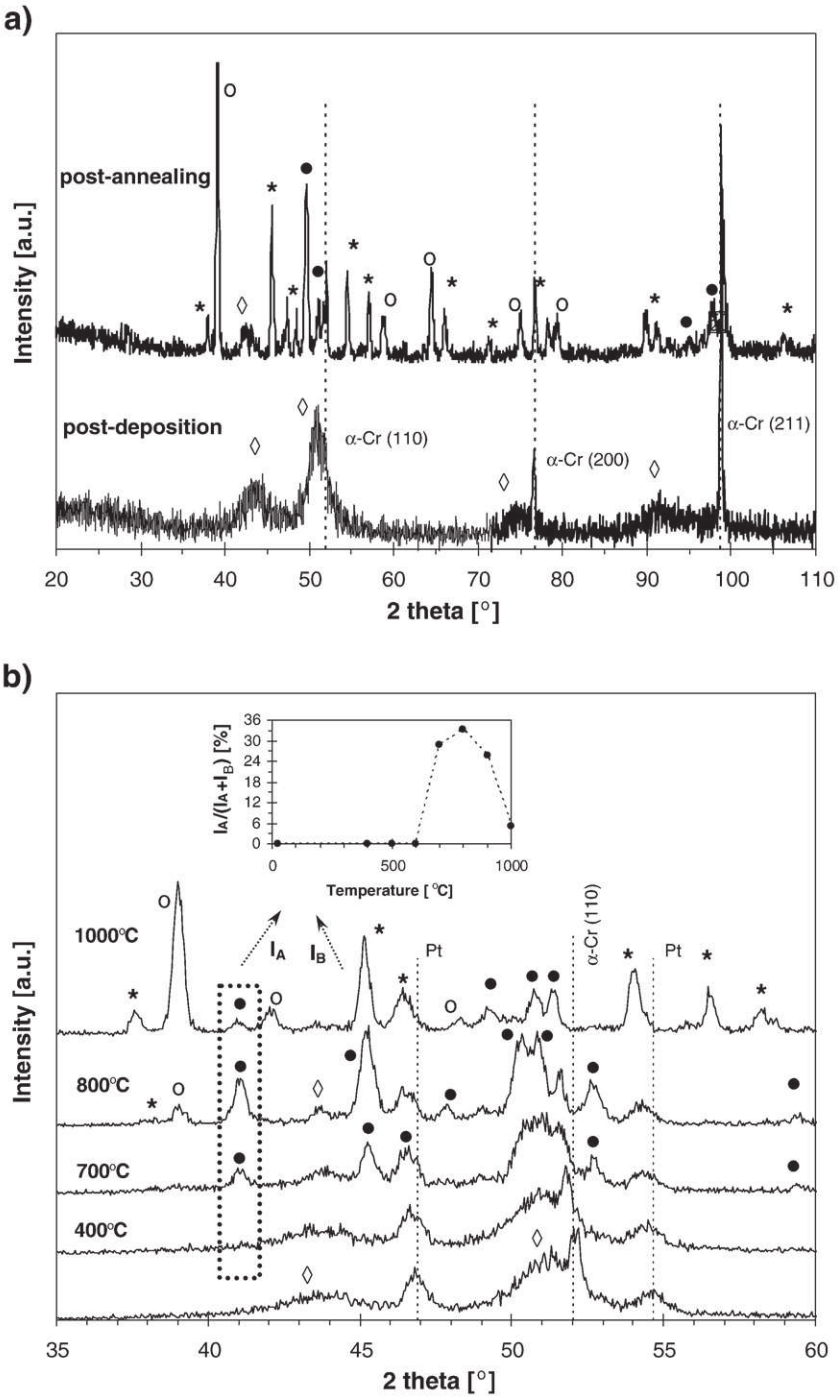

Fig. 2. XRD patterns of Cr–N–C coating: a) as-deposited and post annealing structure, b) structural evolution with annealing temperature; ◊ = δ-Cr(C,N), ● = $Cr_3(C_{0.92}N_{0.08})_2$, * = Cr_3C_2, ○ = Cr_2O_3, Pt = platinum plate.

(110) and (111) planes. The interplanar distance is increasing as a function of the annealing temperature up to 700 °C followed by an opposite trend for higher temperatures values. The first trend is well understood due to the lattice expansion under the heating effect ($\alpha_{CrN} = 2.3 \times 10^{-6}\ K^{-1}$ [14]). In this temperature range only small structural rearrangements of a typical recovery process could exist. This process becomes increasingly more intense at 700 °C as shown by the decrease in the interplanar distance (second trend of structural parameters variation in Fig. 4), suggesting stress relaxation and loosing of either the interstitial contaminant elements or the exceeding N from the Cr–N structure [15]. No significant crystallite size variation is observed during heating from RT to 800 °C. For higher temperatures, the β-Cr_2N peaks become narrower, more intense and the preferential orientation changes from (300) to (110), features characteristic of a recrystallization and grain growth processes. However, even though the grain size grows, the $Cr_{60}N_{40}$ film does not loose its nano-characteristics, presenting a mean grain size of 34 nm after *in situ* tempering. These results are better than those reported for CrN coatings, which decompose into β-Cr_2N by N_2 release at temperatures as low as 400 °C [16–18].

The addition of carbon to binary Cr–N films changes the as-deposited structure (compare Fig. 1a) with Fig. 2a)). The replacement of N by bigger C atoms increases the local stresses and leads to the instability of the hexagonal nitride phase in addition to a strong decrease of the film crystallinity. The $Cr_{41}N_{27}C_{32}$ film presents, after deposition, a broad and

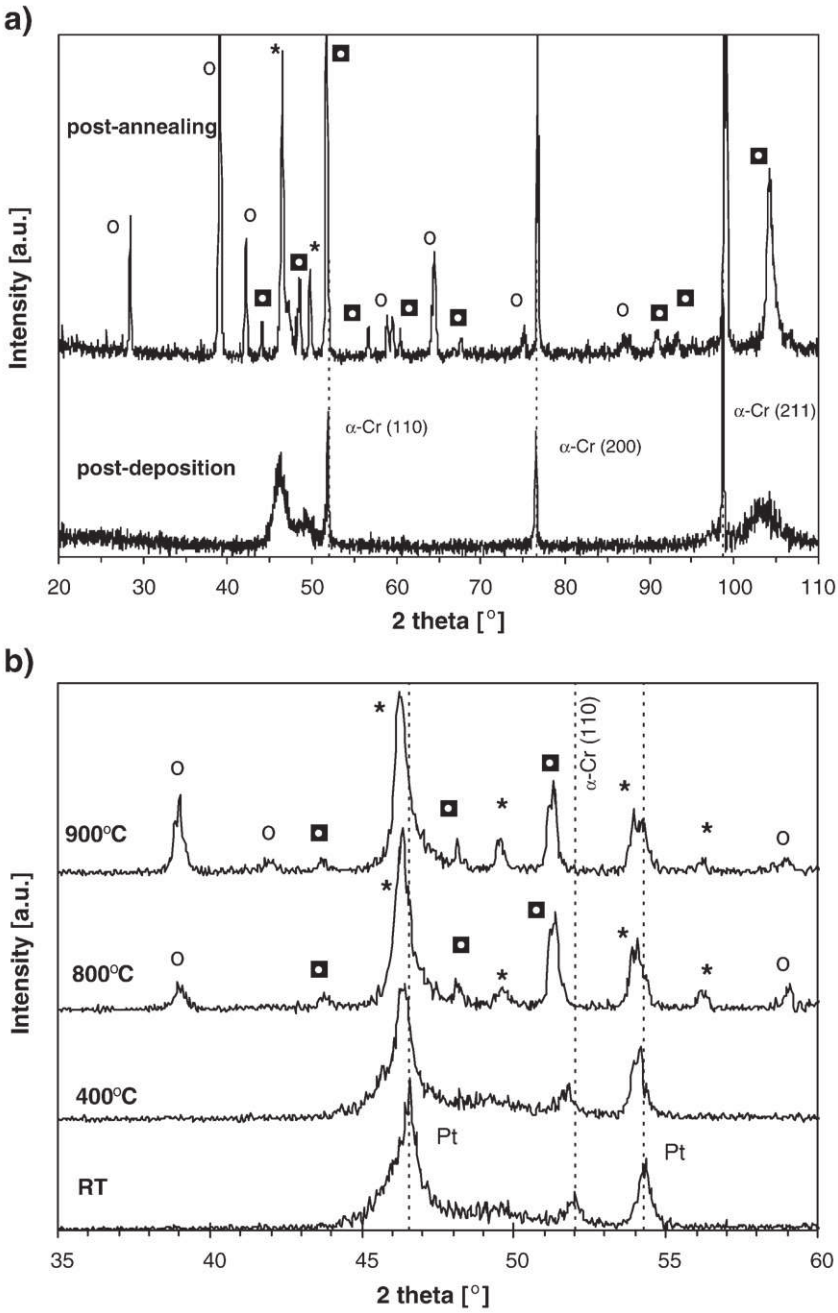

Fig. 3. XRD patterns of $Cr_{67}C_{33}$ coating: a) as-deposited and post annealing structure, b) structural evolution with annealing temperature; *=Cr_3C_2, =$Cr_{23}C_6$, ○=Cr_2O_3, Pt=platinum plate.

low intensity XRD patterns with a mean feature size of only 4 nm, characteristic of a quasi-crystalline or nanocrystalline structure. Taking into account the 2θ maximum peak position, the d values obtained after peak fitting match quite well with the fcc-CrN [ICDD 76-2494] structure. Thus, the as-deposited structure of Cr–N–C is dominated by a metastable cubic phase similar to that reported in others works [9,10] and denominated as δ-Cr(C,N) phase. After annealing at 1000 °C, the coating is completely crystallized presenting mainly a mixture of Cr_3C_2 [ICDD 71-2287] and $Cr_3(C_{0.92}N_{0.08})_2$ [ICDD 19-0326] phases, both from the orthorhombic system (Fig. 2a)). No nitride phases were detected in spite of the N and C similar contents after the deposition.

During the thermal treatment at increasing temperatures, the initial δ-Cr(C,N) phase remains unchanged up to 600 °C (Fig. 2b)). The only remark is the shift of the broad peak position to lower diffraction angles, similar to that observed for Cr–N coating, due to the expansion of the lattice under the heating effect. At 700 °C, well defined XRD peaks can be detected being the new phase indexed as an orthorhombic chromium carbonitride $Cr_3(C_xN_{1-x})_2$: the $Cr_3(C_{0.92}N_{0.08})_2$. The content of this phase increases with further annealing. However, at 900 °C, an interesting occurrence can be detected: the intensity of some $Cr_3(C_xN_{1-x})_2$ peaks

Table 1
Chemical composition of the Cr-based coatings (at.%)

Sample	Cr	N	C	O
$Cr_{60}N_{40}$	60.1	39.7	0.0	0.2
$Cr_{41}N_{27}C_{32}$	41.6	26.8	31.6	0.0
$Cr_{67}C_{33}$	66.5	–	33.3	0.2

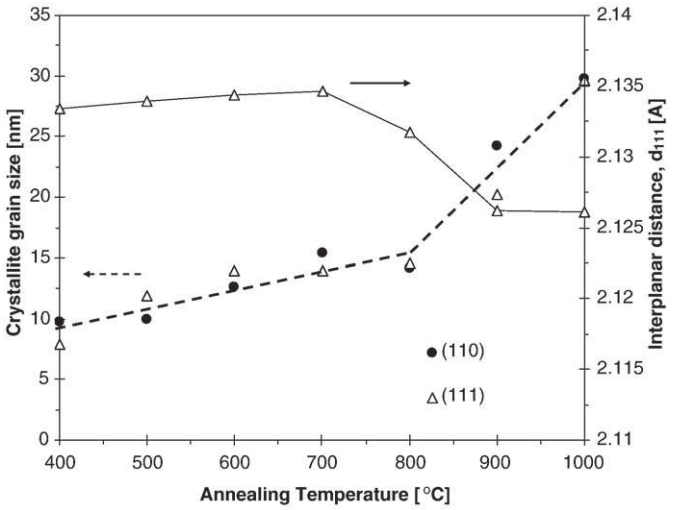

Fig. 4. Evolution of the structural parameters of the β-Cr_2N phase as a function of *in situ* XRD annealing temperature.

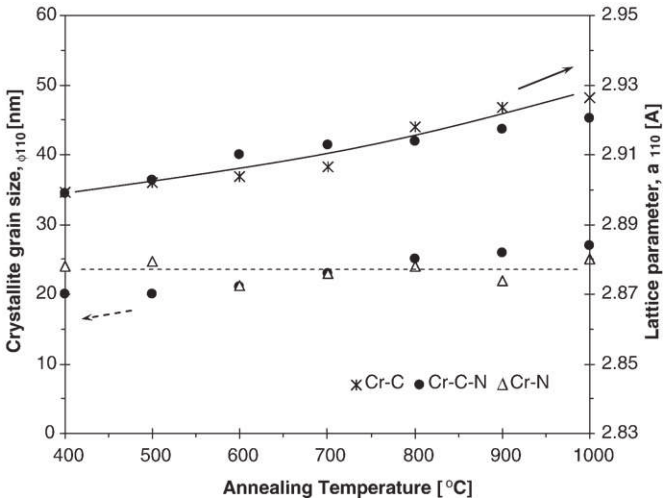

Fig. 6. Evolution of the structural parameters of the bcc α-Cr phase as a function of *in situ* XRD annealing temperature.

increases while others strongly decrease. This behaviour is illustrated in Fig. 2b (see inset graphic), suggesting a progressive transformation of the carbonitride phase. As the peaks remain in the same position, a phase of the same type should be forming: the orthorhombic Cr_3C_2. This proposal, which needs further investigation, is supported by the N loss detected by EPMA analysis on the remaining non-oxidized part of the coating. Fig. 5 illustrates that in an oxide spalled zone (see discussion below) only a small amount of the as-deposited N content was found after 1000 °C. It is reported that $Cr_3(C_xN_{1-x})_2$ are metastable crystallographic structures being stable only at high temperatures and/or under high N_2 pressure [19]. Thus, the N content loss could be the driving force for the Cr_3C_2 phase formation.

Similarly to Cr–N–C coatings, also in Cr–C system broad and low intensity XRD peaks, with a mean feature size of ~4 nm, can be detected together with the α-Cr phase (see Fig. 3a)). These low order structured films have already been deposited by other authors by arc evaporation, sputtering or electrodeposition processes [20–24]. The quasi-crystalline phase is stable up to 600 °C, starting to recrystallize at 700 °C in the Cr_3C_2 orthorhombic form (see the structural evolution in Fig. 3b)). Further annealing leads to the formation and growth of another chromium carbide, the fcc-$Cr_{23}C_6$ [ICDD-85-1281]. This phase transition can be expected since originally the C content is not enough to satisfying the stoichiometry of Cr_3C_2 (33 at.% against 40 at.%). Thus, the tendency for equilibrium requires the formation of a new carbide phase with lower C content, as is the case of $Cr_{23}C_6$. The occurrence of $Cr_{23}C_6$ instead of Cr_7C_3 (the predicted in the binary Cr–C phase diagram) is probably due to its lower free formation energy. It should be remarked that EPMA analysis carried out in a clear zone after annealing (analogous to that shown in Fig. 5) revealed almost exactly the same C content in the coating as post deposition (34.5 at.% against the as-deposited 33.3 at.%).

Finally, it is important to state that no significant structural changes were detected on the cubic α-Cr droplets. As can be seen in Fig. 6, the crystallite size evaluated from the (110) peak reveals no significant change with increasing temperature up to 1000 °C, whereas the lattice parameter steadily increases. This phenomenon is much more evident for α-Cr droplets than for Cr–N phases (see e.g. Fig. 4) due to its higher thermal expansion coefficient ($\alpha_{Cr} = 6.5 \times 10^{-6}\ K^{-1}$ [IUPAC-Periodic Table] against $\alpha_{Cr-N} = 2.3 \times 10^{-6}\ K^{-1}$ [14]).

The oxidation is a common phenomenon observed in all coatings during the *in situ* analysis despite the use of a reducing atmosphere. Even with all precautions (good initial vacuum—10^{-3} Pa, 2–3 Ar/H_2 flushes before starting the experiments) the formation of an external oxide layer,

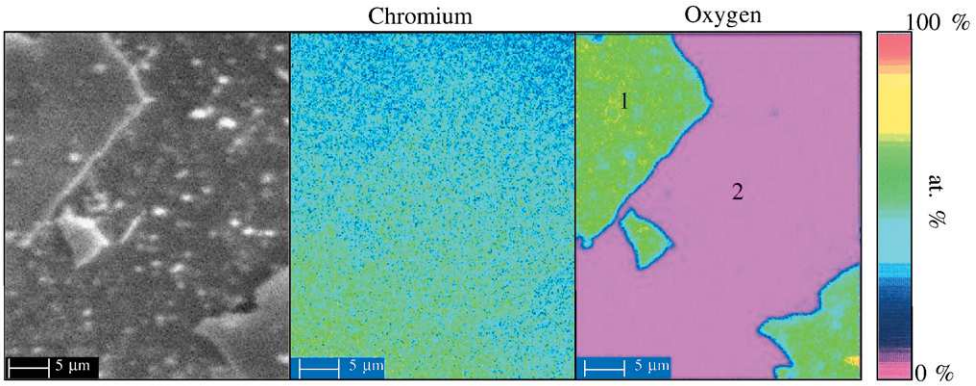

layer	O (at.%)	N (at.%)	C (at.%)	Cr (at.%)
1	44.9	0.76	12.4	41.9
2	0.8	6.1	36.0	57.1

Fig. 5. SEM surface top morphology of $Cr_{41}N_{27}C_{32}$ sample and the respective elemental EPMA maps for chromium and oxygen after thermal treatment; layer 1 = external Cr_3O_2 layer; layer 2 = inner non-oxidised coating.

indexed as Cr_2O_3 phase [ICDD 85-0869], could not be avoided for temperatures higher than 800 °C, as it has already been reported by other authors [25]. For the oxidation reaction progression it is necessary to replace N and C by O in their matrix positions. Since arc-evaporated Cr–N–C films present less compact morphologies than those observed for binary Cr–N and Cr–C coatings, the increased number of paths facilitates the N out-diffusion in small N_2 molecules more easily than C through CO_2/CO gases. The oxidation process seems to be more intense in this coating in comparison to the binary ones, as can be concluded from the comparative analysis of the intensities of the oxide peaks in Figs. 1 to 3. During cooling down to RT, oxide layer delamination was detected. Parts of the external oxide layer, shown in Fig. 5 for $Cr_{41}N_{27}C_{32}$, spalled out readily in powder form during its subsequent handling. For $Cr_{60}N_{40}$ coating only a change from grey to a green color was observed.

4. Conclusions

Arc-deposition technique was successfully used to deposit Cr–N, Cr–N–C and Cr–C coatings. The following conclusions can be drawn from the HTXRD analysis of these films:

i) Hexagonal β-Cr_2N is the major phase deposited for 40 at.% N coatings, being stable up to 900 °C before recrystallization and grain growth takes place. The mean grain size is only 34 nm after treatment.
ii) The deposition with N_2 and C_2H_2 reactive gases leads to quasi-crystalline Cr-based coatings with feature size of only 4 nm. The as-deposited metastable δ-Cr(C,N) phase remains unchanged up to 600 °C. Further annealing induces phase transition from chromium carbon nitride $Cr_3(C_{0.92}N_{0.08})_2$ to chromium carbide Cr_3C_2 phase.
iii) For Cr–C coatings the phase transition starts at 700 °C by forming Cr_3C_2; after *in situ* treatment a mixture of carbides phases is presented in accordance to thermodynamic equilibrium.
iv) All coatings exhibit small amounts of Cr-rich droplets, keeping almost constant their structural characteristics during tempering.
v) Finally, the oxidation of the coatings is detected during *in situ* XRD analysis at temperatures higher than 800 °C, despite the use of reducing atmosphere.

Acknowledgements

This work was supported by the Grant Agency of the Academy of Sciences of the Czech Republic through the project KJB201240701 and by the Ministry of Education of the Czech Republic (project MSM 6840770038).

References

[1] P.A. Dearnley, Wear 225–229 (1999) 1109.
[2] H. Dong, Y. Sun, T. Bell, Surf. Coat. Technol. 90 (1997) 91.
[3] H. Mayrhofer, H. Willmann, C. Mitterer, Surf. Coat. Technol. 146–147 (2001) 222.
[4] J. Vetter, E. Lugscheider, S.S. Guerreiro, Surf. Coat. Technol. 98 (1998) 1233.
[5] M. Uchida, et al., Surf. Coat. Technol. 177–178 (2004) 627.
[6] P. Panjan, et al., Surf. Coat. Technol. 98 (1998) 1497.
[7] H.Y. Lee, et al., Surf. Coat. Technol. 200 (2005) 1026.
[8] B. Rother, H. Kappl, Surf. Coat. Technol. 96 (1997) 163.
[9] M. Cekada, P. Panjan, M. Macek, P. Smıd, Surf. Coat. Technol. 151–152 (2002) 31.
[10] J. Almer, M. Odén, G. Hakansson, Philos. Mag. 84 (2004) 611.
[11] E.Y. Choi, et al., J. Mater. Process. Technol. 187–188 (2007) 566.
[12] T. Polcar, L. Cvrcek, P. Siroky, R. Novak, Vacuum 80 (2005) 113–116.
[13] T. Polcar, N.M.G. Parreira, R. Novak, Surf. Coat. Technol. 201 (2007) 5228.
[14] H. Holleck, J. Vac. Sci. Technol., A 4 (1986) 2661.
[15] J. Almer, M. Odén, G. Hakansson, J. Vac. Sci. Technol., A 18 (1) (2000) 121.
[16] C. Heau, R.Y. Fillit, F. Vaux, F. Pascaretti, Surf. Coat. Technol. 120 (1999) 200.
[17] M. Odén, J. Almer, G. Hakansson, Surf. Coat. Technol. 120 (1999) 272.
[18] A. Andrievski, et al., Thin Solid Films 261 (1995) 83.
[19] E. Bauer-Grosse, Thin Solid Films 447–448 (2004) 311.
[20] Da-Yung Wang, et al., Surf. Coat. Technol. 120–121 (1999) 622.
[21] J. Esteve, J. Romero, M. Gómez, A. Lousa, Surf. Coat. Technol. 188 (2004) 506.
[22] S.C. Kwon, et al., Surf. Coat. Technol. 183 (2004) 151.
[23] D.B. Lee, S.C. Kwon, Mater. Sci. Forum 510–511 (2006) 418.
[24] A. Paul, J. Lim, K. Choi, C. Lee, Mater. Sci. Eng., A 332 (2002) 123.
[25] M.-A. Djouadi, et al., Surf. Coat. Technol. 151 (2002) 510.

Sensing of human plasma fibrinogen on polished, chemically etched and carbon treated titanium surfaces by diffractive optical element based sensor

Raimo Silvennoinen[1a], Vladimir Vetterl[2a,4], Stanislav Hasoň[2], Heikki Tuononen[1], Martti Silvennoinen[1], Kari Myller[3], Ladislav Cvrček[5], Jiři Vanek[4] and Patrik Prachař[4]

[1]*University of Joensuu, Department of Physics and Mathematics, P.O. Box 111, FI-80101 Joensuu, Finland*

[2]*Institute of Biophysics, Academy of Sciences of the Czech Republic, v.v.i. Královopolská 135, CZ-612 65 Brno, Czech Republic*

[3]*MGM-Devices Ltd., Länsikatu 15, FI-80110 Joensuu, Finland*

[4]*Centre for Dental and Craniofacial Research, Faculty of Medicine, Masaryk University, Komenskeho nam. 2, 662 43 Brno, Czech Republic*

[5]*HVM Plasma Ltd., Na Hutmance 2, 158 00 Prague 5, Czech Republic*

Corresponding authors: [1a] raimo.silvennoinen@joensuu.fi; [2a] vetterl@ibp.cz

Abstract:
Adsorption of human plasma fibrinogen (HPF) on 6 differently treated titanium samples (polished, polished and etched, and 4 titanium carbide coatings samples produced by using plasma-enhanced chemical vapour deposition (PECVD) method) is investigated by using diffractive optical element (DOE) sensor. Permittivity (susceptibility) change and fluctuation in optical roughness (R_{opt}) of treated titanium surface in the presence of background electrolyte without and with HPF molecules are sensed by using DOE sensor and optical ellipsometry. Correlation between transmitted light and thickness of molecule layer was found. The findings allow to sense temporal organization and severity of adsorption of nano-scale HPF molecules on polished, on polished and etched, and on titanium carbide surface.

OCIS codes: (120.6710) Susceptibility; (120.4530) Optical constants; (050.1965) Diffractive lenses; (120.6660) Surface measurements, roughness; (120.2130) Ellipsometry and polarimetry; (170.0170) Medical optics and biotechnology.

References and links

1. B. Walivaara, B. O. Aronsson, M. Rodahl, J. Lausmaa, and P. Tengvall, "Titanum with different oxides-in-vitro studies of protein adsorption and contact activation," Biomaterials **15**, 827-834 (1994).
2. M. I. Jones, I. R. McColl, D. M. Grant, K. G. Parker, and T. L. Parker, "Protein adsorption and platelet attachment and activation, on TiN, TiC, and DLC coatings on titanium for cardiovascular applications," J. Biomed. Mater. Res. **52**, 413-421 (2000).
3. N. Juany, P. Yang, Y. X. Leng, J. Y. Chen, H. Sun, J. Wang, G. J. Wang, P. D. Ding, T. F. Xi, and Y. Leng, "Hemocompatibility of titanium oxide films," Biomaterials **24**, 2177-2187 (2003).
4. F. Hook, J. Voros, M. Rodahl, R. Kurrat, P. Boni, J. J. Ramsden, M. Textor, N. D. Spenser, P. Tengvall, J. Gold, and B. Kasemo, "A comparative study of protein adsorption on titanium oxide surfaces using in situ ellipsometry, optical waveguide lightmode spectroscopy, and quartz crystal microbalance/dissipation," Colloid Surf. B **24**, 155-170 (2002).

#94893 - $15.00 USD Received 11 Apr 2008; revised 27 May 2008; accepted 27 May 2008; published 23 Jun 2008

5. D. L. Cochran, “A Comparison of Endosseous Dental Implant Surfaces,” J. Periodontol. **70**, 1523-1539 (2000).
6. T. J. Webster, R. W. Siegel, and R. Bizios, “Osteoblast adhesion on nanophase ceramics,” Biomaterials **20**, 1221-1227 (1999).
7. P. M. Brett, J. Harle, V. Salih, R. Mihoc, I. Olsen, F. H. Jones, and M. Tonetti, “Roughness response genes in osteoblasts,” Bone **35**, 124-133 (2004).
8. E. Jansoon and P. Tengvall, “Adsorption of albumin and IgG to porous and smooth titanium,” Colloid Surf. B **35**, 45-51 (2004).
9. P. Cacciafesta, A. D. L. Humphris, K. D. Jandt, and M. J. Miles, “Human Plasma Fibrinogen Adsorption on Ultraflat Titanium Oxide Surfaces Studied with Atomic Force Microscopy,” Langmuir **16**, 8167-8175 (2000).
10. P. Cacciafesta, K. R. Hallam, A. C. Watkinson, G. C. Allen, M. J. Miles, and K. D. Jandt, “Visualisation of human plasma fibrinogen adsorbed on titanium implant surfaces with different roughness,” Surf. Sci. **491**, 405-420 (2001).
11. H. Nygren, P. Tengvall, and I. Lundstrom, “The initial reactions of TiO_2 with blood,” J. Biomater. Res. **34**, 487-492 (1997).
12. S. Kidoaki, T. Matsuda, “Adhesion forces of the blood plasma proteins on self-assembled monolayer surfaces of alkanethiolates with different functional groups measured by an Atomic Force Microscope,” Langmuir **15**, 7639-7646 (1999).
13. A. G. Hemmersam, M. Foss, J. Chevallier, and F. Besenbacher, “Adsorption of fibrinogen on tantalum oxide, titanium oxide and gold studied by the QCM-D technique,” Colloid Surf. B **43**, 208-215 (2005).
14. M. Rouahi, E. Champion, O. Gallet, A. Jada and K. Anselme, “Physico-chemical characteristics and protein adsorption potential of hydroxyapatite particles: Influence on in vitro biocompatibility of ceramics after sintering,” Colloid Surf. B **47**, 10-19 (2006).
15. R. Silvennoinen, K.-E. Peiponen, and T. Asakura, “Diffractive optical elements in materials inspection”: in T. Asakura (ed.) *The International Trends in Optics and Photonics ICO IV*, Part VI Optical Metrology (Optical Systems), pp. 281-293 (Springer-Verlag, Berlin Heidelberg, 1999).
16. S. Hason, S.-P. Simonaho, R. Silvennoinen, and V. Vetterl, “On the adsorption and kinetics of phase transients of adenosine at the different carbon electrodes modified with a mercury layer,” Electrochim. Acta **48**, 651-668 (2003).
17. S. Hason, S.-P. Simonaho, R. Silvennoinen, and V. Vetterl, “Detection of phase transients in two-dimensional adlayers of adenosine at the solid amalgam electrode surfaces,” J. Electroanal. Chem. **568**(1), 65-77 (2004).
18. Y. L. Su and W. H. Kao, “Tribological behaviour and wear mechanisms of Ti-C:H/TiC/TiCN/TiN/Ti coatings when sliding against steel, bronze and alumium alloy rods” J. Mater. Sci. **36**, 189-199 (2001).
19. V. Kulikovsky, A. Kuzmichev, P. Bohaca, Z. Hubicka, K. Jurek, and L. Jastrabik, “Composition of Ti-C:H films obtained by pulsed and continuous magnetron sputtering,” Surf. Coat. Technol. **200**, 620-624 (2005).
20. T. Vitu, T. Polcar, L. Cvrcek, R. Novak, J. Vyskocil, and A. Cavaleiro, “Structure and Tribology of Biocompatible Ti-C:H Coatings,” Surf. Coat. Technol. (in press).
21. J. Räsänen, M. Savolainen, R. Silvennoinen, and K. E. Peiponen, “Optical sensing of surface roughness and waviness by computer generated hologram,” Opt. Eng. **34**, 2574-2580 (1995).
22. E. Chan, T. Menovsky, and A. J. Welch, “Effects of cryogenic grinding on soft-tissue optical properties,” Appl. Opt. **35**, 4526-4532 (1996).
23. W. W. Layne, D. J. Hnatowich, P. W. Doherty, R. L. Childs, D. Lanteigne, and J. Ansell, “Evaluation of the Viability of In-111-Labeled DTPA Coupled to Fibrinogen,” J. Nucl. Med. **23**, 627-630 (1982).
24. S. N. Roy, R. Procyk, B. J. Kudryk, and C. M. Redman, “Assembly and Secretion of Recombinant Human Fibrinogen,” J. Biol. Chem. **266**, 4758-4763 (1991).
25. H. A. Kramers, “Some remarks on the theory of absorption and refraction of x-rays,” Nature **117**, 775-778 (1926).
26. V. Lucarini, J. J. Saarinen, K.-E. Peiponen, and E. Vartiainen, *Kramers-Kronig Relations in Optical Materials Research*, (Springer, Berlin, 2005).
27. R. Silvennoinen, K.-E. Peiponen, and K. Myller, *Specular gloss* (Elsevier, Amsterdam, 2007).
28. P. Beckmann and A. Spizzichino, *The Scattering of Electromagnetic Waves from Rough Surface*, (Pergamon Press, Oxford, 1963).
29. R. Silvennoinen, S. Hason, and V. Vetterl, “Organization of nano-scale synthetic oligonugloetides on immersed electrode surface: an optical study,” *Technical digest of the Seventh Finnish-Japanese Joint Symposium on Optics in Engineering*, K.-E. Peiponen, R. Hernberg and T. Yatagai eds., (8-10 August, Tampere, Finland, 2007), pp. 101-102.
30. S. Donati, “Coupling dynamics in lasers and applications in self-mixing interferometry,” *Summaries of the 2nd International Meeting on Optical Sensing and Artificial Vision (OSAV’2008)*, p. 67, 2008.
31. O. V. Angelsky and P. P. Maksimyak, “Optical diagnostics of random phase objects,” Appl. Opt. **29**, 2894-2898 (1990).
32. O. V. Angelsky, A. P. Maksimyak, P. P. Maksimyak, and S. G. Hanson, “Optical correlation diagnostics of rough surfaces with large surface inhomogeneities,” Opt. Express **14**, 7299-7311 (2006).
33. R. A. M. Azzam and N. M. Bashra, *Ellipsometry and Polarized Light*, (North-Holland, Amsterdam, 1977).
34. S.-M. F. Nee and T.-W. Nee, “Principal Mueller matrix of reflection and scattering measured for a one-

#94893 - $15.00 USD Received 11 Apr 2008; revised 27 May 2008; accepted 27 May 2008; published 23 Jun 2008

dimensional rough surface," Opt. Eng. **41**, 994-1001 (2002).
35. X. H. Zhang, A. Quinn, and W. A. Ducker, "Nanobubbles at the Interface between Water and a Hydrophobic Solid," Langmuir, ASAP Article; DOI: 10.1021/la703475q (2008).

1. Introduction

The investigation of the interactions of blood plasma proteins at different surfaces is a challenging task in biomedicine. Titanium is frequently used as a biomaterial for hard tissue replacement, such as dental and orthopaedic implants. Thus the understanding of the protein adsorption on titanium surface is of great importance [1, 2, 3, 4]. Biomaterial devices made of titanium give a satisfactory performance. The surface morphology, which can be varied by different processing methods influence the final interactions of the implant with the surrounding environment. Rough surfaces promote better oseointegration than smooth surfaces [5, 6, 7, 8].

Soon after implantation - within a few seconds - the biomaterial surface becomes coated with a film of adsorbed proteins, which mediate the interaction between the implant and the body environment. Since most implants are exposed to blood during implantation, the initial protein film is mainly composed of plasma proteins. Human plasma fibrinogen (HPF) is one of the most relevant proteins that are adsorbed on biomaterial surfaces. HPF takes part in blood coagulation, facilitates adhesion and aggregation of platelets [9, 10]. The structure and composition of the adsorbed protein layer determine the type and extent of the subsequent biological reactions, such as activation of coagulation and immune response and oseointegration [11]. Thus the initially adsorbed protein layer is a factor conditioning the biocompatibility [12, 13, 14]. The mechanisms and the factors important for protein adsorption and desorption are still subject of scientific research and not very well understood. Therefore it is important to investigate how different titanium surfaces influence the formation and properties of adsorbed protein layers.

The need to develop novel methods for the investigation of biopolymer adsorption at surfaces is arisen from the observation that conventional surface characterization methods and tools (as Scanning Electron Microscopy - SEM, Transmission Electron Microscopy - TEM, Environmental Scanning Electron Microscopy - ESEM, diamond stylus and optical profilometer) can be used in most of the case only for the dry surfaces. There are a restricted number of methods, which can be applied for the investigation of surfaces immersed into a liquid (like Atomic Force Microscopy AFM with a special liquid cell). The optical method described in this paper can provide information on the optical roughness (contrary to the mechanical roughness obtained from AFM profilometer) and reflectance of the surfaces immersed into a liquid. This method can be thus used for the study of the interactions of the molecules dissolved in the liquid with the surface. Previously we have applied diffractive optical element (DOE) based sensor for inspection of different type of bulk and fragile materials [15], and later the same principle is applied to investigate quality of electrode surface used in electrochemistry [16, 17].

In this paper we report results from our recent DOE sensor investigations concerning the organisation of biopolymers as human blood plasma fibrinogen adhered on polished, on chemically etched titanium surfaces, and on titanium carbide coatings. The titanium carbide coated surfaces were realized by using plasma-enhanced chemical vapour deposition (PECVD) method [18, 19, 20]. The data is gained by using the DOE sensor through optical window of a cuvette to sense permittivity change and fluctuation in optical roughness (R_{opt}) of treated titanium surface, when the surface is subjected to the absorption of the ions of electrolyte without and with HPF molecules on these treated surfaces.

#94893 - $15.00 USD Received 11 Apr 2008; revised 27 May 2008; accepted 27 May 2008; published 23 Jun 2008

2. Experimental

2.1. A diffractive optic sensor setup

In the DOE sensor measurements we investigated the permittivity change and fluctuation in optical roughness R_{opt} of polished, polished and chemically etched titanium surfaces, and surfaces with titanium carbide coatings (denoted by complex refractive index N_4) in the presence of buffer (N_2) without and with HPF molecules (N_3) (see Fig. 1). The DOE sensor utilizes expanded and focused laser beam ($\lambda = 632.8$nm) realized by using the lens system L_1 - L_2 to hit treated titanium surface N_4 locating in liquid of cuvette via beam splitter BS and cuvette window N_1.

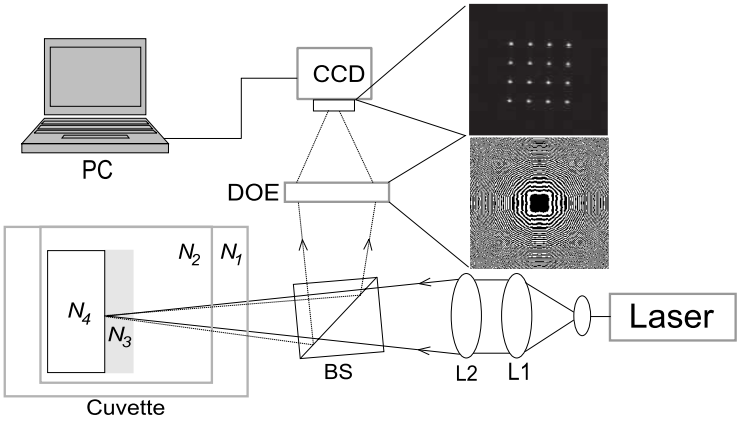

Fig. 1. DOE sensor geometry including sample cuvette compartment.

Backscattered laser light is directed by using BS on DOE aperture, which analyzes if the wavefront is distorted by adsorbed HPF molecules denoted by N_3 from buffer N_2 on treated Ti surface. Distorted 4×4 light spot DOE image is grabbed from two-dimensional (2D) photoarray of the charge coupled device (CCD) and analyzed by using a personal computer (PC). The DOE sensor utilizes non-coherent response for permittivity changes and coherent response for R_{opt} changes, which relate to surface roughness R_{a} [21].

2.2. Non-coherent response of DOE sensor

Although the DOE sensor principle and procedure is described in the reference 15 and in the chapter 8 of the reference 27, we show how the reflectance of normal incidence from the treated Ti interface depends both on n and κ if the interface is immersed in the electrolyte solution (Fig. 2). The complex permittivity ε and complex refractive index $N_{n\kappa} = n - i\kappa$ is assumed to relate to each other as follows $\varepsilon = \varepsilon' + i\varepsilon'' = (n - i\kappa)^2$, where $\varepsilon' = n^2 + \kappa^2, \varepsilon'' = 2n\kappa$. The loss angle δ denotes the relation $\tan(\delta) = \varepsilon''/\varepsilon'$. The reflectance R is calculated from the relation $R = |(1 - N_{n\kappa})/(1 + N_{n\kappa})|^2$. Next we demonstrate how to utilize the pseudo-dielectric function shown in Fig. 2 to draw out information from a treated Ti interface. In Fig. 2 is also shown a locus of contour line, which is now an example projection of a contour line from the reflectance surface on the level of $R_{\text{Ti}_{0.82}-\text{C}_{0.18}} = 0.30$ at 632.8 nm. The locus of reflectance value of 0.30 includes also the $\text{Ti}_{0.82} - \text{C}_{0.18}$ reflectance at the complex refractive index $N_{\text{Ti}_{0.82}-\text{C}_{0.18}} = 1.54 + i1.96$ at 632.8 nm. The origin of the radius of the curvature of the projected circular locus $\text{CL}_{\text{Ti}_{0.82}-\text{C}_{0.18}}$ locates on the n -axis. When the adsorption of HPF molecules from background electrolyte on the $\text{Ti}_{0.82} - \text{C}_{0.18}$ surface starts, the reflectance from that interface will also change. This will

#94893 - $15.00 USD Received 11 Apr 2008; revised 27 May 2008; accepted 27 May 2008; published 23 Jun 2008

change the curvature and the origin of the projected locus.

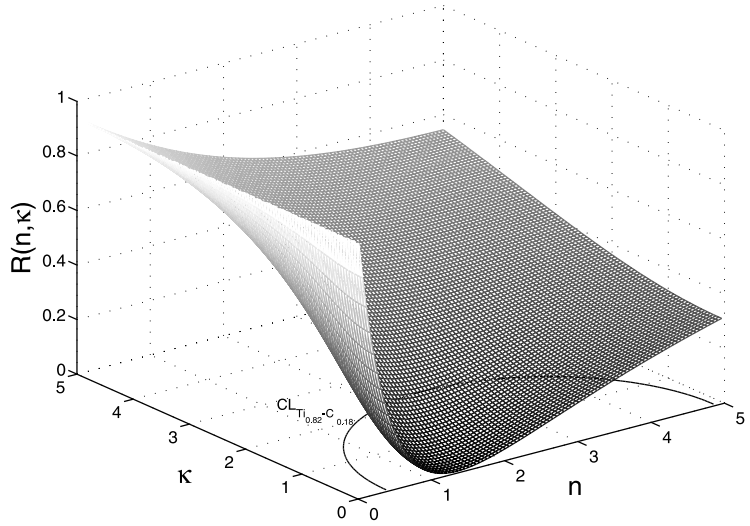

Fig. 2. Reflectance from the molecule - titanium carbide ($Ti_{0.82} - C_{0.18}$) interface as a function of n and κ, when the interface locates inside the electrolyte solution in the cuvette as shown in Fig. 1. Zero reflection appears at the refractive index of electrolyte solution as a consequence of complete refractive index matching. Locus of contour line in (n, κ) -plane, which is projected from the reflectance surface at the level of $R_{n\kappa} = 0.30$. The locus $CL_{Ti_{0.82}-C_{0.18}}$ shown in (n,κ) -plane is projected from $R_{Ti_{0.82}-C_{0.18}} = 0.30$ and it includes also reflectance of $Ti_{0.82} - C_{0.18}$ surface, which $N_{Ti_{0.82}-C_{0.18}} = 1.54 + i1.96$ at 632.8 nm.

By sensing the reflectance value by the DOE sensor at single wavelength (632.8nm) it is possible to gain information to plot the reflectance contour line and project it into (n, κ) -plane to be CL_x. The data for the reflectance value is captured by using the 2D photo array of the CCD camera from the DOE image window, which locates at the focal plane of DOE element and is shown in the inset including the 4×4 light spot matrix of Fig. 1. The image window shown in the inset of Fig. 1 includes the non-coherent and coherent image portions. The non-coherent image portion appears outside the 4×4 light spot matrix whereas the coherent components perform the spots. The reflectance value is calculated from the non-coherent irradiance I_{NC} by utilizing Eq. (1) as follows

$$I_{NC} = \frac{1}{n_w m_w} \sum_{i_w=1, j_w=1}^{n_w, m_w} I_{i_w, j_w} - \frac{1}{n_{pk} m_{pk}} \sum_{i_{pk}=1, j_{pk}=1}^{n_{pk}, m_{pk}} I_{i_{pk}, j_{pk}}, \tag{1}$$

where n_w and m_w are the dimensions of the DOE image window and I_{i_w, j_w} is the image irradiance observed by the $(i_w, j_w)^{th}$ element of the CCD camera array. To be sure that the irradiance of peaks (coherent response) do not make any uncertainties, the irradiance portion of peaks denoted by subscript pk are subtracted from the total irradiance of that DOE image. Here we point out that the non-coherent response obeys the following procedure for each pixel $I_{NC} = \sum |A_j|^2$, where $A_j = A_{oj} \exp(i\phi_j)$ is the j^{th} complex wavefront amplitude, i denotes the imaginary unit and $\phi_j = 2\pi r_j / \lambda_j$ is the respective phase angle, where r_j is the optical path and λ is the wavelength used.

To find out the changes in n and κ values really caused by the HPF adsorption from electrolyte solution on treated Ti surface, we measured first the fluctuations in optical density (OD)

#94893 - $15.00 USD Received 11 Apr 2008; revised 27 May 2008; accepted 27 May 2008; published 23 Jun 2008

respecting the optical path length (OPL), which is used in our DOE experiments. The OD value respecting the wavelength of 632.8 nm was observed to be negligible being 0.004 ± 0.001, which respects the accuracy limit of the spectrophotometer used in the measurements. On the other hand, basing on the data reported in the literature, optical properties of soft-tissue [22] as well as HPF molecules [23, 24] do not have strong absorption anomalies in the visible VIS regime, which may in turn if the absorption anomalies are strong affect changes in extinction coefficient κ according to Kramers-Kronig relation [25, 26]. Mainly however the strong absorption appears in ultraviolet UV regime [23, 24]. In the final detection of the changes in n and κ values of N_x caused by the molecules attached on the $\mathrm{Ti}_{\mathrm{treat}}$ surface we made projection from $N_{\mathrm{Ti}_{\mathrm{treat}}}$ located on $\mathrm{CL}_{\mathrm{Ti}_{\mathrm{treat}}}$ via it's curvature origin onto CL_{x} just compensating the shift of the curvature origin of $\mathrm{CL}_{\mathrm{Ti}_{\mathrm{treat}}}$.

2.3. Coherent response of DOE sensor

To sense the thickness of the adsorbed portion on treated titanium surface immersed background electrolyte in the absence or presence of HPF molecules we utilize the coherence response of DOE sensor. The data to calculate the thickness of adsorbed layer on treated titanium surfaces is calculated utilizing the captured DOE image data of the 4×4 light spot matrix as already described in the section 2.2. To calculate the irradiance of the peaks we utilize Eq. (2) as follows

$$I_C = \frac{1}{n_{pk} m_{pk}} \sum_{i_{pk}=1, j_{pk}=1}^{n_{pk}, m_{pk}} I_{i_{pk}, j_{pk}}, \tag{2}$$

where n_{pk} and m_{pk} are the dimensions of each 16 peaks in DOE image and $I_{i_{pk},j_{pk}}$ is the image irradiance observed by the $(i_{pk}, j_{pk})^{th}$ element of the peak in DOE image captured by CCD camera. Caused by the fact that DOE aperture consist of 16 different diffractive lenses obeying coherent response for each pixel as follows $I_C = |\sum A_j|^2$, which satisfies the principle of compact and phase sensitive interferometer. Moreover the DOE images the 4×4 light spot matrix in its focal plane. If the reconstructing wavefront do not satisfy the terms of hologram imaginary, the spot image matrix do not appear in the image plane. The same holds e.g. for the case, where the radiant exitance from the laser resonator in TEM_{00} mode start to suffer from appearance of side modes, and DOE will spatially filter out those images from its original 4×4 light spot image. After tedious numerical simulations it is showed that the irradiance of the 4×4 spots will decrease as a function of OPL and disappears when the OPL exceeds $\lambda/4$. This response is published and appears in the Fig. 8.21(b) of the reference [27]. It is also observed that this response resembles the response of Beckmann-Spizzichino model [28]. To consider the thickness of the adsorbed portion on treated titanium surface immersed background electrolyte in the absence or presence of HPF molecules we first measure the irradiance of the peaks and after that the optical path difference Δr, which is also understood as an optical roughness (R_{opt}), is solved inversely by utilizing this response. In our previous measurements we have noted that the accuracy of 0.2nm can be achieved by using this one arm interferometric technique [29]. The similar accuracy limits is also reported recently for the coupling dynamics of lasers of self-mixing interferometers in vibrometer applications ranging from 0.1 nm to 100μm [30], whereas the accuracy of conventional two arm interferometers used in optical diagnostics of random phase objects [31] as well as in optical diagnostics of rough surfaces [32] are estimated to be $\sim 0.005\mu$m, which is not reasonable for sensing of adsorption of HPF molecules on treated titanium surface.

#94893 - $15.00 USD Received 11 Apr 2008; revised 27 May 2008; accepted 27 May 2008; published 23 Jun 2008

2.4. DOE sensor and ellipsometric measurements of treated titanium surfaces

In the experiments six different types of treatments for titanium were used as follows: polishing, polishing and chemical etching with surface material loss of 0.03mm, and plasma-enhanced chemical vapour deposition (PECVD) method to produce titanium carbide surfaces with four different concentrations of carbon: $Ti_{0.82} - C_{0.18}$; $Ti_{0.38} - C_{0.62}$; $Ti_{0.09} - C_{0.91}$ and $Ti_{0.00} - C_{1.00}$ (diamond). The experiments were repeated three times for each treated titanium surfaces immersed in water and in background electrolyte without and with HPF molecules.

The thickness of titanium oxide layer was measured to be down 220 nm of the polished, and polished and chemically etched titanium surface. The thickness of $Ti_x - C_{1-x}$ coatings produced by using plasma-enhanced chemical vapour deposition (PECVD) were ranged from $2.5\mu m - 3.5\mu m$, which is thick enough in optical sense to consider it as solid bulk layer [20].

In the begin of all measurements the DOE sensor images for reference signal level from test surface were made in water for 100 seconds, and during that time frame 1000 reference samples were grabbed. After that the water was removed by syringe from cuvette and the buffer solution, in turn, was injected in the cuvette. Immediately after injection of buffer, grabbing of the DOE images was started, and the image grabbing was repeated after two minutes interval. Before HPF measurement, the cuvette was washed, and after washing the new treated titanium sample was installed in the sample holder inside the cuvette. The water was injected in the cuvette, and the DOE image references from the new sample surface were taken. Before adding the HPF solution in the cuvette, the immersion water was removed, and grabbing process of DOE images was started. The image grabbing was repeated two times consecutively after two minutes interval. The diameter of the laser beam waist on the all surfaces was 1mm.

Immediately after the DOE sensor measurements in buffer and HPF solutions the samples were subjected for ellipsometric measurements, which were made during a half hour time frame (in room temperature) when surface sample is taken out from the solution. The measurements were performed by using Woollam spectroellipsometer working in the wavelength range from 200nm to 1700nm. The ellipsometric measurements were performed in aim to gain information about the adsorbability and compare the $N_{\mathrm{Ti}_{\mathrm{treat}}}$ values caused by the adsorption of the ions of electrolyte without and with HPF molecules on the $\mathrm{Ti}_{\mathrm{treat}}$ surface already drawn out by the DOE sensor. The corroborative ellipsometric measurements were performed at the incidence angle of 75° for probe beam to avoid the harmful effects caused by the possible appearance of surface roughness [33, 34]. Here we measured the complex refractive index $N_{n\kappa}$ of each treated titanium surfaces (polished, chemically etched and titanium carbide surfaces) used in our experiments in dry environment. We point out that it is also possible to measure complex refractive index values from the interface of treated titanium with adsorbed short molecules in dry environment, and calculate the effective thickness value of adsorbed molecule volume from the extinction coefficient κ obtained by ellipsometric measurement. However, in the case of HPF molecules, which are long molecules, the strong scattering of light will disturb the determination of thickness of the absorbed HPF molecule volume on treated titanium surface in dry environment.

2.5. Chemicals

Human plasma fibrinogen (HPF), fraction I, type III was purchased from Sigma. In all experiments the HPF was dissolved in phosphate buffer solution (PBS) + 0.136 M sodium citrate, which serve as a background electrolyte at a concentration of 500 nM. Measurements were performed at room temperature.

#94893 - $15.00 USD Received 11 Apr 2008; revised 27 May 2008; accepted 27 May 2008; published 23 Jun 2008

3. Results and discussion

In Fig. 3 are shown six respective reflectance bar sets from the polished titanium, from the polished and chemically etched titanium and from the four titanium carbide $Ti_x - C_{1-x}$ surfaces immersed in background electrolyte without and with HPF molecules. The mutual concentrations of titanium and carbon are consecutively from left to right as follows: $Ti_{0.82} - C_{0.18}$, $Ti_{0.38} - C_{0.62}$, $Ti_{0.09} - C_{0.91}$ and $Ti_{0.00} - C_{1.00}$, which respects the diamond structure of carbon.

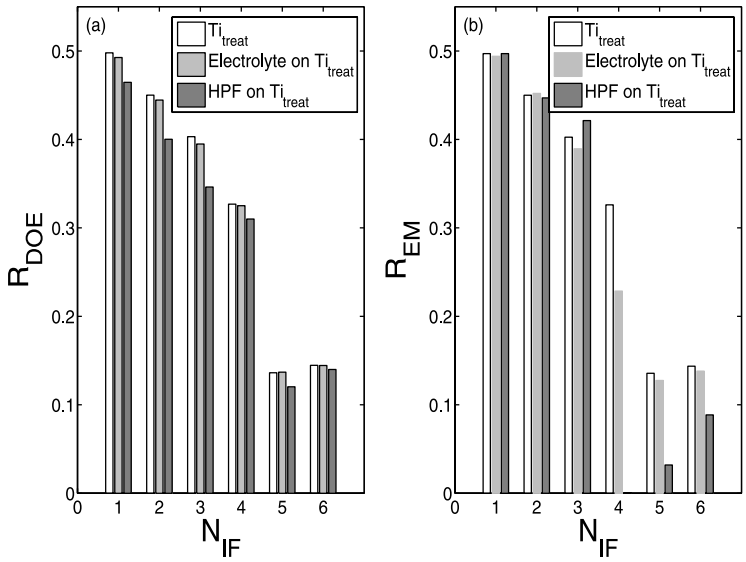

Fig. 3. Reflectance of treated titanium surfaces immersed in background electrolyte in the absence or presence of HPF molecules as follows: $N_{IF}=1 \equiv$ polished titanium; $N_{IF}=2 \equiv$ polished and chemically etched titanium; $N_{IF}=3 \equiv Ti_{0.82} - C_{0.18}$; $N_{IF}=4 \equiv Ti_{0.38} - C_{0.62}$; $N_{IF}=5 \equiv Ti_{0.09} - C_{0.91}$ and $N_{IF}=6 \equiv Ti_{0.00} - C_{1.00}$ (diamond) measured by using (a) DOE sensor in cuvette (respecting wet environment) and (b) ellipsometry in air (respecting dry environment).

The responses were calculated from the n and κ data (at 632.8nm) sensed with the aid of the DOE sensor and corroboratively by using ellipsometry. The DOE sensing was performed in cuvette, which procedure respects the n and κ sensing in wet environment and the ellipsometric measurements were drawn out after DOE measurements in air respecting the sensing in dry environment. The reflectance responses show decreasing tendency in treated titanium surfaces from $N_{IF}=1$ to $N_{IF}=5$, whereas diamond surface ($N_{IF}=6$) makes exception from the decreasing evolution of reflectance. The attachment of electrolyte fractions on the treated titanium surfaces seems to have insignificant influences to the reflectance. In R_{DOE} responses the attachment of HPF molecules from electrolyte has extra decreasing influences to reflectance, whereas in R_{EM} reflectance performed by ellipsometry this trend is even higher when the carbon concentration in titanium exceeds 18 per cent. The strong decrease in R_{EM} reflectance is believed to be caused from the higher scattering of light from HPF molecules in air than in electrolyte solution, where the refractive index matching is more dominate than in air.

Thereafter we compared the optical roughness R_{opt} values measured by DOE sensor as a function of time from the treated titanium surface - electrolyte interface in the absence or presence of HPF molecules. The threshold of optical roughness of the treated titanium surface was cancelled out by measuring the base line of R_{opt} in distilled water, which refractive in-

#94893 - $15.00 USD Received 11 Apr 2008; revised 27 May 2008; accepted 27 May 2008; published 23 Jun 2008

dex ($n = 1.3334$) was close to electrolyte [19]. As an example we present here two temporal responses for the optical roughness R_{opt} responses from a polished titanium surface in background electrolyte with the presence of HPF molecules (Fig. 4(a)), and respectively from a titanium carbide (Fig. 4(b)).

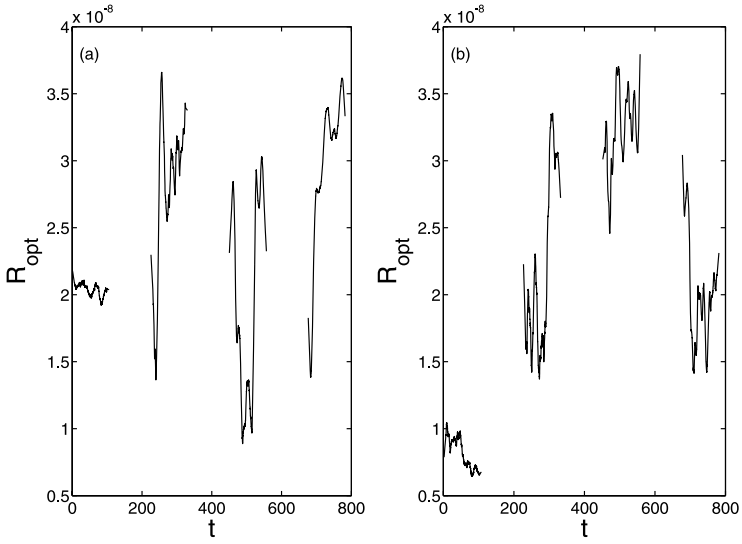

Fig. 4. Temporal optical roughness in meters sensed from treated titanium surfaces in background electrolyte (t_1=0-100s) and in background electrolyte with HPF molecules (t_2=220-320s, t_3=440-540s and t_4=660-760s). (a) polished titanium and (b) titanium carbide ($Ti_{0.38} - C_{0.62}$). To make the temporal trends visible each R_{opt} raw data sequence with 1000 points is filtered by using Savitzky-Golay digital filter in MATLAB© with the parameters K=1 and F=101.

Table 1. Average optical roughness values with standard deviations calculated from each R_{opt} non-filtered raw data sequence with 1000 points shown in Fig. 4.

	$Ti_{polished}$		$Ti_{0.38} - C_{0.62}$	
	R_{opt} (nm)	ΔR_{opt} (nm)	R_{opt} (nm)	ΔR_{opt} (nm)
t_1	20.4	2.1	8.2	3.4
t_2	28.0	7.9	22.3	9.2
t_3	20.0	8.7	32.3	5.5
t_4	29.4	6.5	20.3	6.6

The temporal response from polished titanium surface in background electrolyte (t_1=0-100s) shows almost two times higher R_{opt} level than that from titanium carbide surface ($Ti_{0.38} - C_{0.62}$) as also shown in Table 1. When the polished titanium is immersed in electrolyte with HPF molecules, the R_{opt} levels show rather strong fluctuation as a function of time (Fig. 4(a)). The temporal increase of R_{opt}, which is greater than average of R_{opt} from the base of polished titanium surface in background electrolyte, indicates that the HPF molecules are attaching to the polished titanium surface but temporally the R_{opt} become lower than the average of R_{opt} of polished titanium surface in background electrolyte, which may indicate that the molecule volume

#94893 - $15.00 USD Received 11 Apr 2008; revised 27 May 2008; accepted 27 May 2008; published 23 Jun 2008

get unstuck from the surface as a consequence of the appearance of huge amount of nanobubbles [35]. For the appearance of huge amount of nanobubbles the DOE sensor will sense the decrease of optical roughness less than the average of R_{opt} obtained from treated titanium surfaces in background electrolyte. The R_{opt} values from ($\mathrm{Ti}_{0.38}-\mathrm{C}_{0.62}$) surface in background electrolyte with HPF molecules indicate that the HPF molecules are attaching to the titanium carbide surface but the molecule volume do not get unstuck from the surface, only some remodelling in molecule volume appears as a function of time (Fig. 4(b)). The severity of the attachments of fractions on treated titanium surfaces in background electrolyte in the absence or presence of HPF molecules was estimated from the six R_{opt} bar sets from the polished titanium, from the polished and chemically etched titanium and from the four titanium carbide $\mathrm{Ti}_x-\mathrm{C}_{1-x}$ surfaces (Fig. 5).

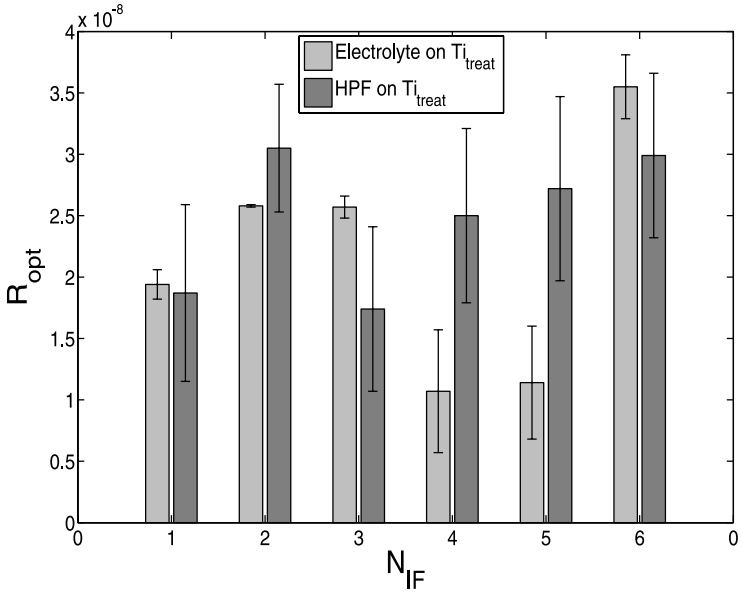

Fig. 5. Optical roughness of treated titanium surfaces immersed in background electrolyte in the absence or presence of HPF molecules as follows: $N_{IF}=1 \equiv$ polished titanium; $N_{IF}=2 \equiv$ polished and chemically etched titanium; $N_{IF}=3 \equiv \mathrm{Ti}_{0.82}-\mathrm{C}_{0.18}$; $N_{IF}=4 \equiv \mathrm{Ti}_{0.38}-\mathrm{C}_{0.62}$; $N_{IF}=5 \equiv \mathrm{Ti}_{0.09}-\mathrm{C}_{0.91}$ and $N_{IF}=6 \equiv \mathrm{Ti}_{0.00}-\mathrm{C}_{1.00}$ (diamond). The numbers shown on the R_{opt} axis are in meters, and the vertical lines on the bars denote standard deviations.

The estimates were performed by comparing the differences of the average R_{opt} values with their standard deviations from surfaces in background electrolyte in the absence or presence of HPF molecules.

From Fig. 5 we can observe that the averaged R_{opt} values in background electrolyte in the absence or presence of HPF molecules falls inside the limits of standard deviations in polished titanium ($N_{IF}=1$), in titanium carbide $\mathrm{Ti}_{0.82}-\mathrm{C}_{0.18}$ surface ($N_{IF}=3$) and in diamond ($N_{IF}=6$) surface, and thus do not differ significantly. This can be understood to implicate weak attachments of the HPF molecules on polished titanium, on $\mathrm{Ti}_{0.82}-\mathrm{C}_{0.18}$ surface and on diamond surfaces, whereas the polished and chemically etched (with 0.03mm material loss) ($N_{IF}=2$) surface and titanium carbide ($N_{IF}=4$-5) surfaces indicate strong attachments of the HPF molecules on their surfaces. It is quite interesting that the HPF adsorption at the titanium carbide surface depends on the mutual concentration of titanium and carbon. The HPF adsorption is weak at

#94893 - $15.00 USD Received 11 Apr 2008; revised 27 May 2008; accepted 27 May 2008; published 23 Jun 2008

low (sample N_{IF}=3) or high (”diamont like” sample N_{IF}=6) carbon concentrations.

4. Conclusion

In the progress of this work we noted that the DOE sensor is effective in sensing of permittivity changes, which bear also information from temporal fluctuations of optical roughness R_{opt} of treated titanium surface, when the HPF molecules modify the surface in wet environment. The reflectance results related to permittivity changes are also in accordance with the ellipsometer results, which are gained from the same surfaces in dry environment. Moreover, the observation of the magnitude of temporal R_{opt} evolution, which relates to the porosity of the molecule layer or volume revealed information from the dynamic processes of organization of the molecules on the biomaterial surface. Optical roughness measurements have shown that the surface treatment of titanium affect the adsorption of HPF molecules. HPF is best adsorbed at the polished and chemically etched titanium as well as at the titanium carbide surfaces $Ti_{0.38} - C_{0.62}$ and $Ti_{0.09} - C_{0.91}$.

Acknowledgment

This work was supported by the Ministry of Education and Sport of the Czech Republic (1M0528 to J. V.), the Academy of Sciences of the Czech Republic (KAN200040651 to S. H.), the grant agency of the Czech Republic (202/08/1688 to V. V.), the Ministry of Education of the Czech Republic (LC06035), and by an institutional research plan (AVOZ 50040507, AVOZ 50040702).

#94893 - $15.00 USD Received 11 Apr 2008; revised 27 May 2008; accepted 27 May 2008; published 23 Jun 2008

Surface & Coatings Technology 202 (2008) 5790–5793

Contents lists available at ScienceDirect

Surface & Coatings Technology

journal homepage: www.elsevier.com/locate/surfcoat

Structure and tribology of biocompatible Ti–C:H coatings

Tomas Vitu [a,*], Tomas Polcar [b,f], Ladislav Cvrcek [c], Rudolf Novak [d], Jan Macak [e], Jiri Vyskocil [c], Albano Cavaleiro [f]

[a] Faculty of Transportation Sciences, Czech Technical University in Prague, Na Florenci 25, 110 00, Prague 1, Czech Republic
[b] Department of Control Engineering, Faculty of Electrical Engineering, Czech Technical University in Prague, Technicka 2, 166 07, Prague 6, Czech Republic
[c] HVM Plasma Ltd., Na Hutmance 2, 158 00 Prague 5, Czech Republic
[d] Faculty of Mechanical Engineering, Czech Technical University in Prague, Technicka 4, 166 07, Prague 6, Czech Republic
[e] Faculty of Environmental Technology, Institute of Chemical Technology, Technicka 5, 166 28 Prague 6, Czech Republic
[f] SEG-CEMUC, Department of Mechanical Engineering, University of Coimbra, 3030-201 Coimbra, Portugal

ARTICLE INFO

Available online 9 June 2008

Keywords:
Ti–C:H coatings
Tribology
Physiological solution
Fetal bovine serum

ABSTRACT

Ti–C:H coatings with different carbon content for biomedical applications were deposited by PECVD. Ti was varied by magnetron sputtering a Ti-target with different power in a dc discharge regime having Ar in the atmosphere. Ti–C:H coating was tribologically tested reflecting its expected use as an interlayer for improving the adhesion of functional a-C:H coatings. The tribological properties were studied using a pin-on-disc CSM Tribometer in order to ensure stable tribological properties of the whole Ti–C:H/DLC system for any case of top layer failure. The sliding tests were carried out at room temperature in room environment with relative air humidity 40±5%, in 0.9% NaCl water solution (physiological solution, PS) and in 10% fetal bovine serum (FBS) dissolved in Ringer's saline solution using 440C steel balls with a diameter of 8 mm. The variation of the C_2H_2 flow led to carbon contents in the range [18–91 at.%]. The Ti-rich coatings exhibited poor wear resistance, while the best tribological properties were achieved for TiC/a-C:H coatings deposited with the highest C_2H_2 flows. When tested in biological solutions, the friction and wear resistance were analyzed with respect to their corrosion properties.

1. Introduction

The carbon coating structures prepared by PECVD – plasma enhanced chemical vapour deposition – methods are widespread in engineering applications mainly because of their excellent mechanical and tribological properties. The a-C:H structure consists usually of a metastable form of amorphous carbon with a mixture of sp^2 and sp^3 bonds in a proportion dependent on the deposition conditions. In some cases, high mechanical hardness, excellent wear resistance, chemical inertness and especially high degree of biocompatibility are possible to be achieved [1–3]. The a-C:H coatings also show lower adhesion in relation to the most frequently used materials, such as steel or Ti alloys, making them suitable for biomedical applications. However, the commonly used interlayer materials based on WC or Cr are not biocompatible and, thus, their use in these applications is disputable [4].

In the aim of this study a suitable interlayer should be developed in order to improve the adhesion of the upper functional a-C:H coating. High toughness and biocompatibility were the most desired parameters for the interlayer. Moreover, low friction and high wear resistance were also required for any case of top layer failure. Therefore, the goal was to design a new stable system using functionally graded Ti-doped C:H layers deposited as interlayer for functional diamond-like coating (DLC) for biomedical applications. In order to avoid possible unstable structures resulting in unsuitable tribological and mechanical properties, different sample sets with varying C:H content were prepared. The main scope was to identify the brittle phases inducing general problems in the functionally graded system. The adjustment in the tests parameters respected the results of previous studies on the tribology of Ti–C:H films which showed that the performance of the coating was dependent on the deposition parameters, sliding conditions and environment [1,5–8].

2. Experimental details

2.1. Deposition process

The functional Ti–C:H layers were deposited by PECVD using as reactive gas acetylene (C_2H_2). Ti is introduced in the coatings by magnetron sputtering a Ti-target in a dc discharge regime with Ar in

* Corresponding author.
E-mail address: Tomas.Vitu@fs.cvut.cz (T. Vitu).

0257-8972/$ – see front matter © 2008 Elsevier B.V. All rights reserved.
doi:10.1016/j.surfcoat.2008.06.040

the atmosphere. Sets of coatings samples were prepared varying the content of C:H component by controlling the C_2H_2 flow rate during the deposition process. The deposition parameters were as follows: fixed Ar flow rate of 75 sccm (1 sccm = 1.690 sccm; the values of acetylene flows were chosen with respect to significant points of the discharge voltage and pressure vs. C_2H_2 flow rate diagram. The pressure was recorded using a capacitance manometer Leybold CERAVAC Transmitters CTR/91. The WNr. 1.2379 steel substrates with a diameter of 20 mm and a thickness of 4 mm were polished to R_a<20 nm. The thickness of Ti–C:H coatings varied from 2.5 to 3.5 μm.

2.2. Coating composition, structure and corrosion measurements

The chemical composition of the coatings was determined in a Cameca SX-50 electron probe microanalysis apparatus (EPMA), the microstructure by Raman spectroscopy (Renishaw 2000, Ar laser 514.5 nm). The diamond pyramid hardness measurements (HV) were performed using a Fischer PICODENTOR HM500 system. The normal stylus load was 50 mN and the maximum penetration depth did not exceed 0.2 μm. Each presented hardness value was calculated from at least five independent indentations. The electrochemical impedance spectroscopy (EIS) measurements were carried out using a Solartron 1250 frequency response analyser and a Solartron 1287 potentiostat. All the measurements were performed at room temperature; 0.9% NaCl water solution was used as electrolyte. The impedance spectra were collected in regular time intervals mostly over an exposure period of 10 h.

2.3. Tribological testing

The tribological properties of Ti–C:H coatings were studied using a pin-on-disc CSM Tribometer. All the tribological measurements were performed at identical conditions: 5000 cycles, normal load 5 N, linear speed 0.05 m s^{-1}. The sliding tests were carried out at room temperature (RT) using 440C steel spherical counterparts with a diameter of 8 mm. The tests were performed in room environment with relative air humidity 40±5%, in 0.9% NaCl water solution (physiological solution, PS) and in 10% fetal bovine serum (FBS) dissolved in Ringer's saline solution. The tribological performance was examined with respect to the friction coefficient, the wear rates of the coating and the counterparts and the analysis of the wear debris. The wear rates of the coating were evaluated on the basis of the wear track profile measurements whereas those of the balls were calculated from the measurements of the spherical wear cap using optical microscopy. The calculation of the wear rate was performed following Ref. [9] as the worn volume per sliding distance and load. Each tribological test was repeated at least three times; the standard deviation was about 10%. In this paper the average values of the friction coefficient and wear rates are presented.

To determine the dominant wear mechanism, the wear tracks were studied using optical microscopy, scanning electron microscopy (SEM — JEOL JSM-6460 LA) and Raman spectroscopy.

Table 1
The samples marking, adhesion and chemical composition with respect to the C_2H_2 flow rate

C_2H_2 flow rate (sccm)	Sample marking	Chemical composition (at. %)		Vickers hardness HV	Critical load L_{C2} (N)
		Ti	C		
10	FR10	82	18	896	70
15	FR15	71	29	837	60
20	FR20	57	43	1253	70
25	FR25	50	50	1454	70
30	FR30	45	55	1480	70
34	FR34	38	62	1500	70
40	FR40	33	67	1149	70
45	FR45	19	81	1050	65
52	FR52	12	88	954	60
60	FR60	9	91	829	40

3. Results

3.1. Coating deposition

Fig. 1 showed the evolution of the total pressure and target potential as a function of increasing and decreasing C_2H_2 flow. The values were recorded 5 min after the pressure was changed. Only a narrow hysteresis has been observed. The local maximum at about 34 sccm acetylene flow rate (Fig. 1) was attributed to the priority growth of a hard titanium carbide film. The local minimum at about 52 sccm of C_2H_2 flow could be connected with the polymerisation of acetylene and the predominant growth of an a-C:H layer. The C_2H_2 flows selected for depositing coatings for this study combined the local extremes observed in the discharge voltage curve (34 and 52 sccm) and uniformly distributed flows in the range 10–60 sccm. To facilitate the coatings description, they were denominated as FR*X*, where *X* was a number corresponding to the C_2H_2 flow. Table 1 shows the selected C_2H_2 flows, the Ti/C ratios and the results of the critical load L_{C2} measurements obtained in the coatings analysis. The minimum critical load of 40 N (FR60) should be sufficient for the tribological stability of the coating.

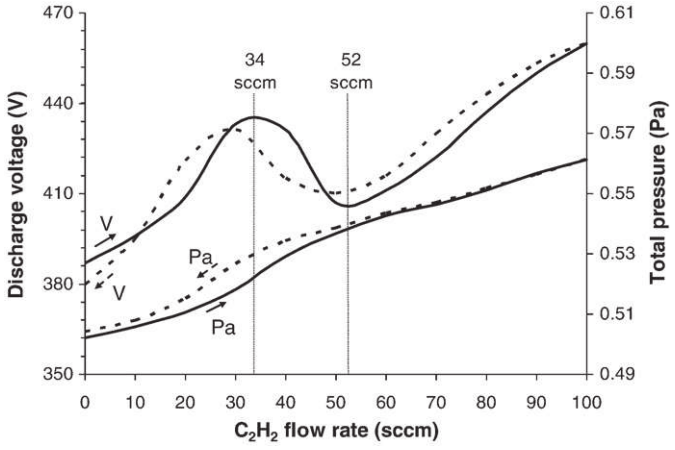

Fig. 1. Discharge power and total pressure vs. C_2H_2 flow rate diagram.

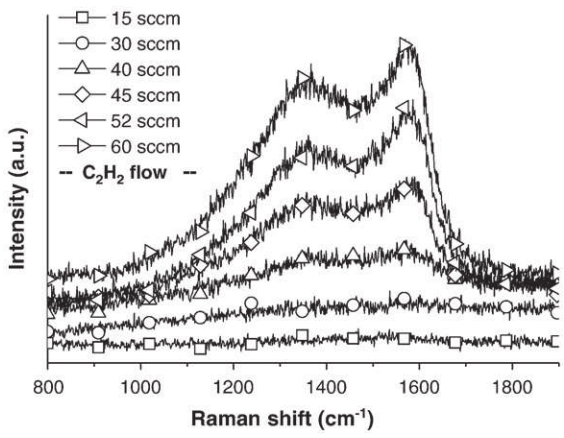

Fig. 2. The part of Raman spectra of Ti–C:H coatings representing carbon peaks.

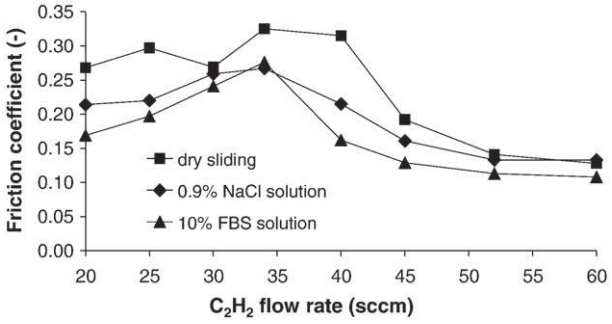

Fig. 3. Friction coefficients of Ti–C:H coatings in different environment conditions.

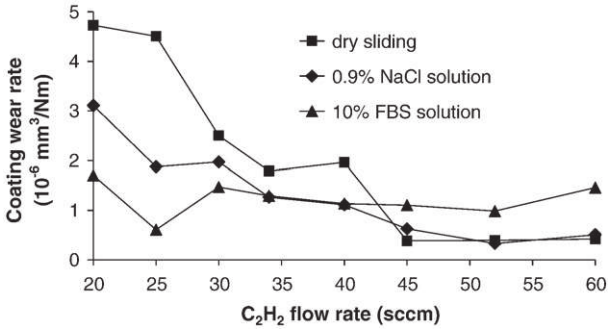

Fig. 5. Wear rates of Ti–C:H coatings in different environment conditions.

3.2. Coating composition and hardness

Chemical composition measurements clearly showed that the selected flows covered a wide range of Ti/C ratios (Table 1). The carbon content increased linearly with increasing C_2H_2 flow from 18 to 91 at.%. The Raman spectra (Fig. 2) only exhibited a very broad peak close to the typical position of C-rich phases (up to FR34); D and G peaks were, then, clearly seen for higher flows. Therefore, it can be concluded that the first C–C bonds appeared for FR34 and a further increase of the flow promoted the DLC formation. This result is similar to that reported by Zehnder and Patscheider, who could identify non-carbidic carbon up to 44 at.% of Ti [10]. Two weak peaks positioned at approximately 265 and 420 cm^{-1} and identified as Ti–C were visible only for FR30–45.

The hardness as a function of the C_2H_2 flow is shown in Table 1. The maximum hardness was achieved for FR30 and FR34 samples, while a further increase of the C_2H_2 flow rate led to the drop of the hardness to the lowest value for FR60 film.

3.3. Tribological behaviour of Ti–C:H coatings

The samples FR10–15 proved to have unsatisfactory tribological properties and were quickly worn out. The wear tracks and the ball scars showed clear severe abrasive damage. Therefore, only the tribological parameters of FR20–60 coatings could be evaluated.

The typical friction curves obtained at humid air were characterized by a clearly distinguishable running-in period before the steady steady-state phase. The running-in period was characterized by reaching the maximum friction coefficient at about 300 cycles followed by a decrease of this parameter to the steady-state value, which started after about 1500 cycles. The local friction maximum value was progressively reduced with increasing C:H content. The sliding tests in PS and FBS solutions showed lower friction values compared to dry sliding and the running-in phase almost disappeared. FR45–60 coatings showed almost constant friction over the entire tests, while instability of actual friction was observed for the coatings deposited with low C_2H_2 flow. In general, the FR20–40 coatings exhibited much higher friction coefficients compared to FR45–60, as shown in Fig. 3.

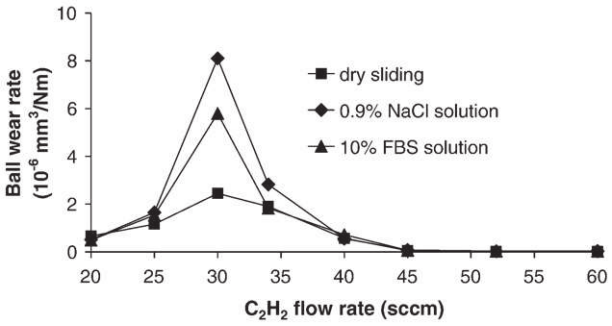

Fig. 4. Wear rates of 440C steel ball when sliding against different Ti–C:H coatings in different environment conditions.

Considering the suggested application for Ti–C:H coatings, the wear rates of both the counterpart and the coating have been analyzed. For FR20–30, a significant increase of the ball wear rate was observed in both dry and liquid environments (Fig. 4), particularly in the later case. The ball wear rate decreased with further increase of C_2H_2 flow regardless of the testing environment. The analysis of the ball wear scars showed a high coverage by wear debris when tested again the coatings deposited with high flows; the balls did not show apparent damage when the wear debris layer was mechanically wiped out.

It should be pointed out that no coating was worn out after the tests with exception of FR10–15 referred to above. In dry tests the coating wear rate monotonically decreased with increasing C:H content up to FR45 (Fig. 5). The tests in PS exhibited similar behaviour compared to dry sliding; however, the wear rates were slightly lower. FBS radically changed the coatings wear behaviour showing almost stable wear rate values regardless of the coating composition.

4. Discussion

The structure, chemical composition, hardness and tribological properties evaluated at humid air of Ti–C:H coatings showed similar results to that obtained by Zehnder and Patscheider [10] on their nc-TiC/a-C:H system deposited by magnetron sputtering. Thus, it could be expected that our coating would follow the same structure evolution: the TiC rich coatings (up to FR34) are transformed to nanocomposite TiC/a-C:H films (FR40–60).

In general, the tested coatings could be divided into three groups with similar wear mechanism: i) FR10–15, mainly free Ti, ii) FR20–40, typically Ti + TiC, and ii) FR45–60 representing DLC alloyed with Ti. The coatings with the high proportion of free Ti were characterized by unsuitable tribological behaviour. For FR20–40 both friction and ball wear rates increased due to the increasing proportion of carbides and, thus, higher hardness of the coatings. The wear tracks observed by SEM and optical microscopy were characterized by a rough surface with deep scratches parallel to the relative ball movement. The analysis of the wear debris produced by sliding revealed the presence of hard wear debris particles between the sliding surfaces causing a high counterpart wear and friction coefficient fluctuations, which corresponds to the results reported by Guu et al. [11]. The FR34 coating exhibited predominantly the hard TiC phase; however, the Raman analysis indicated the presence of C–C bonds which can have a possible positive effect in the friction and wear. In fact, the wear debris of FR34 analyzed by Raman spectroscopy contained a significant amount of the graphitic carbon, which was not observed in case of coatings deposited with lower C_2H_2 flow. The increase of the graphitic peaks intensity in the wear track suggested as well the formation of a carbon-rich tribolayer, which facilitated the sliding. The last group of

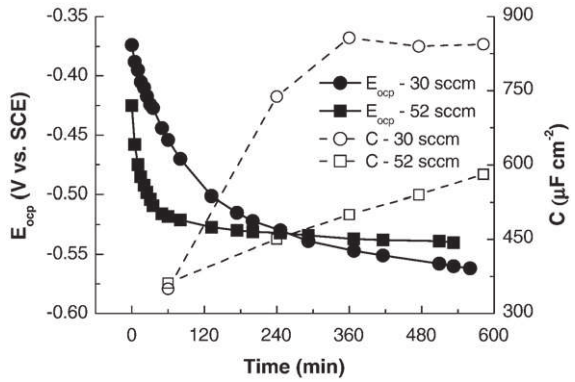

Fig. 6. Time dependence of open circuit potential and electrode capacitance during electrochemical testing of Ti–C:H coatings.

the coatings, FR45–60, showed the lowest friction and wear rate. The wear tracks were rather smooth with a minimum degree of failure. The wear debris was clearly identified as graphitic carbon forming probably a sliding interlayer between the surfaces in the contact. The adhered wear debris was observed mainly on the counterpart; its compactness and thickness increased with C content.

The sliding process in the presence of the biological solutions could be strongly influenced by the tribocorrosion; moreover, the tribolayer formation and its performance in the presence of PS or FBS is different from that in air environment [12,13]. Therefore, considering the ball wear rates shown in Fig. 4, FR30 and FR52 were selected as typical cases for the corrosion tests. The open circuit potential (OCP) was −0.37 and −0.43 V for FR30 and FR52, respectively, when the corrosion tests started. Thus, FR30 is a more noble electrochemical material. However, its OCP decreased monotonically during the entire test to a level corresponding to the substrate material (−0.55 V), while the OCP of FR52 reached a stable level of −0.52 V after one half of the test (300 min) remaining constant thereafter. The decrease of OCP could be connected with the progressive growth of the existing pores. The stabilization of OCP for FR52 indicated the termination or significant reduction of the pore growth, which is supported by the slight increase of the capacity (Fig. 6). On the other hand, FR30 rapid capacity increases and monotonic OCP decreases suggesting galvanic stimulation of pore corrosion. This conclusion was further supported by the amount of corrosion products, which were much higher in the case of FR30. However, the morphology of the coatings must be taken into account, since higher carbon coatings are denser preventing pitting corrosion. Therefore, coatings with all carbon content will undergo a detail corrosion study, which will be discussed in next paper. Nevertheless, the corrosion products, most of the cases were metal oxides or hydroxides, could act as abrasive material quickly wearing the counterpart when the tribological tests are being performed in solutions. Indeed, the ball wear scars were fully covered by deep scratches when tested against FR30, while they are quite smooth when tested against FR52. Obviously, the combination of the abrasive wear and tribocorrosion of the ball material could lead to the high ball wear rates, as shown in Fig. 4.

5. Conclusion

Ti–C:H layers were analyzed reflecting their possible use as interlayer for improving adhesion of functional DLC coatings on Ti-alloy substrates for biomedical applications, mainly surgical tools and prostheses. The variation of C_2H_2 flow led to a wide range of chemical compositions from Ti-rich coatings with predominant TiC phase to nanocomposite structured TiC/a-C:H. films. The best frictional and wear properties were achieved for the highest C_2H_2 flows, while critical wear rate of the coating was observed for the lowest flows. The moderate flows led to high counterpart damage, particularly when tested in biological solutions. As a final conclusion, a successful adhesive interlayer should avoid either a high thickness or low and moderate carbon contents.

Acknowledgements

This work has been supported by research project EUREKA E!3412 “BIOMUCOAT”, research project of Ministry of Trade and Industry MPO 2A-1TP1/031, by Ministry of Education of the Czech Republic (project MSM 6840770038), by FCT (PTDC/EME-TME/66471/2006) and CTU grant 05 71903. The authors wish to thank Joao Carlos Oliveira for EPMA measurements.

References

[1] J. Robertson, Mater. Sci. Eng. R 37 (2002) 129.
[2] W.J. Yang, T. Sekino, K.B. Shim, K. Niihara, K.H. Auh, Thin Solid Films 473 (2005) 252.
[3] A. Bruinink, A. Schroeder, G. Francz, R. Hauerit, Biomaterials 26 (2005) 3487.
[4] S. Meskinis, M. Andrulevicius, S. Tamulevicius, V. Kopustinskas, K. Slapikas, J. Jankauskas, B. Ciziute, Vacuum 80 (2006) 1007.
[5] D.Y. Wang, Y.Y. Chang, Ch.L. Chang, Y.W. Huang, Surf. Coat. Technol. 200 (2005) 2175.
[6] W. Precht, A. Czyzniewski, Surf. Coat. Technol. 174–175 (2003) 979.
[7] R. Gilmore, R. Hauert, Thin Solid Films 398–399 (2001) 199.
[8] V.-M. Tiainen, Diamond and Related Materials 10 (2001) 153–160.
[9] K. Holmberg, A. Mathews, Coatings Tribology, Elsevier, Amsterdam, 1998.
[10] T. Zehnder, J. Patscheider, Surf. Coat. Technol. 133–134 (2000) 138.
[11] Y.Y. Guu, J.F. Lin, Ch.F. Ai, Wear 208 (1997) 147.
[12] D.-H. Kim, H.-E. Kim, K.-R. Lee, Ch.-N. Whang, I.-S. Lee, Mater. Sci. Eng. C 22 (2002) 9–14.
[13] H. Liu, A. Tanaka, K. Umeda, Thin Solid Films 346 (1999) 162.

Solid State Sciences 11 (2009) 1757–1761

Contents lists available at ScienceDirect

Solid State Sciences

journal homepage: www.elsevier.com/locate/ssscie

Tribological behaviour of nanostructured Ti-C:H coatings for biomedical applications

Tomas Polcar [a,b,*], Tomas Vitu [c], Ladislav Cvrcek [d], Rudolf Novak [e], Jiri Vyskocil [d], Albano Cavaleiro [b]

[a] Department of Control Engineering, Faculty of Electrical Engineering, Czech Technical University in Prague, Technická 2, 166 27 Prague 6, Czech Republic
[b] SEG-CEMUC – Department of Mechanical Engineering, University of Coimbra, Rua Luís Reis Santos, P-3030 788 Coimbra, Portugal
[c] Faculty of Transportation Sciences, Czech Technical University, Na Florenci 25, 110 00 Prague 1, Czech Republic
[d] HVM Plasma Ltd., Na Hutmance 2, 158 00 Prague 5, Czech Republic
[e] Faculty of Mechanical Engineering, Czech Technical University, Technicka 4, 166 07 Prague 6, Czech Republic

ARTICLE INFO

Article history:
Received 6 May 2008
Received in revised form
15 October 2008
Accepted 16 October 2008
Available online 22 October 2008

Keywords:
Ti-C:H
Tribology
Coating
Nanocomposite
Biocompatibility

ABSTRACT

The development of a mechanically stable, functionally graded Ti-doped a-C:H interface layer in combination with a functional a-C:H coating requires a reduction of the brittle phases which induce generally problems in the transitions from Ti to TiC/a-C:H. The core objective of this study was to develop an optimum interlayer between the substrate and the functional top layer for biomedical applications, namely for tooth implants. Since the interlayer may be exposed to the sliding process, in the case of local failure of the top layer it has to fulfil the same criteria: biocompatibility, high wear resistance and low friction.

The functional Ti-C:H layers with thickness in the range 2.5–3.5 μm were deposited by a magnetron sputtering/PECVD hybrid process by sputtering a Ti-target in a $C_2H_2 + Ar$ atmosphere in dc discharge regime. The sets of coating samples were prepared by varying the C and H concentrations controlled by the C_2H_2 flow during the deposition process. The tribological properties were evaluated on a pin-on-disc tribometer at room temperature (RT) and at 100 °C using 440C balls with a diameter of 6 mm. The tests at 100 °C were performed to investigate the effect of the sterilization temperature on the tribological properties and the coating lifetime as well. The tribological performance was examined with respect to the friction coefficient, the wear rates of the coating and the counter-parts and the analysis of the wear debris. The Ti/C ratio decreased almost linearly from 4.5 to 0.1 with increasing C_2H_2 flow; the hydrogen content showed a minimum of 5 at.% at C_2H_2 flow of 30 sccm, while for lower flows it was about 10 at.%. The coatings could be divided into three groups based on the C_2H_2 flow: (i) 10–15 sccm, exhibiting severe abrasive damage during the sliding tests, (ii) 20–45 sccm, showing the highest hardness and friction values, and (iii) 52–60 sccm, with moderate hardness and minimal values of the friction coefficient and the wear rate.

1. Introduction

Nanostructured amorphous hydrogenated carbon coatings prepared by Plasma Enhanced Chemical Vapour Deposition (PECVD) are frequently used in engineering applications benefiting from their excellent mechanical and tribological properties. Their structure is composed of a metastable form of amorphous carbon with a significant content of sp^3 bonds, which leads to high hardness, chemical inertness and excellent wear resistance [1,2]. In biomedical tribological applications, a-C:H coatings outperform traditional nitrides and carbonitrides [3]. These referred structures show a very high degree of biocompatibility [4–7]. Since the a-C:H film adhesion on standard substrate materials, such as steel or Ti-alloy substrates, is often very low, metal or carbide interlayers are frequently used [8,9]. From the three widely used elements for an interlayer, Ti, W and Cr, it is expected that Ti layers should adhere better on the most typical material for implants, the titanium alloys. Thus, Ti-C:H coatings exhibit a high potential for biomedical applications [10].

Our study deals with the development of an interlayer for improving the adhesion of a-C:H coatings used for biomedical applications. The vital parameters of such a layer are biocompatibility, low friction and high wear resistance, which are required for the case of a failure in the top a-C:H layer. The main aim is to recognize the brittle phases which induce severe problems in the

* Corresponding author. Department of Control Engineering, Faculty of Electrical Engineering, Czech Technical University in Prague, Technická 2, 166 27 Prague 6, Czech Republic. Tel./fax: +420 224 352 439.
E-mail address: tomas.polcar@dem.uc.pt (T. Polcar).

1293-2558/$ – see front matter © 2008 Elsevier Masson SAS. All rights reserved.
doi:10.1016/j.solidstatesciences.2008.10.006

functionally graded system. The tribological properties of these sample sets were studied in order to ensure stable tribological properties of the whole Ti-C:H/a-C:H system until the coating would be almost worn through completely. The adjusted tests parameters respected the results of the previous studies on Ti-C:H tribology showing the dependence of the tribological properties on the deposition parameters, the sliding conditions and the environment [1,11,12,13].

2. Experimental details

2.1. Deposition process

The functional Ti-C:H layers were deposited by a hybrid process involving PECVD and magnetron sputtering where a Ti-target was sputtered in a $C_2H_2 + Ar$ atmosphere in dc discharge regime. The sets of coatings samples were prepared by varying the content of the C:H components controlled by the C_2H_2 flow rate during the deposition process. The fixed deposition parameters were as follows: Ar flow rate of 75 sccm, deposition temperature of 350 °C and d.c. substrate bias voltage of −70 V. The deposition process was stabilized in the range 10–60 sccm of C_2H_2 flow; several values of acetylene flow were chosen with respect to significant points selected in a previously obtained diagram plotting the discharge power and pressure vs. C_2H_2 flow rate. The coatings were deposited on polished circular HSS samples with a diameter of 20 mm. The thickness of Ti-C:H coatings was varied from 2.5 to 3.5 μm. To facilitate the text understanding, the coatings were denominated as FRX, where X was a number corresponding to the C_2H_2 flow.

2.2. Coating composition, structure and hardness measurements

The chemical composition of the coatings was determined by electron probe microanalysis (EPMA) and by elastic recoil detection analysis (ERDA), the structure by X-ray diffraction (XRD) and the chemical bonding was accessed by Raman spectroscopy (Ar laser 514.5 nm). The hardness measurements were performed using a Vickers indenter with a nominal applied stylus load of 50 mN, which led to a maximum penetration depth that did not exceed 0.2 μm. Each presented hardness value was calculated from at least five independent indentations.

2.3. Tribological testing

The tribological properties of the Ti-C:H coatings were studied using a high temperature pin-on-disc CSM Tribometer. All the tribological measurements were performed in identical conditions: 5000 cycles, normal load of 5 N, linear speed of 0.05 ms^{-1}, relative air humidity of 40 ± 5%. The sliding tests were carried out at room temperature (RT) and at 100 °C using 440C steel spherical counterparts with a diameter of 6 mm. The tests at 100 °C were performed in air to investigate the effect of the sterilization temperature on the tribological properties as well as on the coating lifetime.

The tribological performance was examined with respect to the friction coefficient, the wear rates of the coatings and the counterparts and the analysis of the wear debris. The coating wear rates were evaluated on the basis of profile measurements on the wear track; the wear rates of the balls were calculated from measurements of the spherical wear cap using optical microscopy. The calculation of the wear rate was performed following Ref. [14], as the worn volume per the sliding distance and the load. Each tribological test was repeated at least three times; the standard deviation was about 10%. In this paper the average values of the friction coefficient and the wear rates are presented. To determine the dominant wear mechanism, the wear tracks were studied using optical and scanning electron microscopy and Raman spectroscopy.

3. Results

3.1. Coating deposition, chemical composition and adhesion

The evolution of the total pressure and the target potential as a function of increasing or decreasing C_2H_2 flow has been shown somewhere else [15]. The ascending discharge voltage curve showed three main features: (i) a local minimum at 8 sccm C_2H_2 flow attributed to the changes in the metallic phase deposition and the initial titanium carbide formation, (ii) a local maximum at about 34 sccm corresponding to the priority growth of titanium carbide, and (iii) a local minimum at 52 sccm which could be connected with the decomposition of the acetylene and the predominant growth of the a-C:H layer. Fig. 1 shows the chemical composition of the deposited films measured by EPMA. All the coatings contained about 5 at.% of oxygen originated from the residual atmosphere. The chemical composition measurements clearly showed that the selected flows covered a wide range of Ti/C ratios. The carbon content increased linearly with increasing C_2H_2 flow from 18 to 91 at.%. The preliminary measurement of the chemical composition by ERDA showed that the hydrogen content was about 10 at.% for FR15–25 then decreased to a minimum down to 5 at.% at FR30, and finally linearly increased with C_2H_2 flow up to a maximum of 25 at.% for FR52, where it remained constant when acetylene flow was further increased. The coatings exhibited a sufficient critical load Lc2, see Fig. 1. The lowest critical load of 40 N (FR60) still allowed the tribological testing of the coating without any adhesion failures being noticed.

3.2. Coating structure and hardness

Fig. 2a shows the part of the Raman spectra of the Ti-C:H coatings representing the carbon peaks. FR34 exhibited a very broad peak whereas D and G peaks were clearly seen for higher flows. Therefore, it can be concluded that amorphous carbon was detected by Raman spectroscopy for flows higher than 34 sccm. Two weak peaks positioned at approximately 265 and 420 cm^{-1}, and identified as TiC, were visible only for flows of C_2H_2 in the range 10–40%. The XRD diffractograms of the Ti-C:H coatings are depicted in Fig. 2b. The FR10 coating exhibited clear titanium peaks as well as very weak reflections of the titanium carbide phase. For the flow of 25 sccm, only the cubic TiC phase (ICDD 73-0472) with two dominant orientations, (111) and (200), was observed. Three main

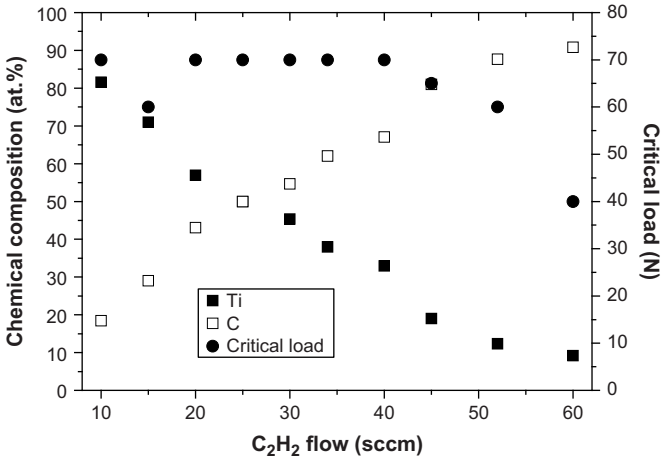

Fig. 1. Chemical composition and critical load of failure of Ti-C:H coatings as a function of the C_2H_2 flow. Note that the chemical composition represents only the Ti/C ratio due to the O and H exclusion (see text).

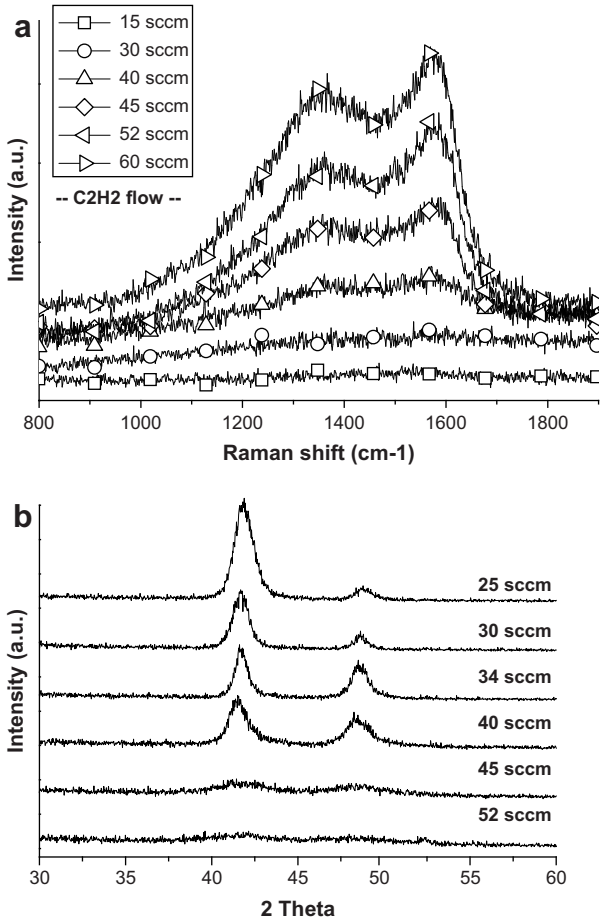

Fig. 2. Raman spectra (a) and XRD diffractograms (b) of Ti-C:H coatings.

features emerged when the C_2H_2 flow was increased from 25 to 40 sccm: (i) the intensity of (111) peak decreased, while that of (200) increased; (ii) the full width at half maximum (FWHM) slightly decreased; (iii) the peaks became asymmetric with a longer tail for the higher 2θ angles, being particularly evident in the cases of FR34 and FR40 samples. Higher C_2H_2 flows led to very broad TiC peaks. The coatings were under compressive stress, since all peaks positions were shifted toward lower 2θ angles compared to the ICDD positions.

The hardness and Young's modulus as a function of C_2H_2 flow are shown in Fig. 3. The maximum hardness was about 15 GPa for FR30–34; this value corresponds to the local maximum in the discharge voltage vs. acetylene flow rate diagram. The hardness of the samples prepared with higher C_2H_2 flows showed a decreasing trend with the lowest value being obtained for the FR60 coating, which reflected the predominance of the a-C:H phase.

3.3. Tribological behaviour of Ti-C:H coatings

The sliding tests carried out on the FR10 and FR15 samples ended after 5000 laps with the coatings completely worn out. The inspection of the wear tracks showed a significant abrasive damage; the friction was very high during all the tests. Based on these results, the coatings FR10 and FR15 were discarded from further tribology analysis.

3.3.1. Friction

A typical friction curve was characterized by a running-in period and a steady-state phase. In all the measurements at RT, the

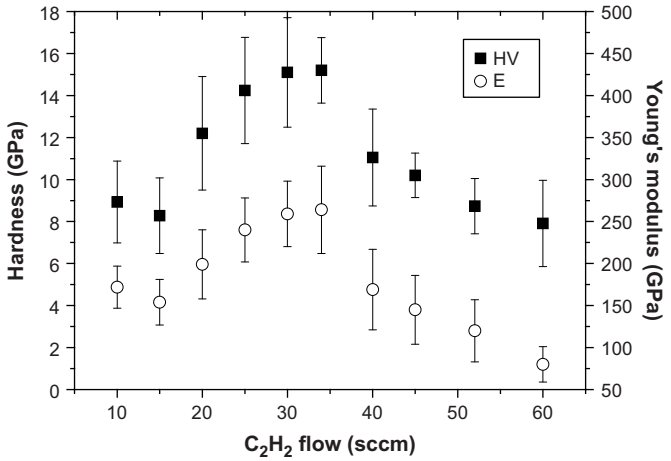

Fig. 3. Hardness and Young's modulus of Ti-C:H coatings as a function of the C_2H_2 flow rate.

running-in phase took usually about 1500 cycles. At 100 °C the running-in was slightly shorter; the steady state was reached after ~1000 cycles. The running-in period was characterized by the reaching of the maximum friction coefficient (~300 cycles) at both testing temperatures followed by the decrease of the friction coefficient down to the steady-state value. The local friction maximum was reduced with increasing a-C:H content. The samples set could be divided into two groups with different frictional behaviour: FR20 to FR40 and FR45 to FR60. The first group exhibited the steady-state friction coefficient in the range 0.22–0.29; no clear dependency on the coating composition was observed. The friction coefficients at elevated temperature were significantly higher than those obtained at RT, varying from 0.35 to 0.49. The maximum value was reached for FR40, which showed the highest fluctuation of the actual friction coefficient values as well. For C_2H_2 flow rates above 45 sccm the friction coefficient at RT decreased slightly to the minimal value of 0.13 for FR60. The same trend was observed at 100 °C but, inversely to the low C_2H_2 flows, the general values are lower than at RT; the friction coefficient dropped from 0.07 (FR45) to 0.02 (FR60). The average friction coefficient of the Ti-C:H coatings is summarized in Fig. 4.

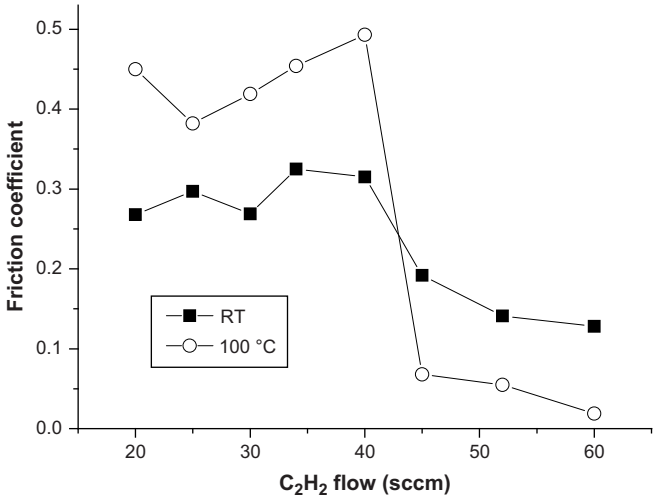

Fig. 4. Friction coefficient of Ti-C:H coatings measured at room temperature and 100 °C.

3.3.2. Wear

Considering the suggested application of the Ti-C:H coatings, both the wear rates of the counter-part and the coating have been analyzed. For FR20–30, a significant increase of the ball wear rate was observed at RT, while it remained almost constant at 100 °C. Nevertheless, with further increasing of the C_2H_2 flow, the ball wear rate decreased regardless on the test temperature. The analysis of the ball wear scars showed a high coverage by wear debris for the highest C_2H_2 flows (FR45–60).

The average values of the coating wear rate at 100 °C were generally higher than at RT (Fig. 5). It should be pointed out that no coating was completely worn out after the tests. The coating wear rate monotonically decreased at RT with increasing C:H content up to FR45. The elevated temperature radically changed the wear rate which showed a sharp maximum for FR40. The lowest wear rate was achieved in the case of FR52–60 coatings.

4. Discussion

The structure analysis of the Ti-C:H coatings, in the C_2H_2 flow region of 25–40 sccm, carried out in order to calculate the TiC grain size, encountered some difficulties due to the asymmetry of the TiC peaks. The existence of other titanium carbide phases deficient in carbon, which could match the peak positions (e.g. hexagonal Ti6C3.75 (ICDD 79-0971)), was not expected since the carbon content was much higher than their stoichiometry (62 and 67 at.% for FR35 and FR40, respectively) and the existence of sub-stoichiometric titanium carbide phases was also highly improbable considering the deposition method. Moreover, a XRD diffractogram obtained at grazing incidence of 2° showed that the asymmetry was slightly lower. Hence, the referred asymmetry could be an effect of the different stresses between the bulk coating and the zone close to the coating-substrate interface. As a consequence, obviously the exact grain size calculation is very difficult and can be used only for qualitative analysis. The grain size estimated from the (111) TiC peak was 20 nm for FR25 and it slightly decreased down to 16 nm at the flow of 40 sccm and, then, fell down to 5 nm for higher flows. Raman spectroscopy showed C–C bonds for a minimum flow of 40 sccm. Considering the chemical composition of the films, the Ti-C:H coatings structure can be described as Ti/(TiC) for FR10–15, TiC for FR20–34 and nanocomposite nc-TiC/a-C:H for higher C:H contents. The results correspond in general to those obtained by Zehnder and Patscheider [16] for the nc-TiC/a-C:H system deposited by magnetron sputtering. The influence of the hydrogen content on the structure was not clear; however, the observed minimum at the flow of 30 sccm could be explained by the predominant TiC growth, since both free Ti [17] and C [1] could accommodate the hydrogen more easily.

In general, the coatings could be divided into three groups with similar wear mechanism at room temperature: (i) FR10–15, (ii) FR20–40, and (ii) FR45–60. The coatings with the high proportion of free Ti were characterized by a low hardness and an unsuitable tribological behaviour. With increasing carbon content the proportion of carbides increased leading to a higher hardness. However, both the friction and the ball wear rate increased as well. The wear tracks observed by SEM and optical microscopy were coarse with deep scratches parallel to the relative ball movement (Fig. 6). The analysis of the wear debris produced by the sliding revealed the presence of hard wear debris particles between the sliding surfaces causing a high counter-part wear and fluctuations on the friction coefficient [18]. The FR34 coating exhibited predominantly the hard TiC phase; however, the Raman analysis indicated the presence of C–C bonds in this coating with a possible positive effect in the friction and the wear. In fact, the wear debris of FR34 analyzed by Raman spectroscopy contained graphitic carbon, which was not observed in the case of the coatings deposited with lower C_2H_2 flows. Nevertheless, the decrease of the friction coefficient and the wear rate due to the nanocomposite nature reported by other authors for nc-TiC/a-C:H coatings [16,19] was not observed.

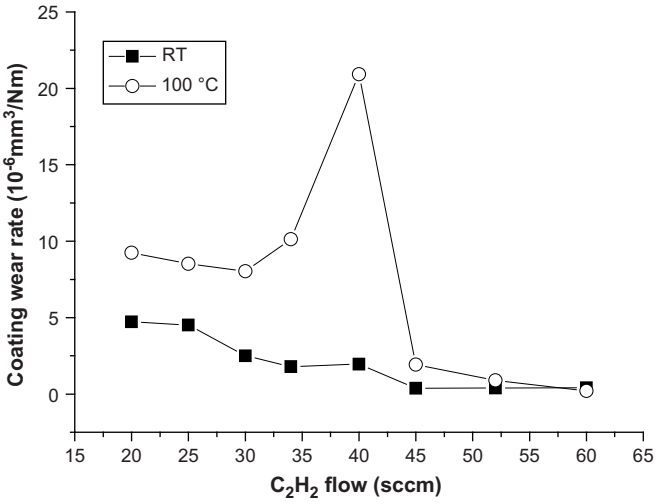

Fig. 5. Wear rates of Ti-C:H coatings measured at room temperature and 100 °C.

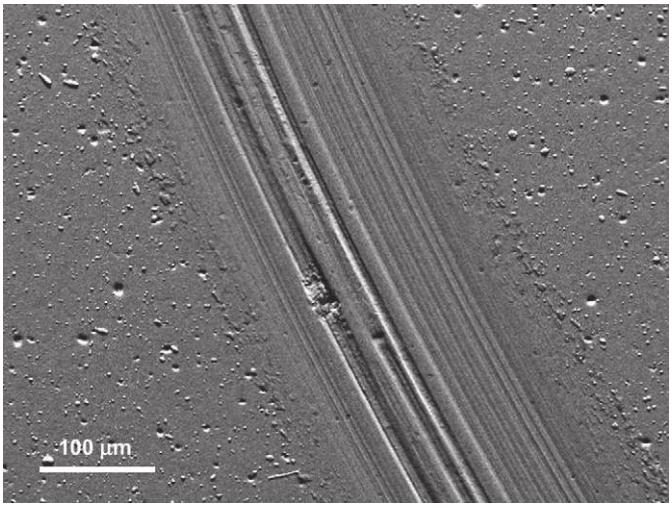

Fig. 6. SEM micrograph of the FR25 wear track, tested with 440C steel ball at RT.

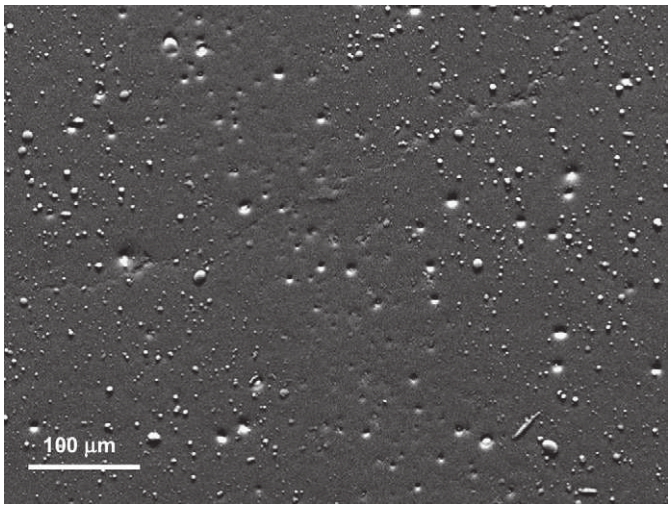

Fig. 7. SEM micrograph of the FR52 wear track, tested with 440C steel ball at RT.

The last group of the coatings with the highest C_2H_2 flow rates (45–60 sccm) showed the lowest friction and a decreasing wear rate despite their lower hardness. The wear tracks were smooth with a minimum degree of failure (Fig. 7). The wear debris was clearly identified as graphitic carbon probably forming a sliding interlayer between the surfaces in the contact. The adhered wear debris was observed mainly on the counter-part; its compactness and thickness increased with the C content.

As expected, the increase of the temperature strongly influenced the friction and the wear behaviour. Nevertheless, the dominant effect of the used temperature (100 °C) on the sliding process seems to be the drying of the air, since neither structural changes nor oxidation was expected and the Raman spectra of the as-deposited and annealed (i.e. the samples tribologically tested at 100 °C) coatings were identical. The lower friction coefficient of the FR45–60 coatings at elevated temperature could be explained by the enhanced formation of the graphite tribolayer [20], while the absence of moisture facilitated the sliding contributing to the higher friction of the coatings with predominant TiC phase [21].

5. Conclusion

The Ti-C:H layers were analyzed reflecting their use as an adhesion improving interlayer for functional DLC coatings on Ti-alloy substrates for biomedical applications, or, alternatively, as a functional coating for such applications themselves. The selected C_2H_2 flow led to a wide range of chemical compositions from Ti-rich coatings, through films with predominant TiC phase and to nc-TiC/a-C:H. The best frictional and wear properties were achieved for the highest C_2H_2 flows, while the critical wear rate of the coating was observed for the lowest flows. As main conclusion, a successful adhesive interlayer should be neither thick nor having low or moderate carbon content.

Acknowledgements

This work has been supported by research projects EUREKA E!3412 "BIOMUCOAT", PTDC/EME-TME/66471/2006, MPO 2A-1TP1/031 and MSM 6840770038. The authors would like to thank J.C. Oliveira for the EPMA measurements.

References

[1] J. Robertson, Mater. Sci. Eng. R 37 (2002) 129.
[2] W.J. Yang, T. Sekino, K.B. Shim, K. Niihara, K.H. Auh, Thin Solid Films 473 (2005) 252.
[3] W. Österle, D. Klaffke, M. Griepentrog, U. Gross, I. Kranz, Ch. Knabe, Wear 264 (2008) 505.
[4] A. Bruinink, A. Schroeder, G. Francz, R. Hauert, Biomaterials 26 (2005) 3487.
[5] E.T. Uzumaki, C.S. Lambert, W.D. Belangero, C.M.A. Freire, C.A.C. Zavaglia, Diamond Relat. Mater. 15 (2006) 982.
[6] David A. LaVan, Robert F. Padera, Thomas A. Friedmann, John P. Sullivan, Robert Langer, Daniel S. Kohane, Biomaterials 26 (2005) 465.
[7] Geoffrey Dearnaley, James H. Arps, Surf. Coat. Technol. 200 (2005) 2518.
[8] S. Meskinis, M. Andrulevicius, S. Tamulevicius, V. Kopustinskas, K. Slapikas, J. Jankauskas, B. Ciziute, Vacuum 80 (2006) 1007.
[9] A.A. Voevodin, M.A. Capano, S.J.P. Laube, M.S. Donley, J.S. Zabinski, Thin Solid Films 298 (1997) 107.
[10] A. Schroeder, G. Francz, A. Bruinink, R. Hauert, J. Mayer, E. Wintermantel, Biomaterials 21 (2000) 449.
[11] D.Y. Wang, Y.Y. Chang, Ch. L. Chang, Y.W. Huang, Surf. Coat. Technol. 200 (2005) 2175.
[12] W. Precht, A. Czyzniewski, Surf. Coat. Technol. 174–175 (2003) 979.
[13] R. Gilmore, R. Hauert, Thin Solid Films 398–399 (2001) 199.
[14] K. Holmberg, A. Matthews, Coatings Tribology, Elsevier, Amsterdam, 1998.
[15] T. Vitu, T. Polcar, L. Cvrcek, R. Novak, J. Macak, J. Vyskocil, A. Cavaleiro, Surf. Coat. Technol. 202 (2008) 5790.
[16] T. Zehnder, J. Patscheider, Surf. Coat. Technol. 133–134 (2000) 138.
[17] X.B. Yu, J.Z. Chen, Z. Wu, B.J. Xia, N.X. Xu, Int. J. Hydrogen Energy 29 (2004) 1377.
[18] Y.Y. Guu, J.F. Lin, Ch.F. Ai, Wear 208 (1997) 147.
[19] Y.T. Pei, D. Galvan, J.Th.M. De Hosson, Acta Mater. 53 (2005) 4505.
[20] H. Liu, A. Tanaka, K. Umeda, Thin Solid Films 346 (1999) 162.
[21] M. Sasaki, Y. Kozukue, K. Hashimoto, K. Takayama, I. Nakamura, I. Takano, Y. Sawada, Vacuum 74 (2004) 455.

Diffractive-optics-based sensor as a tool for detection of biocompatibility of titanium and titanium-doped hydrocarbon samples

Raimo Silvennoinen,[1,*] Stanislav Hasoň,[2] Vladimír Vetterl,[2] Niko Penttinen,[1] Martti Silvennoinen,[1] Kari Myller,[3] Pavlína Černochová,[4] Sonia Bartáková,[4] Patrik Prachár,[4] and Ladislav Cvrček[5]

[1]Department of Physics and Mathematics, University of Eastern Finland, P.O. Box 111, FI-80101 Joensuu, Finland

[2]Institute of Biophysics, Academy of Sciences of the Czech Republic, v.v.i. Královopolská 135, CZ-612 65 Brno, Czech Republic

[3]MGM-Devices Ltd., FI-82210, Suhmura, Finland

[4]Centre for Dental and Craniofacial Research, Faculty of Medicine, Masaryk University, Komenskeho nam. 2, 662 43 Brno, Czech Republic

[5]HVM Plasma Ltd., Na Hutmance 2, 158 00 Prague 5, Czech Republic

*Corresponding author: raimo.silvennoinen@uef.fi

Received 2 April 2010; revised 4 August 2010; accepted 28 August 2010; posted 7 September 2010 (Doc. ID 126411); published 7 October 2010

Adsorption of the elongated human plasma fibrinogen (HPF) and globular human serum albumin molecules on a titanium-based surface is monitored by analyzing permittivity and optical roughness of protein-modified surfaces by using a diffractive optical element (DOE)-based sensor and variable angle spectro-ellipsometry (VASE). Both DOE and VASE confirmed that fibrinogen forms a thicker and more packed surface adlayer compared to a more porous and weakly adsorbed albumin adlayer. A linear relation of the permittivity (ε') and dielectric loss (ε'') was found for some of the dry titanium-doped hydrocarbon (TDHC) surfaces with excellent HPF adsorption ability. We discuss some aspects of TDHC's aging and its possible effects on fibrinogen adsorption.

OCIS codes: 050.1970, 240.2130, 240.5770, 170.3890, 170.1850.

1. Introduction

The most frequently used biomaterial in hard tissue replacement, such as dental and orthopedic implants, is titanium. Biomaterial devices made of titanium are satisfactory products from a human health point of view [1–7]. The effective surface tension, as well as the surface energy related to the topography of surface, which can be varied by different processing methods, is assumed to influence the final interactions of the implant with the surrounding environment. It is also reported that rough surfaces promote better osseointegration than smooth surfaces [8–11]. After implantation, within a few seconds, the biomaterial surface becomes coated with a film of adsorbed proteins that mediate the interaction between the implant and the body environment. Since an implant is exposed to blood during implantation, the initial protein layer is mainly composed of plasma proteins. Human plasma fibrinogen (HPF) is the relevant protein that adsorbs on biomaterial surfaces. HPF partakes in blood coagulation, and facilitates adhesion and aggregation of platelets

0003-6935/10/295583-09$15.00/0

[12,13]. The structure and composition of the adsorbed protein layer determine the type and extent of the subsequent biological reactions, such as activation of coagulation and immune response and osseointegration [14]. Thus, the initially adsorbed protein layer is a factor determining biocompatibility [15–23]. In recent years, interest has been focused on preparation of hydrocarbons doped with Ti and researchers have used different methods to analyze biocompatibility of important proteins [24,25].

However, the mechanisms and factors that are important for protein adsorption and desorption are still not well understood. Therefore, it is of interest to focus scientific research on finding out how different surfaces influence the formation of the protein layers and their properties.

In this paper, we chose two model plasma proteins with significant differences in their size and shape [HPF as a rodlike protein having a mass of 340 kDa, compared to a globular human serum albumin (HSA) with a mass of 66 kDa]. The aim is to distinguish their adsorption behavior on mechanically polished titanium surfaces (frequently used biomaterial in hard tissue replacement) with the aid of DOE (dynamical measurement of adsorption process of protein on surface in electrolyte solution—wet measurement) and VASE (measurement of thickness of adsorbed protein layer on material surface after removal the protein-modified surface from protein solution followed by half-hour drying in air-dry measurement). Secondly, quite recently we found a significant correlation between the complex dielectric constant of dry titanium-doped hydrocarbon surfaces and ability for HPF adsorption on these treated surfaces supposing a linear relation of the permittivity ε' and dielectric loss ε'' of studied surfaces [26,27]. Therefore we start to study how aging process of TDHC surfaces influenced the fibrinogen adsorption for possible use the TDHCs as an appropriate material for dental implants productions.

2. Materials and Methods

A. Treated Titanium Surfaces

The titanium-doped hydrocarbon (TDHC) surfaces (Ti_xC_{1-x}) and diamondlike carbon (DLC, $Ti_{0.00}C_{1.00}$) were prepared by the plasma-enhanced chemical vapor deposition (PECVD) method (see, e.g., [28,29]). We prepared three Ti_xC_{1-x} differing in carbon proportion as follows: $Ti_{0.82}C_{0.18}$, $Ti_{0.38}C_{0.62}$, and $Ti_{0.09}C_{0.91}$. In the beginning the thickness of titanium oxide layer was measured with a polished titanium surface and its depth was about 220 nm. The thickness of Ti_xC_{1-x} coatings produced by using PECVD ranged from 2.5 to 3.5 μm, which is thick enough in the optical sense to consider it as a solid bulk layer [28,29]. To investigate the biocompatibility of different TDHC surfaces, we measured the adsorption of HPF, an elongated protein molecule with dimensions of 45 nm × 9 nm × 6 nm [12] and mass of 340 kDa, on these TDHC surfaces either immediately after their preparation or after two-year storage. The adsorption ability of different TDHC surfaces for HPF has been compared with the HPF adsorption on mechanically polished titanium surfaces (a frequently used biomaterial in hard tissue replacement), which serves in this study as a reference surface. With mechanically polished titanium, we also studied the adsorption behavior of HSA) a protein with an ellipsoid shape and dimensions of 14 nm × 4 nm (the HSA molecule is frequently approximated with a sphere with a radius of about 6 nm [20] and mass of 66 kDa).

B. Chemicals

HPF (fraction I, type III) and HSA (97%–99%) were purchased from Sigma. In all experiments, both proteins were dissolved in a phosphate buffer solution of +0.136 M sodium citrate, which serves as a background electrolyte. Measurements were performed at room temperature.

C. Coherent and Noncoherent Response of DOE Sensor

The thicknesses of the adsorbed protein layers on differently treated titanium surfaces were sensed utilizing the coherence response of a DOE sensor, as shown in Fig. 1. The DOE sensor utilizes an expanded and focused laser beam ($\lambda = 632.8$ nm), which is realized by using the lens system L1–L2 to hit on the studied surface, which has a complex refractive index N_4 through a comparison liquid (water) in a cuvette via a beam splitter (BS) and a cuvette window having a complex refractive index N_1. The BS directs a backscattered laser beam on the DOE aperture (shown in the lower inset of Fig. 1), which detects if the wavefront is distorted either after chemical reactions of the ions of the background electrolyte with studied surface or adsorption of added proteins (denoted as complex refractive index N_3) on the examined surface, which is immersed in the solution of background electrolyte (denoted as N_2). A distorted 4 × 4 light spot DOE image is grabbed from two-dimensional photo array of the charge-coupled device (CCD) and is

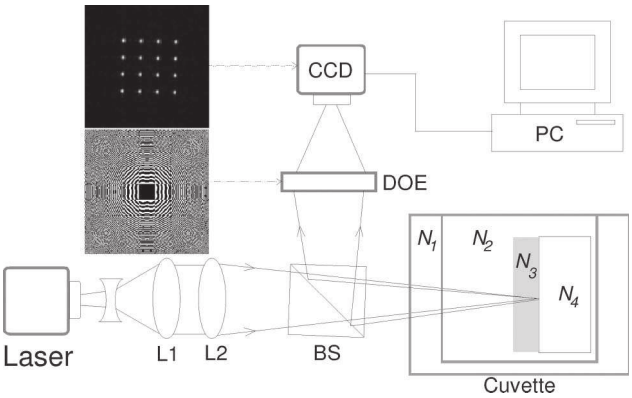

Fig. 1. Geometric setup of DOE sensor with sample cuvette compartment for R_{opt} measurements. The lower inset denotes the aperture of the DOE, whereas the upper inset denotes a reconstructed 4 × 4 spot matrix image of the DOE by using nondistorted wavefront.

analyzed using a computer (PC). The changes in R_{opt}, which relate to surface roughness R_a [30,31], are detected utilizing the coherent response of the DOE sensor. The layer thickness adsorbed on treated titanium surfaces is calculated from the captured DOE image data of the 4 × 4 light spot matrix, which is shown in the upper inset of Fig. 1. The irradiance of the peaks were calculated utilizing Eq. (1) as follows:

$$I_C = \frac{1}{n_{pk} m_{pk}} \sum_{i_{pk}=1, j_{pk}=1}^{n_{pk}, m_{pk}} I_{i_{pk}, j_{pk}}, \tag{1}$$

where n_{pk} and m_{pk} are the pixel dimensions of each of the 16 peaks in the DOE image and $I_{i_{pk},j_{pk}}$ is the image irradiance observed by the (i_{pk},j_{pk})th element of the peak in the DOE image captured by the CCD camera. The 16 different diffractive lenses are integrated utilizing the superposition principle in the DOE aperture, obeying coherent response for each pixel with complex wavefront amplitude $A_{i,j}$ as follows $I_C = |\sum A_{i,j}|^2$, which satisfies the principle of compact and phase sensitive interferometer. The DOE element images the 4 × 4 light spot matrix in its focal plane. If the reconstructing wavefront does not satisfy the terms of hologram imaginary, the spot image matrix does not appear in the image plane. The same disappearance of spot images holds, for instance, in the case where the radiant exitance from the laser resonator in the TEM_{00} mode starts to suffer from the appearance of sidemodes, and the DOE will spatially filter out those images from its original 4 × 4 light spot image. It is shown with tedious numerical simulations that the irradiance of the 4 × 4 spots will decrease as a function of optical path length (OPL) and will disappear when the OPL exceeds $\lambda/4$. This response is published and appears in Fig. 8.21(b) of Ref. [32]. It is also observable that this response resembles the response of the Beckmann–Spizzichino model [33]. To discover the thickness of the adsorbed layer N_3, we first calculated the irradiance of the peaks utilizing Eq. (1) and, after that, the optical path difference Δr, which can be understood as an optical roughness (R_{opt}), is solved inversely by using this response. During our previous measurements, we have noted that the accuracy of 0.2 nm can be achieved by using this one-arm interferometric technique [34]. Similar accuracy limits are also reported for the coupling dynamics of lasers of self-mixing interferometers in vibrometer applications ranging from 0.1 nm to 100 μm [35], whereas the accuracy of conventional two-arm interferometers used in optical diagnostics of random phase objects [36], as well as in optical diagnostics of rough surfaces [37], is estimated to be ~0.005 μm.

To be sure that the irradiance of peaks (coherent response) do not contribute any uncertainties in the noncoherent response, we subtract the irradiance portion of peaks from the total irradiance of the DOE image:

$$I_{\mathrm{NC}} = \frac{1}{n_{\mathrm{SW}} m_{\mathrm{SW}}} \sum_{i_{\mathrm{SW}}=1, j_{\mathrm{SW}}=1}^{n_{\mathrm{SW}}, m_{\mathrm{SW}}} I_{i_{\mathrm{SW}}, j_{\mathrm{SW}}} - \frac{1}{n_{pk} m_{pk}} \sum_{i_{pk}=1, j_{pk}=1}^{n_{pk}, m_{pk}} I_{i_{pk}, j_{pk}}. \tag{2}$$

The upper picture of the inset of Fig. 1 shows the total region of the signal window of the DOE sensor. Respecting the signal window (SW) the total numbers of sensor pixels in Eq. (2) are denoted by n_{SW} and m_{SW} in the perpendicular direction. Although the 16 different diffractive lenses are integrated by utilizing the superposition principle in the DOE aperture, the noncoherent response (pixel areas outside of the coherent peaks) for each pixel with complex wavefront amplitude $A_{i,j}$ now satisfies the relation $I_{\mathrm{NC}} = \sum |A_{i,j}|^2$, which relates to the gloss of the surface. Typically the gloss is a function of (1) reflectance (related to complex refractive index or complex permittivity), (2) angle of light incidence in the specular case, and (3) surface texture. If the angle of light incidence and the texture of a surface are assumed to be constant, it is possible to sense the possible permittivity change when the surface is located in water or in an electrolyte solution. In the case of a DOE sensor, the gloss (G) and optical roughness (R_{opt}) are measured simultaneously from the same surface area by using the respective noncoherent and coherent response of DOE.

D. DOE Sensing of Proteins Adsorption on Treated Titanium Surfaces

First, DOE sensor images were made from surfaces immersed in triply distilled water for 100 s; the images serve as a reference signal for each of the studied materials. Second, the water was removed from the cuvette and either the background electrolyte or the protein solution was injected into the cuvette, followed by recording of the DOE images during a 600 s period. The diameter of the laser beam waist on the all surfaces was 1 mm. Thereafter, we compared the optical roughness R_{opt} values, which were measured by the DOE sensor as a function of time from the interface of the treated titanium surface and the electrolyte in the absence or presence of protein molecules. The threshold of optical roughness of the treated titanium surface was canceled out by measuring the baseline of R_{opt} in distilled water, whose refractive index ($n = 1.333$) was close to that of the background electrolyte ($n = 1.342$.

E. VASE Sensing of Protein Adsorption on Treated Titanium Surfaces

To compare a dynamic measurement (time dependent) of the adsorption process of model proteins on the studied material surfaces sensed by the DOE, VASE was used to corroborate the thicknesses of the adsorbed protein layers on the studied surfaces after the protein-modified surfaces were removed from the protein solution and air dried for a half-hour.

The complex refractive index values $N_{n\kappa} = n + i\kappa$ are functions of wavelength λ and they were utilized in the calculation of the effective dielectric constant $\varepsilon = \varepsilon' + i\varepsilon'' = N_{n\kappa}^2$, where $\varepsilon' = n^2 - \kappa^2$ and $\varepsilon'' = 2n\kappa$. The harmful effects caused by the possible appearance of surface roughness [38,39] were avoided by performing the ellipsometric measurements at an incidence angle of 75° for the probe beam with a Woollam variable angle spectro-ellipsometer (W-VASE). The W-VASE was operated in the wavelength range from 200 to 1700 nm. The complex permittivity values of all studied surfaces were calculated from the complex refractive index data, which were obtained by the spectro-ellipsometer.

3. Results and Discussion

A. Optical Sensing of Adsorbed Model Proteins on Treated Titanium Surfaces

We chose two model plasma proteins with significant differences in their size and shape (HPF is a rodlike protein having a mass of 340 kDa, compared to a globular HSA with a mass of 66 kDa). The aim is to distinguish their adsorption behavior on mechanically polished titanium surfaces with the aid of a DOE (dynamic measurement of the adsorption process of protein on surfaces in an electrolyte solution—wet measurement) and ellipsometry (measurement of the thickness of the adsorbed protein layer on a protein-modified surface after it is removed from a protein solution air dried for a half-hour).

First, we measured the dynamics of the gloss (G) and optical roughness (R_{opt}) of the mechanically polished titanium surface [Fig. 2(a)] in the presence of either 500 nM HPF or 500 nM HSA solutions using the DOE sensor within a 10 min period [Figs. 2(b)–2(e)]. Before measurement of both the G and R_{opt} parameters of the mechanically polished Ti surface in the presence of proteins, the reference measurements of this surface in water and background electrolyte were made. From Fig. 2, it can be seen that the ions of the background electrolyte (we can assume chemical interaction between the ions of the background electrolyte and the polished Ti surface) affected the permittivity of the mechanically polished Ti surface (difference of the G parameter for polished Ti in electrolyte compared to water), but did not change the surface texture of the polished Ti (the R_{opt} of polished Ti is practically identical for both water and electrolyte). A similar dependence for G and R_{opt} parameters after replacing the water with the background electrolyte was also observed for the nanostructured $Ti_{0.82}C_{0.12}$ surface Fig. 3. After addition of both the HPF and HSA molecules (500 nM), we can recognize the increase of the optical roughness (R_{opt}) of the polished Ti surface, which indicates protein adsorption. The optical roughness of adsorbed fibrinogen adlayer was about 5.1 nm, which is about 4 times higher than that of the adsorbed adlayer of albumin, which was 1.3 nm thick [Figs. 2(c) and 2(e)]. The DOE results may indicate that fibrinogen at a 500 nM concentration initially adsorbs rapidly with its long axis parallel to the polished Ti surface. This orientation is usually energetically favorable because of the possibility that the protein will form additional bonds to the surface. From the DOE results, we can assume either that the albumin is weakly adsorbed on a polished Ti surface in comparison with fibrinogen, or that the albumin adlayer is less packaged (more porous) due to the spherical shapes of albumin molecules. The presence of both HPF and HSA molecules also caused higher changes in the permittivity (displayed by means of higher dynamics of the G parameter) of the polished Ti surface compared with those observed for polished Ti surface in contact with either the water or the background electrolyte, which also indicates protein adsorption [Figs. 2(b) and 2(d)]. The presence of lower (500 nM) and higher (4 μM) HPF solutions also caused changes of both the G and R_{opt} parameters of the nanostructured $Ti_{0.82}C_{0.12}$ surface [Figs. 3(b) and 3(c)]. Nevertheless, the average optical roughness of $Ti_{0.82}C_{0.12}$ surface is about 55 nm, which is much higher than the increase of roughness of the protein-modified $Ti_{0.82}C_{0.12}$ [Fig. 3(c)] and implies only weak HPF adsorption on $Ti_{0.82}C_{0.12}$. Also, the relative changes in permittivity of the $Ti_{0.82}C_{0.12}$ surface after addition of protein molecules are very close to those observed in the presence of the background electrolyte [Fig. 3(b)]. This can suggest that chemical interaction between the ions of the electrolyte and the $Ti_{0.82}C_{0.12}$ surface have a much higher effect on the permittivity change of the $Ti_{0.82}C_{0.12}$ interface than the presence of 500 nM HPF molecules in the solution, which are only weakly adsorbed on the nanostructured $Ti_{0.82}C_{0.12}$ surface. Here we point out that the extension coefficients of the solutions (water, electrolyte without and with HPF molecules) are negligible even in the ultraviolet wavelength range, as shown in Fig. 4, being $\kappa = 1.55 \times 10^{-8}$, 4.87×10^{-8}, and 1.30×10^{-8} for water and for electrolyte without and with HPF molecules measured at a photon energy of 1.959 eV (632 .8 nm) of the DOE probe laser beam.

Second, we analyzed with the aid of VASE measurement the effective thickness [the effective thickness was calculated from the spectral complex refractive index ($N_{n\kappa}$) by utilizing the Beer–Lambert law [$I_E(n,\kappa) = I_{E0}\exp(-4\pi\kappa z/\lambda)$] of both the HPF and HSA adlayers adsorbed on a polished Ti surface that was removed from a protein solution and followed by a half-hour drying process (Fig. 5). The effective thickness of the HPF and HSA adlayers at the DOE probe wavelength of 632.8 nm were 1.1 and 0.4 nm, respectively. Both methods thus confirmed that fibrinogen forms a thicker and more packed surface adlayer compared to a more porous and weakly adsorbed albumin adlayer on a mechanically polished Ti surface.

B. Effect of Aging of TDHC Samples on Adsorption Behavior of Fibrinogen

On the basis of our recently published DOE and ellipsometry measurements, we found significant

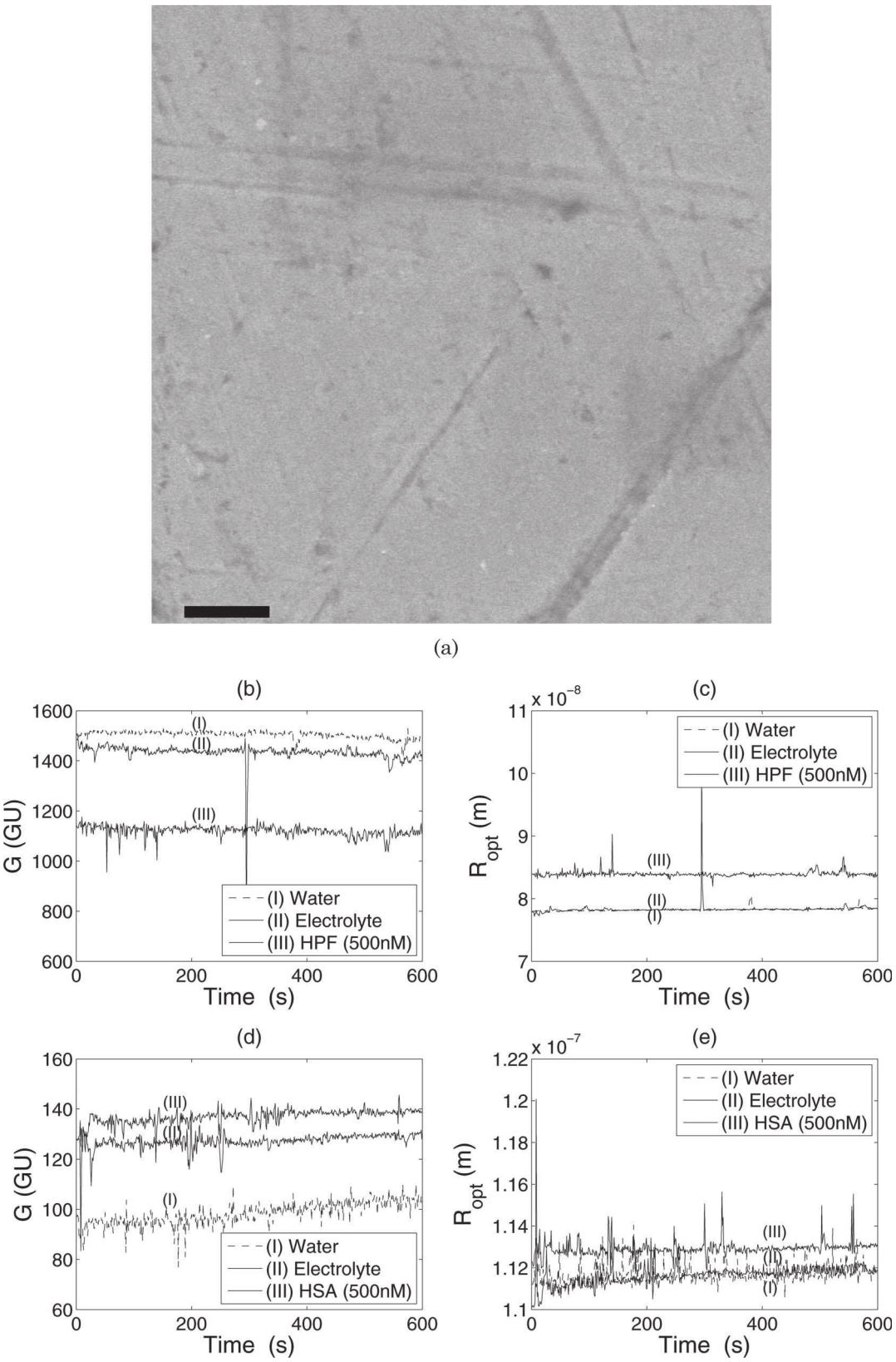

Fig. 2. (a) SEM image from a mechanically polished titanium surface. The length of the scale bar is 1 μm. Temporal gloss (G) in GU and optical roughness (R_{opt}) in meters of a mechanically polished titanium surface, when the surface, immediately after polishing, is in water, in electrolyte, and in electrolyte with HPF or HSA molecules with concentration of 500 nM. Gloss of (b) HPF and (d) HSA, optical roughness of (c) HPF and (e) HSA.

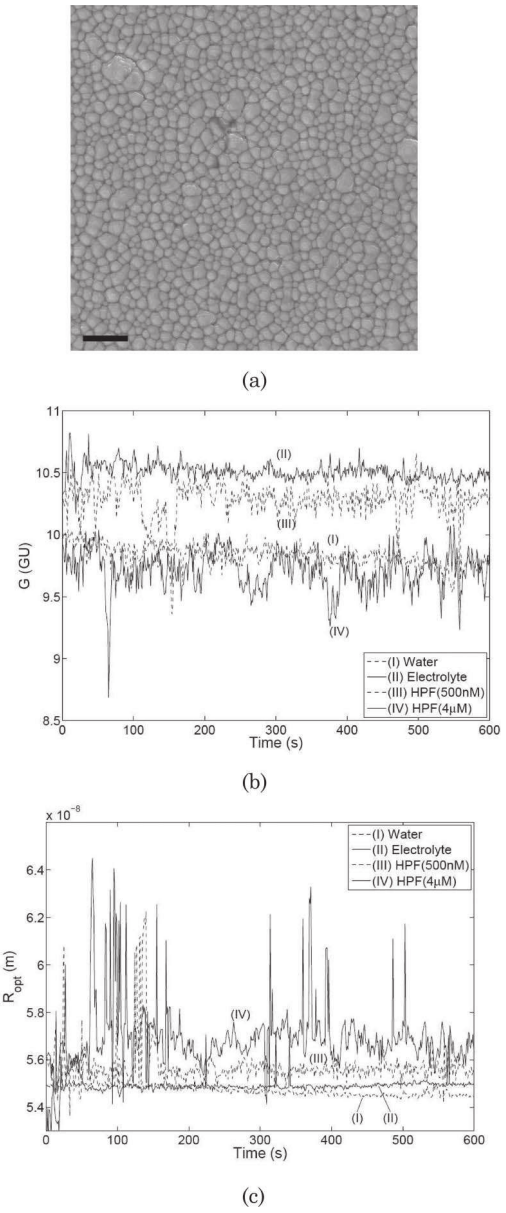

Fig. 3. (a) SEM image from a nanostructured $Ti_{0.82}C_{0.12}$ surface. The length of the scale bar is 1 μm. (b) Temporal gloss (G) in GU from a carbon treated titanium surface ($Ti_{0.82}C_{0.12}$), when the surface is in water, in electrolyte, in electrolyte with HPF (500 nM) and in electrolyte with HPF (4 μM). (c) Temporal optical roughness (R_{opt}) in meters from the same $Ti_{0.82}C_{0.12}$ surface. Note that the average optical roughness of the nanostructured surface is 55 nm.

correlation between the complex dielectric constant of dry TDHC surfaces and the ability for HPF adsorption on these treated surfaces. The adsorption of fibrinogen molecules relates to a slope of dielectric loss and permittivity ($\partial\varepsilon''/\partial\varepsilon'$) as follows: $\varepsilon'' = a\varepsilon' + b$, where $a = 1.634$ and $b = -5.877$ [26,27]. We observed that the very good adsorption of HPF can be achieved on TDHC samples having 34% and 9% Ti content (these surfaces have, in a ε'–ε'' plane, a small distance deviation from the line $\varepsilon'' = 1.634\varepsilon' - 5.877$, $\varepsilon' = -5.877$, as shown in Fig. 6) in comparison with a poor HPF adsorption on surfaces either rich in

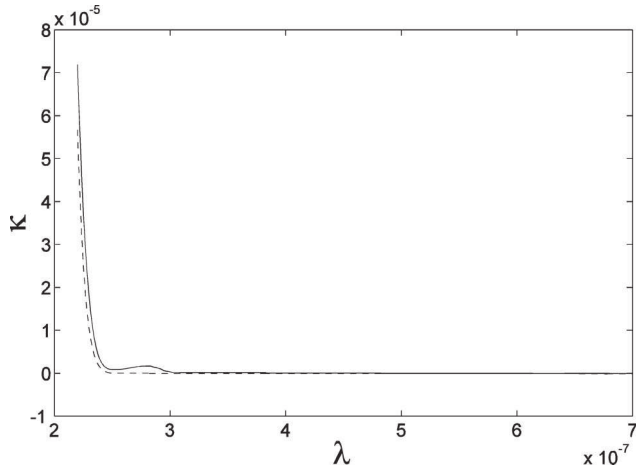

Fig. 4. Extinction coefficient of the electrolyte without (dashed curve) and with HPF molecules (5 μM) (solid curve), whereas the extinction coefficient of water meets the wavelength axis in the ultraviolet range. The numbers shown on the λ axis are in meters.

titanium (Ti content higher than 50%) or only on pure DLC coatings (the distances of these surfaces from the line in the ε'–ε'' plane are at the least 1 order higher, as shown in Fig. 6). From tribological testing it has been observed that nanostructured TDHC surfaces (Ti content is lower than 15%) have moderate hardness and minimal values of the friction coefficient and the wear rate [28,29]. Because of these mechanical parameters, it seems that these nanostructured TDHC materials could be, in the near future, used as an appropriate material for dental implant production. Therefore, we start to study how the aging process of TDHC surfaces influences the fibrinogen adsorption.

In Fig. 6 are shown the effective dielectric constants (dielectric permittivity) from five studied

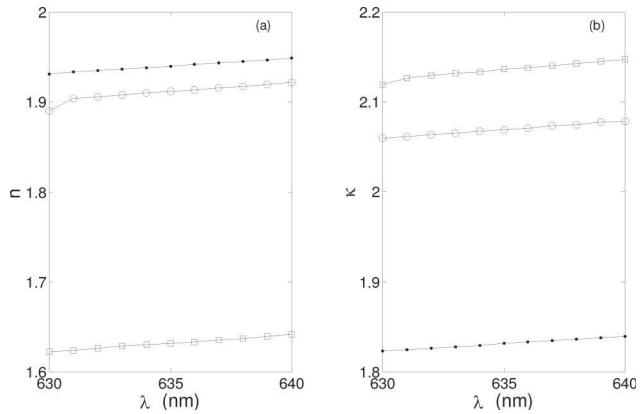

Fig. 5. Spectral complex refractive index ($N_{n\kappa}$) of mechanically polished titanium surfaces modified by HPF (squares) and HSA (circles). Ellipsometric measurements were performed in air after a half-hour of drying to remove the protein-modified surface from the protein solution (500 nM concentration), where the spontaneous adsorptions during 15 min proceed. Dotted curves represents the response from the titanium surface in the presence of only background electrolyte. (a) Real part and (b) imaginary part of $N_{n\kappa}$ for the respective interface layers.

surfaces measured at photon energy $E\lambda = 1.959$ eV. The first value represents the averaged dielectric constant from the equal numbered sets of mechanically polished and polished + heat-treated (170 ° C/30 min) Ti surfaces, which act as the comparison (Ti_{comp}) surface. The standard deviation of the averaged permittivity $\varepsilon = -1.83(\pm 0.65) - 9.16i(\pm 1.74i)$ is quite wide from sample to sample due to different mechanical polishing procedures (remains and defects of surface texture and roughness). The three TDHC samples and the DLC sample were produced by the PECVD method, controlling the severity of chemical vapor deposition in plasma enhancement to satisfy the carbon concentrations. The samples are denoted as follows: $Ti_{0.82}C_{0.18}$, $Ti_{0.38}C_{0.62}$, $Ti_{0.09}C_{0.91}$ and DLC ($Ti_{0.00}C_{1.00}$). For clarity, in the Fig. 6 we indicate the standard deviations in permittivity ε' and dielectric loss ε'' by the horizontal and vertical lines only for the case of Ti_{comp} reference measurements (the standard deviations in permittivity and dielectric loss for other surfaces are plotted in Table 1). Figure 6 and Table 1 show a consecutive increase in permittivity ε' and dielectric loss ε'' values, as well as in water contact angles for all long-term stored TDHC surfaces, except for the $Ti_{0.09}C_{0.91}$ surface. This behavior might arise from the consecutive adsorption of carbon oxides from air on the surface of long-term stored material. Similar results have been recently published for patterned metal surfaces that were stored about 51 days in air using the water contact angle measurement and x-ray photoelectron spectroscopy [40].

The R_{opt} values of freshly prepared, differently treated Ti surfaces in the presence of 500 nM HPF showed that a significant adsorption of fibrinogen was detected with Ti_{comp}, $Ti_{0.38}C_{0.62}$, and $Ti_{0.09}C_{0.91}$, in contrast to a weak adsorption detected on $Ti_{0.82}C_{0.18}$ and DLC (white bars in Fig. 7). From Fig. 7 it can be also seen that the $Ti_{0.82}C_{0.18}$ and DLC surfaces show negative R_{opt} values, which means that the surface has become smoother during contact with the background electrolyte in the absence and/or in the presence of HPF. Both the $Ti_{0.82}C_{0.18}$ and DLC materials contained, on the top of their surfaces, different nanometer-scale carbide agglomerates, the growth of

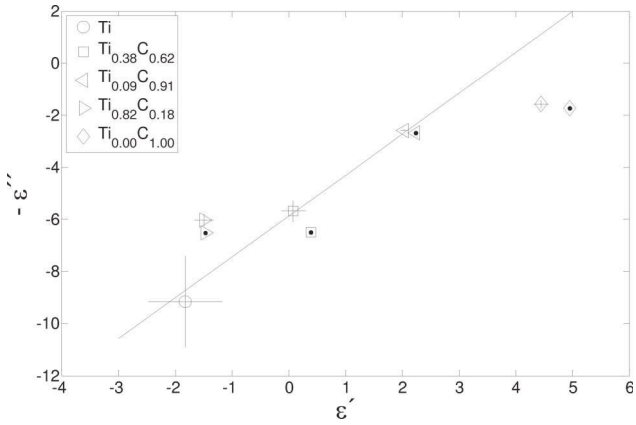

Fig. 6. Complex effective dielectric constants (dielectric permittivity) for the Ti_{comp} surface and four carbon treated titanium surfaces at $E_\lambda = 1.959$ eV. The markers without (reference surfaces) and with dots denote the two-year time frame between the measurements. For clarity, the standard deviations in permittivity ε' and dielectric loss ε'' directions are indicated by horizontal and vertical lines on each dielectric constant marker without a dot. Parameters for the line are as follows: $\varepsilon'' = a\varepsilon' + b$, where $a = 1.634$ and $b = -5.877$.

which is probably surface-energy-driven [41]. We can speculate that (i) a chemical interaction between ions of the electrolyte and surface can change the distribution and dimension of these nanometer carbide agglomerates, which is reflected by lowering of R_{opt} values in comparison with those measured in water as a reference for each of the studied materials or (ii) a part of fibrinogen molecules can be repeatedly desorbed from weakly adsorbed, rather porous fibrinogen adlayers that formed on these surfaces. Preliminary results of Fig. 7 show also that adsorption of carbon oxides from air on long-term stored surfaces can affect the surface textures and values of R_{opt} of these surfaces during repetitive measurements in the presence of background electrolyte without or with added protein molecules.

When compared the R_{opt} data measured after long-term storage of the surfaces to the R_{opt} data measured from the freshly prepared (reference) surfaces, HPF is still adsorbed on both the $Ti_{0.38}C_{0.62}$ and $Ti_{0.09}C_{0.91}$ surfaces, but with smaller magnitude, as shown by the gray bars in Fig. 7. A water contact

Table 1. Complex Effective Dielectric Constants (Dielectric Permittivity) $\varepsilon = \varepsilon' + i\varepsilon''$ at $E\lambda = 1.959$ eV and Water Contact Angles (θ in Degrees) with Standard Deviations for the Five Studied Surfaces[a]

Treatment of Samples	ε_{2007}	ε_{2009}	ε_{2007}	ε_{2009}
Ti_{comp}	—	—	—	—
PECVD $Ti_{0.82}C_{0.18}$	$-1.49 - 6.02i$	$-1.47 - 6.50i$	81.1 ± 2.6	86.7 ± 6.5
PECVD $Ti_{0.38}C_{0.62}$	$0.08 - 5.68i$	$0.39 - 6.49i$	77.9 ± 3.1	85.7 ± 2.7
PECVD $Ti_{0.09}C_{0.91}$	$2.03 - 2.58i$	$2.23 - 2.68i$	75.0 ± 0.4	78.9 ± 6.5
DLC $Ti_{0.00}C_{1.00}$	$4.45 - 1.57i$	$4.95 - 1.72i$	70.7 ± 2.0	79.9 ± 2.9

[a]The subscripts 2007 and 2009 denote the two-year time frame between the measurements. The dielectric losses ε'' of samples (with magnitude of standard deviations shown in Fig. 6) are listed according to severity.

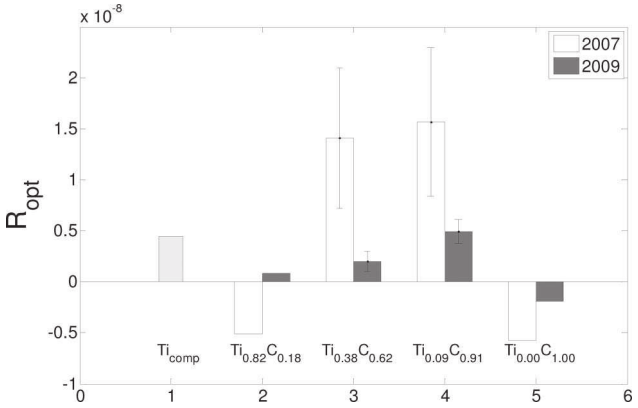

Fig. 7. Optical roughness (R_{opt}) in meters of the Ti_{comp} and four carbon treated titanium surfaces, when R_{opt} of the surface immersed in background electrolyte in the absence of HPF molecules is subtracted from R_{opt} of the same surface immersed in background electrolyte in the presence of HPF molecules. The bar legends 2007 and 2009 denote the two-year time frame between the measurements. The vertical lines denote standard deviations on the bars, where adsorption of HPF molecules on the surface is significant.

angle measurement revealed that aged TDHC surfaces are characterized by higher water contact angles (about 8%) than those of the freshly prepared TDHC surface, as shown in Table 1, which suggests that air aging of TDHC materials produces a slightly hydrophobic surface. It is well known that fibrinogen exhibits a less organized secondary structure upon adsorption onto a hydrophobic surface than onto a hydrophilic one. Computation of surface energy density (γ) from water contact angles showed that the TDHC surfaces have a smaller surface energy density than the surfaces of other carbon/graphite materials [42,43], which can be connected with the occurrence of nanometer carbide agglomerates that decrease the effective contact area of a water droplet with the TDHC surface and increase the effective area of the gas–water interface under the droplet. In addition, the increase of the hydrophobic character of aged TDHC surfaces may be contributed to by the appearance of gaseous nanobubbles [44].

The effective thickness of the HPF molecule layers on the $Ti_{0.82}C_{0.18}$, $Ti_{0.38}C_{0.62}$, $Ti_{0.09}C_{0.91}$, and DLC surfaces after the long-term storage were 0.47, 0.51, 1.59, and 0.13 nm, which were calculated from the $N_{n\kappa}$ data of the VASE measurements in air utilizing the Beer–Lambert law at the DOE probe wavelength of 632.8 nm. These effective thicknesses estimated for adsorbed HPF adlayers from the VASE measurements are in accordance with the respective R_{opt} values of the HPF layers sensed by the DOE sensor (see the gray bars in Fig. 7).

4. Conclusion

In this paper, it is shown that a DOE-based sensor and a VASE can serve as efficient tools for monitoring the adsorption processes of proteins that differ in size and shape on differently treated titanium surfaces. On the basis of a permittivity change and fluctuation of an optical roughness of differently treated titanium surfaces, we were able to distinguish between adsorption behavior of a rodlike protein represented by HPF and globular HSA. Both methods confirmed that fibrinogen forms a thicker and more packed surface adlayer compared to a more porous and weakly adsorbed albumin adlayer. In addition, we found a significant correlation between the complex dielectric constant of dry TDHC surfaces and the ability of fibrinogen adsorption on these surfaces, supposing a linear relation of the permittivity ε' and dielectric loss ε'' of the surfaces studied. The fibrinogen adsorbs well on the following surfaces: mechanically polished titanium and TDHC samples having 34% and 9% Ti content. Poor fibrinogen adsorption was observed either on hydrocarbons rich in Ti content (higher than 50%) or on pure DLC coatings. After two years of storage, favorable fibrinogen adsorption was still detected on a TDHC surface having 9% Ti. The hydrocarbons with low Ti content have moderate hardness and a minimal wear rate, which increases the focus of these materials for a new dental implant production.

This work was supported by the Ministry of Education and Sport of the Czech Republic (1M0528), the Academy of Sciences of the Czech Republic (KAN200040651), the Grant Agency of the Czech Republic (202/08/1688 and 205/10/2378), the Ministry of Education, Youth and Sports of the Czech Republic (LC06035), institutional research plans (Ministry of Education, Youth and Sports of the Czech Republic AVOZ50040507, AVOZ50040702), and the Academy of Finland (131539/31.03.2009).

References

1. B. Walivaara, B. O. Aronsson, M. Rodahl, J. Lausmaa, and P. Tengvall, "Titanum with different oxides—in-vitro studies of protein adsorption and contact activation," Biomaterials **15**, 827–834 (1994).
2. V. Ball, A. Bentaleb, J. Hemmerle, J.-C. Voegel, and P. Schaaf, "Dynamic aspects of protein adsorption onto titanium surfaces: mechanism of desorption into buffer and release in the presence of proteins in the bulk," Langmuir **12**, 1614–1621 (1996).
3. M. I. Jones, I. R. McColl, D. M. Grant, K. G. Parker, and T. L. Parker, "Protein adsorption and platelet attachment and activation, on TiN, TiC, and DLC coatings on titanium for cardio vascular applications," J. Biomed. Mater. Res. **52**, 413–421 (2000).
4. Y. Yang, R. Cavin, and J. L. Ong, "Protein adsorption on titanium surfaces and their effect on osteoblast attachment," J. Biomed. Mater. Res. A. **67**, 344–349 (2003).
5. N. Juany, P. Yang, Y. X. Leng, J. Y. Chen, H. Sun, J. Wang, G. J. Wang, P. D. Ding, T. F. Xi, and Y. Leng, "Hemocompatibility of titanium oxide films," Biomaterials **24**, 2177–2187 (2003).
6. F. Hook, J. Voros, M. Rodahl, R. Kurrat, P. Boni, J. J. Ramsden, M. Textor, N. D. Spenser, P. Tengvall, J. Gold, and B. Kasemo, "A comparative study of protein adsorption on titanium oxide surfaces using in situ ellipsometry, optical waveguide lightmode spectroscopy, and quartz crystal microbalance/dissipation," Colloids Surf. B **24**, 155–170 (2002).

7. K. Imamura, M. Shimomura, S. Nagai, M. Akamatsu, and K. Nakanishi, "Adsorption characteristics of various proteins to a titanium surface," J. Biosci. Bioeng. **106**, 273–278 (2008).
8. D. L. Cochran, "A comparison of endosseous dental implant surfaces," J. Periodontol. Periodontics **70**, 1523–1539 (1999).
9. T. J. Webster, R. W. Siegel, and R. Bizios, "Osteoblast adhesion on nanophase ceramics," Biomater. **20**, 1221–1227 (1999).
10. P. M. Brett, J. Harle, V. Salih, R. Mihoc, I. Olsen, F. H. Jones, and M. Tonetti, "Roughness response genes in osteoblasts," Bone **35**, 124–133 (2004).
11. E. Jansoon and P. Tengvall, "Adsorption of albumin and IgG to porous and smooth titanium," Colloids Surf. B **35**, 45–51 (2004).
12. P. Cacciafesta, A. D. L. Humphris, K. D. Jandt, and M. J. Miles, "Human plasma fibrinogen adsorption on ultraflat titanium oxide surfaces studied with atomic force microscopy," Langmuir **16**, 8167–8175 (2000).
13. P. Cacciafesta, K. R. Hallam, A. C. Watkinson, G. C. Allen, M. J. Miles, and K. D. Jandt, "Visualisation of human plasma fibrinogen adsorbed on titanium implant surfaces with different roughness," Surf. Sci. **491**, 405–420 (2001).
14. H. Nygren, P. Tengvall, and I. Lundstrom, "The initial reactions of TiO_2 with blood," J. Biomed. Mater. Res. **34**, 487–492 (1997).
15. S. Kidoaki and T. Matsuda, "Adhesion forces of the blood plasma proteins on self- assembled monolayer surfaces of alkanethiolates with different functional groups measured by an atomic force microscope," Langmuir **15**, 7639–7646 (1999).
16. A. G. Hemmersam, M. Foss, J. Chevallier, and F. Besenbacher, "Adsorption of fibrinogen on tantalum oxide, titanium oxide and gold studied by the QCM-D technique," Colloids Surf. B **43**, 208–215 (2005).
17. M. Rouahi, E. Champion, O. Gallet, A. Jada, and K. Anselme, "Physico-chemical characteristics and protein adsorption potential of hydroxyapatite particles: influence on in vitro biocompatibility of ceramics after sintering," Colloids Surf. B **47**, 10–19 (2006).
18. I. van derKeere, R. Willaert, A. Hubin, and J. Vereecken, "Interaction of human plasma fibrinogen with commercially pure titanium as studied with atomic force microscope and x-ray photoelectron spectroscopy," Langmuir **24**, 1844–1852 (2008).
19. J. M. Garguilio, B. A. Daves, M. Buddie, F. A. M. Köck, and R. J. Nemanich, "Fibrinogen adsorption onto microwave plasma chemical vapor deposited diamond films," Diam. Relat. Mater. **13**, 595–599 (2004).
20. X. Wang, L. Yu, C. Li, F. Zhang, Z. Zheng, and X. Liu, "Competitive adsorption behaviour of human serum albumin and fibrinogen on titanium oxide films coated on LTI-carbon by IBED," Colloids Surf. B **30**, 111–121 (2003).
21. C. Galli, M. C. Coen, R. Hauert, V. L. Katanaev, M. P. Wymann, P. Gröning, and L. Schlapbach, "Protein adsorption on topographically nanostructured titanium," Surf. Sci. Lett. **474**, L180–L184 (2001).
22. W. J. Ma, A. J. Ruys, R. S. Mason, P. J. Martin, A. Bendavid, Z. Liu, M. Ionescu, and H. Zreiqat, "DLC coatings: effect of physical and chemical properties on biological response," Biomaterials **28**, 1620–1628 (2007).
23. K. Cai, J. Bossert, and K. D. Jandt, "Does the nanometer scale topography of titanium influence protein adsorption and cell proliferation?" Colloids Surf. B **49**, 136–144 (2006).
24. A. Choukourova, A. Grinevicha, D. Slavinska, H. Biedermana, N. Saitob, and O. Takaib, "Scanning probe microscopy for the analysis of composite Ti/hydrocarbon plasma polymer thin films," Surf. Sci. **602**, 1011–1019 (2008).
25. A. Grinevich, L. Bacakova, A. Choukourov, H. Boldyryeva, Y. Pihosh, D. Slavinska, L. Noskova, M. Skuciova, V. Lisa, and H. Biederman, "Nanocomposite Ti/hydrocarbon plasma polymer films from reactive magnetron sputtering as growth support for osteoblast-like and endothelial cells," J. Biomed. Mater. Res. A. **88**, 952–966 (2009).
26. R. Silvennoinen, V. Vetterl, S. Hasoň, M. Silvennoinen, K. Myller, J. Vanek, and L. Cvrček, "Sensing of parameters behind attachment of human plasma fibrinogens on carbon doped titanium sur1aces: an optical study," Proc. SPIE **7388**, 73881A (2009).
27. R. Silvennoinen, V. Vetterl, S. Hasoň, M. Silvennoinen, K. Myller, J. Vanek, and L. Cvrček, "Optical sensing of attached fibrinogen on carbon doped titanium surfaces," Adv. Opt. Technol.**2010**, 942349, doi:10.1155/2010/942349.
28. T. Vitu, T. Polcar, L. Cvrcek, R. Novak, J. Macak, J. Vyskocil, and A. Cavaleiro, "Structure and tribology of biocompatible Ti–C:H coatings," Surf. Coat. Technol. **202**, 5790–5793 (2008).
29. T. Polcara, T. Vitu, L. Cvrcekd, R. Novak, J. Vyskocild, and A. Cavaleirob, "Tribological behaviour of nanostructured Ti-C:H coatings for biomedical applications," Solid State Sci. **11**, 1757–1761 (2009).
30. J. Räsänen, M. Savolainen, R. Silvennoinen, and K. Peiponen, "Optical sensing of surface roughness and waviness by computer generated hologram," Opt. Eng. **34**, 2574–2580 (1995).
31. R. Silvennoinen, "Sensing of waviness of glossy and rough surface by DOE sensor," Proc. SPIE **7388**, 73880N (2009).
32. R. Silvennoinen, K-E. Peiponen, and K. Myller, *Specular Gloss* (Elsevier, 2008).
33. P. Beckmann and A. Spizzichino, *The Scattering of Electromagnetic Waves from Rough Surface* (Pergamon, 1963).
34. R. Silvennoinen, V. Vetterl, S. Hasoň, H. Tuononen, M. Silvennoinen, K. Myller, L. Cvrček, J. Vaněk, and P. Prachár, "Sensing of human plasma fibrinogen on polished, chemically etched and carbon treated titanium surfaces by diffractive optical element based sensor," Opt. Express **16**, 10130–10140 (2008).
35. S. Donati, "Coupling dynamics in lasers and applications in self-mixing interferometry," in *Summaries of the 2nd International Meeting on Optical Sensing and Artificial Vision* (Editorial Department of Saint Petersburg State University of Information Technologies, Mechanics and Optics, 2008), p. 67.
36. O. V. Angelsky, and P. P. Maksimyak, "Optical Diagnostics of random phase objects," Appl. Opt. **29**, 2894–2898 (1990).
37. O. V. Angelsky, A. P. Maksimyak, P. P. Maksimyak, and S. G. Hanson, "Optical correlation diagnostics of rough surfaces with large surface inhomogeneities," Opt. Express **14**, 7299–7311 (2006).
38. R. A. M. Azzam and N. M. Bashra, *Ellipsometry and Polarized Light* (North-Holland, 1977).
39. S-M. F. Nee and T-W. Nee, "Principal Mueller matrix of reflection and scattering measured for a one-dimensional rough surface," Opt. Eng. **41**, 994–1001 (2002).
40. A-M. Kietzig, S. G. Hatzikiriakos, and P. Englezos, "Patterned superhydrophobic metallic surfaces," Langmuir **25**, 4821–4827 (2009).
41. J.-M. Zhang, F. Ma, K.-W. Xu, and X.-T. Xin, "Anisotropy analysis of the surface energy of diamond cubic crystals," Surf. Interface Anal. **35**, 805–809 (2003).
42. S. Bar-Chaput and C. Carrot, "Interactions of active carbon with low- and high-molecular weight polyethylene glycol and polyethylene oxide," J. Appl. Polym. Sci. **100**, 3490–3497 (2006).
43. W. Brandl, G. Marginean, V. Chirila, and W. Warschewski, "Production and characterisation of vapour grown carbon fiber/polypropylene composites," Carbon **42**, 5–9 (2004).
44. X. H. Zhang, A. Quinn, and W. A. Ducker, "Nanobubbles at the interface between water and hydrophobic solid," Langmuir **24**, 4756–4764 (2008).

Tribology International 43 (2010) 1228–1233

Contents lists available at ScienceDirect

Tribology International

journal homepage: www.elsevier.com/locate/triboint

Effects of carbon content on the high temperature friction and wear of chromium carbonitride coatings

T. Polcar [a,*], T. Vitu [a], L. Cvrcek [a,b], J. Vyskocil [b], A. Cavaleiro [c]

[a] Department of Control Engineering, Faculty of Electrical Engineering, Czech Technical University in Prague, Technická 2, Prague 6, Czech Republic
[b] HVM Plasma Ltd., Na Hutmance 2, 158 00 Prague 5, Czech Republic
[c] SEG-CEMUC, Mechanical Engineering Department, University of Coimbra, 3030-788 Coimbra, Portugal

ARTICLE INFO

Article history:
Received 30 June 2009
Received in revised form
8 October 2009
Accepted 10 December 2009
Available online 23 December 2009

Keywords:
Chromium nitride
Carbonitride coatings
Tribology
Elevated temperature

ABSTRACT

Chromium nitride-based coatings are often used in application at high temperature. They possess high wear and oxidation resistance; however, the friction coefficient is typically very high. Therefore, we doped CrN coatings by carbon with the aim to improve tribological properties at elevated temperature, particularly to lower the friction. CrCN coatings were prepared by cathode arc evaporation technology using constant N_2 flow and variable C_2H_2 flow. The coatings with a thickness of 3–4 μm were deposited on hardened steel substrates and high-temperature resistant alloy. The carbon content varied from 0 at.% (i.e. CrN) up to 31 at.%. The standard coating characterization included the nano-hardness, adhesion, chemical composition and structure (including hot X-ray diffraction). Wear testing was done using a high temperature tribometer (pin-on-disc); the maximum testing temperature was 700 °C. The coatings with carbon content 12–31 at.% showed almost identical tribological behaviour up to 700 °C.

1. Introduction

Chromium nitride coatings have been extensively used as protective coating on various tools and dies due to high hardness and excellent wear, corrosion and oxidation resistance [1,2]. The oxidation resistance could be considered as the dominant factor for the successful application at elevated temperature conditions. The high oxidation limit of CrN coatings, typically about 700 °C [3], was attributed to the formation a protective Cr_2O_3 layer.

Ternary CrXN coatings were prepared with the goal to improve the oxidation resistance and the tribological properties at elevated temperature. Compared to other alloying elements, such as Al [4,5], Ti [6], or Si [7], Cr–C–N has been relatively less studied. Cekada et al. [8] analyzed Cr–C–N coatings deposited by evaporation. The films were subjected to oxidation tests showing the formation of a thin chromium oxide layer on the top followed by a nitrogen-rich layer demonstrating that nitrogen diffused towards the surface [8]. The microstructure and the thermal stability of arc-deposited CrCN system were complexly analyzed by Almer et al. [9]. The comparison of the tribological properties between CrN and CrCN coatings [10] showed the advantage of the latter; however, the difference in the friction coefficient and the wear rate was negligible. Tribological properties of gradient CrCN films measured by pin-on-disc films outperformed CrN coating [11]; CrCN showed promising protection to Ti6Al4V interfaces [12]. CrCN is a potential coatings for duplex treated steels [13] or as a supporting layer for carbon-based films [14]. In our previous study [15], CrCN coatings were tribologically tested *in situ* up to 500 °C showing that the wear rate was almost independent of the temperature and lower than that of CrN coatings deposited and tested under similar conditions [16].

The aim of this work was to determine whether changes in the carbon content of CrN-based coatings would result in improved friction and wear behaviour at temperatures up to 700 °C.

2. Experimental details

CrCN coatings were deposited onto steel substrates (WNr. 1.2379-DIN X153CrMoV12) and high-temperature resistant Fecralloy™ substrates (in wt.%: Fe 72.8, Cr 22, Al 5, Y 0.1, Zr 0.1—Goodfellow, Ermine Business Park, England) by cathodic arc evaporation from two rectangular cathodes using the commercial Hauzer's HTC-35 plant with two cathodes. The arc parameters were kept constant for all depositions: the current 80 A, the substrate bias −70 V and the coating temperature 350 °C. The chromium was evaporated from a Cr target (99.8% purity) in N_2 (99.999% purity) and C_2H_2 (99.6% purity) atmospheres. For binary CrN coating a reactive gas partial pressure of 0.17 Pa was set up at a constant value of 100 sccm, while for CrCN films the flow of acetylene was increased up to 48 sccm.

* Corresponding author.
E-mail address: polcar@fel.cvut.cz (T. Polcar).

0301-679X/$ - see front matter © 2009 Elsevier Ltd. All rights reserved.
doi:10.1016/j.triboint.2009.12.010

High temperature X-ray diffraction (HTXRD) measurements were done using a Philips X' Pert diffractometer with cobalt radiation (K_α=0.178897 nm) in the Bragg–Brentano geometry. The samples (12 mm × 10 mm, Fecralloy substrate) were fixed on a Pt plate and heated from RT up to 1000 °C in steps of 100 °C. The heating rate was 40 °C/min between each temperature step followed by maintenance of ~20 min for XRD acquisition in 35–60° range. The analyses were carried out in a vacuum chamber, coupled to the diffractometer and specially designed for *in situ* analysis. The experiments were performed under continuous gas (Ar – 5% H_2) flux at low pressure (1–10 Pa) after evacuating the chamber down to a value lower than 10^{-3} Pa.

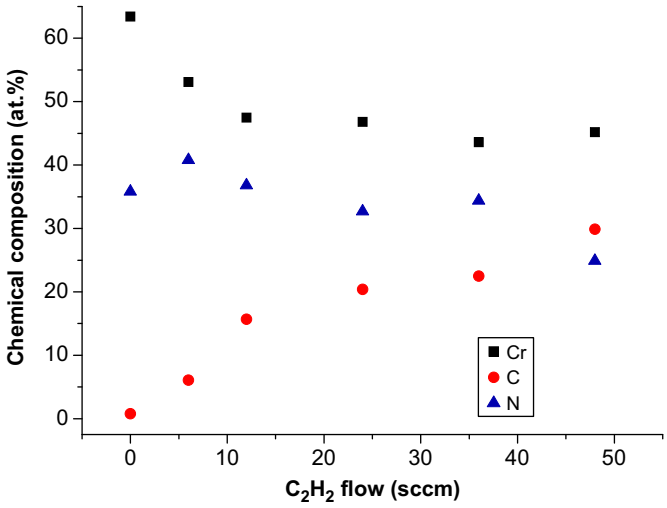

Fig. 1. Chemical composition of CrCN coatings.

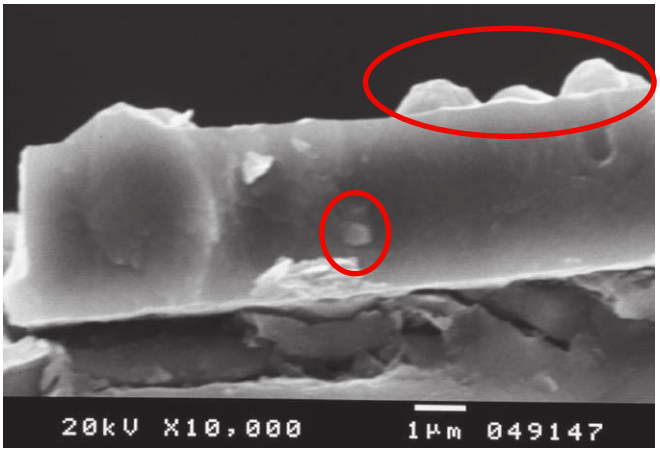

Fig. 2. SEM micrograph of the CrCN-06 coating cross-section. The Cr droplets are clearly visible (see highlighted parts).

A Cameca SX-50 Electron Probe Microanalysis (EPMA) apparatus was used to determine the chemical composition of the coatings. The hardness and Young's modulus of the coatings was evaluated by depth-sensing indentation technique using Picoindentor® HM500(Fischer Instruments). The indentation load was increased in 60 steps up to 50 mN and the same steps were used during unloading. The testing procedure includes the correction of the experimental results for geometrical defects in the tip of the indenter, thermal drift of the equipment, and uncertainty in the initial contact. The maximum indentation depth was 340 nm (about 10% of the coating thickness). Wear testing was done using a high temperature pin-on-disc tribometer (CSM Instruments, Switzerland). Based on our previous experience with tribological testing of CrN and CrCN coatings at elevated temperature [15,16], where the steel balls were not suitable for testing due to their high wear and transfer of ball material (mainly iron oxides) to the coating surface, only ceramic sliding partners were selected: Si_3N_4 and Al_2O_3 balls with a diameter of 6 mm. The applied load was 5 N, the sliding speed was 50 mm s^{-1}. The morphology of the coating surface, ball scars, wear tracks and wear debris were examined by scanning electron microscopy (SEM). The profiles of the wear tracks were measured with a mechanical profilometer (AlphaStep 500). The wear rates of the ball and coating were calculated as the worn material volume per sliding distance and normal load. The average value of three profiles measured in each wear track was used to calculate the coating wear rate. Every test was repeated three times; average value of the three test is presented as the friction coefficient or the wear rate.

To facilitate reading, the CrCN coatings will be denominated as CrCN-A, where A is the C_2H_2 flow in sccm.

3. Results and discussion

3.1. Synthesis of CrCN coatings and chemical composition

Chemical composition of the CrCN coatings is presented in Fig. 1. The CrN coating, i.e. film deposited without C_2H_2 reactive gas, showed a very high Cr/N ratio (about 1.8). Increasing flow of C_2H_2 led to an increase of carbon content mainly on expense of chromium, while the nitrogen content decreased only slowly. The C_2H_2 flow 48 sccm could be considered as a functional limit for our experimental setup, since further rise in C_2H_2 flow led to a disintegration of a cathodic spot. The SEM analysis of the coating surface and cross-section identified a large number of chromium droplets, see Fig. 2. The size and number of droplets was significantly lower when the coatings were prepared with higher C_2H_2 flows. It should be pointed out that the chemical composition was measured in the areas with no evident presence of Cr droplets. The coating thickness is shown in Table 1.

Table 1
Thickness, adhesion and mechanical properties of CrCN coatings.

C_2H_2 flow (sccm)	Thickness (µm)	Adhesion			Young's modulus (GPa)
		Scratch-test Lc2/Lc1 (N)	Rockwell —	Hardness (GPa)	
0	3.40	40/30	2	23.9 ± 1.2	292 ± 9
6	3.54	70/60	1	25.8 ± 2.3	297 ± 15
12	3.15	80/30	2	29.3 ± 1.1	331 ± 10
24	3.57	70/30	1	25.4 ± 1.8	305 ± 10
48	4.05	50/20	2	28.1 ± 1.3	305 ± 9

3.2. Coating structure

The XRD diffractograms of selected as-deposited CrCN coatings are shown in Fig. 3. The structure of the CrN coating was dominated by the hexagonal β-Cr_2N [ICDD 35-0803] with a mean crystallite size of 12 nm and a preferred (300) orientation. Besides nitride phase, also bcc α-Cr phase was detected in all coatings. This phase was attributed to Cr-rich droplets, typical phenomenon of Cr-based coatings deposited by arc evaporation [9]. Since the chemical composition was measured in the areas without Cr droplets, the coating was slightly over-stoichiometric considering Cr_2N phase, as referred to above. However, no vestiges of CrN phase were observed.

The addition of carbon to binary CrN films changed the as-deposited structure. The film produced with 48 sccm C_2H_2 flow showed, after deposition, a broad and low intensity XRD patterns with a mean feature size of only 4 nm. Taking into account the 2θ maximum peak position, the d values obtained after peak fitting matched quite well with the fcc-CrN [ICDD 76-2494] structure. Thus, the as-deposited structure of CrCN was dominated by a metastable cubic phase similar to that reported in Ref. [9] and denominated as δ-Cr(C,N) phase.

The thermal stability of the CrN and CrCN-48 coatings was described in detail in Ref. [17]; therefore, only summary will be presented here. The coatings were analyzed by XRD at elevated temperature *in situ* in protective atmosphere, which significantly minimized surface oxidation. The β-Cr_2N phase in CrN film was thermally stable up to 900 °C. Only narrowing of the peaks and the shift towards the equilibrium position with increasing temperature in comparison to the post-deposition state was observed. Up to 800 °C, no significant grain size increase was observed. Further rise in temperature led to changes in the preferential orientation (from (300) to (110) and peaks became narrower and more intense, which was attributed to recrystallization and grain growth process. Nevertheless, the grain size increased from 12 nm at room temperature to only 34 nm at 1000 °C.

During the thermal treatment of CrCN-48 film, the initial δ-Cr(C,N) phase remained unchanged up to 600 °C. At 700 °C, well-defined XRD peaks can be detected being the new phase indexed as an orthorhombic $Cr_3(C_{0.92}N_{0.08})_2$. The content of this phase increases with further annealing up to 900 °C, where the intensity of some $Cr_3(C_{0.92}N_{0.08})_2$ peaks increased while others strongly decreased. At this temperature, a new phase was formed: the orthorhombic Cr_3C_2.

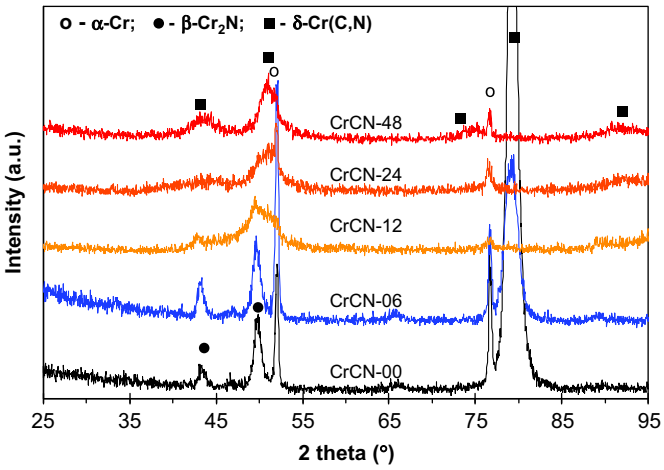

Fig. 3. XRD diffractograms of CrCN coatings.

Almost no structural changes were detected on the cubic α-Cr droplets. The crystallite size evaluated from the (110) peak showed no significant change with increasing temperature up to 1000 °C; only the lattice parameter steadily increased due to thermal expansion.

3.3. Mechanical properties and adhesion

The hardness of CrCN coatings varied from ~24 to ~29 GPa with no relation to coating carbon content. Therefore, a decrease of hardness with increased carbon content reported in Ref [18] was not observed in our study. On the other hand, one of the important factors influencing hardness was the presence of Cr droplets. As referred to above, the size and number of droplets changed significantly for different coatings and it is difficult to quantify droplets effect on composite coating hardness. Adhesion measured by scratch-tests was high enough for following tribology testing; Rockwell C indents showed a very good adhesion with grade 1 or 2. Mechanical properties and adhesion of the coatings are summarized in Table 1.

3.4. Tribology

The results of CrCN-00 (CrN) and CrCN-06 tribological tests showed unsatisfactory wear resistance. Both films were penetrated when tested with Si_3N_4 and Al_2O_3 balls at 500 °C. Moreover, the friction exhibited strong fluctuations compared to CrCN films with higher carbon content. This behaviour could be attributed to high number of Cr droplets. High wear rate of CrN films at 500 °C was observed as well in our previous studies [16,19]. Therefore, we will focus only on the tribological properties of CrCN coatings prepared with C_2H_2 flow of 12–48 sccm. Since there were only small differences in tribological properties among CrCN coatings with different carbon content, we will describe general evolution of friction and wear of all CrCN films (CrCN-12 to 48) as a function of temperature.

3.4.1. Friction and wear against Si_3N_4 balls

Typical friction curves at room temperature were characterized by gradual growth of friction coefficient during first 4000 cycles to a value of 0.6 (Fig. 4). With increasing carbon content a slightly higher mean value of friction coefficient was observed.

In general, the average friction increased with the temperature reaching maximum values for ~0.9 at 300 or 400 °C. Finally, the friction decreased in the temperature range 500–700 °C exhibiting significant fluctuations.

The ball wear rates were negligible at room temperature and remained very low up to 200 °C. Regardless on coating composition, the ball wear sharply increased at 300 °C reaching maximum at 400 °C. The ball wear scars examination showed very rough surface in this temperature range, particularly compared to smooth worn surface at room temperature. We suppose that the extensive damage of Si_3N_4 balls was caused by accelerated tribochemical reaction between the ball and coating, as described in our previous work [16]. The sudden decrease of ball wear at the highest temperatures was attributed to a formation of third-body consisting of small and fine wear debris particles, as confirmed by SEM observations of the wear debris adhered to ball surface. Therefore, the wear mechanism changed at approx. 400 °C from two-body to three-body wear resulting in significant decrease of coating and ball damage. The formation of tribolayer was probably enhanced by progressive oxidation; the presence of oxides in the contact reduced friction.

The coating wear track showed only superficial damage when tested at room temperature. The shallow scratches did not change

the wear track profile enough to measure wear rate by profilometer. The critical wear was observed at 400 °C, where the films were almost penetrated (Fig. 5). Further rise in testing temperature was followed by a strong decrease in coating wear due to formation of a thick third-body between surfaces in the contact (Fig. 6).

3.4.2. Friction and wear of CrCN coatings against Al_2O_3 balls

Tribological measurements with Al_2O_3 counterparts showed significantly different features. The ball wear scars were completely covered by adhered wear debris forming a thick layer; therefore, a third-body wear occurred when CrCN coatings were sliding against Al_2O_3 balls. Typical friction curves were

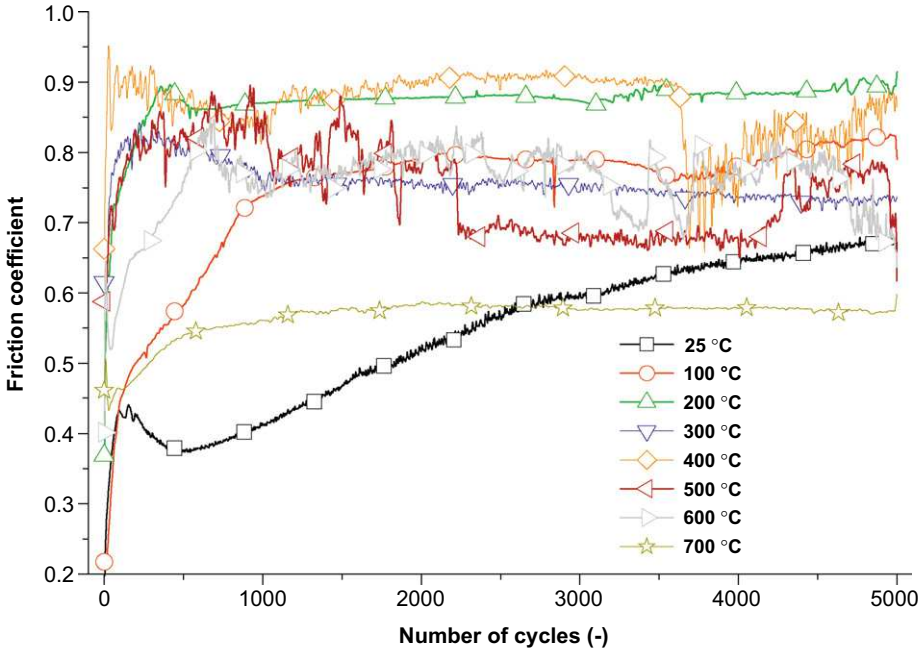

Fig. 4. Friction curves of CrCN-24 coating, tests with Si_3N_4 balls at different temperatures.

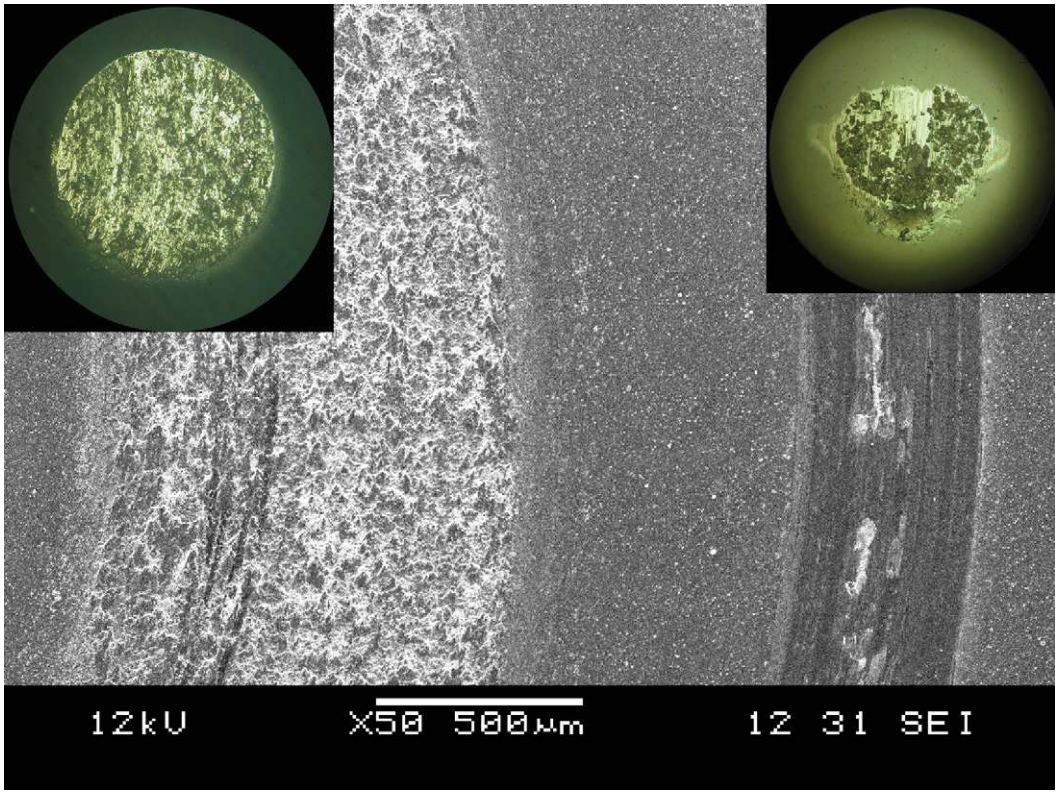

Fig. 5. SEM micrograph of the wear tracks produced by sliding with Si_3N_4 (left) and Al_2O_3 (right) ball; coating CrCN-12, testing temperature 400 °C. The insets show optical photographs of the corresponding ball wear scars. Note that insets are in a different scale.

characterized by short running-in period and consequent stabilization of friction coefficient at steady state value, as shown in Fig. 7. The friction curves at room temperature were very smooth with mean friction values about 0.4, then increased to reach maximum 0.6–0.7 at 400 °C and again decreased to 0.3–0.4 at the highest temperature (700 °C). Compared to Si_3N_4 balls, the Al_2O_3 counterparts showed significantly lower wear. Consequently, the wear track width was lower and the contact pressure during the tests was higher.

The evolution of coating wear rate with temperature is shown in Fig. 6. The maximum coating wear was observed in temperature region 300–500 °C; the wear track depth reached in some place even Cr interlayer. However, at 700 °C, only polishing of the initial ball and coating surfaces was observed with negligible volumes of worn material.

3.4.3. *Running-in characteristics of CrCN coatings and dominant wear mechanisms*

As referred to above, the friction curves exhibited distinctive running-in period. We observed that the friction stabilization was strongly temperature dependent. The running-in at lower temperatures (up to 200 °C) was characterized by gradual growth of friction coefficient reaching the maximum value representing the steady state wear regime. On the other hand, higher temperatures (300–500 °C) exhibited either hardly distinguishable running-in period or progressively decreasing friction coefficient before steady state was reached. At highest temperatures (600–700 °C), the friction during running-in was again lower than that of steady state. This feature was more evident for sliding with Al_2O_3 balls, see Fig. 8.

The analysis of ball wear scars and wear tracks indicated general aspects of the wear process. The main wear mechanisms

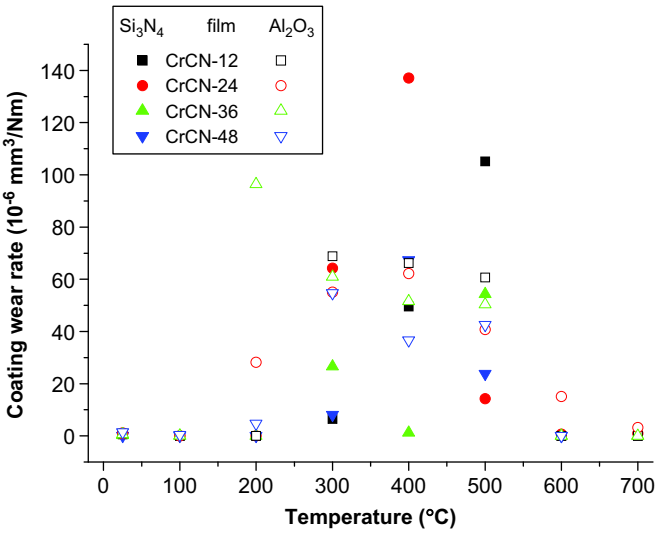

Fig. 6. CrCN coating wear rates as a function of temperature.

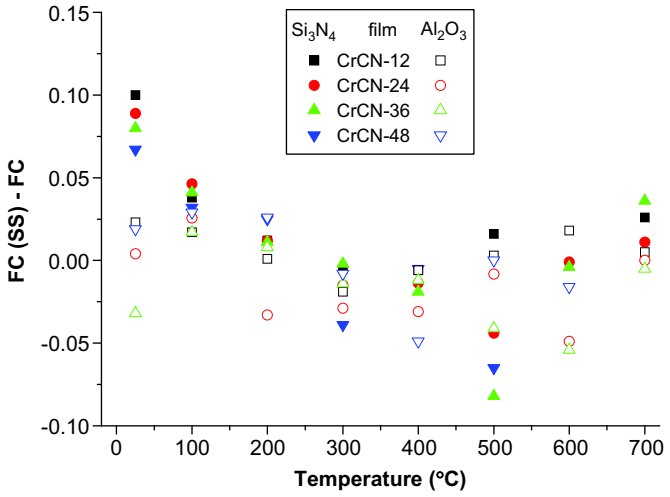

Fig. 8. Difference between friction at steady state regime (FC(SS)) and mean friction calculated from entire test (FC).

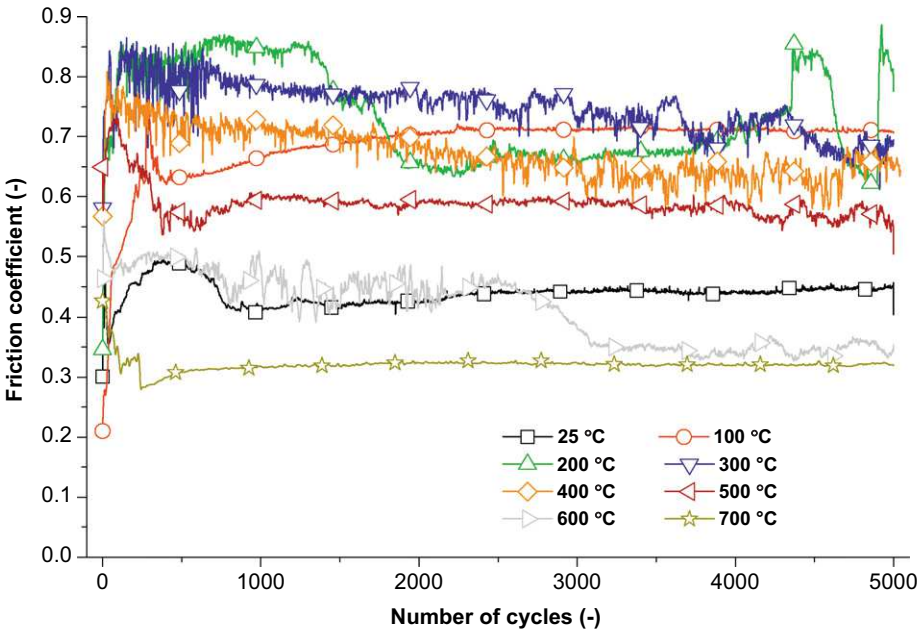

Fig. 7. Typical friction curves of CrCN-24 coating, Al_2O_3 ball as counterpart.

of CrCN coatings when sliding with Si_3N_4 balls at elevated temperatures could be described as follows: (i) 25 to 200 °C —two-body wear; abrasive wear; (ii) 300–400 °C —two-body wear; combination of abrasive and tribochemical wear; (iii) 500–700 °C —three–body wear, mild wear. Similar description could be applied to sliding with Al_2O_3 balls: 25 to 200 °C —three-body wear; abrasive wear; (ii) 300–400 °C —three-body wear; abrasive wear; (iii) 500–700 °C —three-body wear, mild wear. The oxidation tests of CrCN coatings and analysis of wear debris particles, which are now in progress, will shed more light on the tribological characteristics of CrCN coatings.

4. Conclusions

Arc-deposition technique was used to deposit CrN and CrCN coatings with carbon content from 0 to 31 at.%. CrN film showed mixture of β-Cr_2N phase and α-Cr; the latter indicated presence of chromium droplets, which was confirmed by SEM. Increase of carbon content led to formation of metastable δ-Cr(C,N) phase. Tribological properties of tested coatings with carbon content 12–31 at.% were remarkably similar. The critical testing temperature was 400 °C with the highest wear rates of both balls and coatings observed. Further increase in temperature resulted in improved wear resistance, which was attributed to change in dominant wear mechanism.

Acknowledgements

This work was supported by the GAAV through the project KJB201240701 and by the Ministry of Education of the Czech Republic (project MSM 6840770038).

References

[1] Dearnley PA. Low friction surfaces for plastic injection moulding dies — an experimental case study. Wear 1999;225–229:1109.
[2] Dong H, Sun Y, Bell T. Enhanced corrosion resistance of duplex coatings. Surf. Coat. Technol. 1997;90:91.
[3] Mayrhofer H, Willmann H, Mitterer C. Oxidation kinetics of sputtered Cr–N hard coatings. Surf. Coat. Technol. 2001;146–147:222.
[4] Vetter J, Lugscheider E, Guerreiro SS. (Cr:Al)N coatings deposited by the cathodic vacuum arc evaporation. Surf. Coat. Technol. 1998;98:1233.
[5] Uchida M, Nihira N, Mitsuo A, Toyoda K, Kubota K, Aizawa T. Friction and wear properties of CrAlN and CrVN films deposited by cathodic arc ion plating method. Surf. Coat. Technol. 2004;177–178:627.
[6] Panjan P, Navinsek B, Cvelbar A, Zalar A, Vlcek J. High-temperature oxidation of TiN/CrN multilayers reactively sputtered at low temperatures. Surf. Coat. Technol. 1998;98:1497.
[7] Lee HY, Jung WS, Han JG, Seo SM, Kim JH, Bae YH. The synthesis of CrSiN film deposited using magnetron sputtering system. Surf. Coat. Technol. 2005;200:1026.
[8] Cekada M, Panjan P, Macek M, Smıd P. Comparison of structural and chemical properties of Cr-based hard coatings. Surf. Coat. Technol. 2002;151–152:31.
[9] Almer J, Odén M, Hakansson G. Microstructure and thermal stability of Arc-Evaporated Cr-–C-–N coatings. Philosophical Magazine 2004;84:611.
[10] Choi EY, Kang MC, Kwon DH, Shin DW, Kim KH. Comparative studies on microstructure and mechanical properties of CrN, Cr–C–N and Cr–Mo–N coatings. J. Mater. Process. Tech. Technol 2007;187–188:566.
[11] Fuentes GG, Díaz de Ceiro MJ, García JA, Martínez R, Bueno R, Rodríguez RJ, et al. Gradient CrCN cathodic arc PVD coatings. Surf. Coat. Technol. 2008;203:670.
[12] Hager CH, Sanders J, Sharma S, Voevodin A. Gross slip fretting wear of CrCN, TiAlN, Ni, and CuNiIn coatings on Ti6Al4V interfaces. Wear 2007;263:430.
[13] Lecis N, La Vecchia GM, Boniardi M, D'Errico F. Fatigue behavior of duplex-treated samples coated with Cr(C,N) film. Surf. Coat. Technol. 2006;201:2335.
[14] Diesselberg M, Stock HR, Mayr P. Friction and wear behaviour of PVD chromium nitride supported carbon coatings. Surf. Coat. Technol. 2004;188–189:612.
[15] Polcar T, Cvrcek L, Siroky P, Novak R. Tribological characteristics of CrCN coatings at elevated temperature. Vacuum 2005;80:113.
[16] Polcar T, Parreira NMG, Novak R. Friction and wear behaviour of CrN coating at temperatures up to 500 °C. Surf. Coat. Technol. 2007;201:5228.
[17] Neves AM, Severo V, Cvrcek L, Polcar T, Louro C, Cavaleiro A. In situ structural evolution of arc-deposited Cr-based coatings. Surf. Coat. Technol. 2008;202:5550.
[18] Warcholinski B, Gilewicz A, Kuklinski Z, Myslinski P. Arc-evaporated CrN, CrN and CrCN coatings. Vacuum 2009;83:715.
[19] Polcar T, Kubart T, Novák R, Kopecký L, Široký P. Comparison of tribological behaviour of TiN, TiCN and CrN at elevated temperatures. Surf. Coat. Technol. 2005;193:192.

CORROSION BEHAVIOR OF DLC COATING ALLOYED BY TITANIUM

Luděk JOSKA, Jaroslav FOJT, *Ladislav CVRČEK, **Vítězslav BŘEZINA, ***Jaroslav Málek

Institute of Chemical Technology Prague, Technická 5, 166 28 Prague 6, joskal@vscht.cz

**HVM Plasma, Na Hutmance 2, 158 00 Prague 5*

***Masaryk University, Faculty of Medicine, Komenského sq. 2, 602 00 Brno*

****UJP Praha, Nad Kamínkou 1345, 156 00 Prague 5*

Abstract

Properties of DLC layers provide for their broad use in medical applications. Their tribological properties are frequently utilized in big joint implants. Another benefit is offered by their barrier effect. In the frame of presented work corrosion behavior of DLC-Ti alloyed coatings formed on TiNbTa alloy in environments to which dental implants may be exposed was studied. Electrochemical impedance spectroscopy, XPS and a cell colonization test were employed in the study.

Influence of DLC alloying by titanium was tested on samples with 3 levels of titanium amount. According to results of XPS analysis, surface concentration of titanium was 3.4, 10.2 and 23.6 % at. Unambiguous and marked peak of titanium carbide was detected only in the case of highest concentration of titanium. Corrosion resistance of TiNbTa/Ti/DLC and TiNbTa/Ti/DLC-Ti was in low-aggressive physiological solution slightly different nevertheless very high in both cases. Electrochemical behaviour of carbon was significantly suppressed by titanium; character of EIS spectra was more capacitive than in the case of pure DLC. Decrease of pH did not influence the level of charge transfer resistance (polarization resistance). The main disadvantage of titanium - sensitivity to fluorides - was emphasized by alloying. Colonization by cells was slightly increased on alloyed samples in comparison with unalloyed DLC.

Keywords: DLC layer, titanium, alloying, corrosion properties, EIS, XPS

1. INTRODUCTION

Layers of the DLC (diamond-like carbon) type are used in human medicine in the treatment of implants surfaces [1]. They offer basically two ways of application: their excellent tribological properties are used on friction areas of big joint replacements, and they may also serve as bio-inert barrier layers on implants made of materials likely to cause a negative response of the organism (e.g. alloys containing nickel, TiAlV, etc.). In the latter case they are able to eliminate the corrosion process relating to the release of soluble corrosion products into the body environment. However, one of the current aims in the field of transplantology is to achieve the fastest possible osseointegration, which requires that the implanted surfaces should be bioactive.

β-titanium alloy Ti36Nb6Ta is a material that might be used in the construction of both orthopaedic and dental implants in the future. In the case of joint replacements, the advantage of coating rests in good tribological properties of DLC layers because a direct combination of titanium and its alloys with, e.g., UHMWPE is not suitable for long-term exposure [2-4]. A pure DLC coating is bio-inert, yet for its application it would be desirable to ensure its bioactivation while preserving its tribological properties. DLC alloying with titanium might represent one of the possible solutions [5]. The use of a bioactive barrier DLC layer also seems to be a good choice for dental implants made of materials of the CoCrMo type because part of their surface gets in contact with the soft tissue. It is specific for

stomatology and important from corrosion point of view that the implants may get in contact with medical preparations containing high amounts of fluorides which destabilize titanium [6].

The presented work studied corrosion behavior of DLC coatings alloyed with titanium on experimental titanium alloy Ti36Nb6Ta. Corrosion behavior in a physiological solution with two pH levels and an addition of fluoride ions was evaluated. The surface colonization with cells was also tested within the study.

2. MATERIALS AND METHODS

Flat substrates with a diameter of 14 mm and thickness of 3 mm made of β-titanium alloy Ti36Nb6Ta (UJP Prague) were used for the coating. The surface was treated to 2 levels of roughness: polished specimens (P) with a roughness of R_a = 0.08 μm modelling the sliding surfaces of implants, and specimens jet-blasted with corundum (JB) with R_a = 1.00 μm corresponding to one of the possible surface treatments of implants.

Ti-C:H coatings were deposited in Hauzer Flexicoat 1200 equipment (configuration with five planar magnetrons, chamber volume 1000 L). The substrates were first degreased in an alkaline ultrasound bath, and subsequently rinsed in deionized water and dried in vacuum. Prior to their placement in the deposition equipment, the substrates surface was cleaned in argon plasma. The deposition itself started with the preparation of an adhesion inter-layer of pure Ti, followed by a gradient layer with a composition changing from Ti to Ti-C:H. This layer was deposited by way of non-equilibrium magnetron sputtering from Ti targets (99.5 %) in an Ar atmosphere (99.999%), with C_2H_2 (99.6%) added step by step. After achieving the selected flow of C_2H_2, deposition of the functional Ti-C:H layer for the selected flows of 60, 100 and 140 sccm C_2H_2 followed. A bias of -200 V, deposition temperature of 200°C, an achieved limiting pressure of 2.10^{-3} Pa, and a deposition pressure of 0.8 Pa were applied. The layers thickness was determined using the calotest method, adhesion to the coated substrate was measured by way of the scratch test (CSEM Revetest).

XPS spectra were measured using an EscaProbe P (Omicron) spectrometer with an excitation monochromatic Al K_α (E = 1486.6 eV) source. Survey spectra in the binding energies range of 280-550 eV and detailed spectra of Ti 2p, C 1s and O 1s were scanned. Energy was normalized to a gold peak 4f7/2 (binding energy E_b = 83.98 eV [7]).

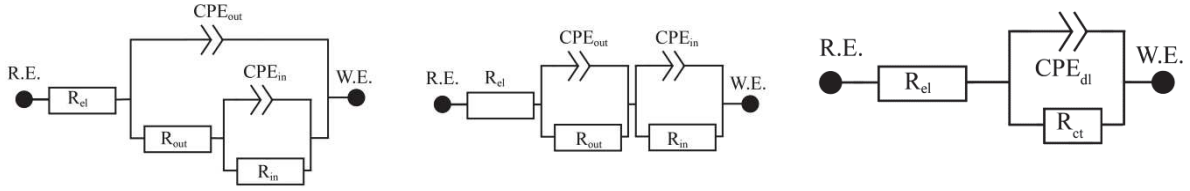

a) b) c)

Fig. 1 Equivalent circuits used in EIS spectra analysis.

Electrochemical impedance measurements were conducted in a standard way (measurement at E_{ocp}, frequency range 100 kHz - 1 mHz, excitation ac signal 20 mV), using potentiostat PCI4/750 with an ECM 8 multiplexer (both Gamry). A silver/silver chloride electrode with a chloride ions concentration of 3 mol/L was used as a reference electrode. An aerated physiological solution (9 g/l NaCl), physiological solution with pH adjusted by way of phthalate buffer to a value of 4.2, and the same solution with 200 ppm fluoride ions added served as exposure environments. The specimens were sterilized (120°C/20 minutes) prior to the exposure. Measurements were conducted in PTFE cells at 37°C for 168 hours, with periodical spectra scanning once in 24 hours. Equivalent circuits shown in Fig. 1 a-c were used for the spectra course analysis. The equivalent circuit a) is a simple circuit

generally used in analyzing corrosion systems with one porous layer, b) is a circuit applied in analyzing corrosion systems with one non-porous layer, and c) describes a corroding/passive system. R_{el} stands for the electrolyte resistance [Ωcm^2]. R_x [Ωcm^2]-CPE_x [$Ss^{\alpha/cm2}$] are RC elements corresponding to the respective phase boundary.

Biological tests were conducted on sterilized specimens. Cell line MG 63 cultivated in a MEM medium with 5% fetal bovine serum added was used for the colonization test. Cells were inoculated directly on the surface of the studied material, and the area colonized by the cells after 72 hours of cultivation was evaluated. After the end of exposure, the cells were fixed and stained using the Giemsa stain diluted 10x with distilled water. The area occupied by the cells on the specimen surface was microscopically evaluated on ten picture fields as minimum, the field of view was $1.29x10^6$ pixels. An area of identically cultivated cells on an unalloyed DLC layer was used for control.

3. RESULTS AND DISCUSSION

The Ti inter-layer thickness was 0.4-0.5 μm for all coating variants with the structure Ti/gradient Ti-C:H/Ti-C:H. The overall thickness of the Ti-C:H 60 coating was 1.5 μm, of which 0.8 μm accounted for

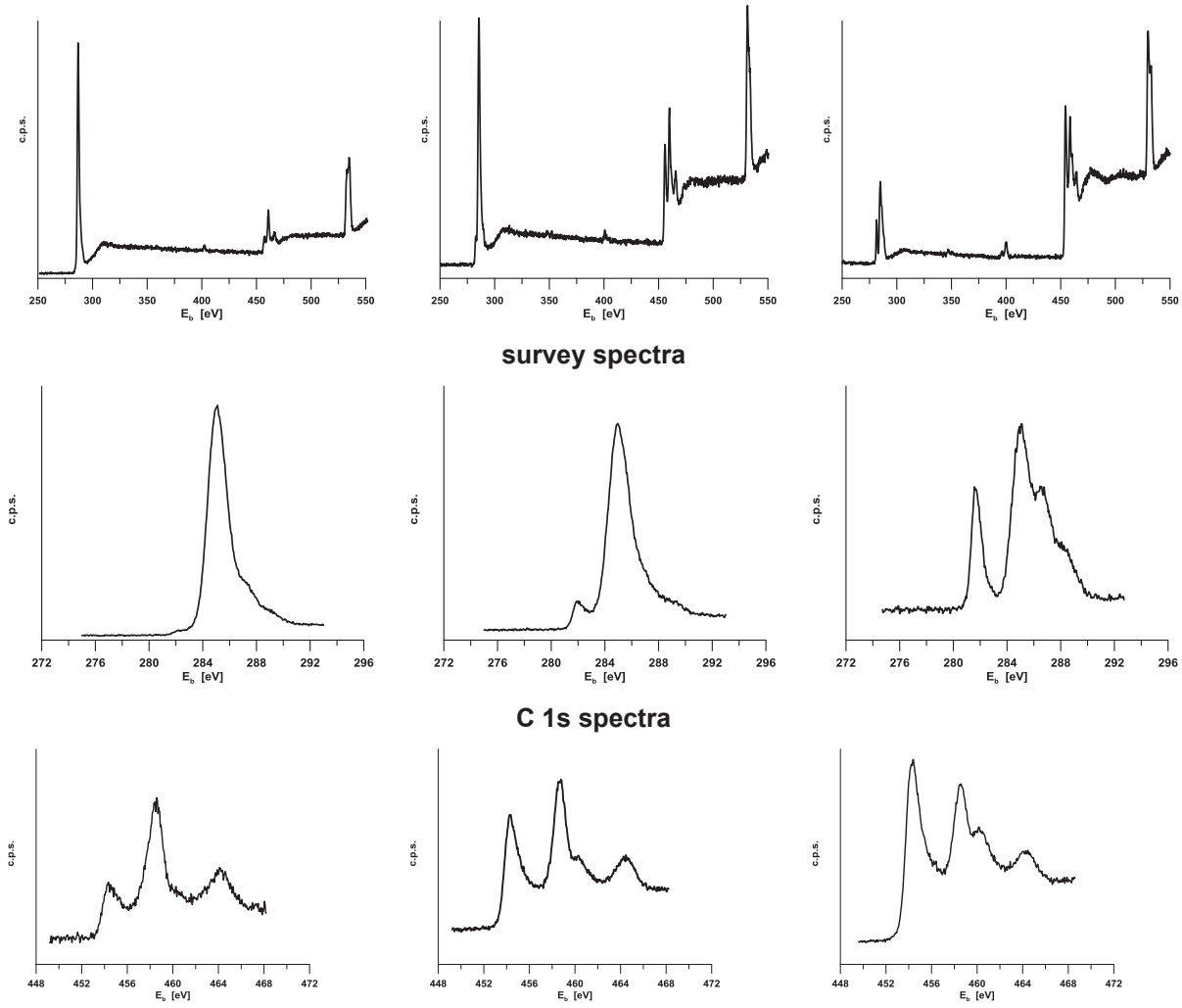

Fig. 2 XPS spectra of DLC layers alloyed by titanium.

the upper functional layer. For the Ti-C:H 100 coating, the overall thickness was 1.6 μm including a functional layer of 0.8 μm, and for Ti-C:H 140 it was 1.4 μm including a functional layer of 0.6 μm. The coating adhesion was impaired at a critical load of 30 N in all cases.

Using the XPS method, titanium content in individual specimens was found on the level 3.4 % at. (Ti-C:H 140), 10.2 % at. (Ti-C:H 100), and 23.6 % at. (Ti-C:H 60). In addition to carbon, oxygen and titanium, nitrogen presence was also recorded on the specimens surface. The state of the surface is documented by way of survey and regions C1s and Ti 2p spectra in Fig. 2. At the lowest titanium concentration in the DLC layer, doublet Ti 2p corresponds to a set of oxides TiO, Ti_2O_3 and TiO_2, with concentration increasing in this order. The carbon peak (C 1s) is not in this case deformed in any significant way. An increasing Ti concentration in the layer brings about a change both in titanium Ti 2p and C 1s spectra. In the case of Ti 2p, the signal grows disproportionately at an energy of 455 eV, where the contributions of TiO (455.2 eV) and TiC (454.9 eV), and possibly also sub-stoichiometric carbides overlap [7]. TiC existence in the layer can be clearly detected in the C 1s spectrum, where a signal appears on the binding energy 281.6 eV, corresponding to the carbon bond in TiC [7, 8]. On binding energies higher than 285 eV, the C 1s peak of the specimen with the highest Ti content is deformed by a number of hydrocarbon contributions. In terms of the surface state, specimens with the lowest level of alloying were the “purest”. Nevertheless, based on the assumed applications, specimens alloyed with 10.2 % at. of titanium (Ti-C:H 100) were chosen for further study. The decision was also affected by the technological point of view. Stability of the process of forming a layer with the lowest level of alloying is rather problematic, which might also cause problems in the reproducibility of layers preparation.

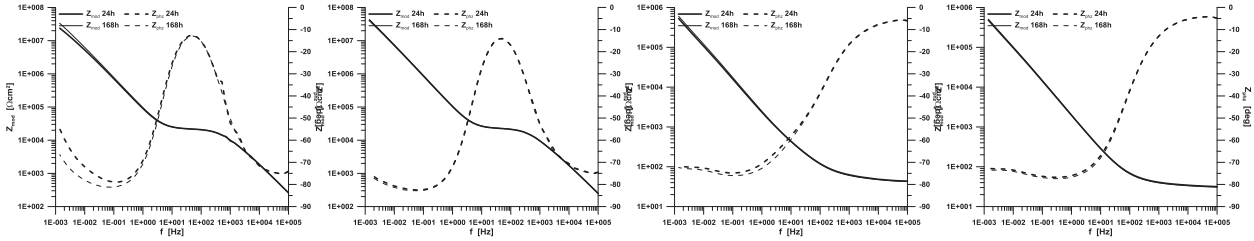

surface state P, pH non-modified | **surface state P, pH=4.2** | **surface state JB, pH non-modified** | **surface state JB, pH=4.2**

Fig. 3 EIS spectra of Ti36Nb6Ta with unalloyed DLC layer.

Fig. 3 shows electrochemical impedance spectra of Ti36Nb6Ta specimens with unalloyed DLC coating deposited on both evaluated surfaces (P and JB), exposed at both pH levels of the physiological solution. The course of all dependences – spectra measured at the 24th and 168th hour – makes it clear that the behavior of coated systems was stable, with spectra practically unchanged throughout the exposure. Impedance dependences of specimens with a polished surface correspond to a system with two time constants. This behavior is an expectable response of the layered structure. The spectra were analyzed using two types of equivalent circuits as shown in Figs 1 a) (porous layer) and 1 b) (non-porous layer). Success of the analysis was on a comparable level in both cases. The selected models of the phase boundary were able to describe the behavior of systems with minimum deviations of calculated values from experimental data. The course of the spectra clearly indicates systems with a very low rate of electrochemical reactions. In the ideal case – in view of graphite inertness - these should be only reactions of the environment components. The basically identical result of analysis conducted using both selected equivalent circuits indicates that this type of EIS measurement does not allow for a clear decision on the layers porosity.

The situation of specimens with a jet-blasted surface was different. In this case the spectra reflect the layered character of the structure (the course of the phase clearly changes at frequencies below 1 Hz),

with the coatings porosity clearly manifesting itself in this case. The quality of experimental data fitting by way of an equivalent circuit as shown in Fig. 1 a) was higher and the errors of parameters estimates were lower as compared with the application of the model shown in Fig. 1 b).

Alloying of a DLC layer with titanium led to a change in the impedance response, mainly in the case of layers deposited on the polished surface. The spectra were formally identical with dependences measured on jet-blasted specimens with an unalloyed DLC layer. Titanium presence in the DLC layer led to prevailing interaction of titanium with the environment on the DLC-electrolyte phase boundary. In terms of medical applications, this fact is positive as it indicates the possibility of affecting the bioactivity of the layer-body environment phase boundary. Unalloyed DLC coatings are bio-inert while titanium oxides may be

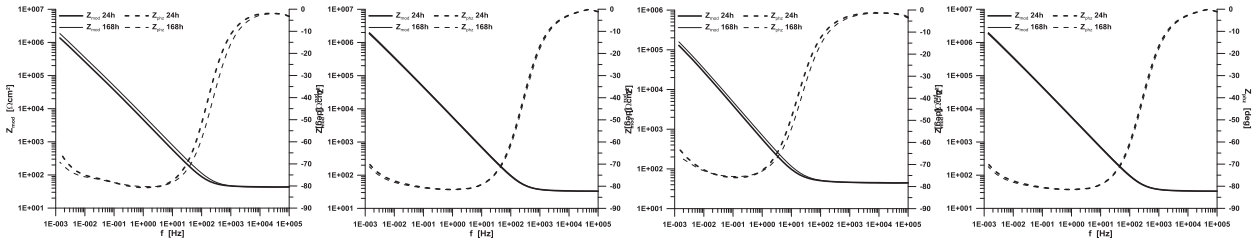

P, pH non-modified P, pH=4,2 JB, pH non-modified JB, pH=4,2

Fig. 4 EIS spectra of Ti36Nb6Ta coated by DLC layer alloyed by titanium (physiological solution, 37°C).

(bio)activated by way of chemical-thermal treatment. The spectra reflect the layered character of the specimens, with a clear change in their course at frequencies below 1Hz. The EIS spectra analysis of specimens with a polished surface led to the same result as that recorded for unalloyed layers – success of experimental data fitting with functions generated on the basis of both equivalent circuits was comparable. In contrast, the effect of porosity was unambiguous in the case of jet-blasted surfaces. DLC layers deposited on a jet-blasted surface displayed porosity regardless of the alloying. Consequently, they cannot be applied as barrier layers.

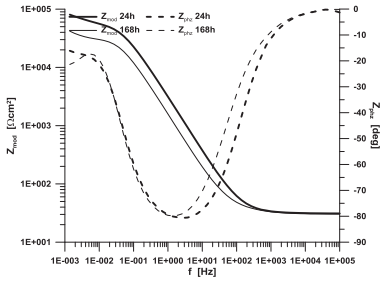

Fig. 5 EIS spectra of TiNbTa with a DLC layer alloyed with titanium (surface state P, physiological solution pH=4.2/200 ppm F, 37°C).

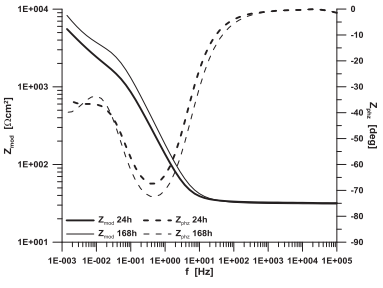

Fig. 6 EIS spectra of TiNbTa with a DLC layer alloyed with titanium (surface state JB, physiological solution pH=4.2/200 ppm F, 37°C).

Addition of fluoride ions to the physiological solution with pH=4.2 resulted in a dramatic change in the course of the spectra. A drop in impedance confirmed instability of titanium oxides in an environment containing fluorides/hydrofluoric acid [6], which also applied in the case of titanium bound in a DLC layer. Quite surprisingly, spectra may be in all cases (both P and JB) successfully fitted only by way of an equivalent circuit modeling a non-porous layered system. This may be due to the layer pores being closed with corrosion products [9]. Based on these results and given the common use of fluorides in medicinal preparations, the application of Ti-alloyed layers in stomatology is likely to be rather limited.

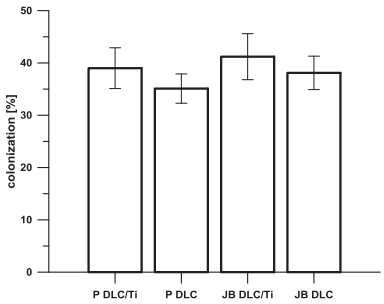

Fig. 7 Surface colonization with cells.

Fig. 7 shows the results of the colonization test. The alloyed specimens were not treated in any way in order to increase their bioactivity prior to the biological testing. The colonization test showed a slight increase in the occupation of the alloyed DLC layer surfaces with cells as compared with unalloyed layers. However, the difference of values was not statistically significant. At the same time, higher colonization was noted on specimens whose surface was jet-blasted prior to the coating in comparison with polished surfaces, yet no statistically significant difference was proved in this case either. These results give hope that subsequent treatment may lead to a more distinct growth of colonization on the alloyed specimens surface.

4. CONCLUSIONS

DLC coatings alloyed with titanium at a level of 3.4 % at. to 23.6 % at. were deposited on a titanium β-alloy Ti36Nb6Ta within the study. At the highest titanium concentration, its significant amount was bound in TiC carbide. Corrosion behavior of specimens with an alloyed layer was significantly different from pure DLC coatings. Electrochemical reactions of the environment on graphite surface were overlapped by titanium interaction with the electrolyte. This fact is rather promising as far as application on implants is concerned as it indicates the possibility of modifying the bioactivity of titanium oxides by way of subsequent treatment. Alloying with titanium led to a slight increase in the surface colonization with cells.

ACKNOWLEDGEMENT

This work was supported by the Grant Agency of the Czech Republic - project P108/10/1782.

REFERENCES

[1] GRILL, A. Diamond-like carbon coatings as biocompatible materials - an overview. *Diamond and Related Materials*, 2003, vol. 12, p. 166-170.

[2] ROMESBURG, J.W., WASSERMAN, P.L., SCHOPPE, C.H. Metallosis and metal-induced synovitis following total knee arthroplasty: Review of radiographic and CT findings. *Radiology Case*, 2010, vol. 4, pp. 7-17.

[3] BREEN, D.J., STOKER, D.J. Titanium lines: A manifestation of metallosis and tissue response to titanium alloy megaprostheses at the knee. *Clinical Radiology*, 1993, vol. 47, pp. 274-277.

[4] YILDIZ, F., YETIM, A., ALSARAN, A., EFEOGLU, I. Wear and corrosion behaviour of various surface treated medical grade titanium alloy in bio-simulated environment. *Wear*, 2009, vol. 267, pp. 695-701.

[5] VITU, T., POLCAR, T., CVRCEK, L., NOVAK, R., MACAK, J., VYSKOCIL, J., CAVALEIRO, A. Structure and tribology of biocompatible Ti-C:H coatings. *Surface and Coatings Technology*, 2008, vol. 202, pp. 5790-5793.

[6] FOVET,Y., GAL, J.Y., TOUMELIN-CHEMLA, F. Influence of pH and fluoride concentration on titanium passivating layer: stability of titanium dioxide. *Talanta*, 2001, vol. 53, pp. 1053-1063.

[7] NIST X-ray Photoelectron Spectroscopy Database, Version 3.5 (National Institute of Standards and Technology, Gaithersburg, 2003); http://srdata.nist.gov/xps/.

[8] CRIST, V. Handbooks of Monochromatic XPS Spectra. XPS International Inc., Ames

[9] JOSKA, L., FOJT, J. Corrosion behaviour of titanium after short-term exposure to an acidic environment containing fluoride ions. *Journal of Materials Science: Materials in Medicine*, 2009, vol. 21, pp. 481-489.

journal

J. Am. Ceram. Soc., 95 [9] 2741–2745 (2012)
DOI: 10.1111/j.1551-2916.2011.05000.x

Potential Application of a Ti–C:H Coating in Implants††

F. Feng,‡ Y. Zhou,‡ H. Yun,‡ A. Rocha,‡ T. Polcar,§ L. Cvrcek,§,¶ and H. Liang‡,†

‡Department of Mechanical Engineering, Texas A&M University, College Station, TX 77843-3123

§Department of Control Engineering, Faculty of Electrical Engineering, Czech Technical University in Prague, Technicka 2, 166 07 Prague 6, Czech Republic

¶HVM Plasma Ltd., Na Hutmance 2, 158 00 Prague 5, Czech Republic

A coating of Ti–C:H was investigated for potential applications as artificial joint materials. Herein, we conducted experimental study using fluid shear method and tribolgoical study to evaluate and analyze the adhesive strength of proteins on Ti–C:H coatings and Ti6Al4V. Sample surfaces were worn against a steel bearing (E52100) under the lubrication of egg white protein solution. The following wear track and debris analysis helped further understand their wear mechanism. Research results showed that Ti–C:H coatings on silicon substrate had a porous topography that enhanced its adhesion with the protein. The friction coefficient and wear rate for Ti–C:H was much lower than Ti6Al4V. This can be attributed to the chemical inertness and functional diamond-like features of Ti–C:H coatings enhancement in wear resistance, making it superior to Ti6Al4V.

I. Introduction

Cell and protein adhesion on different bio-materials is one of the most important aspects for long lasting implants.[1–3] When a foreign material enters into our body and contacts body tissue or bio-fluid, protein adhesion occurs.[1,4] Without protein adhesion, cells cannot attach on the implant surface and form a good interface with the implant. The protein adhesion is especially important for materials used for artificial joints.

High wear resistance and protein adhesion on the surface of the materials used for femoral head and femoral stem of artificial joints are also very important. That is because, first, artificial joints are under the lubrication of synovial fluid (SF). SF is the natural lubricant for human's articular joints. SF is mainly composed of protein. Therefore, a material that has higher adhesive strength with protein will benefit the lubrication of artificial joints. Secondly, the patient's activity will wear the femoral head and release debris particles into the tissue around the joint. The accumulation of debris will cause tissue irritation and finally lead to osteolysis and to the loosening of the artificial joint components.[5,6] So, a material with lower wear rate could elongate the life span of artificial joints.

Currently, the widely used material for artificial femoral head and stem is titanium-alloy, Ti6Al4V.[7] This material is successful because of its outstanding mechanical properties and chemical inertness. Ti6Al4V can aid in the successful osseointegration after the implantationof artificial joints. Ti–C:H is a functional diamond-like coating (DLC), the structure of which usually consists of an amorphousmetastable carbon with a high concentration of sp^3 bonds.[8,9] This structure leads to chemical inertness, high hardness, and outstanding wear resistance. All its properties meet the demands of biomedical implant materials, especially artificial joints.

The aim of this study was to find suitability of Ti–C:H as a biologic coating for artificial joint. The friction and wear resistance of the coating as well as the protein adhesion will be evaluated. Fluid shear stress tests and tribology tests will be carried out for adhesive strength of albumen to Ti–C:H coating and Ti6Al4V, and their wear properties.[10] The comparison of these results will allow the design and selection of biomaterials.

II. Materials

(1) Ti–C:H Coating

Titanium hydrocarbon coating was fabricated using PECVD (plasma enhanced chemical vapor deposition) process with acetylene (C_2H_2) as a reactive gas. Ti was sputtered on a silicon substrate by magnetron sputtering in an argon atmosphere. In our previous works, the series of Ti–C:H films were deposited with carbon content in the range 18–91%at;[8,9] the films were characterized with respect to structure, mechanical properties, and tribology. The coating deposited with a C_2H_2 flow 45 sccm was selected for this study due to its high adhesion. The chemical composition of the surface film was measured using X-ray photoelectron spectra (XPS) on Omicron Nanotechnology ESCAProbeP spectrometer with resulting composition (%at): Ti4.2, C77.6, O18.2. Ti–C, and C–C bonds were identified, whereas Raman spectroscopy showed D and G bands of carbon confirming existence of C–C bond. X-Ray diffraction analysis showed very broad peaks of TiC phase with orientations (111) and (200); the grain size of TiC was estimated to ~5 nm using Sherrer formula. The results suggest nanocomposite coating structure with TiC nanograins embedded in amorphous carbon matrix. The microhardness of the film measured by nanoindentation on Fischer PICODENTOR® HM500 (Helmut Fischer GmbH, Sindelfingen, Germany) was 10.20 ± 1.06 GPa. Adhesion of layers to the substrate material (tool steel X153CrMoV12) was tested using the standard scratch test device CSEM Revetest, and critical load was measured 65 N.

(2) Sample Preparation for Tribological Test

Ti6Al4V grade 2 (McMaster-Carr, Elmhurst, IL) was polished with grinding papers. To make the titanium-alloy surface having a similar surface roughness as the Ti–C:H coating, the Ti-alloy were cut into 28 mm × 28 mm pieces and polished by three types of grinding papers. Samples were polished using the Polisher Ecomet Π Grinder (Buehler Ltd., Lake Bluff, IL). Tapwater was used as the lubricant. Samples were firstly polished by a 400-grit silicon carbide grinding paper (Buehler Ltd.), followed by a 600 grit grinding paper

A. Bandypadhyay—contributing editor

Manuscript No. 30095. Received August 04, 2011; approved November 07, 2011.
††Paper presented at Bangalore INDIA BIO 2011 Conference
†Author to whom correspondence should be addressed. e-mail: hliang@tamu.edu

(AlliedHigh Tech Products Inc., Compton, CA). Finally, the sample surface was finished using an 800 grit grinding paper. The optical profilometer scans show that the titanium-alloy sample surface polished using this procedure has a macro-scale surface roughness similar to the Ti–C:H coating.

(3) Protein Coating for Shear Stress Test

As Ti–C:H could be used for artificial joint coating, the shear stress test is designed to imitate the behavior of artificial joints once implanted into the body. Rheometer has been used to carry out the shear stress experiments, because it is similar to the working conditions of artificial joints. Artificial joints are a ball-cup bearing system, whereas the rheometer is a rotating and stationary disk system. The rotating disk comparable to the femoral head of artificial joint and the stationary disk are similar to the acetabular cup positioned in the pelvic bone. In this research, distilled water is used to imitate the bio-fluid in the body.

Egg white protein (albumen) is coated on the sample surface to imitate the protein adhesion on the surface in an artificial joint. When the surface of a foreign material contacts a bio-fluid or body tissue, protein adsorption takes place. Cells start to grow on that layer of protein. Finally, the body forms an interface with the material.[1]Without protein adsorption, cell does not adhere to material surface, and the body will reject the implants. A SF, which is the natural lubricant for human's articular joints, is composed of lipids, hyaluronic acid (HA), and lubricin. Lubricin is a water-soluble glycoprotein, and it plays an important role in joint lubrication. Egg white protein contains 54%wt ovalbumin and 12%wt ovotransferrin, both glycoproteins.[11,12] Furthermore, collagen fibers, proteoglycan, and elastin fibers are major components of cartilage. All these components are proteins similar to albumen. Egg white protein has sufficient similarities with SF and cartilage. It is valid to use it in this study. Overall, using a rheometer, the combination of water and egg white albumen is a good simulation of the working conditions of artificial joints.

The sample preparation process for the shear stress test is nearly the same as the tribology test, but added with some egg white protein coating steps. First, samples were cleaned with DI (deionized) water and allowed to air dry in individual petridishes to prevent further contamination. The sample surface was then coated with an albumen solution. The 2.91%wt albumen solution was prepared by mixing 0.300 ± 0.005 g albumen powder into 10 mL DI water. It was stirred for 20 min using a magnetic stirrer. The amount of 100 μL of albumen solution was coated on the surface of each Ti–C:H coating or Ti6Al4V sample using a pipette. In case of low humidity, the protein coating would crack and/or peel off the surface prior to testing. To prevent this, each sample, along with two DI water saturated facial tissues, was paced into a partially covered petridish and allowed to air dry for 12 h.

III. Experiments

(1) Surface Characterization

An AFM (Nano R; Pacific Nanotechnology, Inc., Santa Clara, CA) was operated with close-contact mode to scan the surface of each sample. Scan sizes of 5 μm × 5 μm were obtained using a silicon cantilever with scan rates of 1 Hz and a resolution of 256 × 256 pixels. Images were analyzed by NanoRule to obtain the surface roughness on the micrometer scale.

The macro-scale surface roughness of all samples, Ti–C:H coating and Ti6Al4V, was measured, respectively, using a profilometer (ZygoNewView 600s optical; Zygo Corporation, Middlefield, CT) in 0.14 mm ×0.11 mm scale. An optical profilometer uses a noncontact mode to measure surface roughness and its profile. The average value for each group was used to represent its macro-scale surface roughness.

(2) Contact Angle Measurement

Contact angle was tested in the following method. The amount of 0.05 mL distilled water was dropped onto the sample surface from a 5 mm height. Once the drop was on the surface, a digital camera was used to take an image. Finally, contact angle was calculated through image analysis. Each measurement was repeated 12 times. Contact angle test is necessary because protein had some preference to hydrophilic surface.[5] Doing so enabled us to study how the contact angle affects the adhesion of protein to a surface.

(3) Shear Stress Measurement

The AR-G2 Rheometer (TA Instruments, New Castle, DE) carried out shear stress experiments by controlling maximum shear stress applied on the sample. The rotating disk was a 25-mm diameter spindle, whereas the sample was fixed on the stationary disk below (Fig. 1).

The stationary plate is a Peltier plate for temperature control. The temperature was maintained at 37°C. The amount of 200 ± 1μL of simulated body fluid (SBF) was poured on the sample to fill the 500 μm gap between the spindle and the sample, and SBF was prepared according to ISO 23317. When lowering the spindle, it was rotated at a lower speed to form an evenly distributed water layer without air bubbles. Each shear stress test ran for 5 min. Shear strain, spindle speed, torque, and temperature were recorded. Immediately after testing, an image of the sample was taken with a digital camera for image analysis (Image-J). Six samples in one group were exposed to different controlled shear stress, namely 25, 26.5, 28, 29.5, 31, and 32.5 Pa.

After each test, proteins were wiped off and rinsed with DI water, followed by 10 min sonication with acetone and ethanol, respectively. After cleaning, the samples were allowed to air dry before being recoated with albumen and retested. For repeatability, each test was repeated three times.

(4) Tribological Tests

A CSM tribometer was used to carry out a linear reciprocal pin-on-disk tribological test. A bearing ball (E52100) of 6 mm diameter was fixed on the top pin to wear against the sample surface. The tribological test for Ti–C:H and Ti6Al4V were conducted in following conditions: 4800 cycles, 5 N normal load, maximum linear speed 2.5 cm/s, and half amplitude 3 mm. The sliding tests were performed at room temperature under the lubrication of the egg white solution. The concentration of albumen solution used here is the same as the solution used for protein coating during the sample preparation process of the shear stress test. The tribological

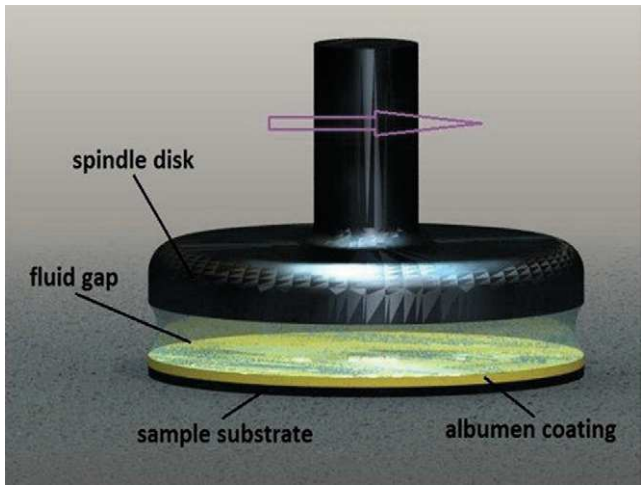

Fig. 1. Therheometer system for adhesive strength measurement.

test of each sample was repeated twice to verify its repeatability.

The tribological characteristics, including the friction coefficient, wear rate of the sample, and wear volume of the bearing ball were investigated. The wear rate of the sample surface was quantified through analysis of the wear track profile tested by using a contact profilometer. The wear volume of the bearing ball was calculated from the diameter of the spherical wear cap on the ball observed by optical microscope. To further determine the wear mechanism, the wear tracks on samples were also studied using optical microscopy.

(5) Debris Analysis

The wear debris for Ti–C:H and Ti6Al4V samples was analyzed using JEOL transmission electron microscope (TEM). As it was an albumen solution lubricated wear test, the debris was mixed into the albumen solution. The debris–albumen solution was collected and mixed with acetone. Then surfactant was added, and the solution was placed in a sonicator for 3 h to separate the debris particles. Finally, the debris–albumen–acetone–surfactant solution was applied on copper TEM grids. The acetone was evaporated, leaving only the debris for TEM imaging.

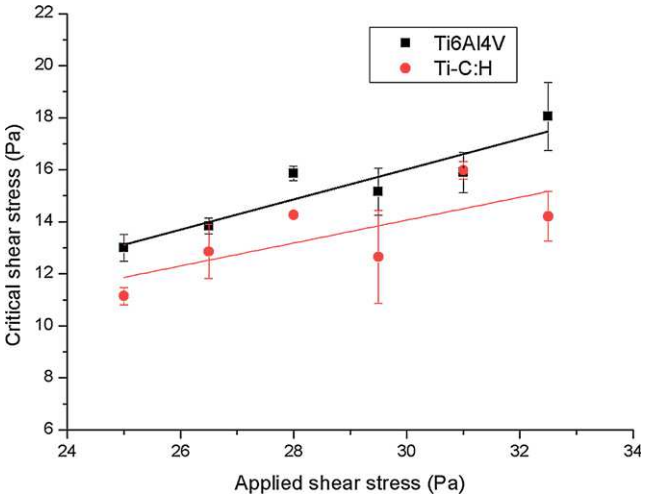

Fig. 2. Comparison of Ti6Al4V (down) in 5 μm × 5 μm and Ti–C:H (up) in 1.5 μm × 1.5 μm.

IV. Results and Discussion

(1) Protein Adhesion

Critical shear stress was used to represent the adhesive strength of egg white protein to a surface. The comparison between Ti–C:H coating and Ti6Al4V shows that protein has similar, but slightly stronger adhesive strength with Ti6Al4V (Fig. 2) than that of Ti–C:H. In comparing both materials, the latter is considered more electron negative, and yet its surface has nanoporous structures (Fig. 3). These effects were somehow suppressed by the hydrophilic nature of the Ti6Al4V (Fig. 4). It has been found that hydrophilic surfaces preferentially adsorb protein than do hydrophobic surfaces.[5] Our result (Fig. 4) is in correlation with the report.

(2) Tribological Characteristics

Figure 5 shows the friction coefficient against time during the tests for Ti–C:H and Ti6Al4V. Figure 5(a) is that of Ti–C:H showing the friction coefficient fluctuated in the range of 0.12 and 0.18, whereas the Ti6Al4V (Fig. 5b) fluctuated between 0.24 and 0.30 . The Ti–C:H coating not only had a lower friction but also is more stable than Ti6Al4V under the protein solution lubrication condition. The friction coefficient for Ti–C:H was slightly increased during the experiment and was featured with a visible running in period. This means that the Ti–C:H surface is better lubricated, which might be due to the adhered proteins on the porous structure. The friction coefficient of Ti6Al4V slightly decreased without a well defined running-in period.

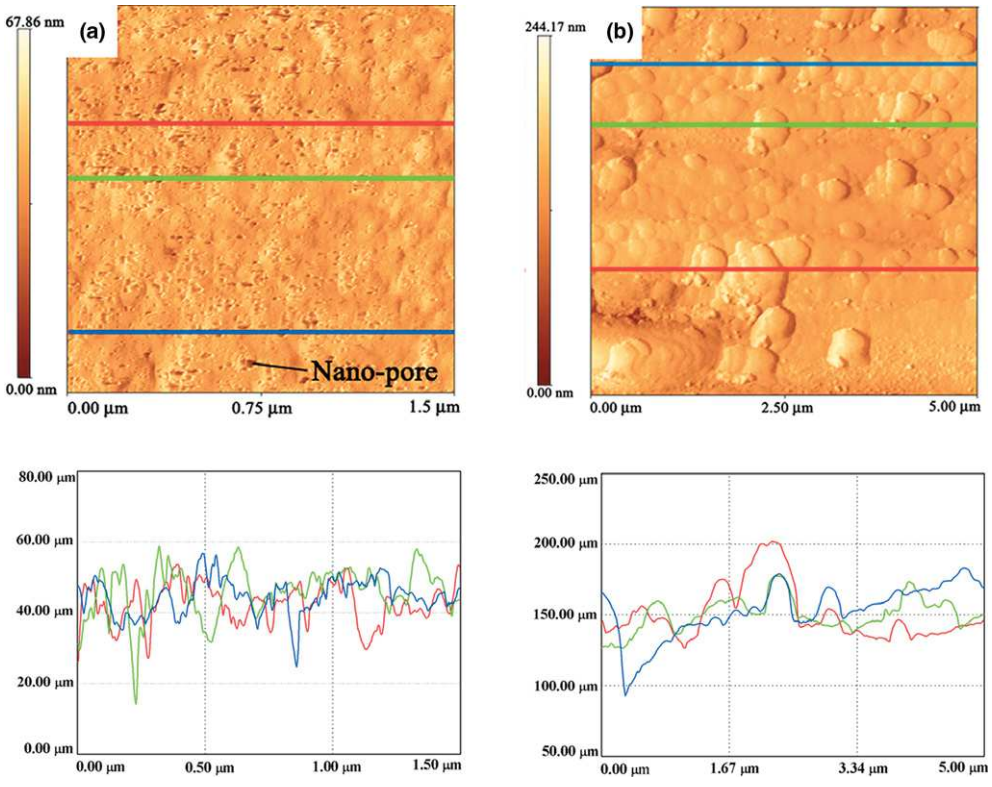

Fig. 3. An AFM scan for Ti–C:H coating (1.5 μm × 1.5 μm).

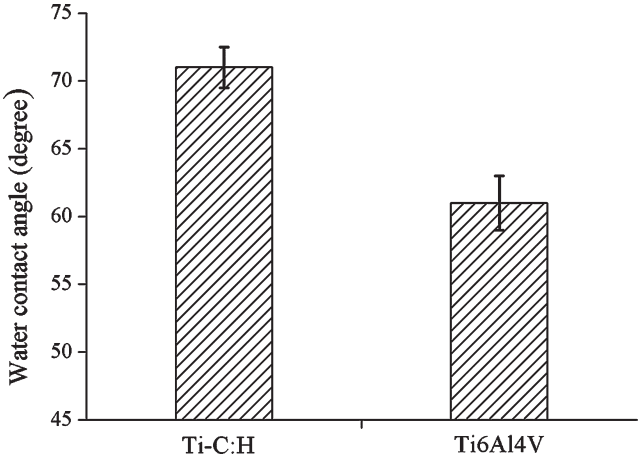

Fig. 4. Contact angle comparison for Ti6Al4V and Ti–C:H.

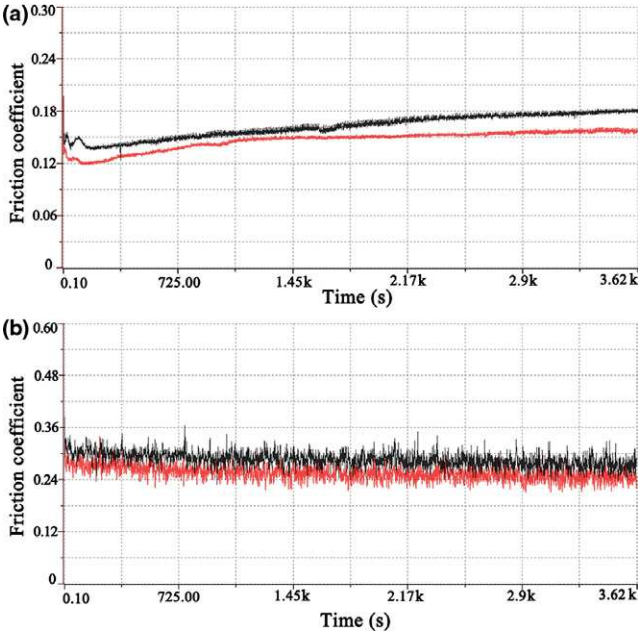

Fig. 5. Friction coefficient against time for (a) Ti–C:H and (b) Ti6Al4V.

The wear rate of Ti–C:H and Ti6Al4V and the wear volume of their bearing ball are shown in Figs. 6(a) and (b), respectively. The chemical inertness and high hardness made the wear rate of Ti–C:H one thousand times less than Ti6Al4V. The excellent properties of Ti–C:H coating also led to the lower wear volume of its bearing ball, which was nearly one hundred times less than the wear volume of the bearing ball worn against Ti6Al4V.

From the optical microscope view of the wear track and wear cap of the ball bearing (Figs. 7 and 8), it was found that the dominant wear mechanism for Ti–C:H and Ti6Al4V was abrasive wear. Some green to blue color spots, however, were observed on the bearing balls that wore against Ti6Al4V and at the end of the Ti6Al4V wear track (Fig. 7). This finding proved tribochemical reactions happened during the tribological experiments. This further showed the outstanding chemical inertness of Ti–C:H. The tribochemical reactions could attribute to the high wear rate of the Ti6Al4V sample and high wear volume of its bearing ball.

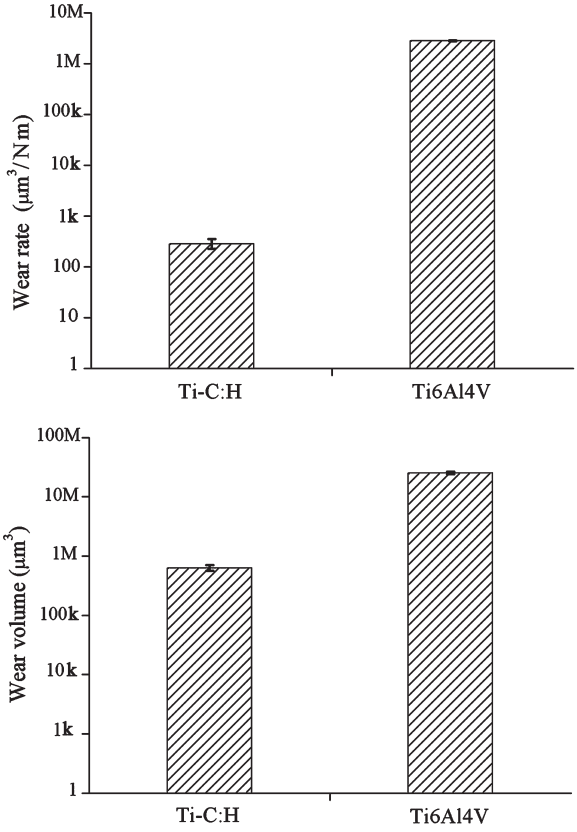

Fig. 6. (a) Wear rate of Ti–C:H and Ti6Al4V samples. (b) Wear volume of ball bearing against Ti–C:H and Ti6Al4V samples.

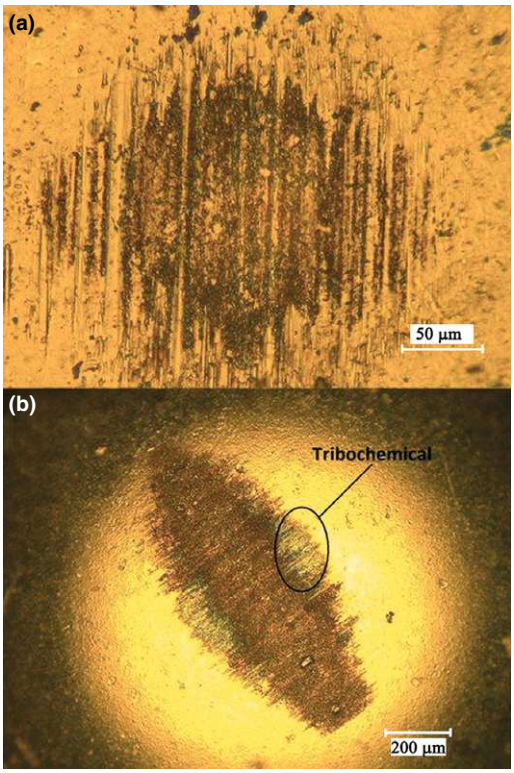

Fig. 7. Optical microscope image for ball bearing wear against (a) Ti–C:H and (b) Ti6Al4V.

(3) Debris Analysis

Figure 9 is the TEM image of the wear debris for Ti–C:H and Ti6Al4V samples. The wear debris of Ti–C:H coating was featured with crystalline structures around 1–2 μm. Debris particles for Ti6Al4V samples are much smaller than Ti–C:H, and have amorphous structures. The amorphous debris

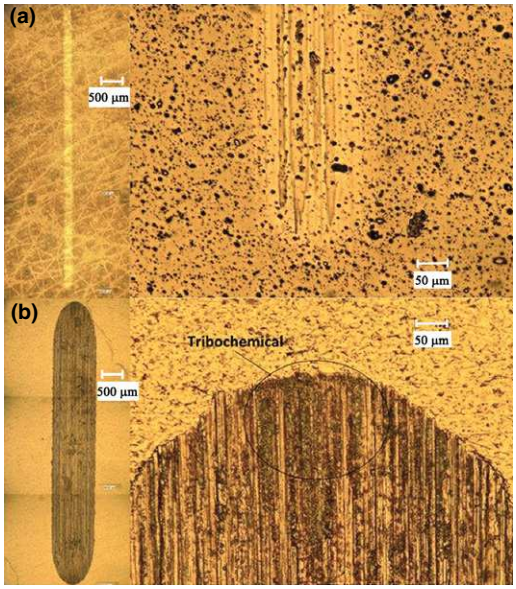

Fig. 8. Optical microscope image for (a) Ti–C:H and (b) Ti6Al4V left and right.

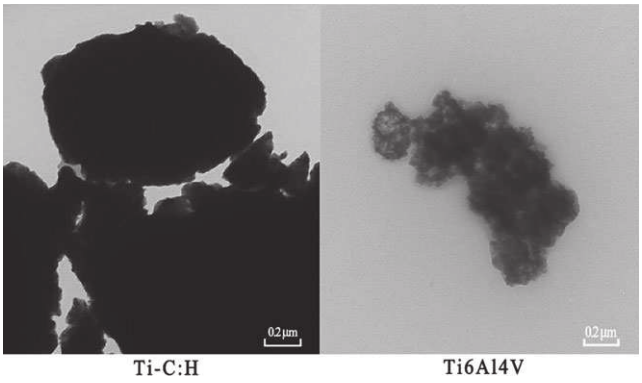

Fig. 9. TEM images of debris collected from Ti–C:H (left) and Ti6Al4V (right).

of Ti6Al4V may be responsible for its higher friction coefficient compared with the Ti–C:H sample under protein lubrication condition. The relation between debris and friction coefficient found in this study correlate with Ribeiro's findings.[13–15]

V. Conclusion

This research used a rheologic methodology to quantitate the adhesive strength of albumen to Ti–C:H coating and Ti6Al5V sample surfaces. Tribological test and related analysis were performed to compare the wear resistance and wear mechanism of Ti–C:H and Ti6Al4V. It was found that protein had similar adhesive strength on both the Ti–C:H and Ti6Al4V surfaces. The Ti–C:H coating reduces the friction significantly, and its hardness and chemical inertness made it wear resistant in comparison with Ti6Al4V. Moreover, the wear debris of Ti–C:H coating showed a crystalline feature that could be deformable with a frictional force.

In summary, the outstanding tribological and protein interaction properties of Ti–C:H over Ti6Al4V indicate that it could be a suitable coating for and artificial joints. The Ti–C:H coating can help improve the service life and performance of these biomedical implants.

Acknowledgments

Assistance provided by Liangxian Chen during data collection was greatly appreciated.

References

[1]S. Kidoaki and T. Matsuda, "Adhesion Forces of the Blood Plasma Proteins on Self-Assembled Monolayer Surfaces of Alkanethiolates with Different Functional Groups Measured by an Atomic Force Microscope," *J. Am. Chem. Soc.*, **15** [22] 7639–46 (1999).

[2]M. Roba, M. Naka, E. Gautier, N. D. Spencer, and R. Crockett, "The Adsorption and Lubrication Behavior of Synovial Fluid Proteins and Glycoproteins on the Bearing-Surface Materials of Hip Replacements," *Biomaterials*, **30** [11] 2072–8 (2009).

[3]A. P. Serro, K. Degiampietro, R. Colaco, and B. Saramago, "Adsorption of Albumin and Sodium Hyaluronate on UHMWPE: A QCM-D and AFM Study," *Colloids Surf. B. Biointerfaces*, **78** [1] 1–7 (2010).

[4]Y. Huang, X. Lu, M. Jingwu, and N. Huang, "*In Vitro* Investigation of Protein Adsorption and Platelet Adhesion on Inorganic Biomaterial Surfaces," *Appl. Surf. Sci.*, **255** [2] 257–9 (2008).

[5]M. P. Heuberger, M. R. Widmer, E. Zobeley, R. Glockshuber, and N. D. Spencer, "Protein-Mediated Boundary Lubrication in Arthroplasty," *Biomaterials*, **26** [10] 1165–73 (2005).

[6]S. H. Su, Z. K. Hua, and J. H. Zhang, "Design and Mechanics Simulation of Bionic Lubrication System of Artificial Joints," *J. Bionic Eng.*, **3** [3] 155–60 (2006).

[7]M. Geetha, A. K. Singh, R. Asokamani, and A. K. Gogia, "Ti Based Biomaterials, the Ultimate Choice for Orthopaedic Implants – A Review," *Prog. Mater. Sci.*, **54** [3] 397–425 (2009).

[8]T. Vitu, T. Polcar, L. Cvrcek, R. Novak, J. Macak, J. Vyskocil, and A. Cavaleiro, "Structure and Tribology of Biocompatible Ti–C:H Coatings," *Surf. Coat. Technol.*, **202** [22–23] 5790–3 (2008).

[9]T. Polcar, T. Vitu, L. Cvrcek, R. Novak, J. Vyskocil, and A. Cavaleiro, "Tribological Behaviour of Nanostructured Ti-C:H Coatings for Biomedical Applications," *Solid State Sci.*, **11** [10] 1757–61 (2009).

[10]A. Rocha, M. Hahn, and H. Liang, "Critical Fluid Shear Stress Analysis for Cell–Polymer Adhesion," *J. Mater. Sci.*, **45** [3] 811–7 (2010).

[11]Y. Mine, "Recent Advances in the Understanding of Egg White Protein Functionality," *Trends Food Sci. Technol.*, **6** [7] 225–32 (1995).

[12]M. Weijers, F. Velde, A. Stijnman, A. Pijpekamp, and R. W. Visschers, "Structure and Rheological Properties of Acid-Induced Egg White Protein Gels," *Food Hydrocolloids*, **20** [2–3] 146–59 (2006).

[13]R. Ribeiro, S. Ingole, M. Usta, C. Bindal, A. H. Ucisik, and H. Liang, "Tribological Characteristics of Boronized Niobium for Biojoint Applications," *Vacuum*, **80** [11–12] 1341–5 (2006).

[14]R. Ribeiro, S. Ingole, M. Usta, C. Bindal, A. H. Ucisik, and H. Liang, "Tribological Investigation of Tantalum Boride Coating Under Dry and Simulated Body Fluid Conditions," *Wear*, **262** [11–12] 1380–6 (2007).

[15]R. Ribeiro, S. Ingole, M. Usta, C. Bindal, A. H. Ucisik, and H. Liang, "A Tribological Comparison of Pure and Boronized Chromium," *J. Tribol.*, **128** [4] 895–7 (2006). □

Surface & Coatings Technology 206 (2012) 4899–4906

Contents lists available at SciVerse ScienceDirect

Surface & Coatings Technology

journal homepage: www.elsevier.com/locate/surfcoat

The effect of a DLC coating adhesion layer on the corrosion behavior of titanium and the Ti6Al4V alloy for dental implants

L. Joska [a,*], J. Fojt [a], O. Mestek [a], L. Cvrcek [b], V. Brezina [c]

[a] Institute of Chemical Technology Prague, Technicka 5, 166 28 Prague 6, Czech Republic
[b] HVM Plasma, Na Hutmance 2, 158 00 Prague 5, Czech Republic
[c] Masaryk University, Faculty of Medicine, Komensky sq. 4, 625 00 Brno, Czech Republic

ARTICLE INFO

Article history:
Received 10 February 2012
Accepted in revised form 22 May 2012
Available online 1 June 2012

Keywords:
DLC
Adhesive inter-layer
Corrosion
Impedance spectroscopy
Biology

ABSTRACT

The properties of DLC layers provide for their broad use in medical applications. Their tribological properties are frequently utilized in big joint implants, and their barrier effect offers another benefit. The present work studied corrosion behavior of DLC coatings formed on titanium and Ti6Al4V alloy with a titanium or chromium inter-layer, in environments to which dental implants may be exposed. Electrochemical impedance spectroscopy, XPS surface analysis, ICP/MS chemical analysis method and a set of standard biological tests were employed in the study.

The behavior of both coated systems, regardless of the basic material, was comparable in an environment that did not contain fluoride ions. An addition of fluorides revealed the occurrence of pores as deep as the DLC layer even in specimens with a surface polished prior to coating. Porosity of layers was clearly evident on jet-blasted specimens. The best corrosion behavior was recorded in specimens with a chromium inter-layer on both types of the basic material. With the titanium inter-layer applied, coatings on TiAlV exhibited higher corrosion resistance than those on commercial-pure titanium. The conducted biological tests indicated applicability of a chromium inter-layer on DLC coated implants.

1. Introduction

Coating with layers of the diamond-like carbon (DLC) type represents a technology with a considerable potential for application in the area of biomaterials. DLC layers display good wear behavior, cytocompatibility and do not increase the risk of post operation infections [1–7]. Their barrier behavior offers another application benefit. Implants are currently made of wide spectrum of materials, e.g. titanium–aluminum–vanadium alloy. In this case the release of mainly vanadium corrosion products may induce immune response in sensitive patients [8,9]. The same problem relates to the release of nickel from a shape-memory nickel–titanium alloy [10]. A DLC coating forms barrier which is able to eliminate the adverse corrosion process linked with the release of soluble corrosion products into the human body environment [9,11].

A DLC layer is always deposited on an adhesive inter-layer. This may be formed by many ways as a simple or multi-component system [12,13]. The corrosion and biological behavior of materials coated with DLC layers have been studied by a number of authors, but the effect of an inter-layer on the overall corrosion behavior of coated systems attracts only limited attention [14,15]. However, its corrosion properties may be of essential significance, particularly in the case of porous coatings. The use of a titanium inter-layer seems to be the most appropriate for systems applied in medicine from the possible release of corrosion products and subsequent negative reaction of the organism points of view.

The application of a barrier DLC layer on the surface of titanium based materials which are commonly used for dental implants seems to be a good choice because part of their surface gets into contact with the soft tissue. Dentistry is rather specific as it employs preparations with a high content of fluorides which destabilize titanium passive layer [16]. Chromium inter-layer might be of advantage in this case. Chromium is a component of many materials commonly used in human medicine [17] — e.g. implants of big joints made of austenitic stainless steel containing 20% chromium have been successfully used for decades, yet some cases of allergic reactions to implants have been documented [8,18,19]. In general, more attention needs to be paid to materials containing nickel, chromium and other components which may be risky in view of a possible negative response of the organism [20].

The present work studied corrosion behavior of DLC coatings formed using titanium or chromium inter-layer on titanium and Ti6Al4V alloy, in a saline solution modeling environment to which materials used for dental implants may be exposed. Samples coated with a chromium adhesive inter-layer were evaluated by a battery of standard biological tests.

* Corresponding author. Tel.: +420 220444204; fax: +420 220444400.
E-mail address: Ludek.Joska@vscht.cz (L. Joska).

0257-8972/$ – see front matter © 2012 Elsevier B.V. All rights reserved.
doi:10.1016/j.surfcoat.2012.05.089

2. Material and methods

Flat specimens with a diameter of 16 mm and a thickness of 3 mm made of commercially pure titanium (Ti grade 2) and titanium alloy Ti6Al4V (Ti grade 5 ELI) and chromium (purity 99.9%, $R_a = 0.08$ μm) were used for measurements. The surface was treated in two levels of roughness: $R_a = 0.08$ μm modeling the implants' sliding surfaces, and $R_a = 1.00$ μm (jet blasting with corundum and subsequent etch cleaning), corresponding to one of the possible treatments of dental implant surface. Corrosion behavior of both materials is not influenced by roughness in principle [21].

Ti/Ti–C:H/a-C:H(DLC) coatings were deposited in a Hauzer Flexicoat 1200 device with chamber volume 1000 l. Prior to the deposition, the substrates were degreased in an alkaline ultrasonic bath, rinsed with de-ionized water, and dried in a vacuum. The specimens, cleaned in argon plasma, were subsequently coated with a gradient adhesive inter-layer. It was deposited by unbalanced magnetron sputtering from titanium targets (purity 99.5%) in an argon atmosphere (99.999%), with the flow of acetylene (purity 99.6%) increasing simultaneously. The composition of the gradient adhesive inter-layer was changing from pure titanium to Ti–C:H. The conditions applied in the chromium adhesive inter-layer preparation process were identical, with a chromium target used in this case (purity 99.8%). The layer composition was changing gradiently from Cr to Cr–C:H. A functional a-C:H layer was deposited on inter-layers created in this way using the PACVD (Plasma Assisted Chemical Vapor Deposition) method. Pulsed bias voltage was applied on the substrate holder with a frequency of 50 kHz and a peak voltage of 200 V. Deposition temperature was 200 °C, C_2H_2 flow rate was 500 sccm, base pressure was 2.10^{-3} Pa and deposition pressure was 1 Pa.

The layers' thickness was determined using the calotest method; adhesion to the coated substrate was measured by way of a scratch test (CSEM Revetest). A second adhesion measurement, so-called Mercedes–Rockwell adhesion test, was conducted for comparison. It consisted an optical evaluation of the surroundings of an indentation formed in consequence of a hardness measurement using the Rockwell method at a load of 150 kg (HRC). It is evaluated with a parameter from 1 to 6. Microhardness was measured using the Picodentor HM500 (Fischer) measuring system.

Electrochemical impedance spectroscopy (EIS) measurements were conducted in the standard way (measurement at E_{ocp}, frequency range 100 kHz–1 mHz, 7 points per decade, excitation ac signal 20 mV), using potentiostat PCI4/750 with a multiplexer ECM 8 (Gamry). All potential-related data in the text refer to the used reference silver–silver chloride electrode (chloride ions concentration 3 mol/l). An aerated physiological saline solution (9 g/l NaCl) with pH buffered to 4.2 using a solution based on potassium hydrogen phthalate and sodium hydroxide [22], and an identical solution with 200 ppm fluoride ions added served as the exposure environments. The specimens were degreased and sterilized prior to exposure (120° C/20 min). Measurements were conducted in PTFE cells at 37 °C for 168 h, with spectra scanned periodically once in 24 h.

X-ray photoelectron spectra (XPS) were measured using an EscaProbe P (Omicron) spectrometer with an excitation monochromatic Al K_α source (E = 1486.6 eV). The analyzed area was 1.3 mm^2. When studying the surface state after the corrosion exposure, the delay between the specimen's withdrawal from the corrosion cell and its insertion in the spectrometer was 120 s maximum. The amount of chromium released to the exposure environment was determined using the inductively coupled plasma-mass spectrometry method (ICP/MS, Elan DRC-e, Perkin-Elmer). Each specimen was exposed individually in 20 ml of the respective solution at 37 °C for 24 h. Measurements were repeated four times.

Prior to biological tests, the specimens of the studied materials coated with a DLC layer on a chromium adhesive inter-layer were sterilized. The MG 63 cell line (from human osteosarcoma) was used for the tests, cultivated in a MEM (Minimum Essential Medium with Earle's balanced salts, without L-glutamine, Sigma-Aldrich) with 5% bovine fetal serum added. In order to determine the adherence and cytotoxicity, each specimen was exposed independently and dynamically (by way of shaking) in 4.7 ml of the MEM at 37 °C for 5 days. The resulting leach was sterilized by filtration and used for measurements. Cell cultures were cultivated under standard conditions (37 °C, air with 5% carbon dioxide added, relative humidity of 95%).

In the colonization test, the cells were inoculated directly onto the studied material surface and the area occupied by the cells after 72 h of cultivation was evaluated. After the end of exposure, the cells were fixed and colored with Giemsa stain, diluted with distilled water 10-times. The area occupied by the cells on the specimen surface was evaluated in ten picture fields minimum. The field of view was 1.29×10^6 pixels. An area of cells cultivated in the same way on glass was used for control.

In order to determine adhesion, the cells were inoculated into a leach prepared by the above procedure, and their adhesion to the bottom of the cultivation vessel was monitored. The test resulted in the quantification of the number of adhered cells, expressed by the adherence index (I_{ad} = number of adhered cells/number of all cells in the picture). The cells' behavior in a MEM prepared without the tested material served as a negative control. An extract of a copper specimen prepared in the same way as that applied for coated materials served as a positive control. The environment is cytotoxic if the adhesion index range from 0.05 to 0.40.

Cytotoxicity and clastogeneity (chromosomal aberrations) were determined in accordance with the ČSN EN ISO 10 993-5 and 10 993-3 standards. In order to evaluate the cytotoxicity, the growth curve was measured in a medium prepared by exposing the specimens. The number of cells was evaluated in a Burker counting chamber in individual time intervals. The cells' behavior in a MEM was used as a negative control while a copper extract in a MEM medium served as a positive control. For the test of chromosomal aberrations, the specimen was deposited in a Quantum PBL (PAA Laboratories) medium added with peripheral blood from a donor, in which the cells were cultivated. In conclusion, the environment was treated in a standard way (inhibition of cell division in the metaphase, hypotonization and fixation). Methotrexate was used as a positive control while the medium itself with peripheral blood added served as a negative control.

3. Results

The total thickness of the Ti/Ti–C:H/DLC layer was 3.20 μm, with the DLC coating itself accounting for 2.2 μm. In the Cr/Cr–C:H/DLC layer with a total thickness of 4.6 μm, the DLC layer accounted for 1.9 μm. In both cases the coating adhesion failed at a critical load of 30 N. The result of Mercedes–Rockwell indentation test was 2. Adhesion was found to be good and satisfactory for the assumed future applications [23,24]. At a load of 20 mN, the microhardness reached a value of HV = 2200.

For the sake of simplification, the individual types of specimens are designated by abbreviations in the following text: Material/Cr/DLC or Material/Ti/DLC used for specimens coated by DLC on individual inter-layers, polished surface is abbreviated P and jet-blasted JB.

The course of EIS spectra measured on both types of substrate materials with layers deposited on a polished or jet-blasted surface in an environment with a non-adjusted pH and pH = 4.2 was almost identical. The effect of fluoride ions on the impedance response of coated systems is summarized in Figs. 1–4. The course of the EIS spectrum measured at the end of exposure in an electrolyte with pH = 4.2 without any fluoride ions added is shown for comparison. In the process of spectrum analyses, several equivalent circuits modeling layered structures were tested. Finally, equivalent circuits shown in Fig. 5

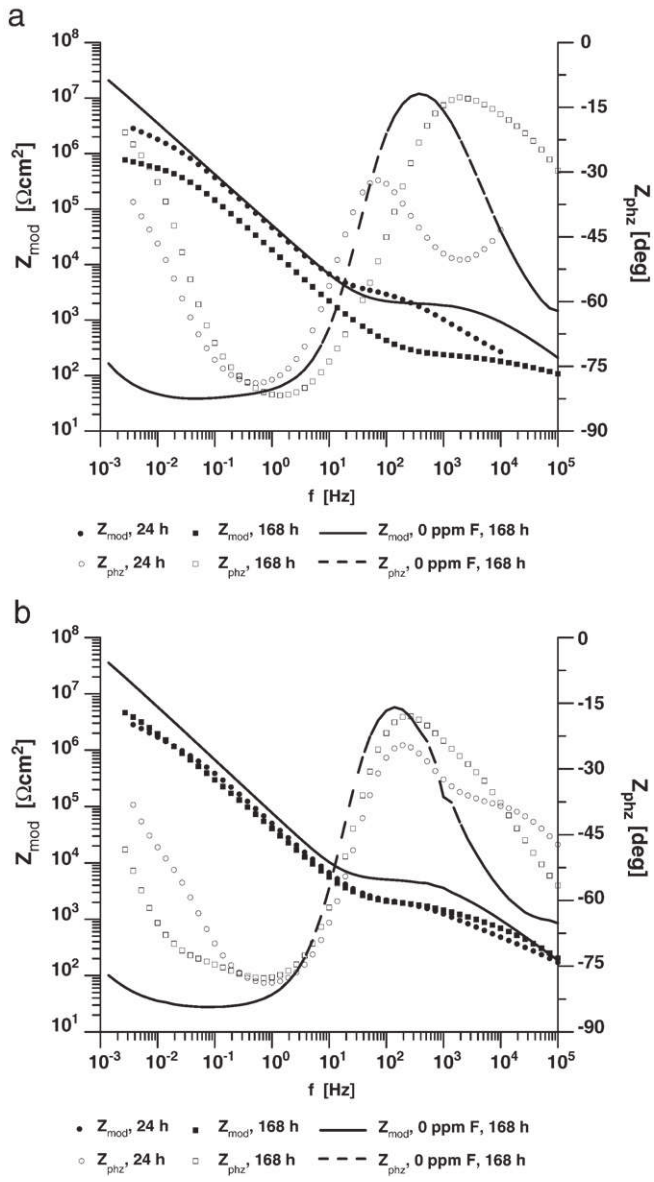

Fig. 1. EIS spectrum of polished specimens (PS, pH = 4.2, 200 ppm F^- — 24 and 168 h, 0 ppm F^- — 168 h); a. Ti/Ti/DLC, b. Ti6Al4V/Ti/DLC.

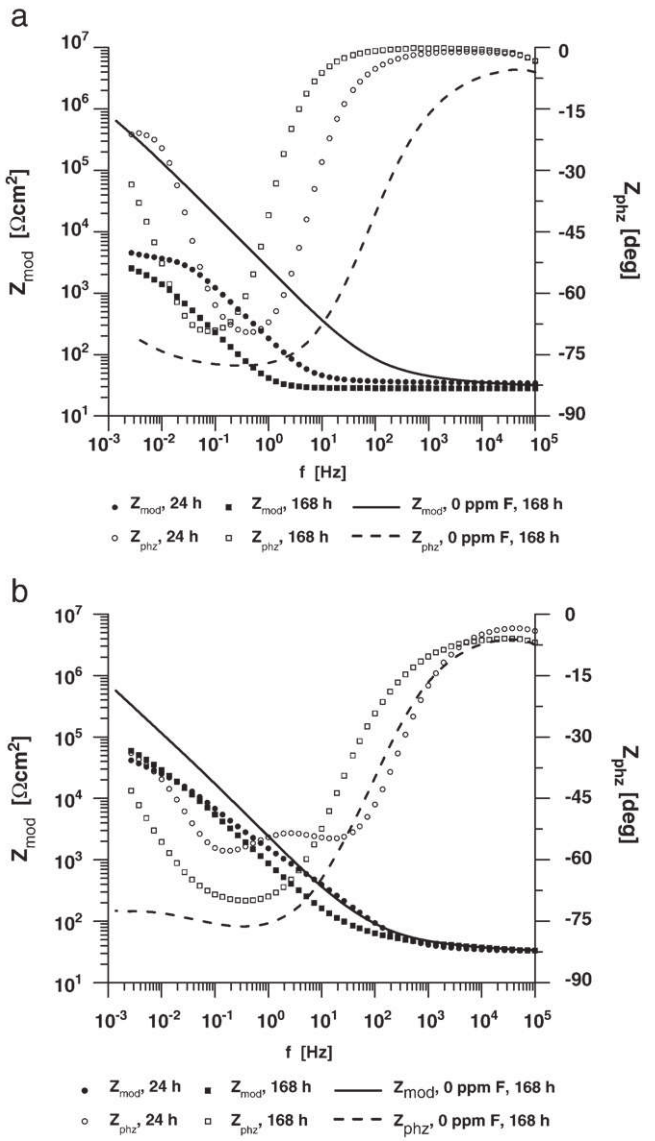

Fig. 2. EIS spectrum of jet-blasted specimens (PS, pH = 4.2, 200 ppm F^- — 24 and 168 h, 0 ppm F^- — 168 h); a. Ti/Ti/DLC, b. Ti6Al4V/Ti/DLC.

were used. The first (Fig. 5a) models a non-porous layered structure while the second (Fig. 5b) takes into account the effect of pores [25–27]. In equivalent circuit 5a, the charge is transferred via a "compact" layer while model 5b assumes the influence of electrolyte in the coating defects. The RC element designated with the index "out" represents the layer-electrolyte phase boundary while the index "in" designates the phase boundary DLC-interlayer (5a) or electrolyte (in pores)-interlayer (5b). The RC element with the index "s" is a correction to surface processes [28]. Tables 1 and 2 show the overall resistance calculated as a sum of individual contributions determined by way of spectrum analysis ($R_{sum} = R_{out} + R_{in}$). The value of R_s part was at the level of tens to hundreds of ohms. Unambiguousness of the EIS spectrum description using an equivalent circuit was decided based on the convergence criterion value (at a distinctly lower level in the case of one of the equivalent circuits). Also, errors in determining the parameters of this equivalent circuit were lower. In other cases the result was considered to be ambiguous.

The effect of fluoride ions on the impedance response of the coated specimens indicated influence layer failures. EIS spectra of the substrate materials and chromium are shown in Fig. 6, R_{sum} values are summarized in Table 3.

The XPS analysis of titanium and Ti6Al4V alloy exposed in physiological solution with pH = 4.2 confirmed the assumable presence of titanium, aluminum and vanadium oxides. After exposure in the same environment electrolyte with 200 ppm fluoride ions added, potassium and fluorine were detected on the surface besides titanium and oxygen. In the case of TiAlV, vanadium concentration increased significantly — the ratio of atomic percentage was Ti/Al = 6.1 in an environment without fluoride ions, it changed to 0.69 in a fluoride-containing environment.

The amount of chromium released into both types of exposure environment (pH = 4.2 and pH = 4.2 + 200 ppm F) was less than 0.5 ng/ml, i.e. below the ICP/MS method detection limit for all specimen variants (Ti, TiAlV, surface P, JB).

Figs. 7–9 and Table 3 summarize the results of the biological tests. In all cases, the colonization of the coated specimens' surface was higher than that recorded for control. It was easier on rougher surfaces, which is a positive fact in relation to implants. MG 63 cell adhesion to individual specimens differed by its dynamics in the course of the measurement, but the results were in the range of negative

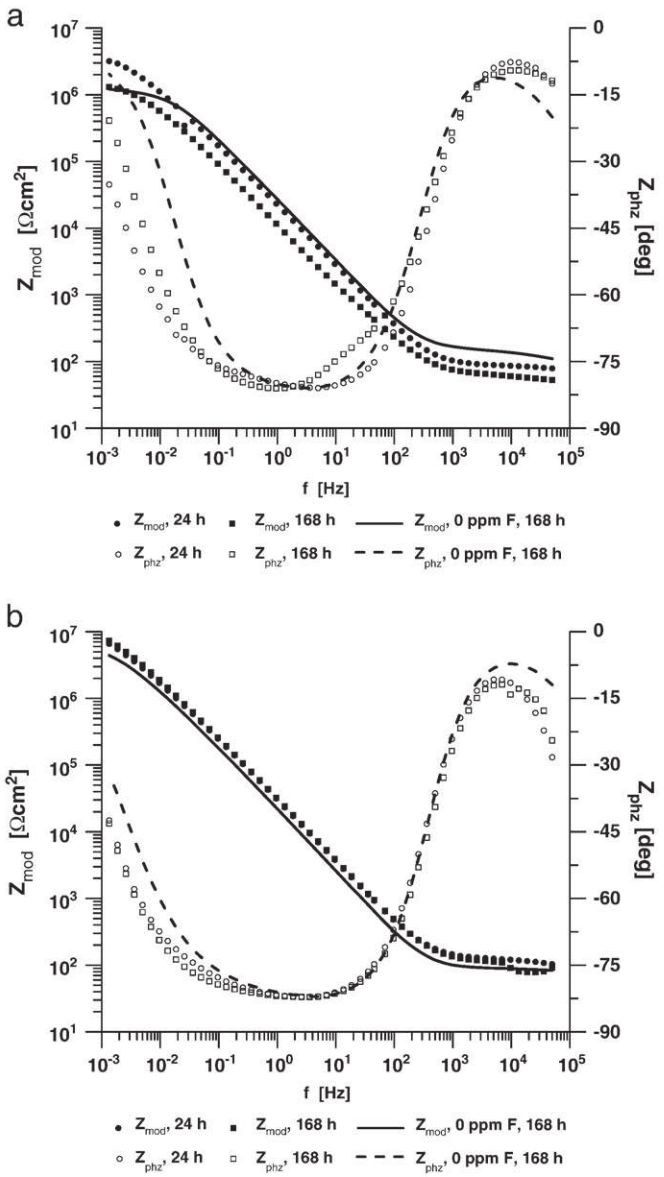

Fig. 3. EIS spectrum of polished specimens (PS, pH = 4.2, 200 ppm F^- — 24 and 168 h, 0 ppm F^- — 168 h); a. Ti/Cr/DLC, b. Ti6Al4V/Cr/DLC.

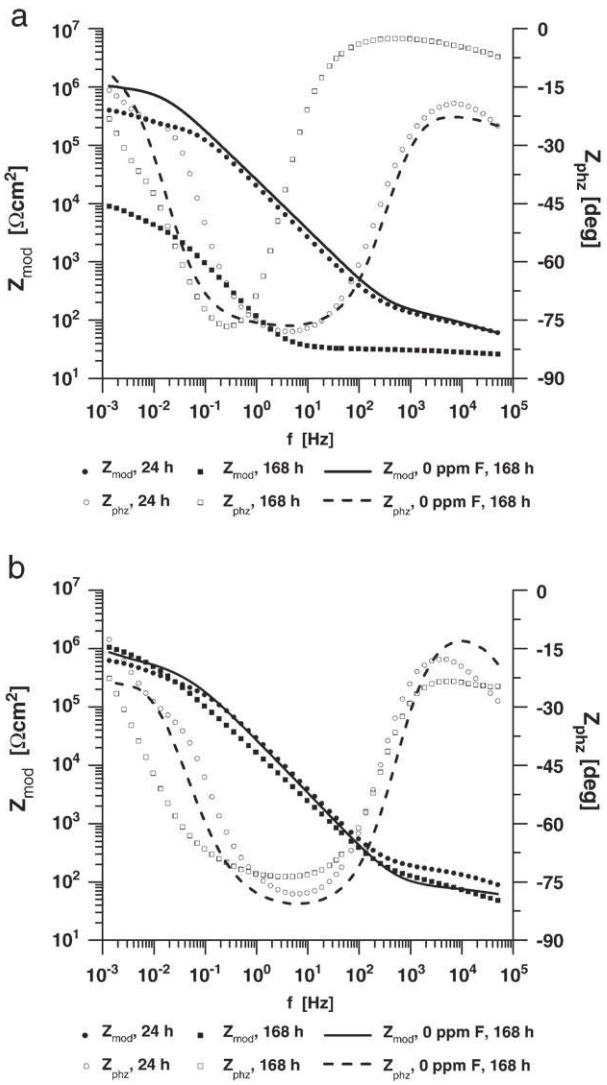

Fig. 4. EIS spectrum of jet-blasted specimens (PS, pH = 4.2, 200 ppm F^- — 24 and 168 h, 0 ppm F^- — 168 h); a. Ti/Cr/DLC, b. Ti6Al4V/Cr/DLC.

control in 1 h. Extracts from individual coated systems were non-cytotoxic, and they did not cause any chromosomal aberrations.

4. Discussion

Implants made of titanium or titanium-based alloys are exposed to the impact of acetylene atmosphere at a temperature of 200–250 °C during their coating. In the course of this process, hydrogen may diffuse into the material causing degradation of the surface mechanical properties due to hydride formation–hydrogen embrittlement [29–31]. It is thus necessary to carefully control the C_2H_2 flow rate at the start of the gradient transition from Ti to Ti–C:H so as to eliminate the origin of a TiH phase. In terms of technology, this procedure is more demanding than the process related to the formation of a chromium inter-layer, which does not allow for the formation of a brittle hydride phase. Technological reasons together with a decreased risk of unacceptable results give preference to chromium as an adhesive inter-layer for DLC coatings on titanium and its alloys.

EIS spectra of a nonporous DLC, i.e. carbon layer, should correspond solely to oxidation–reduction reactions of the environment,

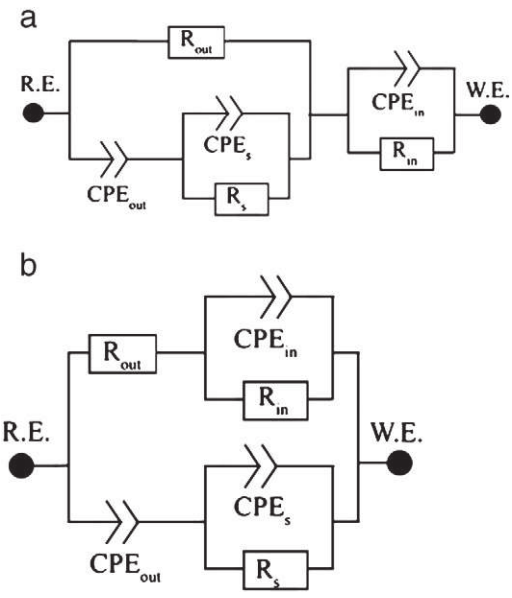

Fig. 5. Equivalent circuits used in EIS spectra analysis.

Table 1
Overall resistance of titanium with a DLC coating.

Surface	Time [h]	Average R_{sum} [Ω cm^2]	Behavior
Cr inter-layer, pH = 4.2, 0 ppm F			
P	24	$6.26 \cdot 10^6$	Ambiguous, comparable fit quality
P	168	$1.28 \cdot 10^6$	Ambiguous, comparable fit quality
JB	24	$3.73 \cdot 10^6$	Ambiguous, comparable fit quality
JB	168	$1.07 \cdot 10^6$	Ambiguous, comparable fit quality
Cr inter-layer, pH = 4.2, 200 ppm F			
P	24	$5.15 \cdot 10^6$	Porosity
P	168	$1.56 \cdot 10^6$	Porosity
JB	24	$4.90 \cdot 10^5$	Porosity
JB	168	$1.32 \cdot 10^4$	Porosity
Ti inter-layer, pH = 4.2, 0 ppm F			
P	24	$1.46 \cdot 10^8$	Ambiguous, comparable fit quality
P	168	$1.60 \cdot 10^8$	Ambiguous, comparable fit quality
JB	24	$6.33 \cdot 10^6$	Ambiguous, comparable fit quality
JB	168	$3.94 \cdot 10^6$	Ambiguous, comparable fit quality
Ti inter-layer, pH = 4.2, 200 ppm F			
P	24	$5.39 \cdot 10^6$	Porosity
P	168	$9.95 \cdot 10^5$	Porosity
JB	24	$9.90 \cdot 10^3$	Porosity
JB	168	$3.98 \cdot 10^3$	Porosity

in this case to electrochemical processes of oxygen in which carbon participates only as a charge carrier. Impedance spectra of titanium and titanium grade 5 with both types of inter-layers exposed in a physiological saline solution are similar. These are systems with a high resistance to charge transfer, as evident from Figs. 1–4, and Tables 1 and 2. The effect of an adhesion inter-layer on the course of these dependences did not really express itself. Based on impedance spectra it is not possible to say definitely whether the layers exhibit porosity. Both applied equivalent circuits can fit data very well; the convergence criterion values were comparable.

The total resistance to the charge transfer (R_{sum}) was higher than 1×10^6 Ω cm^2 for all specimens with a coating formed on a polished surface in the PS environment, which corresponded to the corrosion rate, calculated for titanium, lower than 1 μm/a. The electrochemical behavior could differ only if the electrolyte got in contact with a phase boundary of a different composition — in our case it could have been contamination of the coating with chromium or titanium. XPS analysis nevertheless did not prove the presence of chromium

Table 2
Overall resistance of Ti6Al4V with a DLC coating.

Surface	Time [h]	Average R_{sum} [Ω cm^2]	Behavior
Cr inter-layer, pH = 4.2, 0 ppm F			
P	24	$6.20 \cdot 10^6$	Ambiguous, comparable fit quality
P	168	$8.91 \cdot 10^6$	Ambiguous, comparable fit quality
JB	24	$6.23 \cdot 10^6$	Ambiguous, comparable fit quality
JB	168	$1.25 \cdot 10^6$	Ambiguous, comparable fit quality
Cr inter-layer, pH = 4.2, 200 ppm F			
P	24	$9.57 \cdot 10^6$	Ambiguous, comparable fit quality
P	168	$1.24 \cdot 10^7$	Ambiguous, comparable fit quality
JB	24	$6.94 \cdot 10^5$	Porosity
JB	168	$1.43 \cdot 10^6$	Porosity
Ti inter-layer, pH = 4.2, 0 ppm F			
P	24	$3.15 \cdot 10^8$	Ambiguous, comparable fit quality
P	168	$2.88 \cdot 10^8$	Ambiguous, comparable fit quality
JB	24	$6.91 \cdot 10^6$	Porosity
JB	168	$2.26 \cdot 10^7$	Porosity
Ti inter-layer, pH = 4.2, 200 ppm F			
P	24	$4.93 \cdot 10^6$	Ambiguous, rather porosity
P	168	$9.61 \cdot 10^6$	Ambiguous, rather porosity
JB	24	$8.43 \cdot 10^4$	Porosity
JB	168	$1.24 \cdot 10^5$	Porosity

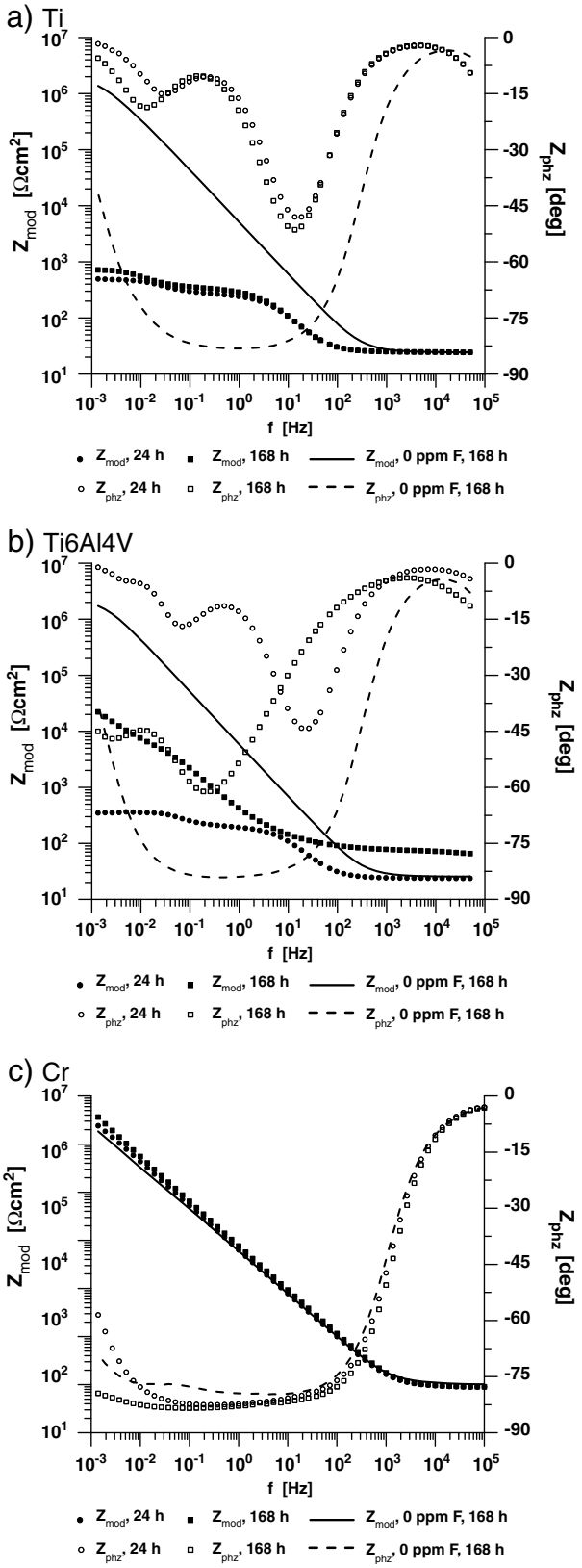

Fig. 6. Ti, Ti6Al4V and Cr EIS spectra (PS, pH = 4.2, 0 ppm F$^-$, 200 ppm F$^-$).

or titanium (in the case of a chromium or titanium adhesive inter-layer, respectively) on the specimens surface. The signal on the respective binding energy (Ti 2p, 452–468 eV; Cr 2p, 570–582 eV) was always on the level of the background. The only signals detected were carbon (C 1s) and oxygen (O 1s) lines. Explanation of the

Table 3
Overall resistance of titanium, Ti6Al4V alloy and chromium.

Material	Environment	R_{sum} [Ω cm^2]	Character
Ti grade 2, polished	pH = 4.2, 0 ppm F	$11 \cdot 10^6$	Passive
	pH = 4.2, 200 ppm F	447	Active, layer of corrosion products
Ti 6Al4V, polished	pH = 4.2, 0 ppm F	$43 \cdot 10^6$	Passive
	pH = 4.2, 200 ppm F	620	Active, layer of corrosion products
Cr, polished	pH = 4.2, 0 ppm F	$13 \cdot 10^6$	Passive
	pH = 4.2, 200 ppm F	$32 \cdot 10^6$	Passive

differences in R_{sum} on polished specimens with a chromium/titanium interlayer, which, however, are of no great significance from the practical point of view, would have to be sought in a more detailed evaluation of the properties and electrochemical behavior of DLC layers.

Carbon is stable/inert in an environment containing fluoride ions at a concentration level tested in this work. Consequently, increase of environment aggressiveness toward titanium, resulting from the presence of fluorides, should have any impact on the course of the EIS spectra of specimens coated by a nonporous layer. Measurements showed that this assumption was not confirmed for any of the studied systems.

Charge transfer resistance of Ti/Ti/DLC specimens with a polished surface dropped about five-times in the course of exposure in a fluoride-containing environment, and the spectra character changed. A far more distinct change was recorded for the same system with a jet-blasted surface. After the first 24 h of exposure, spectra were diametrically different from the dependences measured in an electrolyte without fluoride ions. The system's behavior did not change in any significant way in the course of the further exposure. For both types of surfaces, data fitting was significantly more successful with the use of an equivalent circuit modeling a porous layer. Similar but less distinct changes were recorded for Ti6Al4V/Ti/DLC specimens. The overall resistance of polished specimens did not practically change after the initial decrease, preserving its high value. Specimens with a layer deposited on a jet-blasted surface behaved in a similar way. The overall resistance dropped by about an order of magnitude in comparison with the dependences measured in an electrolyte without fluoride ions. Unlike the spectra character, however, it did not change in the course of exposure.

It is a generally well-known that the presence of fluoride ions, more strictly speaking the presence of hydrofluoric acid originating by hydrolysis, in an environment destabilizes titanium oxides [32–34]. These oxides form the passive layer which is the bearer of corrosion resistance. Changes in the character of the spectra of specimens with a titanium inter-layer recorded in a fluoride-containing environment proved that even layers formed on polished surface contained through-thickness defects. The electrolyte may have got in contact with the inter-layer or with the bulk material through these defects.

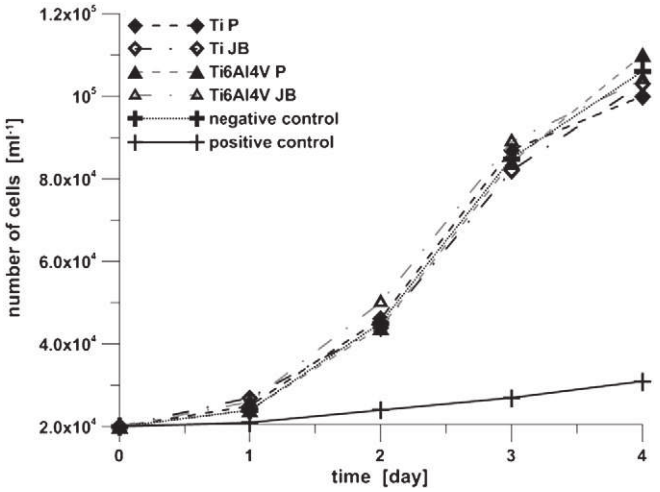

Fig. 8. Cytotoxicity test (samples with chromium interlayer).

EIS spectra of non-coated titanium, Ti6Al4V and chromium (Fig. 6, Table 3) exposed in a physiological saline solutions without fluorides represent passive materials with an almost identical behavior. Spectra may be fitted using a simple model containing only one R-CPE element [35]. An addition of fluoride ions led to a sharp change in the corrosion behavior of titanium. Impedance dropped by three orders of magnitude as soon as after 24 h of exposure, but it did not change in any significant way afterwards. XPS analysis of exposed samples confirmed the presence of fluorine and potassium, in addition to the predictable elements. This fact was explained formerly by the formation of a low-soluble saline layer containing fluoride ions [36]. The response of the Ti/Ti/DLC specimens with a jet-blasted surface to the presence of fluorides in the electrolyte roughly corresponded to this behavior. The electrolyte got in contact with titanium, which intensified the corrosion process and decreased overall resistance. In specimens of the same type but with a polished surface, the response intensity rate was less pronounced due to a lower number of through-layer thickness defects. Non-coated Ti6Al4V alloy responded to the presence of fluoride ions in a different way. The initial impedance drop was less distinct, but spectra were changing permanently

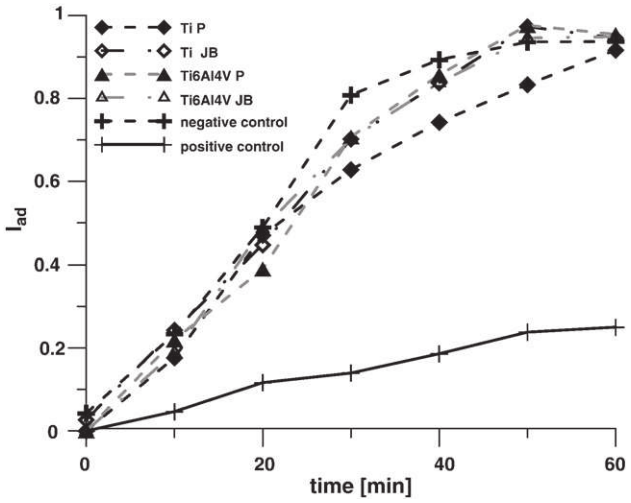

Fig. 7. Cell adhesion test (samples with chromium interlayer).

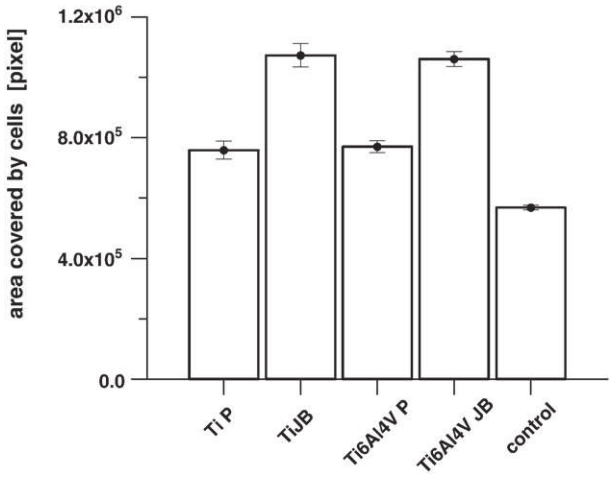

Fig. 9. Colonization test (samples with chromium interlayer).

for the whole time of exposure. In its final stage, i.e. after 168 h, the spectra of the alloy and titanium were basically identical. XPS analysis of a non-coated TiAlV specimen exposed in a fluoride-containing environment for 24 h showed that the surface concentration of aluminum rose to a level exceeding its content in the alloy several times. The signal of potassium and fluorine indicating the origin of a compound was detected again. The drop in the coated system corrosion resistance slowed down due to the change in the character of passive layer. At the same time, communication with the electrolyte volume was probably limited due to the compound origin.

The effect of a change in the environment's corrosion aggressiveness was far less evident in both titanium and Ti6Al4V samples coated with a system containing a chromium inter-layer. The presence of fluorides had practically no effect on the behavior of specimens with a DLC coating deposited on a polished surface. The overall resistance stayed high, with no change in the spectra character recorded. The behavior of jet-blasted specimens with different substrates was different. A lasting impedance decrease was recorded for specimens on titanium. The effect of porosity was unambiguous in this case. Impedance of specimens with a Ti6Al4V substrate dropped by an order of magnitude at the beginning of exposure, but it did not change in any way afterwards. Basic explanation may be deduced from the behavior/corrosion resistance of chromium in an environment containing fluorides. Pure chromium, as shown in Fig. 6c, is highly corrosion-resistant in the given environment. The electrolyte in pores of polished samples gets in contact with a corrosion-resistant chromium inter-layer and, probably also due to a limited electrolyte exchange through pores, the corrosion process does not significantly continue. A number of factors may be expected to manifest themselves in the case of layers formed on jet-blasted surfaces, such as an easier electrolyte exchange, probable existence of chromium partly in the form of carbide, and the substrate effect.

The above results indicate that coated systems with both types of the adhesive inter-layer display comparable behavior in a common chloride containing environment. Under critical conditions of corrosion exposure, which may occur when a patient with dental implants is treated with fluoride preparations, the properties of systems with a chromium inter-layer are better.

Tests of biological acceptability of coated systems with a chromium inter-layer are inevitable for their use in biomaterial applications, in which titanium is applied without any problems. A basic test of the release of soluble corrosion products showed that during a 24-hour exposure, chromium was not released at a level that would be detected by the highly sensitive ICP/MS analytical method, this applying even to an electrolyte containing fluorides. A set of standard biological tests led to similar conclusions. According to the results (Fig. 7), the cells' primary contact with the material, evaluated by the adherence test whose kinetics was slightly different on different surfaces in the course of the measurement, led to comparable colonization of the specimen surfaces with cells at the end of the measurement, with the adherence index corresponding to the negative control (Fig. 7). The growth of the cell culture, characterized by the cytotoxicity test (Fig. 8), was again almost identical and comparable with the negative control. In general we may say that the cell culture colonized the surface and the products of the specimen's interaction with the cultivation environment did not have any negative effect on its development. According to the results of the colonization test (Fig. 9) colonization by a comparable number of cells, according to the adherence test results, was much easier on a rougher surface, again regardless of the interlayer or the substrate material composition. The occurrence of chromosomal aberrations ascertained by the measurement (Table 4) corresponded to the general level in the population. The studied materials did not have any negative effect on their frequency. As to the applicability of a chromium inter-layer in human implantology, the results of all the conducted measurements were positive. Based on this data we may assume that the use of a chromium inter-layer in implant coatings should not represent health risk for patients.

Table 4
Chromosomal aberration test.

Sample	Aberrated cells [%]
Ti P	4
Ti JB	3
Ti6Al4V P	4
Ti6Al4V JB	4
Positive control	18

5. Conclusions

The present work studied the effect of a titanium or chromium adhesive inter-layer on the interaction of DLC-coated titanium and Ti6Al4V with a physiological saline solution with a decreased pH and fluoride ions added. Both coated systems regardless of the basic material behaved comparably in an environment without fluoride ions. An addition of fluorides proved the existence of through-layer thickness defects even in specimens with a surface polished prior to coating. The best corrosion behavior was recorded for specimens with a chromium inter-layer on both types of substrates. In the case of a titanium inter-layer, corrosion resistance of coatings on Ti6Al4V was higher than that on titanium. The conducted biological tests indicated applicability of a chromium inter-layer for DLC-coated implants.

Acknowledgment

This work was supported by the Grant Agency of the Czech Republic project no. P108/10/1782.

References

[1] R. Matsumoto, K. Sato, K. Ozeki, K. Hirakuri, Y. Fukui, Diamond Relat. Mater. 17 (2008) 1680.
[2] M. Jelínek, K. Smetana, T. Kocourek, B. Dvořánková, J. Zemek, J. Remsa, T. Luxbacher, Mater. Sci. Eng., B 169 (2010) 89.
[3] W.J. Ma, A.J. Ruys, R.S. Mason, P.J. Martin, A. Bendavid, Z. Liu, M. Ionescu, H. Zreiqat, Biomaterials 28 (2007) 1620.
[4] E. Salgueiredo, M. Vila, M.A. Silva, M.A. Lopes, J.D. Santos, F.M. Costa, R.F. Silva, P.S. Gomes, M.H. Fernandes, Diamond Relat. Mater. 17 (2008) 878.
[5] F. Chai, N. Mathis, N. Blanchemain, C. Meunier, H.F. Hildebrand, Acta Biomater. 4 (2008) 1369.
[6] A. Soininen, V.-M. Tiainen, Y.T. Konttinen, H.C. van der Mei, H.J. Busscher, P.K. Sharma, J. Biomed. Mater. Res. Part B 90B (2009) 882.
[7] G. Dearnaley, J.H. Arps, Surf. Coat. Technol. 200 (2005) 2518.
[8] A. Sargeant, T. Goswami, Mater. Des. 28 (2007) 155.
[9] K. Gutensohn, C. Beythien, J. Bau, T. Fenner, P. Grewe, R. Koester, K. Padmanaban, P. Kuehnl, Thromb. Res. 99 (2000) 577.
[10] J. Sui, W. Cai, Diamond Relat. Mater. 15 (2006) 1720.
[11] Y. Cheng, Y.F. Zheng, Surf. Coat. Technol. 200 (2006) 4543.
[12] S. Gayathri, R. Krishnan, T.R. Ravindran, S.T. Sundari, S. Dash, A.K. Tyagi, B. Raj, M. Sridharan, Mater. Res. Bull. (2010), http://dx.doi.org/10.1016/j.materresbull.2011.11.042.
[13] M. Nöthe, U. Breuer, F. Koch, H.J. Penkalla, W.P. Rehbach, H. Bolt, Appl. Surf. Sci. 179 (2001) 122.
[14] M. Azzi, P. Amirault, M. Paquette, J.E. Klemberg-Sapieha, L. Martinu, Surf. Coat. Technol. 204 (2010) 3986.
[15] G. Wu, L. Sun, W. Dai, L. Song, A. Wang, Surf. Coat. Technol. 204 (2010) 2193.
[16] Y. Fovet, J.Y. Gal, F. Toumelin-Chemla, Talanta 53 (2001) 1053.
[17] B.D. Ratner, A.S. Hoffman, F.J. Schoen, J.W.E. Lemons, Elsevier, Amsterdam, 2004, p. 1237.
[18] X. Gao, R.-x. He, S.-g. Yan, L.-d. Wu, J. Arthroplast. 26 (2011) 665.e613.
[19] Y. Niki, H. Matsumoto, T. Otani, T. Yatabe, M. Kondo, F. Yoshimine, Y. Toyama, Biomaterials 26 (2004) 1019.
[20] A.J. Ortiz, E. Fernandez, A. Vicente, J.L. Calvo, C. Ortiz, Am. J. Orthod. Dentofacial Orthop. 140 (2011) e115.
[21] V. Barranco, M.L. Escudero, M.C. Garcia-Alonso, Electrochim. Acta 52 (2007) 4374.
[22] W.M. Haynes (Ed.), CRC Handbook of Chemistry and Physics, 92nd edition, Taylor & Francis group, LLC, London, 2008, Internet Version 2011.

[23] R. Jacobs, J. Meneve, G. Dyson, D.G. Teer, N.M. Jennett, P. Harris, J. von Stebut, C. Comte, P. Feuchter, A. Cavaleiro, H. Ronkainen, K. Holmberg, U. Beck, G. Reiners, C.D. Ingelbrecht, Surf. Coat. Technol. 174–175 (2003) 1008.
[24] Z.X. Zhang, H. Dong, T. Bell, Surf. Coat. Technol. 200 (2006) 5237.
[25] J. Pan, D. Thierry, C. Leygraf, Electrochim. Acta 41 (1996) 1143.
[26] M.E.P. Souza, M. Ballester, C.M.A. Freire, Surf. Coat. Technol. 201 (2007) 7775.
[27] V. Moutarlier, M.P. Gigandet, B. Normand, J. Pagetti, Corr. Sci. 47 (2005) 937.
[28] G. Nurk, J. Eskusson, R. Jaaniso, E. Lust, J. Solid State Electrochem. 7 (2003) 421.
[29] A. Efron, Y. Lifshitz, I. Lewkowicz, M.H. Mintz, J. Less Common Metals 153 (1989) 23.
[30] L. Luo, Y. Su, J. Guo, H. Fu, J. Alloys Compd. 425 (2006) 140.
[31] Y. Ohgoe, S. Kobayashi, K. Ozeki, H. Aoki, H. Nakamori, K.K. Hirakuri, O. Miyashita, Thin Solid Films 497 (2006) 218.
[32] G. Boere, J. Appl. Biomater. 6 (1995) 283.
[33] F. Toumelin-Chemla, F. Rouelle, G. Burdairon, J. Dent. 24 (1996) 109.
[34] M. Nakagawa, S. Matsuya, T. Shiraishi, M. Ohta, J. Dent. Res. 78 (1999) 1568.
[35] B. Cottis, S. Turgoose, Corrosion Testing Made Easy: Impedance and Noise Analysis, 1999.
[36] L. Joska, J. Fojt, J. Mater. Sci. Mater. Med. 21 (2010) 8.

Tribology International 63 (2013) 61–65

Contents lists available at SciVerse ScienceDirect

Tribology International

journal homepage: www.elsevier.com/locate/triboint

Hinge-type knee prosthesis wear tests with a mechanical load and corrosion properties monitoring

Lukas Franta [a,*], Jaroslav Fojt [b], Ludek Joska [b], Jakub Kronek [a], Ladislav Cvrcek [c,d], Jiri Vyskocil [c], Zdenek Cejka [e]

[a] Czech Technical University in Prague, Department MBM, Technicka 4, 166 07 Prague 6, Czech Republic
[b] Institute of Chemical Technology Prague, Department of Metals and Corrosion Engineering, Technicka 5, 166 28 Prague 6, Czech Republic
[c] HVM PLASMA Ltd., Na Hutmance 2, 158 00 Prague, Czech Republic
[d] Czech Technical University in Prague, Department of Control Engineering, Technická 2, 166 27 Prague, Czech Republic
[e] ProSpon Ltd., Jiřího Voskovce 3206, 272 01 Kladno, Czech Republic

ARTICLE INFO

Article history:
Received 20 October 2011
Received in revised form
30 January 2012
Accepted 21 February 2012
Available online 1 March 2012

Keywords:
Wear conditions
DLC layer
PEEK polymer
Corrosion monitoring

ABSTRACT

The primary goal was to compare model replacements with and without DLC layer. Components were made of the Ti6Al4V alloy and coated with a DLC layer, the sliding sleeve made of a PEEK polymer. Testing was done in the saline physiological solution (9 g/L NaCl). The measuring system was supplemented with the corrosion behavior monitoring.

The results show that the applied DLC coating significantly increases the service life of the implant. Based on the results it is possible to state that an accurate mechanical load together with corrosion behavior monitoring shifts testing in the given field to a qualitatively higher level.

1. Introduction

The hinge type of total knee replacement stands away from the main stream of related research due to its non-anatomic joint movements, yet it is the only possible option for some medical indications. A great part of implantations are conducted on patients after a bone tumor operation in the vicinity of the knee joint. Given the ever growing rate of success in the field of tumor treatment, mechanical and tribological requirements on implants are increasing accordingly. Similarly as in the case of anatomic replacements, younger patients in particular wish to preserve their active life style in spite of the seriousness of their illness, and perform their everyday activities with the aid of total replacement. From patients' point of view, joint replacement implantation represents a radical medical intervention in their body followed by convalescence. Consequently, their logical and justified requirement is for the implant to fulfill its function in the body as long as possible even after the primary illness has been cured. In vitro simulations may serve as an important tool in predicting the abrasive behavior of the implant and/or of new materials applied in the implant contact pair. Since a simulation cannot provide for entirely identical conditions as those of the joint dynamic movement after implantation, in vitro testing of implant components is conducted with some sets of movement and load parameters simplified [1]. However, this modification must not decrease the informative value of experiments with regard to the clinical practice [2].

Mechanical load may significantly affect the properties of materials applied in orthopedic implants. Consequently, scientists search for ways allowing for the use of current materials, well-tested in a number of other biological applications, in highly loaded implants as well. DLC layers (Diamond-Like-Carbon layers) represent a suitable choice for bio-tribological applications due to their high wear resistance [3]. Another reason for using these layers in biomedical applications rests in their bio-inert character, low friction coefficient, high hardness, and good wear and corrosion resistance. DLC coating may be obtained by way of various coating technologies [4–6]. Lasting interest is devoted to assessing the efficacy of DLC coating and the mechanisms of its wear.

While testing real components, it is usually impossible to fix the time of the damage initiation and then interrupt the test in order to evaluate the implant state and search for its cause. It is therefore desirable to supplement the obtained set of monitored values with a quantity that would sensitively react to the implant surface conditions/corrosion behavior. Corrosion resistance of

* Correspondence to: Czech Technical University in Prague, Faculty of Mechanical Engineering, Department MBM, Technicka 4, 166, 07 Prague, Czech Republic.
Tel.: +420 224352746; fax: +420 233322482.
E-mail address: frantal@biomed.fsid.cvut.cz (L. Franta).

0301-679X/$ - see front matter © 2012 Elsevier Ltd. All rights reserved.
doi:10.1016/j.triboint.2012.02.014

titanium and its alloys is based on their ability to passivate, which ensues from the existence of the passive layer. In the given case it is a thin (thickness in the order of nanometers) oxide layer which forms very quickly in the air or in electrolytes containing oxygen [7]. Coating with a DLC layer, aimed primarily at improving tribological properties, has a neutral or positive effect on the corrosion properties of a coated Ti-DLC system. The DLC layer takes over part of the cathodic process (oxygen reduction), thus increasing the passive state stability in layer pores.

Corrosion behavior of metallic materials, or layers deposited on a metallic base, can be monitored by way of a number of methods providing good-quality information about corrosion behavior as well as corrosion rate quantification. Open circuit potential monitoring is the simplest method of examining passive materials. Its changes (decrease) at a passive layer breakdown may range in the order of several hundreds of millivolts. The instrumental part of such monitoring system is relatively simple. Its outcome is the open circuit potential time dependence, on which the passive layer degradation manifests itself by a gradual decrease in the measured value or, in case of a local breakdown, by jumps of the potential. Similarly, electrochemical noise measurement method also provides rather qualitative information about the state of the passive layer. This method consists of scanning the oscillation of the same quantity as in the preceding case, i.e. the open circuit potential (frequency in the order of 10^1 Hz and lower), around its mean value. Passivity breakdowns are indicated by increasing electrochemical noise. More quantitative information about the rate of corrosion processes, even in systems with a changing mechanical load, can be provided by polarization resistance measurement [8]. However, application of the last mentioned methods requires more sophisticated instrumentation.

The presented study is aimed to assess the DLC layer effect on the tribological properties of a model knee joint prosthesis, and to ascertain applicability of open circuit potential measurement in identifying an early stage of damage.

2. Material and methods

The tested implants were coated with a DLC layer using Hauzer Flexicoat 1200 equipment (chamber volume 1000l). Prior to deposition, the implants were degreased in an ultrasound alkaline bath, rinsed in deionized water and dried in vacuum. Ti6Al4V (Ti Grade 5 ELI) was used for the implants. Then the implants were cleaned in argon plasma and coated with an adhesive interlayer with a gradient composition changing from Ti to Ti-C:H. The interlayer was deposited by way of nonequilibrium magnetron sputtering from Ti (99.5) targets in Ar (99.999% purity) and C_2H_2 (99.6% purity) atmosphere. The upper layer a-C:H was deposited using the PACVD (Plasma Assisted Chemical Vapor Deposition) method, with a pulsed bias 50 kHz applied on the substrates holder and peak voltage 200 V. Deposition temperature was 200 °C, C_2H_2 flow 500 sccm, base pressure 2.10^{-3} Pa and exposition pressure 1.0 Pa.

The measurement of the layers mechanical properties was carried out on metallographically polished DIN X153CrMoV12 steel specimens hardened to 62 HRC. They were placed in the same positions as the coated implants. The thickness of the deposited layers was determined using a calotest method, the layers adhesion to the coated material was tested on CSEM Revetest equipment using the standard scratch test method. A second adhesion measurement, Mercedes test, was conducted for comparison. The surroundings of the stab created by the hardness measuring device with a diamond Rockwell tip at a load of 150 kg (HRC) was optically assessed, and evaluated using a parameter from 1 to 6. The Fischer PICODENTOR® HM500 device was used to measure the layers hardness. The measurement was carried out at a load of 20 mN. HV values corresponding to the standard Vickers hardness were calculated.

The simulator—KKK ELO 2007 (Fig. 1) was developed for the testing according to the ISO standard for knee joint prostheses [9]. The knee joint simulator was designed so as to simulate flexion, AP movement (forward–backward) and IE rotation (internal–external). This means that the simulator had three controlled kinematical degrees of freedom. The component movements were controlled by one linear and two torsion independent motors. The exposed component was placed in a cell closed with a flexible latex element coated with a layer of silicon rubber. Saline solution containing 9 g/L sodium chloride was used as the testing medium at 37.0 ± 0.2 °C. The cell diagram is shown in Fig. 1. The hinge, the femoral section and the tibial components of the studied implants were made of the Ti6Al4V alloy (Ti Grade 5). The pair of sliding sleeves placed in the tibial component was made of PEEK polymer.

In terms of the load kinematics and dynamics, the experiment was designed in agreement with requirements on the real range

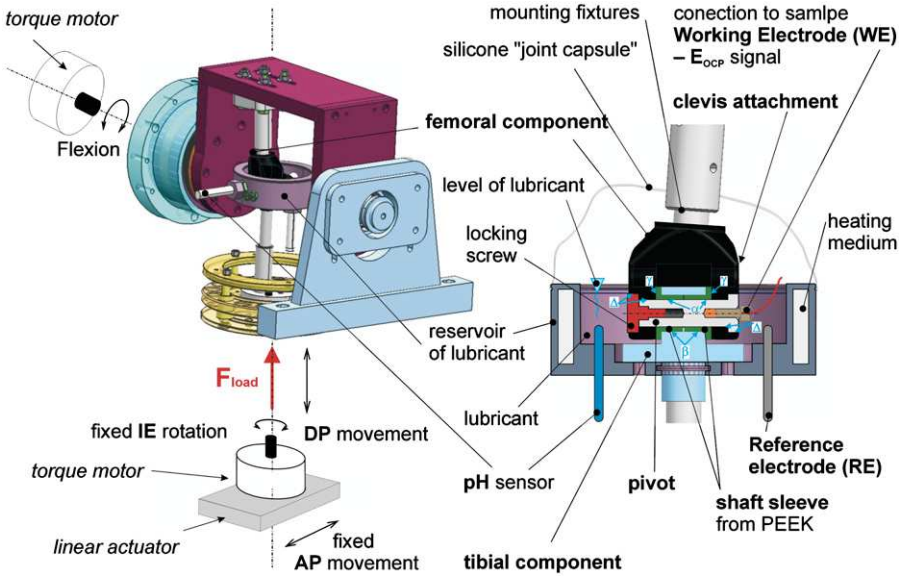

Fig. 1. Exposure system diagram.

of motion and the loading force. Loading close to the real movements could be performed either on the basis of a movement analysis or, in a more simple way, according to the ISO 14 243 standard [9]. The latter alternative was chosen for measurements due to the absence of movements in the anatomic direction of the AP displacement and IE rotation. Contact pairs Ti Grade 5 with a DLC coating (pivot, fork of femoral component and rod eye of tibial component) set against PEEK polymer (joint bearing sleeve) were tested. A comparative measurement was carried out with the same non-coated components of Ti Grade 5, again set against PEEK polymer.

The damage of the replacement contact pairs was evaluated periodically after every 0.5×10^6 cycles, according to the standard requirements. The measurement was interrupted at the moment of evident damage or an overall mechanical failure of the implant.

The open circuit potential of the implant was scanned on a continuous basis (period 5 s) in the course of its exposure. The implant pivot was monitored where the highest load and consequently the most probable damage of the coating was assumed. The open circuit potential was measured against a silver-silver chloride-chloride electrode (Ag/AgCl/KCl 3 mol/L), to which all potentials given in the presented work are related. The measurements were performed using the Magic XBC E (Gryf HB) system allowing to record the open circuit potential, temperature and the pH value of the exposure environment.

3. Results and discussion

In the first part of the testing, the reference specimen of a non-coated replacement was exposed in order to verify the functionality of the applied evaluation methods. The measurement was performed using an implant made of Ti6Al4V in combination with PEEK sleeves. As evident from available literature [10–13], combination of material based on a Ti alloy and PEEK sleeves is not really suitable for similar construction elements. The model thus indicated possible behavior of an implant in case the coating failed. According to expectations, continuous evaluation of contact areas revealed clear damage as early as after 1.5×10^5 loading cycles. The experiment conducted with this reference model knee replacement was terminated after 3.0×10^5 cycles due to total damage of the surface of frictional elements causing loss of functionality.

In the course of measurements, three risk points were identified in terms of tribology. The first was sliding contact (α) between the pivot and the inner cylindrical surface of the bearing sleeve made of a PEEK polymer. In terms of construction, this contact was designed primarily to provide for interrelated movement. The second point of risk was sliding contact (β) between the outer cylindrical surface of the PEEK sleeve and the rod eye of the tibial component. The primary purpose of this contact was not to provide for interrelated movement. The third risk point was sliding contact (γ) between the surface of the sleeve perpendicular to the rotational axis and the adjacent fork surface of the femoral component.

The immobile contact (Δ) of the pivot or the locking screw in the fork turned out to be an entirely specific point in the course of the experiment. The implant pivot is secured against rotation in relation to the fork by a shape lock. However, a micro-movement in this connection is possible as a result of production and assembly tolerance. We may thus say that in terms of tribology, this type of construction represents a complicated connection with various possible mechanisms of surface damage, due to a considerable number of risky points of contact. Fig. 2(a–c) illustrates two types of implant pivot damage which occurred in the course of exposure. The first mechanism affected the place of

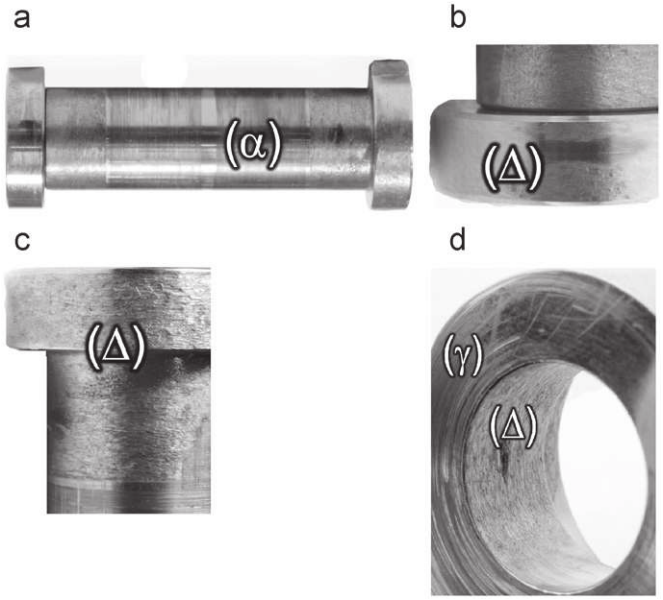

Fig. 2. Non-coated model implant damage—(a) pivot, (b) pivot detail 1, (c) pivot detail 2, and (d) clevis attachment fork.

contact (α) where abrasive damage of the sliding cylindrical surface occurred. Contact (β) was damaged identically, with characteristic circular traces of degradation recorded on the pivot and inside the PEEK bearing sleeves. Point (Δ) displayed characteristic adhesive wear (Fig. 2d—inner cylindrical surface of the fork). The damage was traced on the surface of that part of the contact where the transfer of the dynamic force effect occurred. At sliding contact (γ) between the sleeve surface perpendicular to the rotational axis and the adjacent surface of the femoral component fork, the surface degradation was of a smaller extent. It was in the form of circular traces on one side of the fork, caused by the sleeves rotation during movement. This asymmetrical damage was due to the dynamic effect resultant. The anatomic inclination of the femoral component axis caused asymmetrical load which resulted in axial dynamic effect acting on the inner (medial) side of the femoral component. PEEK sleeves damage was evident on contacts (α), (β) and (γ). The performed surface geometry analyses revealed that the most serious damage occurred in contact (α). After the experiment, the original circular cross section of the sleeves inner holes turned into an elliptical one in consequence of the load. The difference between the main and the side semi-axis of the fitted ellipsis was at a level of 0.1 mm in order of magnitude.

In the course of exposure, the open circuit potential of the implant was scanned. On-line monitoring of the potential was applied in order to allow for interrupting the experiment when surface damage occurred, indicated by a significant decrease in the open circuit potential. This procedure allowed for subsequent visual evaluation of the surface at the very moment of damage occurrence. It is a great advantage over the standard procedure evaluating the state of the implant after a previously set number of simulator cycles. In that case the surface damage could be rather extensive and the identification of the damage initiation point ambiguous.

The open circuit potential of the Ti6Al4V alloy in a saline physiological solution, unexposed to a tribological load, ranged at a level of 12.0 ± 4.5 mV. This value corresponds to a material in the stable passive state in a relatively – for titanium and its alloys – non-aggressive aerated environment [14]. Fig. 3 shows a section of the recorded open circuit potential of the implant reference specimen without DLC coating. Region I of the diagram shows

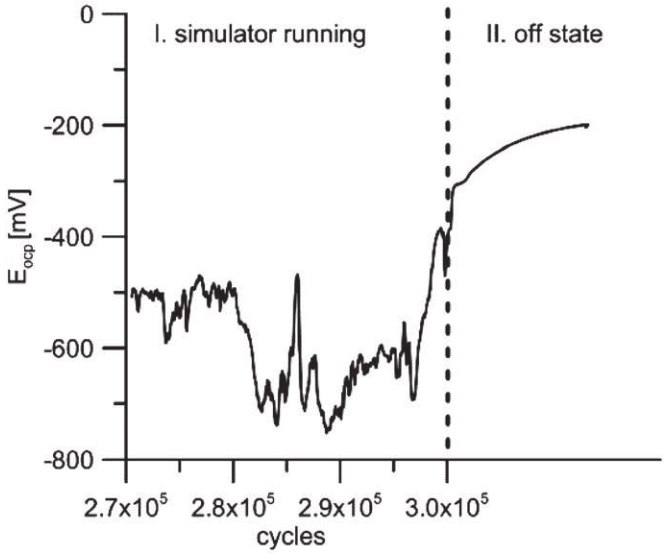

Fig. 3. Time dependence of the non-coated implant open circuit potential.

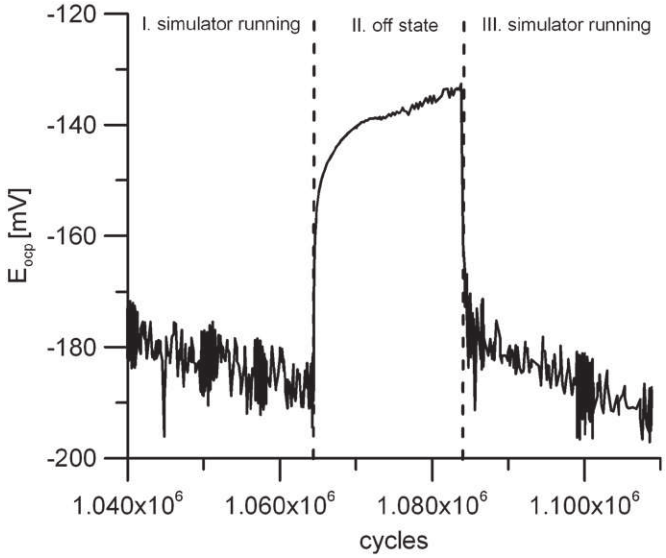

Fig. 4. Open circuit potential of a coated implant.

part of the data scanned in the course of the experiment, i.e. with the simulator running. It is obvious that the open circuit potential ranged at a considerably negative level, its mean value was 740 ± 71 mV. The given region of values, corresponding to still passive titanium [14] indicates continuous damage and reverses formation of a passive layer on the material. This damage evidently occurred in consequence of interrelated movement of the construction individual components. This kept the open circuit potential at the noted relatively negative value. Region II of the diagram shows the course of this quantity after the simulator shutdown. The potential grew in consequence of the surface repassivation by oxygen contained in the electrolyte. After a sufficiently long delay, its value would reach the level corresponding to the specimen non-exposed to a tribological load.

In the second phase of measurements, another model replacement with a DLC coating was exposed. The tested system was produced in the same way as in the case of replacement discussed above. The total thickness of the coating was 4.9 μm, with the DLC coating itself accounting for 1.9 μm. The coating adhesion evaluated by the scratch method was broken at a critical load of 30 N, this values of results were published in previous works [15,16]. In the Mercedes test, the area surrounding the stab was evaluated with parameter 2. This adhesion was found satisfactory for the given application. The coating micro-hardness reached HV 2200 ± 78 at a load of 20 mN.

The testing was carried out under the same conditions as applied in the reference specimen study. The state of the surface was evaluated after 0.5×10^6, 1.0×10^6 and 1.5×10^6 cycles. The implant components did not show any problems visually. The stabilized open circuit potential of the Ti6Al4V alloy coated with a DLC layer and exposed in a saline physiological solution without any mechanical load ranged from 140 to 190 mV. This value corresponded to the reactions of the environment, just as in the case of the passive surface of the titanium alloy, but here it was mainly on the DLC layer. The open circuit potential of the system shifted to a slightly more negative region of 190 ± 20 mV in the course of the implant exposure under load, as evident from Fig. 4. This was probably due to different availability of oxygen from the electrolyte to all the exposed parts of the implant. Fig. 4 illustrates three regions of the open circuit potential. Regions I and III show its course with the simulator running while Region II shows it during the simulator shutdown—from the electrochemical point of view, the system was returning to the stationary state.

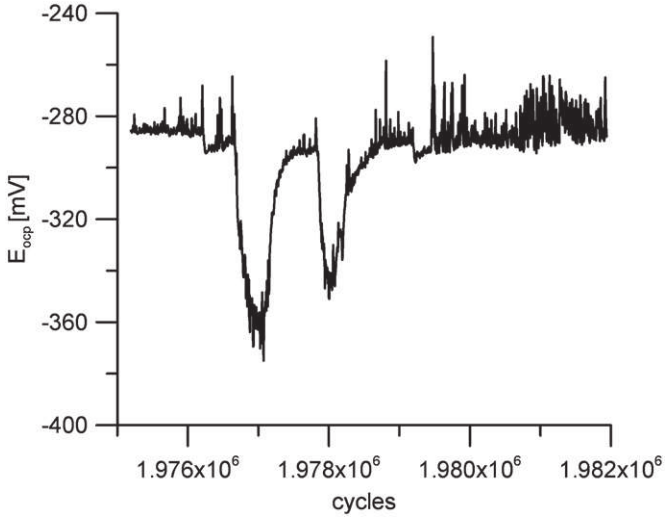

Fig. 5. Open circuit potential of a coated implant at coating damage.

The value of the potential at this level and its course did not testify to any damage of either the coating or the basic material. Its decrease occurred in the fourth part of the measurement (from 1.5 to 2.0×10^6 cycles). Based on these changes, the test was terminated after 1.98×10^6 cycles, and the state of the implant components was analyzed.

Fig. 5 shows part of the open circuit potential as recorded for the implant coated with a DLC layer. Its repeated decrease by about 100 mV is clearly evident at the simulator reaching 1.9766×10^6 loading cycles. This testifies to a local damage of the surface which, however, was eliminated by the system—the increase corresponded to the damaged surface repassivation.

The conducted analysis of the state of the implant at this stage of measurements revealed that there were three critical points of contact between the individual parts of the implant. The pivot with a DLC coating in contact with the PEEK bearing sleeve showed only negligible surface damage at border of contacts (α) and (Δ) throughout the experiment (Fig. 6). In contrast, contact (β), at which the construction allows for the rotation of bearing sleeves in the tibial component—the rod of the pivot connection, is not suited for interrelated sliding mounting in terms of either

Fig. 6. Pivot damage of the coated implant.

construction or technology. From the tribological point of view, this is another risky point where coating would be difficult to apply for technological reasons. In addition, the applied technology cannot ensure the same properties on the entire area of the inner cylindrical surface. The most effective solution in this case seems to be avoidance of interrelated movement of bearing sleeves. Preliminary measurements with blocked sleeves showed this approach to be rather promising. No damage of contact (γ) was noted on the coated implant in the course of the test. The results of tribological measurements reveal that both the coating adhesion and its tribological properties are very good and significantly improved model implant properties.

4. Conclusion

A sliding pair made of the Ti6Al4V alloy covered by DLC coating and a PEEK bearing sleeve represents a solution enhancing the application potential of this combination of materials in joint prosthetics. The conducted measurements proved a qualitative increase in the service life at sliding contact (α) between the pivot and the bearing sleeves of the applied joint implant construction. In order to avoid defects during practical exposure, it has to be ensured that interrelated movement is performed solely by surfaces designed primarily for this purpose. Small damage was indicated on the border of contact surfaces (α) and (Δ) only. Problem free application also requires avoidance of movement on inner surfaces (β), where a corresponding layer quality cannot be guaranteed for technological reasons.

Continual monitoring of the open circuit potential during tribological measurements represents a qualitative shift in detecting the damage of contact surfaces of passivable materials. The obtained results prove the possibility to identify the initial phase of damage and thus make the process of testing more effective.

Acknowledgments

This work was financially supported by research projects MSM 6840770012 (Ministry of Education, Youth and Sports of the Czech Republic), TA01010185 (Ministry of Education, Youth and Sports of the Czech Republic), FR-TI1/573 (Ministry of Industry and Trade of the Czech Republic) and GAP108/10/1782 (Grant Agency of the Czech Republic).

References

[1] Franta L, Novotný P, Suchánek J. Influence of dynamic loading on the wear of knee prosthesis. Workshop Action—COST 533. Eibar, Fundacion Techniker; 2008. p. 97–108.
[2] Franta L, Kronek J, Suchánek J. TKA wear testing input after kinematic and dynamic meta-analysis: technique and proof of concept. Wear 2011;271: 2687–2692.
[3] Tiainen V. Effect of isotopic substitution on IR and ESR properties of mass selected ion beam deposited ta-C films. Diamond and Related Materials 2003;12:900–4.
[4] Liu FX, Yao KL, Liu ZL. Raman spectroscopy of a-C:H:N films deposited using ECR-CVD with mixed gas. Applied Surface Science 2007;253:6957–62.
[5] Akita N, Konishi Y, Ogura S, Imamura M, Hu YH, Shi X. Comparison of deposition methods for ultra thin DLC overcoat film for MR head. Diamond and Related Materials 2001;7:1017–23.
[6] Beghi MG, Ferrari AC, Teo KBK, Robertson J. Bonding and mechanical properties of ultrathin diamond-like carbon films. Applied Physics Letters 2002:81.
[7] Kreysa G, Schütze M.. Corrosion handbook—revised and extended. 2nd ed. Dechema; 2008.
[8] Jones D. Principles and prevention of corrosion. 2nd ed. New Jersey: Prentice-Hall; 1995.
[9] ISO 14 243 (1–3) Implants for surgery—wear of total knee-joint prostheses; 2009.
[10] Romesburg JW, Wasserman PL, Schoppe CH. Metallosis and metal-induced synovitis following total knee arthroplasty: review of radiographic and CT findings. Journal of Radiology Case Reports 2010;4:7–17.
[11] Breen DJ, Stoker DJ. Titanium lines: a manifestation of metallosis and tissue response to titanium alloy megaprostheses at the knee. Clinical Radiology 1993;47:274–7.
[12] Budinski KG. Tribological properties of titanium alloys. Wear 1991;151: 203–217.
[13] Yildiz F, Yetim A, Alsaran A, Efeoglu I. Wear and corrosion behaviour of various surface treated medical grade titanium alloy in bio-simulated environment. Wear 2009;267:695–701.
[14] Pourbaix MN. Atlas of electrochemical equilibria in aqueous solutions. 2nd ed. Houston: NACE; 1974.
[15] Jacobs R, Meneve J, Dyson G, Teer DG, Jennett NM, Harris P, et al. A certified reference material for the scratch test. Surface and Coatings Technology 2003;174:1008–13.
[16] Zhang ZX, Dong H, Bell T. The load bearing capacity of hydrogen-free Cr-DLC coatings on deep-case oxygen hardened Ti6Al4V. Surface and Coatings Technology 2006;200:5237–44.